

Influence of Processing Methods on Microstructure and Multiscale Functional Properties of Nitinol

Zifan Wang

Exeter College



Supervisor:

Prof. Alexander M. Korsunsky

A thesis submitted for the degree of *Doctor of Philosophy*

Department of Engineering Science

University of Oxford

January 2022

Preface

In line with corresponding regulations from the University of Oxford, the content of this thesis is assembled in an integrated format that is based on published papers. According to the regulations (as stated on p.13, GSO.20a guidance document, updated 24 January 2020), "a pre-print version of any published papers should be included as standard". Hence, unlike in conventional thesis, no "List of Figures", nor "List of Tables" were included in this thesis, as each chapter contains a pre-print version of individual papers with notation introduced, and figures and tables numbered.

The assembled papers are all first-authored by the candidate, indicating the candidate's role that consisted of conceiving the study (with supervisor), establishing and maintaining collaborative links with partners, identifying and procuring specimens, performing preparatory processing and characterisation, conducting the experiments described as leader of the team, interpreting the results, and writing them up for publication.

This collection of papers includes a separate introduction that provides an overview of all the papers included, and a separate conclusion that summarises the key findings and assesses their significance. A separate literature review was not included since a focused version of it is present in each constituent paper of this thesis.

All effort has been made to ensure this thesis can be read as a single, coherent document.

Abstract

This thesis focuses on investigating the processing-microstructure-property relationships for the Nitinol material. Processing routes include metal forming process and heat treatment process. Metal forming processes include casting, hot rotary swaging, hot rolling, and cold drawing. The following aspects of the microstructure were taken into consideration: grain morphology (shape), grain size, grain boundary type, crystallinity, preferred grain orientation, precipitates, lattice defects, and phase composition. The functional properties of Nitinol considered in this thesis include Superelasticity and Shape Memory Effect. The mutual link between the functional properties and microstructure evolution is explored.

State-of-the-art experimental techniques were employed to studying the microstructure evolution during functional use of the material. Several key techniques applied form part of synchrotron science that in particular enables bulk material characterisation under *operando* conditions. An X-ray powder diffraction technique was used to provide mesoscale information regarding the lattice strain, phase volume fraction, texture, and microstrain within the material volume. Synchrotron X-ray Laue micro-diffraction provided microscale information regarding crystal lattice orientation, deviatoric elastic strain, and phase distribution. Time-Of-Flight neutron diffraction provided mesoscale information on the lattice strain, phase volume fraction, texture, microstrain, lattice parameters, and precipitate population. In addition, electron microscopy (EM) was extensively used to provide complementary observations from microscale down to the nanoscale. EM techniques included Focused Ion Beam (FIB) milling, Scanning Electron Microscopy, Transmission Electron Microscopy, Electron Back Scatter Diffraction, Energy-dispersive X-ray Spectroscopy. This thesis presents

comprehensive employment of the advanced techniques mentioned above, and demonstrates how the combination of the techniques can bring about new findings to the field.

Computer simulations were conducted to mimic the microstructure evolution *in silico*. The modelling approaches included are Elastic-Plastic Self Consistent (EPSC) modelling and Crystal Plasticity Finite Element Modelling (CPFEM). Once the models were calibrated and verified by experimental observations, they could be used to predict the material microstructure evolution under much wider range of conditions than those used for model validation and refinement.

Through integrating both the experiment and simulation results, this thesis can be used as a systematic / practical guidance to customise the functional properties of Nitinol by means of microstructure engineering.

Acknowledgements

Despite the fact that people of the names mentioned below would probably not have a chance to read this document, this is actually a reminder to myself of their grace and of the blissful time in Oxford.

First and foremost, like what I always wrote in the termly online report, I am very thankful to my supervisor, Professor Alexander Korsunsky, for his powerful support in spirit and material. Being his pupil has been, and will always be one of the greatest honour in my life. He is the icon that I respect and try to pursue forever. It has been a great fortune and pleasure to work under his guidance in the past three years plus four months, I wish I could always have such a star leading my way through the darkness.

The main contributors have been acknowledged in the form of co-authorship in the papers. Besides that, I would like to express my gratitude to Prof. John Huber and Dr. Kalin Dragnevski for examining my transfer and confirmation, and Prof. Barbara Rossi (University of Oxford) and Prof. David Brown (University of Birmingham) for taking time out to read this thesis and sparking discussions during the DPhil viva. Other contributors are Dr. Ali Marie, Dr. Sisini Sasidharan and Dr. Igor Dyson.

I was born into an ordinary family as the only child of my parents. Both of them are school teachers, whose salaries merely match my expenditure in Oxford as a family-funded student. I clearly remember their firm determination to support my studies, which meant that they would have earned nothing for three and half years. They never complained even a single word. They always tell me, once and once again, if I am happy, they are happy. I owe them a debt of gratitude which I shall never be able to repay. My deepest emotion goes to them – Mrs. Qian Yong and Mr. Weizhong Wang.

Today is Chinese New Year 2022, thanks to my relatives and friends for their care.

Publications

All of the candidate's publications are peer-reviewed articles in high-quality journals/encyclopedia:

[1] **Z Wang**, et al., Grain structure engineering of NiTi Shape Memory Alloys by Intensive Plastic Deformation, **ACS Applied Materials & Interfaces** (2022).

[2] **Z Wang**, et al., Ultra-fast quantification of polycrystalline texture via single shot synchrotron X-ray or neutron diffraction, **Materials Characterization** 186 (2022) 111827.

[3] **Z Wang**, et al., Effect of Temperature on Shape Memory Materials, **Encyclopedia of Smart Materials** 4 (2022) 239-253.

[4] **Z Wang**, et al., *In situ* neutron diffraction investigation of texture-dependent Shape Memory Effect in a near equiatomic NiTi alloy, **Acta Materialia** 202 (2021) 135-148.

[5] **Z Wang**, et al., Microstructure evolution in a severely cold-worked NiTi wire during ageing treatment: An *in situ* neutron diffraction study, **Materials Letters** 281 (2020) 128676.

[6] **Z Wang**, et al., Evolution of thermal and mechanical properties of Nitinol wire as a function of ageing treatment conditions, **Journal of Alloys and Compounds** 819 (2020) 153024.

[7] J Chen, **Z Wang** et al., Multiscale stress and strain statistics in the deformation of polycrystalline alloys, **International Journal of Plasticity** 152 (2022) 103260.

[8] F Uzun, C Papadaki, **Z Wang**, et al., Neutron strain scanning for experimental validation of the artificial intelligence based eigenstrain contour method, **Mechanics of Materials** 143 (2020) 103316.

[9] J Chen, E Salvati, F Uzun, C Papadaki, **Z Wang**, et al., An experimental and numerical analysis of residual stresses in a TIG weldment of a single crystal nickel-base superalloy, **Journal of Manufacturing Processes** 53 (2020) 190-200.

[10] LR Brandt, JJ Marie, T Moxham, DP Forstermann, E Salvati, C Besnard, C Papadaki, **Z Wang**, et al., Synchrotron X-ray quantitative evaluation of transient deformation and damage phenomena in a single nickel-rich cathode particle, **Energy & Environmental Science** 13 (2020) 3556-3566.

[11] F Uzun, A Salimon, ES Statnik, C Besnard, J Chen, T Moxham, E Salvati, **Z Wang**, et al., Polar transformation of 2D X-ray diffraction patterns and the experimental validation of the hDIC technique, **Measurement** 151 (2020) 107193.

[12] ES Statnik, A Salimon, C Besnard, J Chen, **Z Wang**, et al., Ovine Bone Morphology and Deformation Analysis Using Synchrotron X-ray Imaging and Scattering, **Quantum Beam Science** 4 (2020) 29-39.

Contents

1 Introduction 1

2 Effect of Temperature on Shape Memory Materials 5

Effect of Temperature on Shape Memory Alloys……...5

Effect of Temperature on Shape Memory Polymers…….23

Effect of Temperature on Shape Memory Ceramics…….32

Summary……..36

3 Evolution of Thermal and Mechanical Properties of Nitinol Wire as a Function of Ageing Treatment Conditions 40

Introduction…….41

Experimental Methodology…….44

Results and Discussion…….46

Conclusion……..…….68

4 Ultra-fast quantification of polycrystalline texture via single shot Synchrotron X-ray/Neutron Diffraction: Methods and Assessments 73

Introduction and objectives……..74

Experimental methods and preliminary analysis……..78

Texture refinement techniques…….81

Results and discussion……..86

Summary and conclusions……98

5 Microstructure evolution in a severely cold-worked NiTi wire during ageing treatment: An *in situ* Neutron Diffraction study 104

Introduction……...104

Experimental and analytical methods…….105

Results and discussion……106

Conclusions……..……111

6 *In situ* neutron diffraction investigation of texture-dependent Shape Memory Effect in a near equiatomic NiTi alloy 113

Introduction and objectives……114

Experimental and analytical procedures…….117

Experimental results and discussion……...123

Summary and conclusions……..148

7 Grain structure engineering of NiTi Shape Memory Alloys: An *in situ* synchrotron X-ray Laue micro-diffraction and powder diffraction study of multiscale lattice rotation, strain field, and phase transformation 154

Introduction and objectives……155

Experimental and analytical details……159

Results and discussion……164

Summary and conclusions……..186

8 Conclusions and outlook 197

Common abbreviations

AC	As Cast
BSE	Back Scatter Electron
CPFE	Crystal Plasticity Finite Element
DSC	Differential Scanning Calorimetry
EBSD	Electron Back Scatter Diffraction
EDS	Energy Dispersive Spectroscopy
EPSC	Elasto-Plastic Self-Consistent
FWHM	Full Width Half Maximum
HAGB	High Angle Grain Boundary
HR	Hot Rolling
HS	Hot Swaging
IPF	Inverse Pole Figure
LAGB	Low Angle Grain Boundary
NiTi	Nitinol
ND	Neutron Diffraction
ODF	Orientation Distribution Function
SEM	Scanning Electron Microscopy
SMA	Shape Memory Alloy
SME	Shape Memory Effect
SMM	Shape Memory Materials
SE	Superelasticity
TEM	Transmission Electron Microscopy
XRD	X-ray Diffraction

Chapter 1

Introduction

The main body of this thesis is composed of six articles, four of which have been published, one is under review after major revision, and the last one has been submitted recently. The articles are listed below sequenced in the list below in a order of logical way:

(1) Effect of Temperature on Shape Memory Materials

(2) Evolution of Thermal and Mechanical Properties of Nitinol Wire as a Function of Ageing Treatment Conditions

(3) Ultra-fast quantification of polycrystalline texture via single shot Synchrotron X-ray/Neutron Diffraction: Methods and Assessments

(4) Microstructure evolution in a severely cold-worked NiTi wire during ageing treatment: An *in situ* Neutron Diffraction study

(5) *In situ* neutron diffraction investigation of texture-dependent Shape Memory Effect in a near equiatomic NiTi alloy

(6) Grain structure engineering of NiTi Shape Memory Alloys: An in situ synchrotron X-ray Laue micro-diffraction and powder diffraction study of multiscale lattice rotation, strain field, and phase transformation.

The first article is a book chapter in the Encyclopedia of Smart Materials, which is an encyclopedia published by ELSEVIER as one of the series of encyclopedias. This article gives an overview of the mechanisms for the three main classes of Shape Memory Materials, while Shape Memory Alloys is the focus of this article. Among all the Shape Memory Alloys, equiatomic Nickel-Titanium alloy (Nitinol) is the focal point. Different processing methods, including the metal forming methods and heat treatment methods

for NiTi alloys, have been reviewed. Meanwhile, the shape memory mechanism of NiTi alloys has been discussed from a crystallographic point of view. The current progress on the effect of processing methods on microstructure and functional properties of Nitinol has also been discussed. Therefore, this article can be read as a full introduction of the scientific background of this thesis.

The second article explores the effect of heat treatment on functional properties of a cold-drawn Nitinol wire. In this article, the processing method is “cold drawing” and “heat treatment”, and the macroscale functional properties include both thermally-induced phase transformation temperature and mechanically-induced phase transformation stress. Besides the mechanical loading test and differential scanning calorimetry, other characterization methods were post-mortem analysis regarding microstructure evolution. A very useful model is proposed that quantifies the effect of heat treatment duration on functional properties.

The third article is about the development of a powerful technique for texture quantification. The article is the second last one being written, but the technique was actually developed at an early stage. Since this technique has been extensively used in the other three articles, it is sequenced as the third one. The technique has two novel features. Firstly, the acquisition time of 30 seconds is incredibly fast compared with that of conventional method of 30 minutes. Secondly, the experiment setup is extremely concise, thus giving a great flexibility in the use of additional equipment for *in situ* sample environment. To some extent, the use of this technique promotes the scientific merit in the subsequent studies.

The fourth article is an *in situ* study of the effect of heat treatment on the mesoscale microstructure of Nitinol. The same material as that used in the second article has been used, and exactly the same heat treatment condition was repeated. However, a Neutron

Diffraction technique was employed to track the microstructure evolution during heat treatment. The results match well with the finding from the second article, and some new findings were made. The second article and this one can be read as a whole as their results are complementary.

The fifth article is a collaboration work with colleagues from Brno University of Technology in Czech Republic. While the Nitinol samples for the first and third articles were obtained from commercial suppliers, in this study we were able to manufacture Nitinol samples ourselves from the very initial state: pure Nickel powder and Titanium powder. Our colleagues have over 20 years of experience in manufacturing NiTi alloys, and they work as consultants for those commercial Nitinol suppliers that produce Nitinol medical stents. Two types of samples were prepared, namely as cast Nitinol and hot rotatory swaged Nitinol. The evolution of crystallographic properties during one-way shape memory effect has been studied by *in situ* neutron diffraction technique. This was a difficult experiment, as the temperature range for shape memory effect was -60°C to 80°C, therefore a cryobox was integrated with an Instron rig, allowing mechanical loading and temperature control at the same time. Meanwhile, neutron diffraction was performed. To the best of author's knowledge, only three scientific facilities have such capabilities in the world, which are located in the UK, US and Japan. In this article, the processing methods are casting and hot rotary swaging, and the functional property that has been investigated is the shape memory effect at mesoscale.

The sixth article is also a collaboration work. The colleagues were from Czech Republic, France, and the UK. Three processing methods were investigated, namely casting, hot rotary swaging, and hot rolling. The functional property that was investigated was superelasticity. This article combines a variety of probing techniques at different scales for a comprehensive study. Synchrotron X-ray powder diffraction technique

provides microstructure information at mesoscale. Synchrotron X-ray Laue micro-diffraction technique provides crystallographic information at microscale. Transmission Electron Microscopy was used for nanoscale probing. Being the last piece of work of this thesis, this article contains all the wisdoms from previous ones.

Chapter 2

Encyclopedia of Smart Materials
Volume 4, 2022, Pages 239-253



Effect of Temperature on Shape Memory Materials

Zifan Wang[1], Alexander M. Korsunsky[1,*]

[1]Department of Engineering Science, University of Oxford, Parks Road, Oxford, OX1 3PJ, U.K.

E-mail: zifan.wang@exeter.ox.ac.uk
E-mail*: alexander.korsunsky@eng.ox.ac.uk

Keywords: Shape Memory Alloys, Shape Memory Polymers, Shape Memory Ceramics, Temperature Effect

Abstract.

This chapter presents a general overview, along with the appropriate details, of the temperature effect on Shape Memory Materials (SMMs). Three main classes of materials, namely, Shape Memory Alloys (SMAs), Shape Memory Polymers (SMPs) and Shape Memory Ceramics (SMCs), are reviewed in terms of the mechanisms of thermo-responsive functional behaviour, the influence of working temperature on functional behaviour, and their microstructure evolution during fabrication and heat treatment, thus covering all important aspects of the topic.

1. Effect of Temperature on Shape Memory Alloys (SMAs)

Despite the fact that the Shape Memory Effect (SME) was observed in an AuCd alloy as early as 1932, it was not until 1971 when significant recoverable strain was found

in a NiTi alloy at the Naval Ordnance Laboratories, USA. Since then, this phenomenon began to arouse extensive interest around the world. According to the type of stimulus that causes SME, SMAs fall into two categories, namely, thermo-responsive, in which the SMA can be activated by heating, and magneto-responsive, in which the SME can be induced by applying a static or alternating magnetic field. In addition to SME, Superelasticity (SE) is another kind of characteristic behaviour of SMMs that has been noted and studied. In SMAs and SMCs, SE shares the same underlying reversible deformation mechanism with the SME, which is known as martensitic transformation. Below, the term 'functional behaviour' in relation to SMMs is used to refer to SME and SE specifically.

Among a wide range of SMAs that were developed and used in different shapes and forms such as wires, films and foams, only three alloy systems, namely NiTi-based (also known as Nitinol), Cu-based (e.g. CuAlNi- and CuZnAl-) and Fe-based (e.g. FeMnSi-, FeNiC- and FeNiCoTi-) are commercially important to a significant extent. NiTi-based SMAs remain the first choice in engineering applications due to their excellent mechanical performance and biocompatibility, although their cost is the highest among the three groups. Cu-based SMAs possess the advantages of moderate cost, good workability in terms of processing, and relatively higher working temperature, due to which they are commonly referred to as High Temperature SMAs (HTSMAs). In contrast, Fe-based SMAs exhibit much weaker SME and lower fatigue life, but can be considered as cheap alternatives.

A systematic overview of the effect of temperature on these three SMA systems is presented in this section. Comparatively speaking, the temperature effect in SMAs is more complex than other SMMs, since the change in temperature may not only trigger SME / SE but also brings about microstructural changes. For instance, one of the main

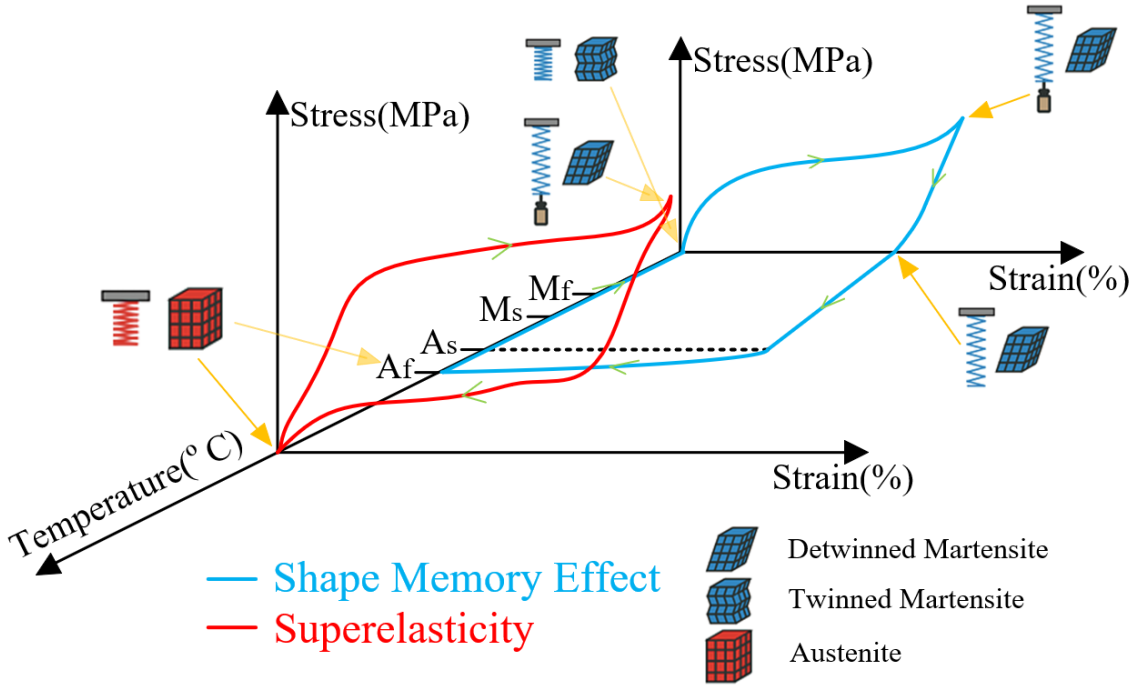


Figure 1. Schematic illustration of functional behaviour of thermo-responsive SMAs. Af, As, Mf, Ms refer to finish temperature of transformation to austenite, start temperature of transformation to austenite, ditto martensite. Red block represents cubic austenite phase, blue block represents monoclinic martensite phase. Phase states during functional behaviour and transformation direction are indicated by arrows.

reasons why Cu-based HTSMAs have shorter fatigue life than NiTi-based SMAs is because these alloys form a brittle γ_2-phase at high temperature which causes intergranular cracking. Hence, the mechanisms of functional behaviour in thermo-responsive SMAs / SMCs, the response of SE to various working temperatures, and the microstructure evolution at high temperature (heat treatment effect) are reviewed in the following section, covering all three prevailing SMA systems as necessary. Besides, the concept and mechanism of a novel functional behaviour, namely temperature memory effect (TME), is also briefly introduced.

1.1 Functional Behaviour of thermo-responsive SMAs / SMCs

The unique functional behaviour, namely SME and SE, as aforementioned, are possessed by SMAs / SMCs that exhibit martensitic transformation. Fig.1 is a schematic illustration of SME and SE. To induce SME, deformation starts at a temperature below M_f in the absence of stress and strain. The material exists in the form of twinned martensite at this state. When stress is applied, the martensite is detwinned, showing pronounced macroscopic strain, usually over 8%. After the stress is withdrawn, the material retains its shape and phase, until the temperature is raised above A_s, at which transformation from martensite to austenite initiates and finishes at A_f. Upon cooling down, austenite transforms back to self-accommodated twinned martensite. To induce SE, deformation starts at temperature above A_f. When stress is applied, austenite directly transforms to detwinned martensite at the strain level similar to that of SME and recovers to austenite upon unloading.

Described above, the functional behaviour and the relevant phase transformation processes are applicable to all thermo-responsive SMA / SMC systems.

1.1.1 The mechanism of thermo-responsive functional behaviour

As described above, the functional behaviour is a phenomenon such that even though a sample is deformed at any temperature through martensite transformation, it regains its original shape by virtue of the reverse transformation upon heating above A_f. The deformation may be of any kind such as tension, compression, torsion, bending etc., as long as the strain does not exceed the critical level.

Martensitic transformation is a diffusionless phase transformation in crystalline solids in which the atoms move cooperatively by a small distance through a shear-like mechanism without changing their relative positions. Here we use a simplified model of a single crystal parent phase, as shown in Fig.2, to present the transformation process at

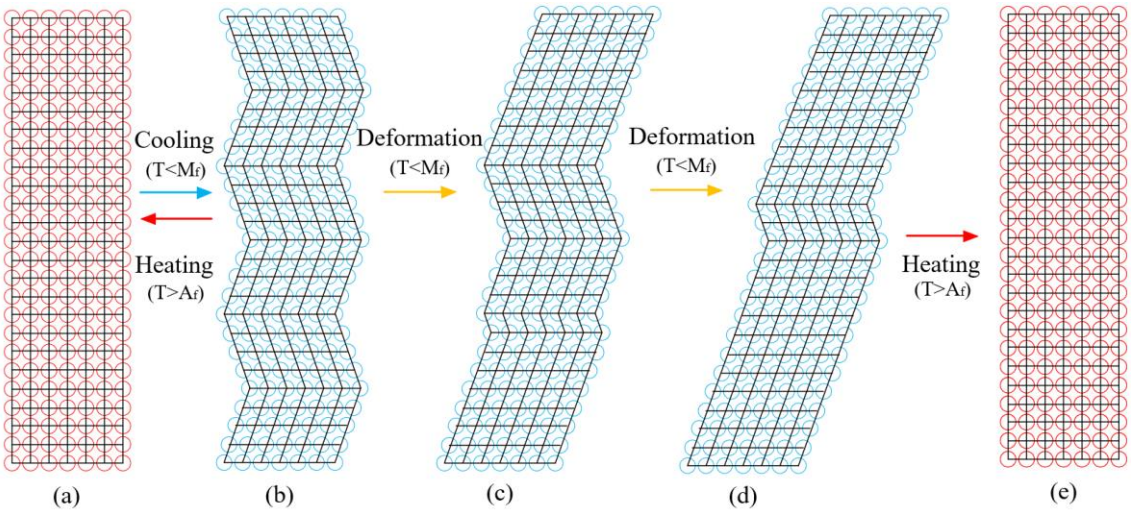


Figure 2. (a) Functional behaviour at the atomic scale. Original austenite single crystal, (b) self-accommodated martensite, (c, d) detwinning deformation in martensite with different variants gradually converge, (e) upon heating detwinned martensite reverts to the original austenite.

atomic scale. Initially the single crystal austenite phase (a) is cooled to a temperature below M_f, martensite is formed in a self-accommodating manner (b). In this process, the macroscopic shape of the sample does not change because of the twin-related deformation and highly mobile lattice planes. If an external force is applied, the twin boundaries move in response in order to accommodate deformation, as illustrated in (c) and (d). Ideally the single crystal becomes a single variant of martensite at high stress level. At this point, martensite transformation finishes. When the sample is heated above A_f, reverse transformation to austenite is induced and the original shape is regained (e). It should be noted that here we assume that the deformation is originated purely from the movement of twin boundaries, and the martensite transformation is crystallographically reversible. If either of the assumptions fails, complete functional behaviour is not obtained. For instance, dislocation movement, grain boundary slides and crack initiation contribute to the degradation of functional behaviour after each working cycle.

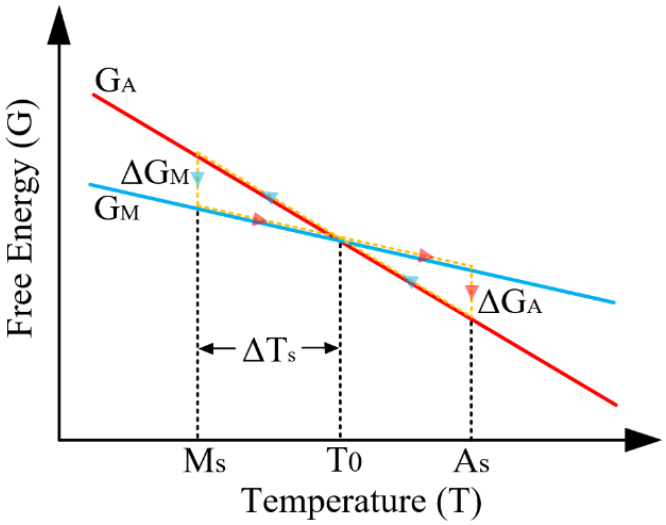
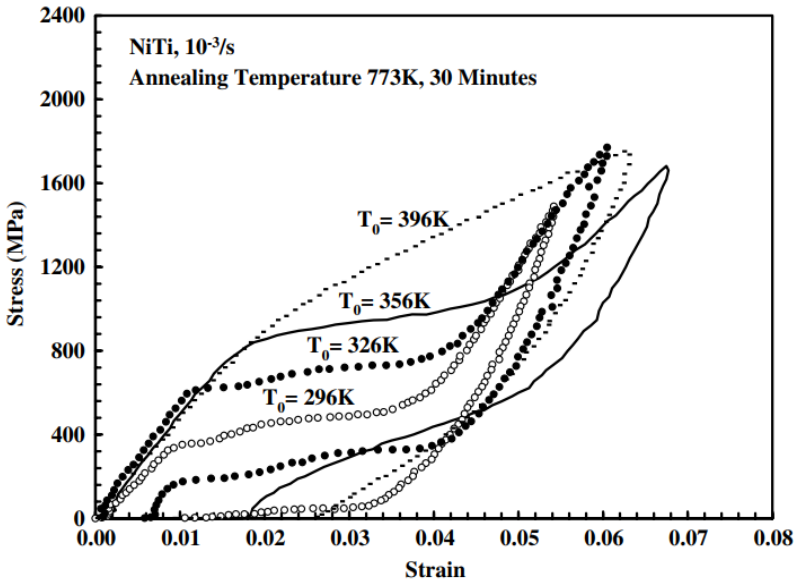


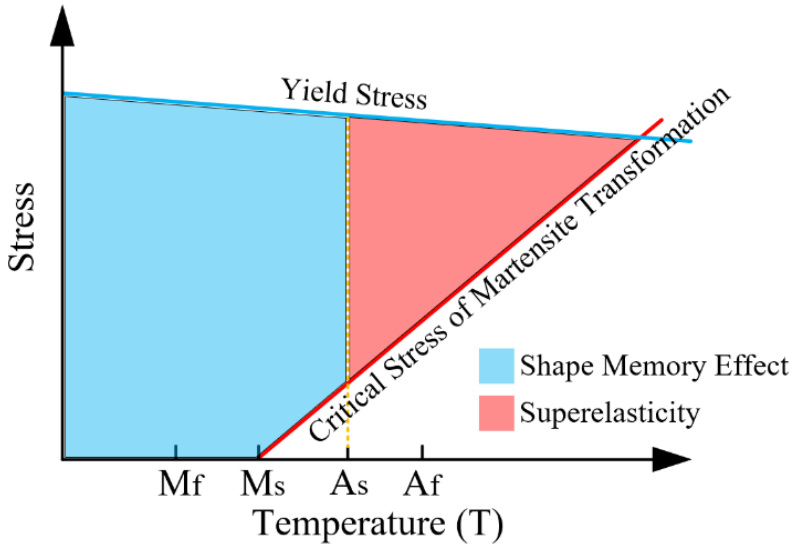
Figure 3. Schematic illustration of relationship between free energy curves for the two phases and M_s and A_s temperatures. Transformation process has been indicated by orange dash line and arrows. ΔT_s is the supercooling and superheating temperature required for transformation.

From the thermodynamic point of view, free energy is the underlying driving force of functional behaviour, whilst the movement of atoms corresponds to the underlying physical phenomenon. Since there is no change in composition during martensite transformation, the free energy curves of both austenite and martensite as a function of temperature may be illustrated as shown in Fig.3. T_0 denotes the thermodynamic equilibrium temperature between these two phases. $\Delta G_M=G_A-G_M$ and $\Delta G_A=G_M-G_A$ represent the driving force for the nucleation of martensite transformation and reverse transformation respectively, where G_A and G_M are the Gibbs free energies of two phases at the same temperature. Previous study has demonstrated $T_0\approx1/2(M_s+A_s)$, which implies that the thermal barriers to induce martensite transformation and reverse transformation are almost the same.

It is important to note that the above mechanism is only applicable to thermo-elastic functional behaviour. For non-thermoelastic Fe-based SMAs, as aforementioned,



(a)



(b)

Figure 4. (a) SE at various working temperatures (Nemat-Nasser and Guo, 2006), Copyright 2006. Reproduced with permission from Elsevier. (b) Schematic illustration of region of functional behaviour and the variation of onset stress of SE with respect to temperature.

the driving force for martensite transformation is so large that the interface between austenite and martensite becomes immobile once the martensite grows to a critical size. In this case, the reverse transformation can only take place by the re-nucleation of

austenite at high temperature approaching the alloy melting point. In other words, the reverse transformation is not truly "reversible" but occurs through the diffusion of atoms, causing difficulties in practical application of Fe-based SMAs.

1.1.2 Effect of temperature on SE

Critical stress (the onset of stress plateau in Fig.1) of martensite transformation is commonly used to characterise superelastic behaviour. Although SE can be induced above A_f, this functional behaviour varies with the varying of working temperature. An experimental demonstration of temperature effect on SE is shown in Fig.4(a). In Fig.4(b), a straight line with positive gradient represents the critical stress to induce SE, following the Clausius-Clapeyron relationship, which can be written as: $d\sigma/dT=-\Delta S/\varepsilon$, where σ is the stress, ε is the transformation strain, ΔS is the entropy of transformation per unit volume. The critical stress level required for SE is proportional to the increment of temperature and ultimately intersects with the slope of yield stress, which is the maximum operational temperature for SMAs. Hence, the domains for functional behaviour are defined, as depicted in Fig.4(b).

1.1.3 Temperature Memory Effect

Temperature Memory Effect (TME), also known as "multi-SME", is the ability to memorize the thermal history. SMAs possessing TME can recover its original shape in a step-by-step manner through one or a few intermediate shapes upon heating.

The "training" process, nominated as "global heating" in Fig.5, is necessary to induce TME. During the reverse transformation in global heating, instead of complete thermal cycling, only partial heating is conducted until a certain temperature Ts (indicated by blue circle). This leads to the incomplete reverse transformation to austenite, that a portion of martensite remains in the matrix. We call the remaining martensite M1 and the

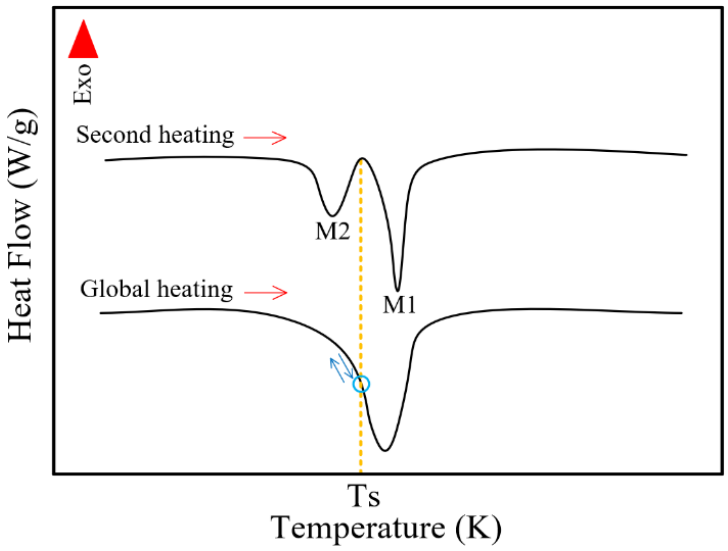


Figure 5. DSC analysis showing the two heating processes to induce TME of NiTi-SMA.

transformed part M2. Decreasing the temperature from the interrupting point down below M_f transforms M2 back into austenite, which marks the completion of "training".

In the second heating process, M2 and M1 transform into the austenite phase sequentially, with a kinetic stop between the transformation. The kinetic stop is always ~3K higher than Ts. Through creating this "breakpoint" in reverse transformation, the material exhibits a two-step shape recovery process, which is the fundamental concept of TME.

Partially different martensite with different levels of elastic strain energy stored in the thermoelastic martensite twins after the thermal training process is believed to be the underlying mechanism for the TME.

1.2 Heat Treatment Effect on SMAs

It should be noted that the fabrication processes preceding heat treatment that involve casting and forming exert a significant influence on the final functional properties of SMAs. In order to obtain cast ingots, pure metals in the form of small

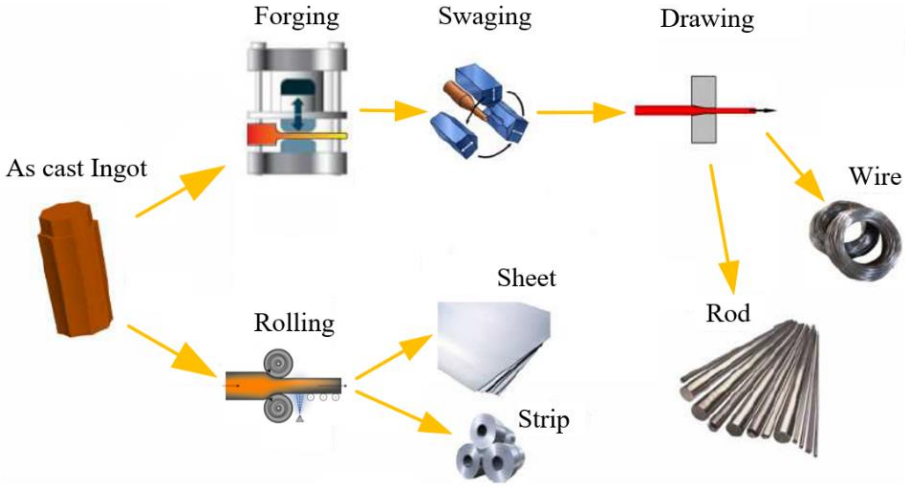


Figure 6. A schematic diagram of common forming operations for shaping SMAs (Kocich, Szurman, Kursa, 2013).

cubes or powder need to be melted in a graphite / alloy crucible using different methods (e.g. vacuum induction melting, plasma melting, vacuum arc melting, etc.). Ingots in the cast state typically exhibit weak functional behaviour (SME / SE). Subsequent forming techniques can shape the ingot into different dimensions, meanwhile improving the functional behaviour, as depicted in Fig.6. Each of the techniques can be divided into hot and cold treatment, indicating the operational temperature during forming. In the cold forming routine it is common to include heat treatment between adjacent steps in order to release the residual stress introduced during plastic deformation, and soften the material to make it easier to shape.

The chosen method of forming leads to distinct microstructural characteristics of the final products. Following (severe) plastic deformation (SPD), SMA products may possess different texture (preferred grain orientation), and grain size varying from tens of nanometers to microns, amorphous phases, crystal defects, surface cracks, etc., especially in sheet and wire where massive lattice distortion occurs, as shown in Fig.7. Introduced during forming processes, the presence of lattice defects (e.g. high density of dislocations)

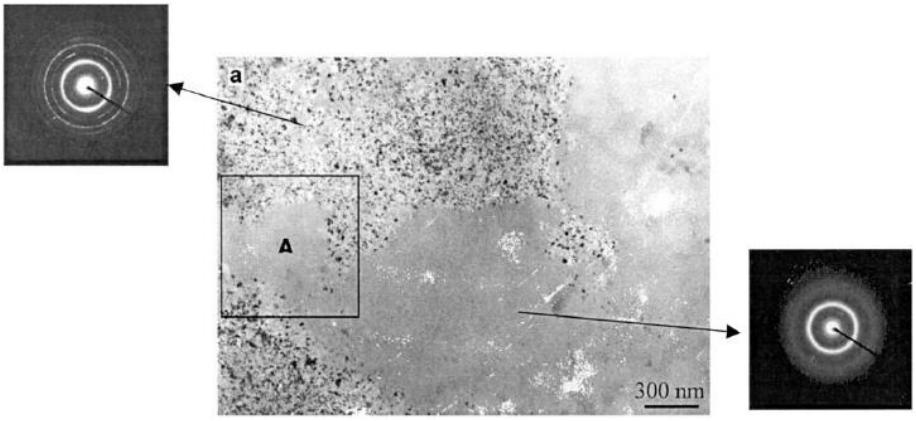


Figure 7. Bright field TEM images of the microstructure of NiTi after SPD, with SAED patterns revealing nanocrystalline (left) and amorphous (right) areas (Sergueeva, Song, Valiev, Mukherjee, 2003), Copyright 2003. Reproduced with permission from Elsevier.

causes internal residual stress and suppresses functional behaviour. Therefore, it becomes essential to apply heat treatment, which ameliorates the microstructural distortion and enhances SME / SE in SMAs.

1.2.1 NiTi-based SMAs

Heat treatment can be classified into annealing and ageing. The temperature of annealing is typically much higher than that of ageing. For equiatomic NiTi- SMAs, for example, annealing is usually done at temperatures above 873K and up to 1273K, during which recrystallization represents the dominant microstructural evolution process in which grains nucleate and grow. Fig.8 (a,b,c) shows EBSD maps of Ti-50.8 at.% Ni alloy subjected to annealing treatments of various duration. The increase of the mean grain size usually follows an exponential relation with heat treatment time, so that there emerges an upper limit of grain size for annealing treatments of practical duration at a given temperature, as shown in Fig.8 (d). This limit is closely affected by the processing history of alloys, including composition and fabrication methods. The main purpose of annealing after forming is to crystallize the amorphous phases and eliminate crystal defects that

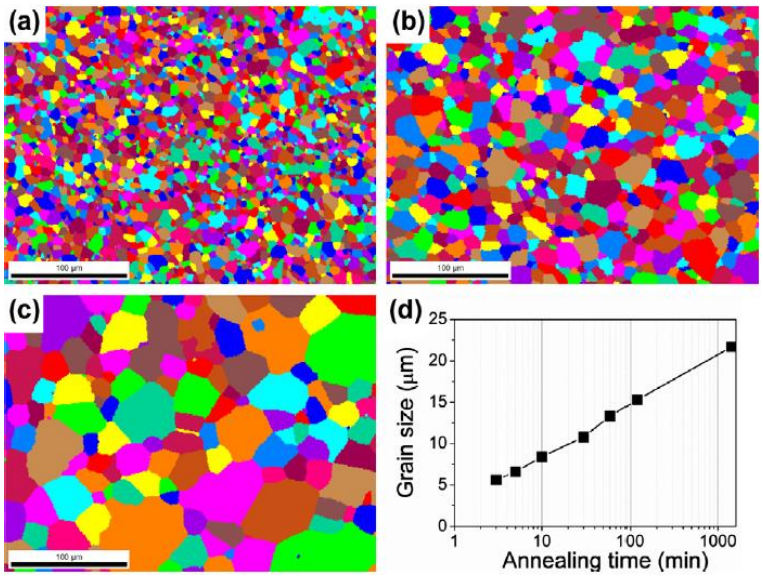


Figure 8. Representative grain morphologies captured by EBSD after annealing at 973K for (a) 3min, (b) 30min and (c)24h. (d) The average grain size as a function of annealing time (Wang, Li, Verlinden, Humbeeck, 2013) , Copyright 2013. Reproduced with permission from Elsevier.

hinder the functional behaviour of SMAs. From another perspective, it is essential to control grain growth, aiming to make the grains neither too large nor too small. SMAs with nanoscale grains have proved to be superior to those with coarse grains in terms of thermal and mechanical properties, such as cyclic stability, ultimate strength, specific latent heat during phase transformation (in most applications this should be as low as possible), temperature variation along gauge length, strain rate and temperature dependence of transformation stress. On the other hand, ultra-fine grain and nanocrystalline microstructures were found to suppress the formation of self-accommodated particle arrays for precipitation during ageing treatment, while precipitation is known to benefit the SME / SE behaviour through giving impetus to phase transformation. With comprehensive consideration of these two factors, the ideal grain size for a balanced performance in NiTi- SMAs should be between 20~150nm.

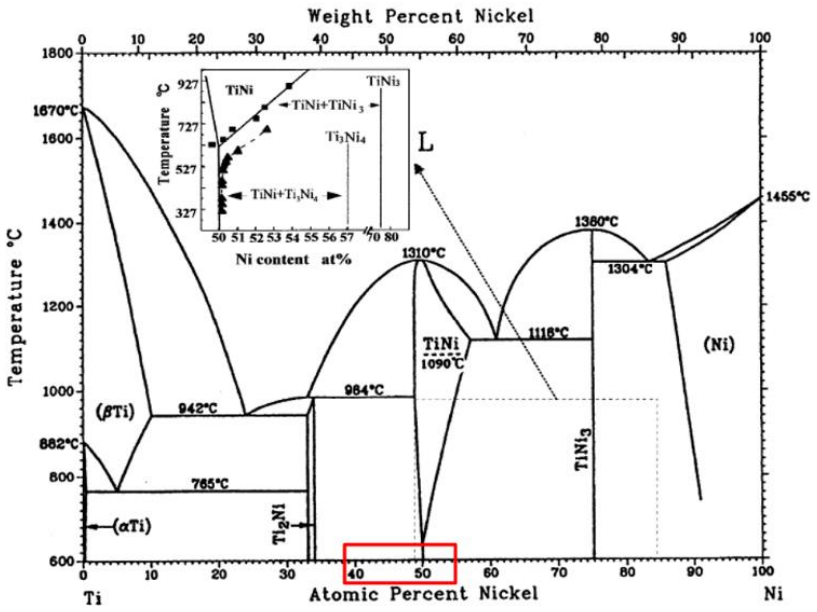
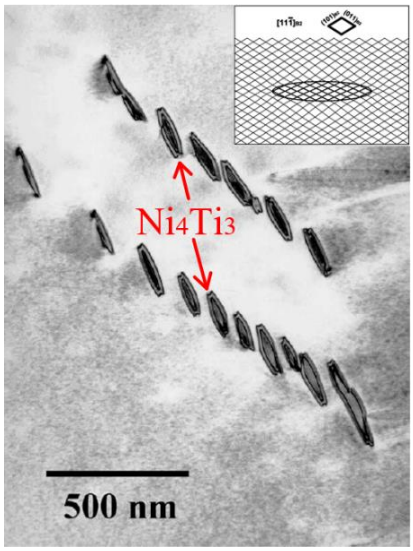
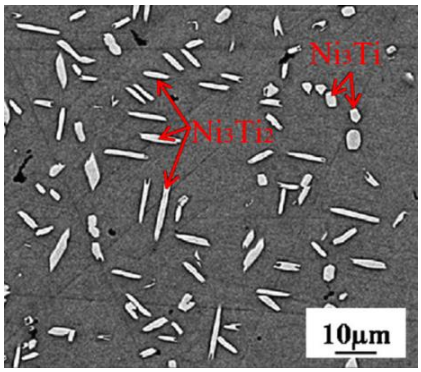


Figure 9. Binary Ni-Ti equilibrium phase diagram with the inset showing the metastable precipitation phases (Otsuka and Ren, 2005), Copyright 2005. Reproduced with permission from Elsevier.

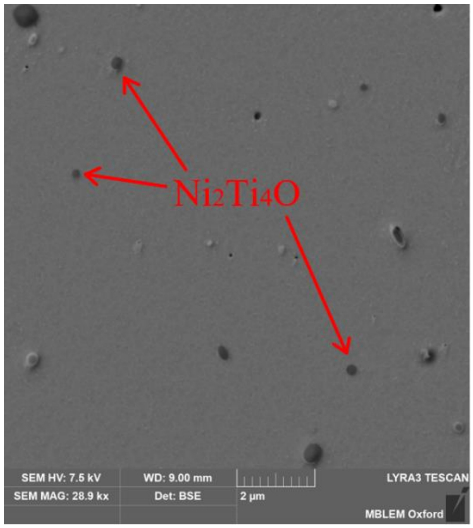
Ageing heat treatment is beneficial for the formation of precipitate phase. Conducted between 573K to 873K for varying durations, the ageing process produces precipitates of different intermetallic compounds in NiTi- SMAs, including Ni_4Ti_3, Ni_3Ti_2, Ni_3Ti and $NiTi_2$. The corresponding phase diagram is shown in Fig.9, and the widely used composition range is marked in red square. At lower ageing temperature and shorter ageing time, Ni_4Ti_3 phase appears. In contrast, Ni_3Ti_2 phase can be observed with medium heat treatment conditions, whilst at higher ageing temperature and longer ageing times Ni_3Ti phase appears. Both Ni_4Ti_3 and Ni_3Ti_2 are intermediate metastable phases, whilst Ni_3Ti is the equilibrium phase. A large proportion of the $NiTi_2$ phase in NiTi- SMAs is found to form a spheroidal Ni_2Ti_4O oxide, which is introduced during annealing treatment at high temperature and retains stable morphology and volume fraction in the subsequent ageing process.



(a)



(b)



(c)

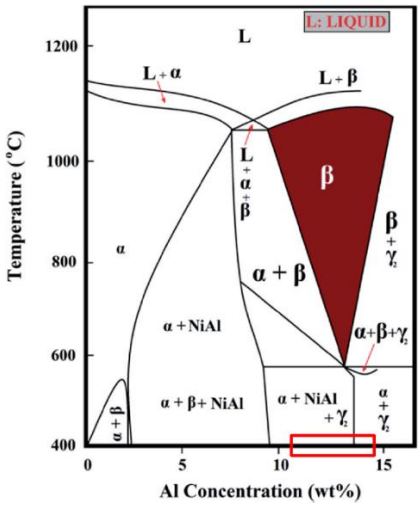
Figure 10. (a) TEM micrograph of coherent Ni_4Ti_3 precipitate, forming two parallel arrays. One precipitate nucleates in the stress field of another. The inset is a schematic illustration of the lattice distortion (stress field) of the matrix surrounding the lenticular precipitate (Otsuka and Ren, 2005; Allafi, Dlouhy, Eggeler, 2002), Copyright 2005, Copyright 2002. Reproduced with permission from Elsevier. (b) SE image of Ni_3Ti_2 and Ni_3Ti precipitate (Hornbuckle, Yu, Noebe et al., 2015), Copyright 2015. Reproduced with permission from Elsevier. (c) BSE image of spheroidal Ni_2Ti_4O oxide (Wang, Everaerts, Salvati, Korsunsky, 2019), Copyright 2019. Reproduced with permission from Elsevier.

It has been extensively acknowledged that the formation of these precipitates, especially Ni_4Ti_3, exerts significant control over the phase transformation behaviour involved in the SME and SE effects in NiTi- SMAs through two interaction mechanisms, i.e. through changing the internal stress state and local Ni concentration in the parent phase. Therefore, this precipitation phenomenon offers a suitable engineering route to tailor the SME / SE behaviour of NiTi- SMAs. The microscopic images of the aforementioned four types of precipitates are depicted in Fig.10. It should be noted that the presence of all types of precipitation largely depend on fabrication history, not simply the ageing treatment conditions.

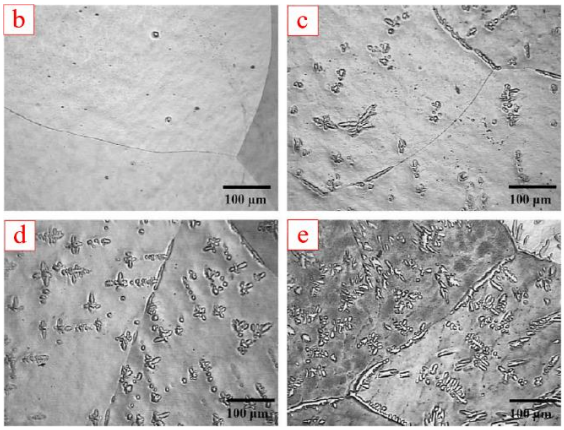
A widely accepted fabrication routine for commercial NiTi- structures involves as the first step grain size refinement by means of plastic deformation often performed as a part of the forming process. As the second step, solution annealing treatment is employed to increase the grain size in a controllable manner, determining the general functional properties of the NiTi- material. Finally, precise adjustment of the functional behaviour can be achieved through precipitation during ageing treatment.

1.2.2 Cu-based SMAs

Among Cu-based SMAs, CuAlNi- alloys possess a higher thermal stability than CuZnAl- alloys. Thus CuAlNi- alloys are developed for applications at around 200 °C while the more ductile CuZnAl- alloys have the maximum working temperature of 120 °C. Above these temperatures rapid degradation in the functional behaviour occurs as a result of ageing effects. Fig.11(a) illustrates the phase diagram for CuAlNi- alloys. Varying Al concentration leads to the change in functional behaviour, but Al content should always be kept within the range marked by the red square so that the alloy exists as single β-phase at high temperatures. In other words, annealing treatment conditions



(a)



(b,c,d,e)

Figure 11. (a) Phase diagram of the CuAlNi- ternary SMA system with 3wt% Ni. Effective range of Al concentration is marked in red square (Lojen, Anzel, Kneissl et al., 2005), Copyright 2005. Reproduced with permission from Elsevier. Micrographs of samples quenched from: (b) 853K, (c) 833K, (d) 823K, (e) 804K, after a slow cooling from 1073K, showing dendrite-shaped γ_2-phase (Cuniberti, Montecinos, Lovey, 2009), Copyright 2009. Reproduced with permission from Elsevier.

should lie within the β-phase domain for equilibrium to produce functional properties. Here the β-phase is equivalent to the TiNi-phase in Fig.9, in that both have superlattices associated with the body centred cubic structure and serve as the parent austenitic phase

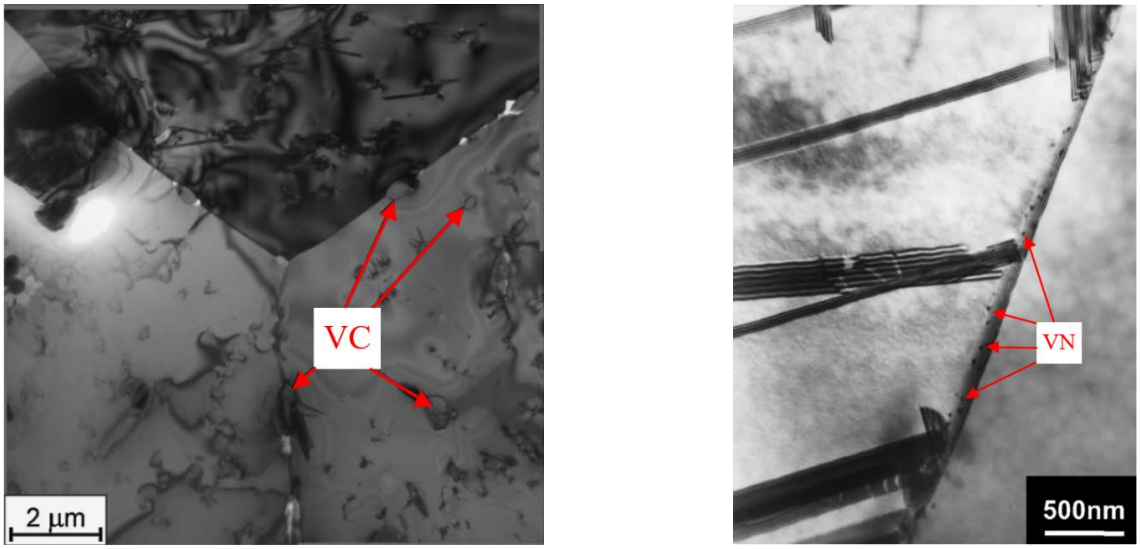
at working temperature. Upon solidification, the β-phase may undergo a eutectoid transformation into undesirable α-phase (F.C.C.) and brittle γ_2-phase (Cu_9Al_4 cubic, shown in Fig.11(b,c,d,e)). Therefore, a sufficiently high cooling rate is required, e.g. water quenching, together with the presence of ternary element Ni, to retard the transformation towards these two phases. It can be deduced from above that the repulsive ageing effect is associated with the precipitation of α-phase and brittle γ_2-phase, which impose restriction on the deformability and applicability of the material. Despite that, mechanical failure caused by brittle intergranular fracture can be relieved through the precipitation of X-phase (Cu_2ZrTi) and Y-phase (Cu_2ZrAl) by incorporating additional elements Ti and Zr.

For CuZnAl- alloys, the phase diagram is similar to Fig.11(a) except for the missing γ_2-phase. Instead, a transitional bainite phase can appear between the low temperature β-phase and high temperature α-phase. Precipitating during ageing treatment above 200 °C, the bainite ultimately transforms to α-phase in CuZn- alloy. In the course of this process the functional metastable β-phase is gradually substituted, which in turn causes the degradation of functional behaviour.

Hence, unlike NiTi- SMAs, the fabrication route of commercial Cu-based SMAs only involves forming and annealing treatment, followed by rapid cooling to prevent high-temperature β-phase from decomposing at room temperature. Meanwhile ageing effects should be avoided.

1.2.3 Fe-based SMAs

The situation in Fe-based SMAs seems to be more complex than the other two classes considered above. In spite of an original discovery of the FeMnSi SMA back in 1982, there has been so far no substantial development of practical applications of Fe-based SMAs due to their intrinsic drawbacks, such as limited functional properties (e.g.



(a) (b)

Figure 12. (a) TEM overview of VC precipitates in grains and at grain boundaries in Fe-17Mn-5Si-10Cr-4Ni-1(V,C) SMA after ageing at 850°C for 2h (Dong, Klotz, Leinenbach et al., 2009), Copyright 2009. Reproduced with permission from John Wiley and Sons. (b) TEM overview of VN precipitates at grain boundaries in Fe-28Mn-6Si-5Cr-1(V,N,C) SMA after annealing at 1150°C for 1h (Kubo, Nakamura, Farjami, Maruyama, 2004), Copyright 2004. Reproduced with permission from Elsevier.

recoverable strain of less than 4%), poor corrosion resistance and "training" difficulties, most of which are attributed to the non-thermoelastic martensitic transformation, either γ(F.C.C.)/ε(H.C.P.) or γ/α(B.C.C. or B.C.T.[body-centred tetragonal]). Over the past two decades, extensive work has been dedicated to improving the functional behaviour of Fe-based SMAs. Among them, precipitation through ageing treatment has proved to be a relatively effective way to tackle the issue. Strengthening of γ-phase (austenite) and the formation of a large elastic strain field that provides preferential nucleation sites for ε-phase (martensite) are believed to be the underlying mechanisms of enhancement of functional properties caused by precipitates.

Owing to the fact that till the present time the functional properties of Fe- SMAs remain unsatisfactory, investigations into additional alloying elements have always been popular. Different compositions of alloys produce numerous types of precipitates, to list exhaustively, for instance, TiC, $Cr_{23}C_6$, VC (Fig.12a), VN (Fig.12b), $(Ni,Fe,Co)_3Ti$, $(Ni,Fe,Co)_3(Al,Ta)$, $Fe_5Ni_3Si_2$, NbC and many others. But one trend is fairly well-established that the higher density, larger size and better coherency of these precipitates, the more enhancement to the functional behaviour.

Besides ageing treatment, annealing treatment also affects SME and SE in Fe- SMAs positively or negatively, depending on the temperature. If the temperature is high, the density of stacking faults is reduced, leading to a low nucleation rate during stress-induced γ to ε transformation. The expansion of martensite plates becomes favoured instead of the formation of new martensite plates. Coarse martensite plates produce local strains which cause local slip deformation and reduction in the reversibility of martensitic transformation, in turn resulting in the degradation of functional properties. If the temperature is low, complex defects (jogs, kinks and vacancy clusters) cannot be eliminated that suppress SME / SE. Meanwhile, those dislocation structures favourable for phase transformation are removed at low temperature. Therefore, a moderate annealing temperature ~600°C is optimal to form dislocation structures beneficial for the functional behaviour of Fe-based SMAs.

2. Effect of Temperature on Shape Memory Polymers (SMPs)

The history of SMPs can be traced back to 1906, which is quarter of a century earlier than the discovery of SME in metallic alloys. In fact, a heat shrinkable polymer can be considered under the category of SMPs. Made of polyethylene (PE) and ethylene-vinyl acetate (EVA), heat shrinkable tubes have been widely used to shield conductors,

welding, and circuits in electrical engineering. Nevertheless, it is the emergence of commercial polynorbornene-based SMP invented by Nippon Zeon Cooperation from Japan in 1984 that has been widely regarded as the beginning of SMP era. The thermoplastic polyurethane (TPU) SMP invented by Hayashi and the thermo-set polystyrene SMP from Cornerstone Research Group, USA, are probably the two most successful marketed SMPs. SMPs can be classified based on the external stimulus of Shape Memory Effect, namely temperature sensitive (can be induced by heat transfer, electric current and induction), light sensitive, water/moisture/solvent sensitive, and redox sensitive.

Unlike SMAs whose thermal and mechanical properties are tuneable through heat treatment, the properties of SMPs are fixed and can no longer be altered once they are fabricated. SMPs are processed or thermally set to have an original permanent shape without causing internal stress. Therefore, the change in temperature only acts as a driving force of SME in thermally responsive SMPs, types of which include polyacrylate copolymers, polynorbornene, segmented polyurethane, epoxy-based polymers, segmented polyurethane ionomers, crosslinked polycyclooctene, crosslinked ethylene-vinyl acetate copolymer and so on.

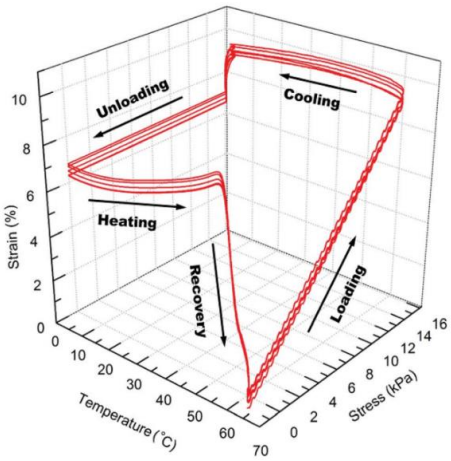
Although thermally responsive SMPs have various compositions, and many more are being proposed, the underlying molecular mechanisms of SME in them is similar. Alongside the most fundamental functional behaviour, namely, the dual-SME, thermally responsive SMPs can also exhibit multi-SME upon heating after proper programming is performed. With multi-SME, the material displays one or a few intermediate shape(s) between the permanent and temporary shapes during recovery. Furthermore, the temperature memory effect (TME), which is similar to that of SMAs discussed in section 1.1.3, was also found in some SMPs. Under TME, the temperature corresponding to the

maximal recovery stress in deformation-constrained recovery (with the strain kept constant upon heating) is close to the temperature at which programming (corresponding to “loading” process in Fig.13(a)) is conducted.

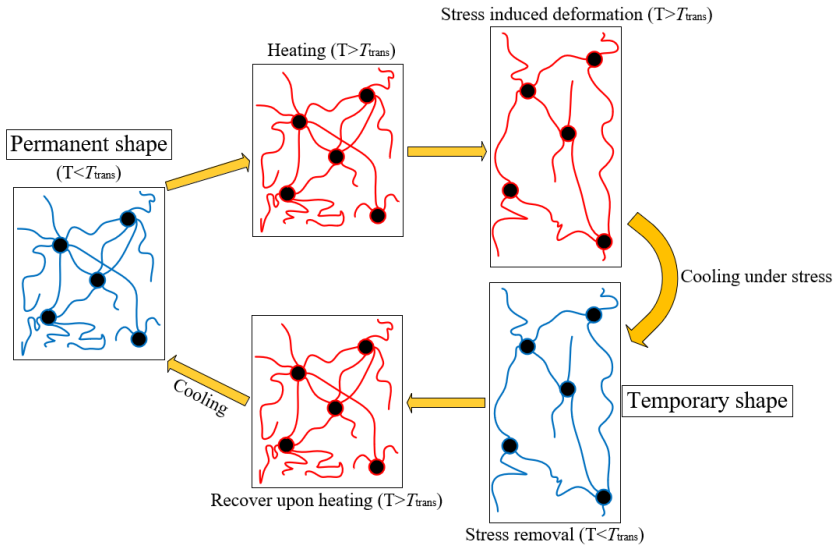
In this section, the mechanisms of thermally responsive functional behaviour, namely dual-SME, multi-SME and TME that are commonly observed in temperature sensitive SMPs, will be elaborated, covering major aspects of temperature effect on SMPs.

2.1 Mechanism of Thermally Responsive Dual-Shape Memory Effect in SMP

The underlying mechanism for the SME in SMPs is the dual segment system. Those common thermally responsive SMPs have a physical cross-linking structure, crystalline/amorphous hard phase, or chemical cross-linking structure to form network points that act as elastic segments, on the one hand, and a low temperature transition of crystalline, amorphous or liquid-crystal phase to form the molecular chains that contain transition segment (also known as switch), on the other. Generally speaking, heat-activated SMPs can be separated into four classes depending on the nature of crosslinking in the elastic segment, and the crystallinity of the transition segment. Accordingly, SMPs may contain chemically crosslinked glassy thermosets or chemically crosslinked semicrystalline rubbers in the elastic segment, and physically crosslinked amorphous thermoplastics or physically crosslinked semicrystalline block copolymers in the ‘switch’.



(a)



(b)

Figure.13 (a) Stress-strain-temperature curves of dual-SME cycles (Xu and Budhlall, 2018)-Published by The Royal Society of Chemistry, Copyright 2018. Reproduced with permission from The Royal Society of Chemistry. (b) The molecular mechanism of dual-SME. Red lines and blue lines correspond to molecular chains of high and low mobility, respectively. Black dots represent network points.

First of all, we take the most fundamental case, i.e. dual-SME, for the discussion of molecular requirements and general mechanism for thermal responsive SMPs. Fig.13(a,b) illustrates typical cycles for thermally induced dual-SME and the molecular mechanism. At ambient temperature, the SMP has a rigid shape. Upon heating above the melting

temperature (T_m), for crystalline SMPs, or glass transition temperature (T_g), for amorphous SMPs, or liquid crystal clearing temperature (T_{cl}), for liquid-crystal phase, the material turns into a soft rubber or elastomer due to the increased mobility of molecular chains. For the sake of simplification, we define this critical temperature as T_{trans}. At high temperature, deformation becomes easier when external force is applied. This macroscopic deformation is associated with changes in the molecular chain conformation and entropy. After cooling down to a temperature below T_{trans}, the deformation remains after the external force is withdrawn. From the molecular level standpoint, this is due to the reduction in chain mobility that freezes the deformed chain conformation; meanwhile, the entropic energy is stored in the system. This temporary shape remains stable until the next heating process above T_{trans}, after which the SMP recovers its permanent shape. At the molecular scale, heating releases the entropic energy and activates the mobility of molecular chains, thus driving the chains back into the highest entropic state corresponding to the permanent shape.

This process suggests the switchable nature of the transition segment. It should be noted that the switches do not exist along the entire molecular chain but segmentally. Segments without switches are not responsible for effecting conformation change, while they can still accommodate the attendant deformation in a highly coordinated manner. What is more, to give rise to entropic change during macroscopic deformation (programming) to provide the driving force for recovery, slippage between polymer chains should be kept to the minimum. Such a mechanism is provided by the network structure consisting of network points as shown in Fig.13(b). As long as the network remains stable, any macroscopic deformation of the elastic segment would raise the internal energy state of the material instead of plastic deformation.

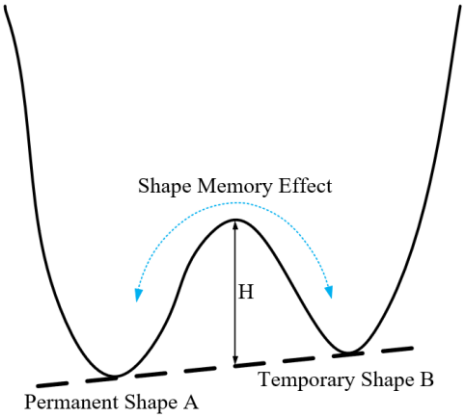


Figure.14 Energy change between two shapes (after Salimon, Senatov, Kalyaev, Korsunsky, 2020).

From the thermodynamic point of view, permanent shape A and temporary shape B of SMPs are separated by an energy barrier H (Fig.14). Shape B possesses higher internal energy than shape A. During the programming process, energy from external source is required to raise the internal energy level, allowing atomic diffusion under applied force. Diffusion ceases when the chemical potentials of all atoms are everywhere the same and the system is in equilibrium, signifying the formation of temporary shape B. To activate SME, the barrier has to be overcome again by applying energy from external stimulus, such as heating.

Overall, network points and molecular chains are the two basic structures of SMPs, the former determining the permanent shape and the latter offering flexibility under external stress.

2.2 Mechanism of Thermally Responsive Multi-Shape Memory Effect in SMP

The triple-shape memory effect in SMP was originally reported in 2006. Since then, many groups have invented different multi-SME SMP systems. Generally, the diverse strategies to achieve multi-SME in SMPs are strongly related to the chemistry / physics intrinsic to the matrix, or to extrinsic factors such as novel activation methods.

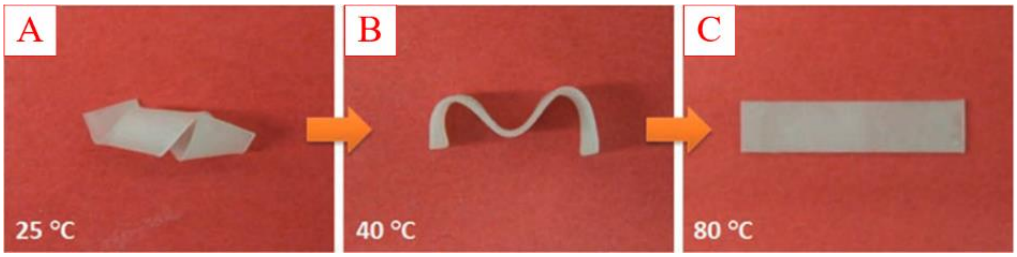


Figure.15 Sequential triple-SME recovery from temporary shape A, B, to permanent shape C (Luo and Mather, 2010), Copyright 2010. Reproduced with permission from John Wiley and Sons.

Hence these strategies can be classified into two categories: intrinsic multi-SME, and extrinsic multi-SME.

2.2.1 Intrinsic Multi-SME

Intrinsic multi-SME is not fundamentally different from the dual-SME. In fact, their molecular mechanisms are quite similar, that the network structure should be present in a multi-SME SMP for memorizing the permanent shape, while the transition segment appears to be more versatile. For instance, to exhibit triple-SME, SMP should possess two transition segments for two independent temporary shapes, and the material also needs to be programmed twice at two different transition temperatures ($T_{trans,1}$ and $T_{trans,2}$). It should be noted that though intermediate shapes also appear in dual-SME via on and off the heating, they are not independent of each other. The multi-SME (triple) SMP in Fig.15 shows its recovery with a discontinuous temporary shape B, “interrupting” the recovery path from shape A to shape C.

The simplest form of a multi-SME SMP possesses distinct thermally responsive switches and one set of network points. One of the examples is the combination of polyethylene glycol (PEG) monoacrylate and polydimethacrylate crosslinker, which yields a crosslinked PCL ($T_{trans,1}$=50°C) network with PEG ($T_{trans,2}$=34°C) chains.

Sufficient studies show that combination of any two thermal responsive switches would enable multi-SME. Other multi-switch design approaches include interpenetrating polymer network (IPN), blending two or more polymers with different T_{trans} followed by crosslinking, and doping small molecules into a dual-SME system to introduce additional transition phases, etc.

Various molecular switching mechanisms other than thermally activated ones can also be utilized to enable multi-SME, either by themselves or by merging with a thermally responsive switch. For instance, in hyperbranched coumarate polyester synthesized by polycondensation between glycol and diester monomer containing cinnamic double bonds, a photo-responsive molecular switch is incorporated into the matrix with a thermal responsive switch. By the same principle, cellulose-whiskers (water responsive switch) can be merged within a polyurethane matrix (thermal responsive switch).

Despite the fact that the above examples seem to imply the fact that the number of temporary shapes is determined by the number of switches, multi-SME can still be achieved within a single transition segment, on the premise that the switch has a broad range of transition temperature. Nafion (transition ranging from 50°C to 130°C), a thermoplastic perfluorosulfonic acid ionomer, is an example of such material. Within its transition temperature range, the material can exhibit numerous temporary shapes at various temperatures after proper programming. In comparison with conventional approaches, the material also allows the change in recovery temperature through reprogramming, instead of synthesizing new switches to the matrix. The mechanism of this approach to multi-SME can be simply understood by regarding the single transition segment as the collective contribution of a large amount of small transition segments distributed in the broad transition temperature range, thus programming at a certain

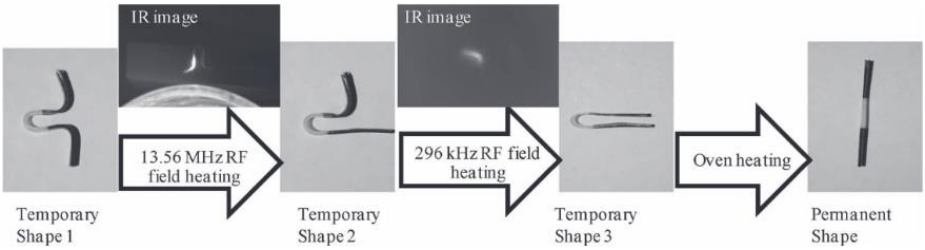


Figure 16. RF selective actuation of extrinsic multi-SME (He, Satarkar, Xie, Cheng, Hilt, 2011), Copyright 2011. Reproduced with permission from John Wiley and Sons.

temperature is actually programming the transition segments corresponding to that temperature.

2.2.2 Extrinsic Multi-SME

Extrinsic thermally responsive multi-SME is activated by various non-direct heating methods, which enables temporal control of the multi-step recovery process, yet the molecular switch mechanism remains the same as dual-SME.

A typical example of the approach taken is to incorporate iron oxide particles and carbon nanotubes into SMP, using the principle that different nanofillers respond to AC magnetic field heating effect of different radiofrequencies (RF). As shown in Fig.16, the sample was programmed into a "Ω" shape. When the sample was exposed to a high RF, transition segments compounded with carbon nanotubes were heated and recovered. At low RF, iron oxide particles took effect, and the remaining segment was finally recovered by direct heating.

2.3 Mechanism of Temperature Memory Effect in SMP

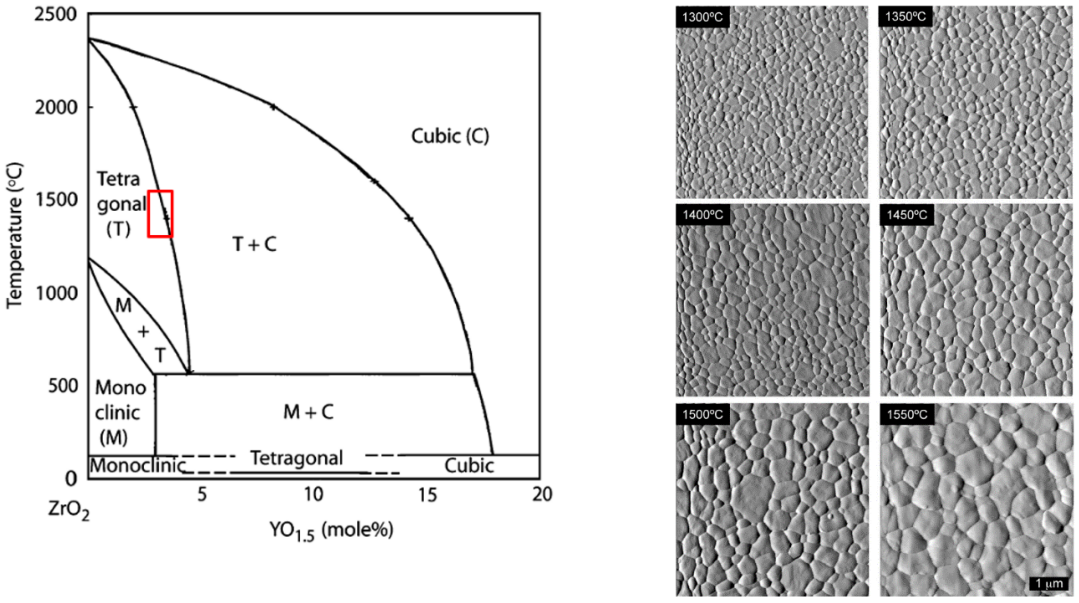
TME was initially discovered in a polyvinyl alcohol (PVA)-carbon fibre SMP in 2007. Likewise, the material also exhibits a broad range of transition temperature as Nafion. Deformed at T_{trans} within the transition temperature range during programming, T_{trans} can be traced back since it is nearly equivalent to the temperature at which the

structure exhibits maximum recovery stress upon heating under constant strain. Later on, the generality of TME was confirmed for other SMPs with a broad transition temperature range.

The mechanism of TME can be readily explained using the same theory as multi-SME behaviour in Nafion. T_{trans} is associated with a particular group of activated transition segments. During the recovery process, this group of transition segments are reactivated at T_{trans}, resulting in the maximum recovery stress. This suggests that though single switch multi-SME and TME are not phenomenologically identical, they share the same molecular basis.

3. Effect of Temperature on Shape Memory Ceramics

The early study of shape memory ceramics (SMCs) dates back to 1988 when Reyes-Morel *et al*. demonstrated SME and SE in a CeO_2-stabilized tetragonal zirconia polycrystal (ZrO_2). Since then, zirconia-based ceramics have been extensively studied due to their potential as shape memory materials. Among all three categories of zirconia containing ceramics (tetragonal zirconia polycrystalline (TZP), partially stabilized zirconia (PSZ) and zirconia toughened/dispersed ceramics (ZTC/ZDC)), TZP is the most promising candidate so far. Unalloyed zirconia ceramics assumes three crystallographic forms from low to high temperature: monoclinic ($T<\approx950°C$) (which here, in the context of SMMs, is referred to as "martensite"), tetragonal ($T>\approx1170°C$) (which is referred to as austenite) and cubic phases ($T>\approx2370°C$), while tetragonal phase offers the best mechanical properties. Stabilized by yttria (Y_2O_3), magnesium oxide (MgO) or ceria (CeO_2) additions, TZP is a material capable of accommodating nearly 100% metastable tetragonal-ZrO_2 phase (corresponding to the cubic austenite phase of NiTi-based SMAs in section 1) at room temperature, thus allowing the maximal transformation strain during



(a) (b)

Figure.17 (a) Phase diagram of yttria-stabilized TZP, with ideal sintering domain marked in red square (Witz, Shklover, Steurer, Bachegowda, Bossmann, 2007), Copyright 2007. Reproduced with permission from John Wiley and Sons. (b) Atomic force micrographs showing the TZP microstructure as a function of sintering temperature (Denry, Peacock, Holloway, 2010), Copyright 2010. Reproduced with permission from John Wiley and Sons.

deformation. Among these, Y_2O_3 is considered the most effective dopant as less than 4mol% is sufficient to stabilize fully the tetragonal phase. Despite all the encouraging advancements of functional properties of TZP, the brittle material still remains at experimental stage because of the propensity for intergranular cracking and only a few life cycles of SME / SE.

The bulk zirconia-based SMCs are prepared using a conventional ceramic fabrication procedure, namely powder → compaction (isostatic pressing) → sintering (between 1300 ~1550°C). In terms of the temperature effect, the topic is closely related to the discussion of SMAs above. The mechanisms of thermally driven functional

behaviour in SMCs are nearly equivalent to those of SMAs from both the molecular and thermodynamic point of view. For more detailed information, the readers are referred to §1.1.1. Below, the effects of the sintering temperature and heat treatment on microstructural evolution are reviewed.

3.1 Effect of Sintering Temperature on Microstructure of SMCs

The equilibrium phase diagram of Y_2O_3-ZrO_2 (Y-TZP) is shown in Fig.17(a), in which the choice of the element ratio (Y_2O_3 to zirconia) and sintering temperature are the key adjustable parameters.

As aforementioned, Y_2O_3 and other dopants serve as stabilizers to retain the metastable tetragonal phase at room temperature, the amount of which should be at least 3mol%. However, excessive addition of Y_2O_3 induces dual phase microstructure consisting of both cubic and tetragonal polymorphs. Detrimental cubic grains are enriched in yttrium, which in turn leads to a depletion of yttrium in the neighbouring tetragonal grains, thus reducing the stability of tetragonal phase at room temperature and weakening the functional behaviour of SMCs. In addition, the presence of cubic grains also has an adverse impact on the ageing resistance of Y-TZP.

Regarding the choice of sintering temperature, neither should it be too low or too high. On the one hand, the processing should be conducted at sufficiently low temperatures to avoid the occurrence of the dual-phase microstructure (tetragonal and cubic). On the other hand, high temperature is favourable to obtain fully dense and homogeneous material. What is more, high temperature sintering leads to coarser grain microstructure (Fig.17(b)) which is advantageous to functional behaviour of SMCs, because intergranular cracking, as one of the dominant reasons of material failure in SMCs, can be improved by introducing larger grains. Nonetheless, several studies show

that the largest tetragonal grain size in Y-TZP that can be meta-stably retained at room temperature is of the order of a few microns, depending on the element ratio. Therefore, a narrow range of sintering temperature, exactly between 1400°C and 1450°C, has to be chosen to process the Y-TZP.

3.2 Effect of Heat Treatment on Microstructure of SMCs

Right after sintering process, annealing treatment is usually employed to improve the properties of SMCs. Conducted within a temperature range between 1100°C and 1850°C, annealing results in the optimization of grain size, phase assemblage and mechanical properties. However, choosing of the annealing conditions also remains to be controversial among investigators.

Long (~100h), isothermal annealing treatment at low temperatures (i.e. 1100-1500°C) is desirable from a technical perspective since it maximizes the fraction of tetragonal phase, and a potentially higher fracture toughness due to the coarsened microstructure. But from an economic perspective, this approach is hardly preferable in industrial environments.

By contrast, increasing the annealing temperature for shorter period becomes a compromise between cost and performance. In spite of decreasing the fraction of transformable tetragonal phase, annealing at elevated temperature does not sharply degrade the functional properties of SMCs due to the coarsening of microstructures. Moreover, tetragonal grain size can be much coarser than that of low temperature annealing, which may greatly enhance the fracture toughness and strength.

Fig.18 depicts the influence of annealing conditions on the microstructure of Y-TZP. As discussed, both (low temperature)-(long time) and (high temperature)-(short time) approaches are applicable to retain the functional tetragonal phase to the maximum,

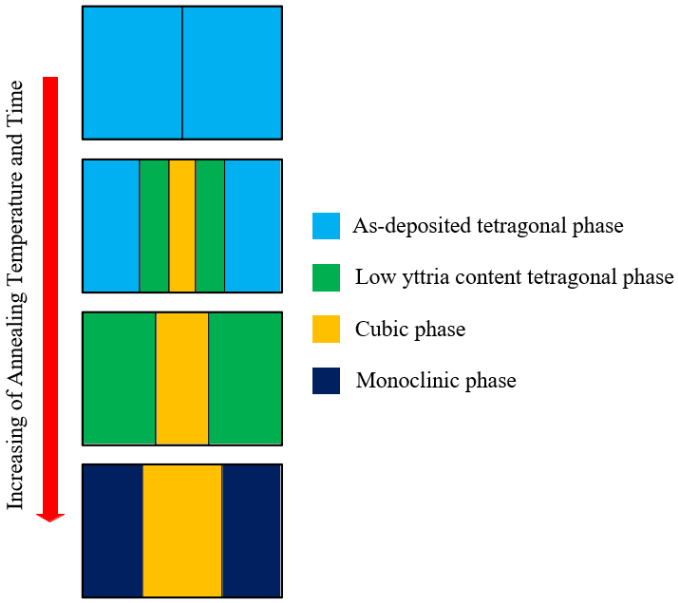


Figure.18 Schematic illustration of phase distribution and evolution upon annealing.

though the latter may induce a small fraction of undesirable cubic phase, whilst (high temperature)-(long time) annealing should always be avoided as it leads to the complete substitution of monoclinic and cubic phase for the tetragonal phase.

4 Summary

The Roman poet Lucretius wrote in the first century BCE: “One man’s meat is another man’s poison”. This saying may well summarize the theme of this chapter, in that there is no specific law of temperature effect that can be uniformly applied to all SMMs.

Taking the heat treatment effect as an example, the functional properties of NiTi- and Fe-based SMAs can be significantly enhanced through proper annealing and ageing treatment conditions. In contrast, Cu-based SMAs require rapid cooling after annealing to avoid ageing effect. The paradox here is that Cu-based SMAs are commonly used as high temperature SMAs whose working temperature is up to a few hundred degrees, thus their performance tends to degrade rapidly after each working cycle. Whilst the heat

treatment of SMCs requires more precise control in temperature and time than its counterparts.

The temperature effects on SMPs seem to be less contradictory. Temperature sensitive SMPs exhibit SME by means of heating, while the functional behaviour is found to be not tuneable through heat treatment. The only way known so far is to change the composition or training routine.

Regarding the mechanisms of thermal responsive functional behaviour, SMAs and SMCs obey the same rule, in that macroscopic deformation originates from the change in lattice structure by the diffusionless rearrangement of atoms.

Importantly, however, from the standpoint of thermodynamics, the functional behaviour of all SMMs has similar triggering mechanism: the enthalpy of the temporary shape is higher than that of the permanent shape, so that increasing the temperature raises the internal energy to overcome the energy barrier between the two shapes, and to re-establish the previous configuration.

Modelling / computational simulation approaches of temperature effect on SMMs, especially SMAs, have been developed extensively throughout the last decade. Among which, the phase field method is probably the most promising due to its advantage in depicting the evolution of multi phases simultaneously. Not only the nucleation and growth of precipitates, but also the details of microstructural evolution can be simulated. Even so, the modelling efforts are hasty to some extent, for they only catch a glimpse of the whole process. What is more, certain assumptions must be obeyed and practical meaning of model parameter is yet to be explained. In consideration of the ‘immaturity’ and ‘complexity’ of those approaches, they are not discussed in this chapter.

The detailed understanding of the intricate properties and behaviour of specific materials has always been restricted by the limits of probing techniques, and the same

applies to the temperature effect on SMMs. The principle of 'inferring the underlying essence from observable phenomena' continues to apply at the time when more effective intra-atomic probing techniques become more readily accessible, opening the prospects of further insightful progress in the materials science of shape memory materials.

References

Allafi, J.K., Dlouhy, A., Eggeler, G., 2002. Ni4Ti3-precipitation during ageing of NiTi shape memory alloys and its influence on martensitic phase transformations. Acta Materialia. 50, 4255-4274.

Cuniberti, A., Montecinos, S., Lovey, F.C., 2009. Effect of γ_2-phase precipitates on the martensitic transformation of a β-CuAlBe shape memory alloy. Intermetallics. 17, 435-440.

Denry, I.L., Peacock, J.J., Holloway, J.A., 2010. Effect of heat treatment after accelerated aging on phase transformation in 3Y-TZP. J Biomed Mater Res Part B: Appl Biomater. 93B, 236-243.

Dong, Z., Klotz, U.E., Leinenbach, C., Bergamini, A., Czaderski, C., Motavalli, M., 2009. A novel Fe-Mn-Si shape memory alloy with improved shape recovery properties by VC precipitation. Adv. Eng. Mater. 11, 40-44.

He, Z.W., Satarkar, N., Xie, T., Cheng, Y.T., Hilt, J.Z., 2011. Remote controlled multishape polymer nanocomposites with selective radiofrequency actuations. Adv Mater. 23, 3192-3196.

Hornbuckle, B.C., Yu, X.X., Noebe, R.D., Martens, R., Weaver, M.L., Thompson, G.B., 2015. Hardening behaviour and phase decomposition in very Ni-rich Nitinol alloys. Mater Sci and Eng A. 639, 336-344.

Kocich, R., Szurman, I., Kursa, M., 2013. The methods of preparation of Ti-Ni-X alloys and their forming. Shape Memory Alloys – Processing, Characterization and Applications, InTech, Croatia, pp.27-52.

Kubo, H., Nakamura, K., Farjami, S., Maruyama, T., 2004. Characterization of Fe-Mn-Si-Cr shape memory alloys containing VN precipitates. Mater. Sci. Eng. A. 378, 343-348.

Lojen, G., Anzel, I., Kneissl, A., Krizman, A., Unterweger, E., Kosec, B., Bizjak, M., 2005. Microstructure of rapidly solidified Cu-Al-Ni shape memory alloy ribbons. J. Mater. Process. Technol. 162-163, 220-229.

Luo, X.F., Mather, P.T., 2010. Triple-shape polymeric composites (TSPCs). Adv Funct Mater. 20, 2649-2656.

Nemat-Nasser, S., Guo, W.G., 2006. Superelastic and cyclic response of NiTi SMA at various strain rates and temperatures. Mechanics of Materials. 38, 463-474.

Otsuka, K., Ren, X., 2005. Physical metallurgy of Ti-Ni-based shape memory alloys. Progress in Materials Science. 50, 511-678.

Salimon, A.I., Senatov, F.S., Kalyaev, V.A., Korsunsky, A.M., 2020. Shape memory polymer blends and composites for 3D and 4D printing applications, in *3D and 4D Printing of Polymer Nanocomposite Materials: Processes, Applications, and Challenges*, Elsevier, 161-189.

Sergueeva, A.V., Song, C., Valiev, R.Z., Mukherjee, A.K., 2003. Structure and properties of amorphous and nanocrystalline NiTi prepared by severe plastic deformation and annealing. Mater Sci and Eng A. 339, 159-165.

Wang, X., Li, C., Verlinden, B., Humbeeck, J.V., 2013. Effect of grain size on aging microstructure as reflected in the transformation behaviour of a low-temperature aged Ti-50.8 at.% Ni alloy. Scripta Materialia. 69, 545-548.

Wang, Z., Everaerts, J., Salvati, E., Korsunsky, A.M., 2019. Evolution of thermal and mechanical properties of Nitinol wire as a function of ageing treatment conditions, Journal of Alloys and Compounds. https://doi.org/10.1016/j.jallcom.2019.153024.

Witz, G., Shklover, V., Steurer, W., Bachegowda, S., Bossmann, H.P., 2007. Phase evolution in yttria-stabilized zirconia thermal barrier coatings studied by Rietveld refinement of X-ray powder diffraction patterns. J Am Ceram Soc. 90 (9) 2935-2940.

Xu, H., Budhlall, B.M., 2018. Gold nanorods or nanospheres? Role of particle shape on tuning the shape memory effect of semicrystalline poly(-caprolactone) networks. RSC Adv. 8, 29283-29294.

Chapter 3

Journal of Alloys and Compounds
Volume 819, 5 April 2020, 153024

Evolution of Thermal and Mechanical Properties of Nitinol Wire as a Function of Ageing Treatment Conditions

Zifan Wang [a], Joris Everaerts [a], Enrico Salvati [a], Alexander M. Korsunsky [a, *]

[a] Department of Engineering Science, University of Oxford, Parks Road, Oxford, OX1 3PJ, U.K.

*Corresponding author. E-mail address: alexander.korsunsky@eng.ox.ac.uk

Keywords: NiTi shape memory alloys, Ageing, EBSD, BSE, DSC, Superelasticity.

Abstract. As-received and cold-worked 55Ni-45Ti wt% Nitinol wire samples were subjected to various ageing treatments. Experiments show that the properties of as-received Nitinol, including microstructure, critical temperatures in thermally induced phase transformation, and critical stresses / strains in mechanically induced phase transformation, change significantly after ageing process at 773K for different durations ranging from 10 minutes to 5 hours. EBSD / BSE / EDS results show that the predominant microstructural evolution is a large increase in Ni_4Ti_3 precipitate volume fraction, while grain growth is negligible. DSC results show that as-received material exhibits little to no phase transformation during heating-cooling cycling at 5K/min, while various ageing durations lead to the emergence of phase transformation that occur at different critical temperatures. Tensile loading experiment conducted using a test rig equipped with a

heater revealed the evolution of mechanically induced phase transformation behaviour. Mathematical models are proposed to predict the dependence of critical temperatures and critical stresses / strains on the ageing treatment conditions and alloy composition.

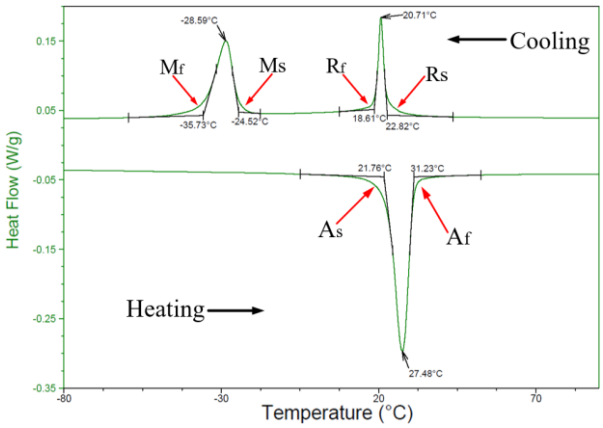
1. Introduction

Shape memory alloys (SMAs) belong to a class of shape memory materials (SMMs), which have the ability to "memorize" and recover their previous form through reversible solid-state phase transformation [1,2]. Among SMAs, NiTi binary alloys, also known as Nitinol, have been widely investigated due to their superior engineering properties, namely Shape Memory Effect (SME) and Superelasticity (SE). Both SME and SE are related to the transformation between Austenite (B2 Cubic) and Martensite (B19' Monoclinic), with the possible emergence of an intermediate R-phase (Trigonal). Phase transformation can be induced thermally, by heating/cooling within a certain temperature range, or mechanically, by loading/unloading in some temperature regimes. The thermally induced phase transformation can be investigated using differential scanning calorimetry (DSC) [3]. Critical phase transformation temperatures (R_s, R_f, M_s, M_f, A_s, A_f) can be determined by processing the DSC heating and cooling curves [4], as illustrated in Fig.1 (a). On the other hand, the mechanically induced phase transformation can be characterized using tension/compression tests conducted at temperatures between A_f and T_d (the highest temperature for stress-induced martensite transformation). A stress plateau due to the austenite to martensite transformation becomes apparent in these tests [5,6]. Critical stresses / strains (σ_{Ms}, σ_{Mf}, σ_{As}, ε_{Ms}, ε_{Mf}, ε_{As}) and dissipated energy density (W_d) can be extracted from complete superelastic curves [4,5,7,8], as illustrated in Fig.1 (b).

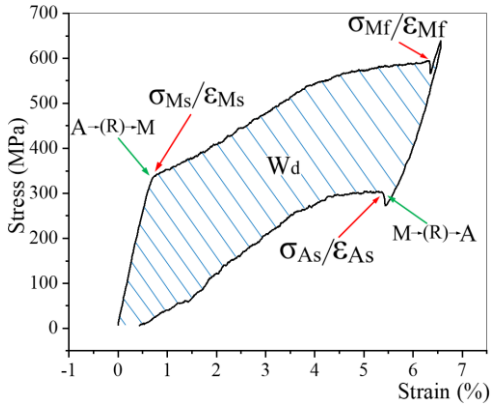
The phase transformation phenomena outlined above underlie the ultimate engineering performance of NiTi shape memory alloy, as they determine the temperature and stress values for material to use in applications.

Heat treatment exerts significant impact on the microstructure of shape memory alloy [9,10,11]. Heat treatment can be classified into annealing and ageing. The annealing temperature is much higher than ageing, usually above 873K and up to 1273K for Nitinol. NiTi alloys recrystallize during solution annealing, grains nucleate and grow, thus annealing is used at initial stage in fabrication. The effect of grain size on the phase transformation behaviour of Nitinol has been discussed in [12,13,14,15]. The ageing treatment is beneficial for the formation of precipitate phases [16]. Conducted between 573K to 873K for varying durations, the ageing process produces precipitates of different intermetallic compounds, including Ni_4Ti_3, Ni_3Ti_2, Ni_3Ti and $NiTi_2$ [17]. It has been extensively acknowledged that the formation of these precipitates, especially Ni_4Ti_3, to a large extent controls the phase transformation behavior in NiTi shape memory alloy through two interaction mechanisms, i.e. through changing the internal stress state and local Ni concentration in the parent phase [18,19,20,21,22,23,24,25].

Although the aforementioned studies have comprehensively discussed the phase transformation behaviour resulting from the microstructure evolution in NiTi alloys subjected to various heat treatment methods, these studies were mostly qualitative, which restrict the application of research conclusions to engineering tasks, since the conditions of each experiment are unique, and the observations are not readily transferable. What is more, most up-to-date published studies lack the establishment of analytical or empirical models for the phase transformation behaviour, leaving a knowledge gap in the quantitative analysis of these results. Therefore, it is necessary to propose mathematical models that can describe and predict the trends in the phase transformation behaviour of



(a)



(b)

Figure.1 Definition of critical temperatures, i.e. start (Rs) and finish (Rf) temperature for austenite to R-phase transformation, start (Ms) and finish (Mf) temperature for R-phase to martensite transformation, start (As) and finish (Af) temperature for martensite to austenite transformation (a), critical stresses and strains, i.e. martensite transformation stress (σ_{Ms}) and strain (ε_{Ms}), upper plateau stress (σ_{Mf}) and strain (ε_{Mf}), lower plateau stress (σ_{As}) and strain (ε_{As}), dissipated energy density (Wd), onsets of phase transformation between austenite (A) and martensite (M) with the potential intermediate rhombohedral (R) (b).

NiTi shape memory alloys after various heat treatment processes. Both mechanically and thermally induced phase transformation behaviours are of critical importance in engineering applications, which can be characterized by critical temperatures (R_s, R_f, M_s,

M_f, A_s, A_f) and critical stresses and strains (σ_{Ms}, σ_{Mf}, σ_{As}, ε_{Ms}, ε_{Mf}, ε_{As}), as shown in Fig.1. Being able to customize these values through conducting proper heat treatment conditions would guide manufacturers to produce the most suitable NiTi shape memory alloys for different applications.

In the present research, effect of ageing treatment conditions on the microstructure and phase transformation was studied on NiTi alloy with a fixed element ratio. Electron backscatter diffraction (EBSD) and backscatter electron (BSE) images of the sample cross section were collected to determine the grain structure and precipitate evolution during heat treatment. The values of critical temperatures and critical stresses / strains were extracted from thermal and mechanical experimental data using widely accepted methods. A model is proposed that establishes the mathematical relationship between the volume fraction of precipitate, the Nickel:Titanium composition ratio and the temperature and duration of heat treatment. Subsequently, general models that can predict the dependence of the critical temperatures and critical stresses / strains in NiTi alloy as a function of composition and heat treatment processing history were built. Model parameters were determined through fitting the experimental results and excellent agreement was found between theory and experiment. The outcome of this study provides guidance for ageing treatment schedules to achieve the desired thermal-mechanical properties of NiTi shape memory alloy, thus saving labour and resources.

2. Experimental Methodology

A commercially available reel of pure binary NiTi wire (Goodfellow, Ni55/Ti45 wt.%) of 0.8mm diameter was used in the present study, the composition of which was verified by EDS. As-received samples were aged at 773K for several durations, namely, 10, 20, 30, 40, 50 minutes, and 1, 2, 3, 4, 5 hours. Together with the as-received sample, all aged

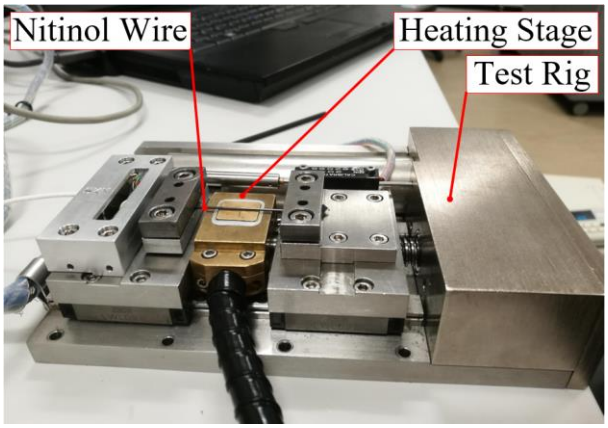


Figure.2 Layout of Deben tensile test rig for superelastic experiments.

samples were subjected to testing using DSC, tensile test, and EBSD / BSE / EDS mapping and imaging.

The thermal phase transformation was induced with a modulated TA DSC Q2000 in the wide temperature range between 183K and 473K to cover the complete transformation process. Samples for DSC tests were first cut into bars 2-3mm in length, aged and immediately quenched in cold water. In the DSC tests, the samples were first cooled down to 183K and held for 5 minutes to stabilize, then heated to 473K, held isothermally for 2 minutes, and cooled again to 183K. The ramp rates for heating/cooling were both 5K/min. Two cycles were conducted at each sample to eliminate random error.

The mechanically induced phase transformation experiments were carried out on Deben MicroTest 600N tensile rig, see Fig.2. The samples were 30mm in gauge length. A copper heating stage was used to keep the samples at a constant temperature. For deformation experiments, the temperature value of 323K was set, approximately 20K higher than A_f, to enable complete recovery in SE behavior. A constant strain rate of 5×10^{-4} s^{-1} was set, as recommended in the literature, to avoid self-heating effect during tensile loading. Two loading/unloading cycles were conducted on each sample to achieve a stable stress-strain response curve for subsequent data analysis. To reveal complete superelastic

stress-strain curve [4,6], the mechanical loading mode was phenomenon control, that each sample was stretched till the completion of the stress plateau where the stress / strain gradient suddenly increases with a nearly linear response distinct from the stress plateau, which indicates that the majority of parent austenite phase has transformed to detwinned martensite, though residual austenite may exist [26].

To prepare for EBSD / EDS / BSE mapping and imaging experiments, the samples were embedded in an epoxy resin base. Only sample cross sections were exposed, 0.5024mm^2 each. The samples within the mount were mechanically ground step by step, down to 1200 grit SiC paper, followed by polishing using 9μm, 3μm, to 1μm diamond suspension. The Buehler PoliMat 2 electropolishing device was used at the final stage, with an electrolyte containing 80% methanol and 20% sulfuric acid (95% concentration) [27]. SEM analysis shows that ~25μm of material was removed by electropolishing in the direction normal to the surface. The high-resolution EDS energy spectra were analyzed and Kikuchi patterns were indexed by commercial software AZtec from Oxford Instruments. The grain size distribution statistics was analyzed through commercial software HKL CHANNEL 5 from Oxford Instruments.

3. Results and Discussion

3.1 EBSD / BSE / EDS

EBSD patterns of the as-received and 5 hours' aged samples are shown in Fig.3 (a) and (b). Phase information used for indexing Kikuchi-pattern is shown in the middle. The hit rate was 85% for as-received sample and 89% for 5 hours' aged sample. Grain size analysis was conducted on both patterns, which indicates that the average grain size (diameter) is approximately 334nm in Fig.3 (c) and 399nm in Fig.3 (d). This confirms that grain growth was very limited during ageing, in agreement with [16,28]. In these two previous studies the effect of ageing temperature on grain growth was studied, and it was

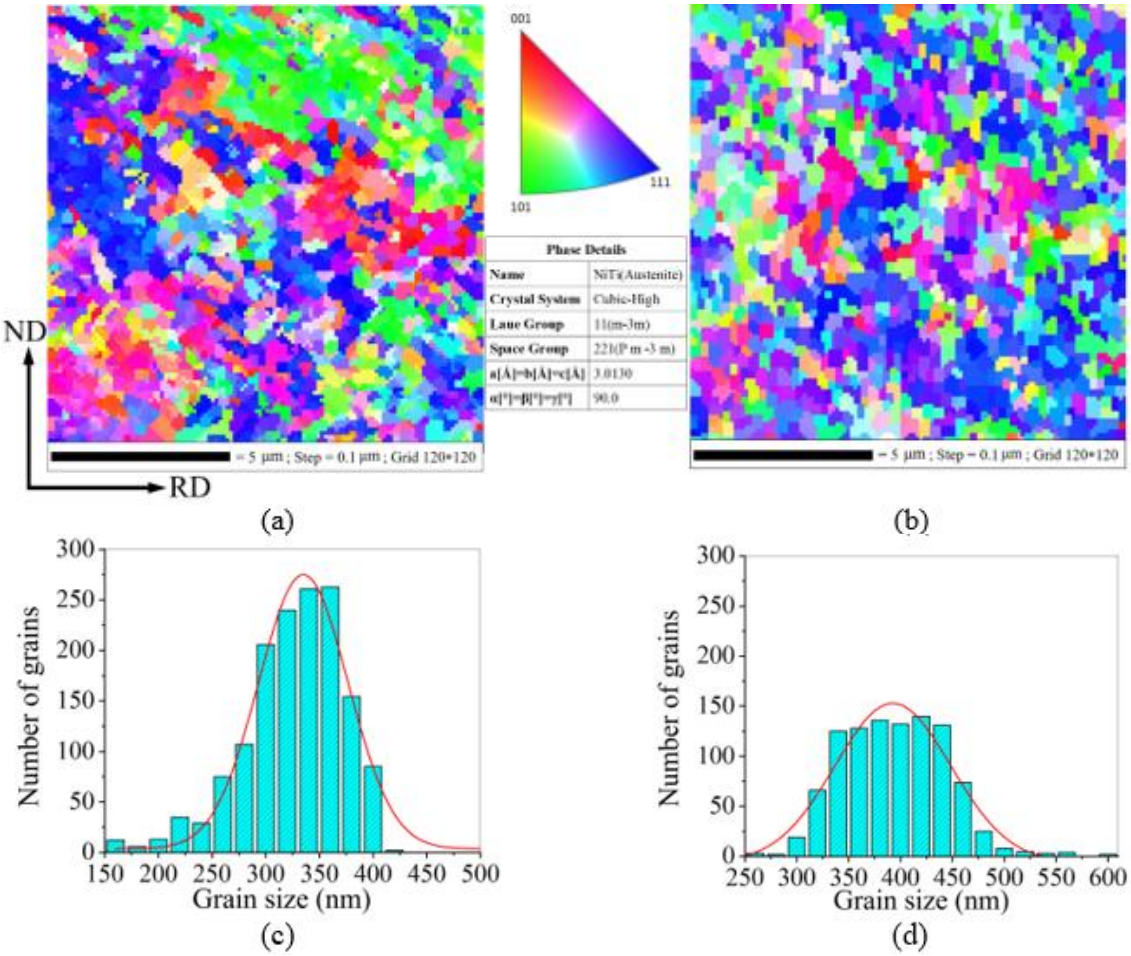


Figure.3 EBSD pattern of (a)as-received (b)5 hours' aged NiTi shape memory alloy, the black bars represent the scales, the phase used for indexing is shown in the middle. Grain size distribution of (c) as-received (d)5 hours' aged samples.

found that hardly any growth occurs below 823K. Obvious change in grain size can be achieved by annealing at temperatures of 973K or higher. The Euler colour distribution between and within grains in Fig.3(a) indicates the nature of lattice orientation variation within the sample. In contrast, the colour distribution within grains in Fig.3(b) appears more uniform, without a sudden change in color within a grain or at grain boundaries. Therefore, in terms of crystallinity, the samples tend to be more amorphous before ageing treatment and recrystallize slightly after.

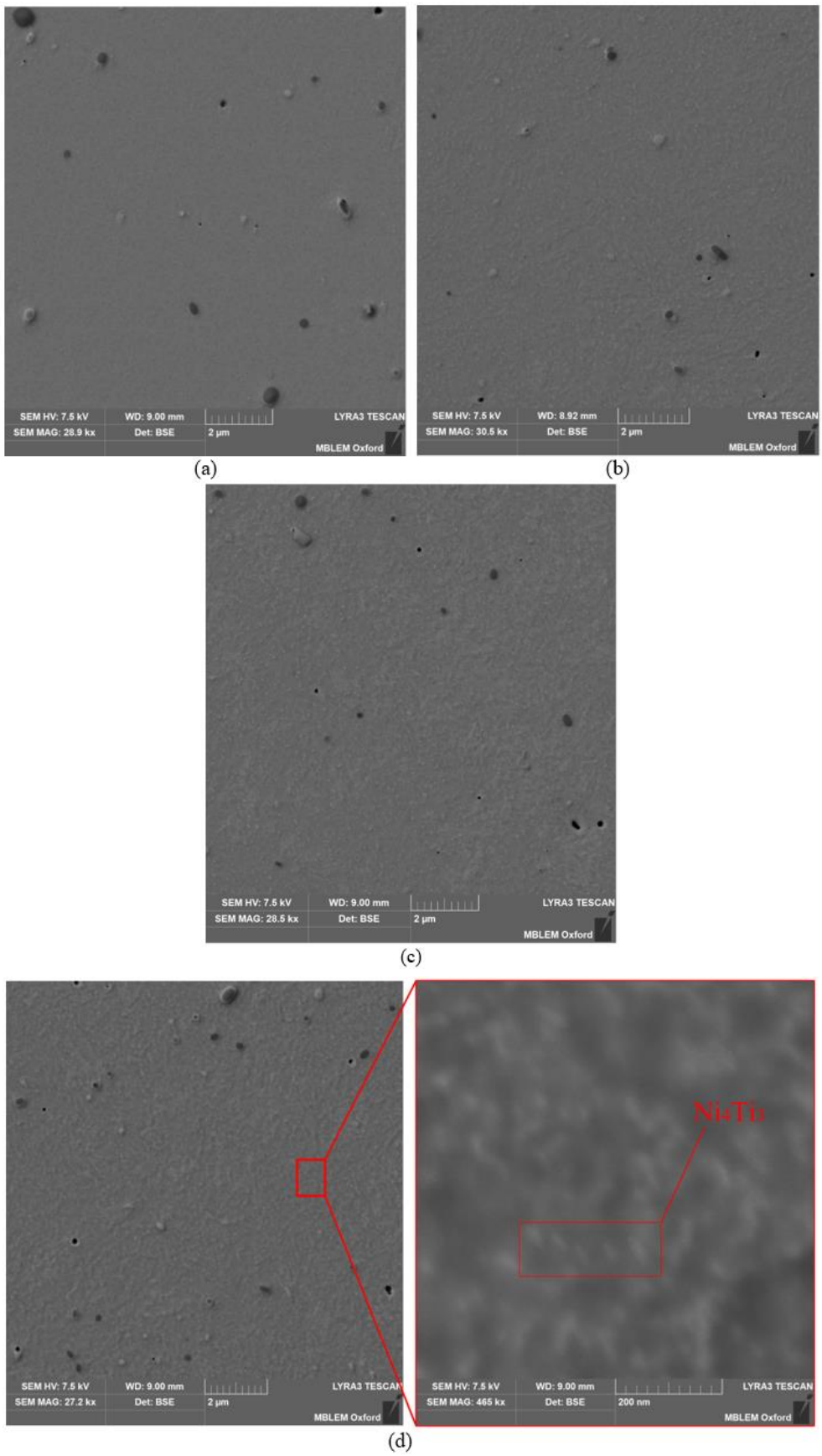


Figure.4 BSE images of sample surface with ageing durations of (a) as-received, (b) 1

hours, (c) 3 hours, (d) 5 hours, with zooming in to nano-scale, showing morphology of Ni_4Ti_3 precipitate.

BSE images of sample cross section surfaces are shown in Fig.4. Compared with SEM imaging using secondary electron (SE) detector that is highly sensitive to surface topography, the use of BSE detector reveals more clearly the variation of composition, such as precipitates in the matrix, and different phases, eliminating the interference from the topography variation due to non-metallic particles. The appearance of a small fraction of black dots (Ni_2Ti_4O oxide particles) results from annealing treatment prior to ageing [19], which can be observed from all samples including the as-received one and the volume fraction does not exhibit a significant growth. Grain boundaries cannot be clearly distinguished in the images due to the intrinsic function of BSE detector. The Ni_4Ti_3 precipitate phase nucleates and grows within the parent phase. A gradual increase of lighter appearing precipitates against grey background (parent phase) can be observed with the extension of ageing duration. This finding agrees with the reported results of earlier research [19,29]. Particularly, a local nano-scale BSE image of the 5 hours' aged sample confirms the precipitation to be the lenticular Ni_4Ti_3 precipitate [16,17,19,20,29,30,31,24,22,25].

A high-resolution EDS map was constructed and superimposed on SE image for the 5 hours' aged sample, as shown in Fig.5. White spots from the background SE image are unknown particles. Red spots represent nickel element and green spots represent titanium element. The averaging element ratio was displayed in the inset, reconfirming the sample composition to be Ni55/Ti45 wt.%. What is more, the homogenous distribution of these two elements over the map reconfirms the precipitation to be Ni_4Ti_3 instead of others (i.e.

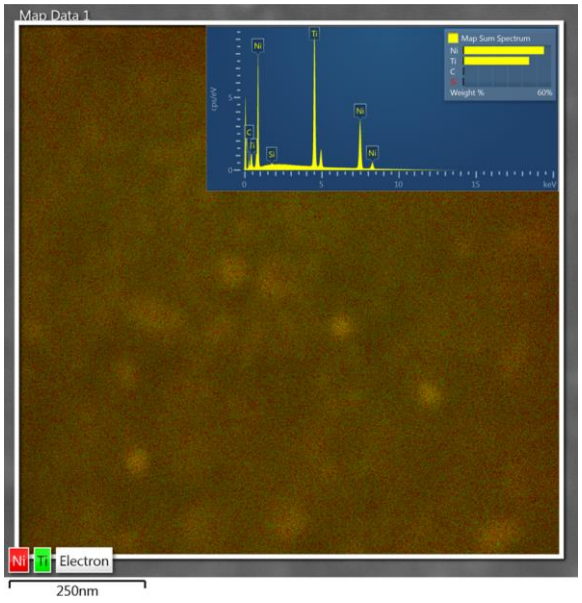


Figure.5 High-resolution EDS map of 5 hours' aged sample and map sum spectrum.

Ni_3Ti_2, Ni_3Ti and $NiTi_2$), since the composition of Ni_4Ti_3 (Ni57/Ti43) is very close to the matrix.

To summarize, EBSD results confirm negligible grain growth after ageing treatment at 773K for 5 hours, whilst BSE and EDS results confirm the emergence of Ni_4Ti_3 precipitate whose volume fraction exhibits a large increase. Previous studies also reported that heat treatment has no significant effect on the volume fraction of martensite/austenite parent phase (773K for 1 hour) [28]. Therefore, a conclusion can be drawn that during ageing treatment below 823K, the formation of Ni_4Ti_3 precipitate dominates the microstructural evolution in binary NiTi shape memory alloy, while the change in the martensite/austenite phase volume fraction and grain growth can be neglected.

3.2 Thermally Induced Phase Transformation

The thermally induced phase transformation behaviour monitored by DSC is shown in Fig.6 for samples subjected to varying ageing durations ranging from 10 mins to 5 hours. The phase transformation behaviour for as-received sample was not detectable in DSC

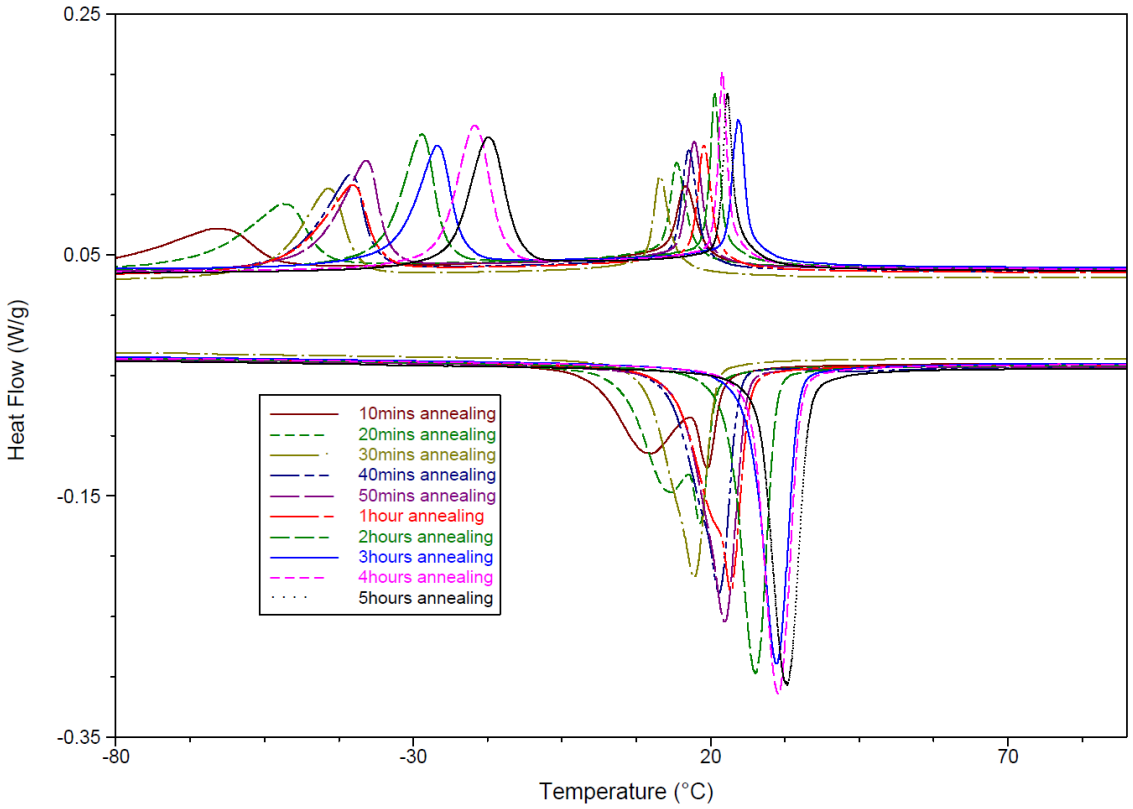


Figure.6 DSC cycles showing the evolution of phase transformation behaviour.

heating-cooling cycling, which means that as-received material prior to heat treatment after cold work hardly undergoes phase transformation.

In the DSC profiles, exothermic process corresponds to positive heat flow, thus upper curves indicate the cooling process. The temperature range of -80°C to 90°C is shown in the graphs, as no transformation behavior was observed at higher temperatures between 90°C and 200°C. It can be clearly seen from Fig.5 that the samples show two phase transformation features during cooling process. Since the average grain size is almost at the same magnitude of nanometer as that of precipitate, it can be assumed that there is no precipitate-free region within grains [13]. Therefore, the first peak in cooling process indicates austenite to R-phase transformation, while the second is R-phase to the martensite transformation [5,10,32,33]. The first peak in heating process indicates martensite to R-phase transformation, which can be observed in the samples with ageing

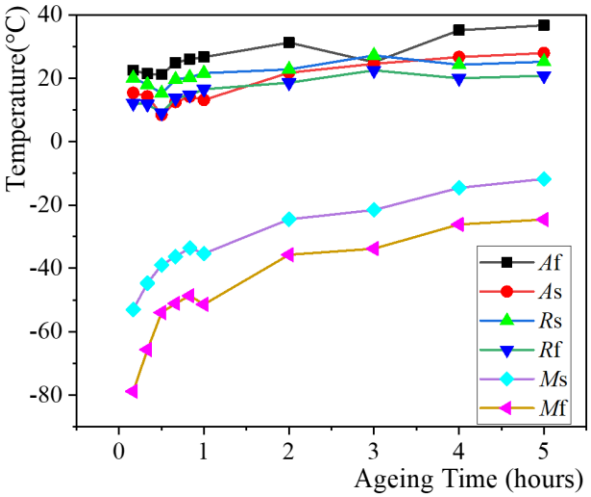


Figure.7 The evolution of critical temperatures with ageing time.

duration of 30 mins or less. The two peaks converge to a single peak for the samples with ageing time longer than 40 mins, indicating that most of martensite directly transforms to austenite whilst R-phase transformation peak may occur but is hidden inside the main peak [22].

It is apparent that the phase transformation peaks shift towards higher temperatures with the increasing of ageing time. The evolution of critical temperatures (R_s, R_f, M_s, M_f, A_s, A_f) of samples with varying ageing time are revealed in Fig.7.

As concluded from the EBSD / BSE / EDS results, grain growth is negligible after ageing treatment at 773K, and the dominant microstructural change in the samples is the precipitation of Ni_4Ti_3, which leads to the vast increase of volume fraction of Ni_4Ti_3 in the parent phase. Hence it can be assumed that the evolution of thermally induced phase transformation behaviour is hardly caused by the change of grain morphology / crystallinity but is tightly linked to the formation of Ni_4Ti_3 precipitate. Relevant mechanisms and corresponding models are discussed in the next section.

3.3 Theoretical description of thermally induced transformation

Johnson-Mehl-Avrami (JMA) nucleation and growth kinetics is one of most useful models to evaluate the evolution of phase volume fractions during heating or cooling processing [34,35]. The non-isothermal phase-transformation kinetic model for the volume ratio of new phases can be described as [36]

$$f = \frac{V_t}{V_\infty} = \xi(T,t) = 1 - \exp\left\{-g \cdot \int_0^{t'} I(T(t)) \cdot \left[\int_{t'}^{t} G(T(\tau))d\tau\right]^n dt)\right\}. \quad (1)$$

Here, V_t is the volume fraction of Ni_4Ti_3 precipitate at time t, V_∞ is the ultimate volume fraction, $I(T(t))$ is the nucleation rate function, $T(t)$ is the function representing the dependence of temperature on time t, $G(T\ (\tau))$ is the growth rate function, and g is the geometrical growth factor depending on the dimensionality of growth that happens in the volume, at surface, according to fractal dimension, etc.

Eq.(1) is the JMA equation that is used to describe the dependence on the process parameters, namely, the time t and temperature T. It incorporates the effects of the two basic processes involved in the formation of the new phase: nucleation and growth. If it is assumed that Ni_4Ti_3 nucleates randomly at pre-existing sites, then the nucleation rate function is set to a constant N_0, so that Eq.(1) can be simplified into

$$f = \xi(T,t) = 1 - \exp\left\{-g \cdot N_0 \cdot \left[\int_{t'}^{t} G(T(\tau))d\tau\right]^n\right\}, \quad (2)$$

where N_0 is the nucleation rate constant.

The growth rate function can be given by the Arrhenius equation commonly used to describe the rate of chemical reaction and phase formation, and can be written as

$$G\big(T(\tau)\big) = A \cdot \exp\left(-\frac{Q}{R \cdot T(\tau)}\right), \quad (3)$$

where the pre-exponential factor A, also known as the frequency factor, represents the frequency of collisions between atoms. The form of Eq. (2) can be further simplified by substituting Eq.(3), which can be written as

$$f = 1 - \exp(-\eta^n) \quad (4)$$

where

$$\eta = k_0 \cdot \int_{t'}^{t} \exp\left(-\frac{Q}{R \cdot T(\tau)}\right) d\tau. \quad (5)$$

Note that k_0 has the same unit as the frequency factor A (s^{-1}) that appears in the JMA model and the Arrhenius equation. The value of k_0 can be expressed as:

$$k_0 = A \cdot \sqrt[n]{g \cdot N_0}, \quad (6)$$

where g is the geometrical growth factor, and N_0 is the number of nucleation sites. For samples obtained by different processing of NiTi alloy of the same composition, the value of k_0 is considered to be fixed.

In Eq.(4) and Eq.(5), Q is the activation energy of phase-transformation. For binary NiTi alloy, the value of Q is in the range 120-160 kJ mol^{-1} [37]. Therefore, in the present study, the mean value of 140 kJ mol^{-1} was taken. n is the JMA index (or Avrami constant). Originally, n was thought to have an integer value between 1 and 4, reflecting the nature of the transformation. Assuming site saturation, the value of n is taken to be 1, corresponding to a constant nucleation rate. T is ageing temperature (in units of K); t is the ageing time (in units of min); f is the volume ratio of the new phase (Ni_4Ti_3), and R is the gas constant (8.314 J mol^{-1} K^{-1}).

If ageing treatment is considered to be an isothermal process, Eq.(5) can be rewritten as

$$\eta = k_0 \cdot \exp\left(-\frac{Q}{R \cdot T}\right) \cdot t. \quad (7)$$

The thermodynamic equilibrium between two phases during binary NiTi alloy phase transformation in the presence of crystal defects can be expressed in the following way [38,30,39]:

$$\Delta G = \Delta H - T \cdot \Delta S + \Delta E_e + \Delta E_i, \quad (8)$$

where $\Delta G=G_1-G_2$ is the change in free energy, G_1 and G_2 refer to Gibbs free energy curves for two phases (i.e. martensite / R-phase or R-phase / austenite or martensite / austenite) in NiTi alloy, ΔH and ΔS are the changes in chemical enthalpy and entropy respectively, T is the temperature, ΔE_e is the change in elastic strain energy and ΔE_i is the reversible work associated with the transformation. ΔE_e can be expressed as:

$$\Delta E_e = -\frac{1}{2} \cdot \sigma_{ij}^{\mathrm{t}} \cdot \varepsilon_{ij}^{\mathrm{t}} - \sigma_{ij} \cdot \varepsilon_{ij}^{\mathrm{t}} - \sigma_{ij}^{\mathrm{d}} \cdot \varepsilon_{ij}^{\mathrm{t}}, \tag{9}$$

where σ_{ij}, σ^{d}_{ij}, σ^{t}_{ij}, are the nonhydrostatic external applied stress, the internal stress field caused by the presence of precipitate and production process (i.e. cold work), and the internal stress field associated with the phase transformation respectively. $\varepsilon^{\mathrm{t}}_{ij}$ is the transformation strain. Rearranging Eq.8 gives expression as:

$$T = T_0 + \left(\frac{\Delta E_e + \Delta E_i}{\Delta S}\right), \tag{10}$$

where T is the equilibrium temperature between two adjacent phases and $T_0=(\Delta H - \Delta G)/\Delta S$. The approach can be taken that when $T=(A_{\mathrm{s}}, A_{\mathrm{f}}, R_{\mathrm{s}}, R_{\mathrm{f}}, M_{\mathrm{s}}, M_{\mathrm{f}})$ both the dissipative energy ΔE_i and reversible elastic stress σ_{ij} can be neglected since nucleation energies and elastic stored energies are small at the beginning/end of the transformation. As external applied stress is absent, $\Delta E_i=0$ and $\sigma^{\mathrm{t}}_{ij}=0$, following expression can be written:

$$(A_{\mathrm{s}}, A_{\mathrm{f}}, R_{\mathrm{s}}, R_{\mathrm{f}}, M_{\mathrm{s}}, M_{\mathrm{f}}) = T_0 + \frac{\Delta E_e}{\Delta S} = T_0 + \frac{-\sigma_{ij}^{\mathrm{d}} \cdot \varepsilon_{ij}^{\mathrm{t}}}{\Delta S}, \tag{11}$$

where $\Delta E_e=-\sigma^{\mathrm{d}}_{ij}\varepsilon^{\mathrm{t}}_{ij}$ is the elastic strain energy induced by precipitates. Eq.11 is a local form of Clausius-Clapeyron equation [40], which shows that critical transformation temperatures are related to the internal stress field σ^{d}_{ij}. It is obvious that the evolution of critical transformation temperatures will be proportional to the elastic strain energy and inversely proportional to the transformation entropy. For a single phase transformation process, e.g. austenite to R-phase or R-phase to martensite, the transformation entropy ΔS

and elastic strain ε^{t}_{ij} are constants. Two mechanisms are considered to affect internal stress field σ^{d}_{ij} during ageing treatment, namely the relaxation and the enhancement.

In the first instance, relaxation of stresses in the matrix during ageing treatment has been widely studied in different alloys [41-43] and can be quantified by Zener-Wert-Avrami function

$$\sigma^{\mathrm{RS}}_{T,t} = \sigma^{\mathrm{RS}}_{0} \cdot \exp\left(-\left(k_2 \cdot \exp\left(-\frac{Q_{\mathrm{a}}}{k \cdot T}\right) \cdot t\right)^{m}\right), \tag{12}$$

where k is the Boltzmann constant ($\approx 8.617\times10^{-5}$ eV/K), T is the ageing temperature (in units of K), t is the ageing time (in units of min), Q_{a} is the activation energy for stress relaxation (≈ 1 eV), m is a numerical term dependent on the dominant relaxation mechanism (≈ 0.5) and k_2 is a material constant.

In the second instance, Ni_4Ti_3 precipitate is assumed to nucleate at pre-determined sites, therefore the increase in precipitate volume ratio is due to the size growth. In [24,31], the internal stress field is simulated surrounding Ni_4Ti_3 precipitate. For simplicity it might be assumed the stress level is directly proportional to precipitate size so that it can be written in the following form:

$$\sigma^{\mathrm{p}}_{ij} = k' \cdot f, \tag{13}$$

where *k'* refers to the scale factor (in units of MPa).

Assuming the two mechanisms are independent, the internal stress field can be expressed as

$$\sigma^{\mathrm{d}}_{ij} = \sigma^{\mathrm{RS}}_{T,t} + \sigma^{\mathrm{p}}_{ij} = k' \cdot f + \sigma^{\mathrm{RS}}_{0} \cdot \exp\left(-\left(k_2 \cdot \exp\left(-\frac{Q_{\mathrm{a}}}{k \cdot T}\right) \cdot t\right)^{m}\right). \tag{14}$$

The following expression can be obtained by combining Eq.4, Eq.7, Eq.11, Eq.14:

$$(A_{\mathrm{s}}, A_{\mathrm{f}}, R_{\mathrm{s}}, R_{\mathrm{f}}, M_{\mathrm{s}}, M_{\mathrm{f}}) = T_0 + \frac{-k' \cdot \left(1 - \exp\left(-\left(k_0 \cdot \exp\left(-\frac{Q}{R \cdot T}\right) \cdot t\right)^{n}\right)\right) \cdot \varepsilon^{\mathrm{t}}_{ij}}{\Delta S} + \frac{-\sigma^{\mathrm{RS}}_{0} \cdot \exp\left(-\left(k_2 \cdot \exp\left(-\frac{Q_{\mathrm{a}}}{k \cdot T}\right) \cdot t\right)^{m}\right) \cdot \varepsilon^{\mathrm{t}}_{ij}}{\Delta S}. \tag{15}$$

Eq.15 reveals the evolution of critical phase transformation temperatures with respect to ageing time and temperature.

In addition to the alteration of internal stress field during ageing treatment, influence of Ni concentration on the critical temperatures has been studied in [19,44,45]. Ture Ni concentration $x_{\mathrm{Ni}}^{\mathrm{p,O,C}}$ can be defined as:

$$x_{\mathrm{Ni}}^{p,O,C} = \frac{n_{\mathrm{Ni}}^{*}}{n_{\mathrm{Ni}}^{*}+n_{\mathrm{Ti}}^{*}}, \tag{16}$$

where n_{Ni}^{*} and n_{Ti}^{*} are numbers of Ni and Ti atoms in the NiTi alloy bulk. The shift in critical phase transformation temperatures associated with Ni concentration in binary NiTi shape memory alloy can be described by equation [44]:

$$(A_{\mathrm{s}}', A_{\mathrm{f}}', R_{\mathrm{s}}', R_{\mathrm{f}}', M_{\mathrm{s}}', M_{\mathrm{f}}') = (A_{\mathrm{s}}, A_{\mathrm{f}}, R_{\mathrm{s}}, R_{\mathrm{f}}, M_{\mathrm{s}}, M_{\mathrm{f}}) + a_1 + a_2 \cdot x_{\mathrm{Ni}}^{p,O,C} + a_3 \cdot {a_4}^{x_{\mathrm{Ni}}^{p,O,C}}, \tag{17}$$

where a_{i} (i=1,2,3,4) are the fitting parameters of experimental data, details of which refer to [44].

Substituting Eq.15 into Eq.17 can give the following equation:

$$(A_{\mathrm{s}}', A_{\mathrm{f}}', R_{\mathrm{s}}', R_{\mathrm{f}}', M_{\mathrm{s}}', M_{\mathrm{f}}') = \frac{-k' \cdot \left(1-\exp\left(-\left(k_0 \cdot \exp\left(-\frac{Q}{R \cdot T}\right) \cdot t\right)^n\right)\right) \cdot \varepsilon_{ij}^{\mathrm{t}}}{\Delta S} + \frac{-\sigma_0^{\mathrm{RS}} \cdot \exp\left(-\left(k_2 \cdot \exp\left(-\frac{Q_{\mathrm{a}}}{k \cdot T}\right) \cdot t\right)^m\right) \cdot \varepsilon_{ij}^{\mathrm{t}}}{\Delta S} + T_0 + a_1 + a_2 \cdot x_{\mathrm{Ni}}^{p,O,C} + a_3 \cdot {a_4}^{x_{\mathrm{Ni}}^{p,O,C}}. \tag{18}$$

Once a NiTi shape memory alloy is fabricated, its overall Ni concentration is fixed, while local composition varies between matrix and the vicinity of precipitate, especially when the overall composition has a huge difference with precipitate (e.g. Ni50/Ti50 and Ni_4Ti_3). However, the overall composition (Ni55/Ti45) and Ni_4Ti_3 (Ni57/Ti43) are nearly identical in this study, therefore the last four items in Eq.18 are constants. As aforementioned, for a particular phase transformation, e.g. austenite to R-phase or R-

phase to martensite, the transformation entropy ΔS and elastic strain ε^{t}_{ij} are constants. k' and σ^{RS}_{0} are constants. T_0 is also a constant when the alloy is at an equilibrium temperature.

Considering all the above factors, Eq.18 can be simplified as:

$$(A_s, A_f, R_s, R_f, M_s, M_f)_{\left(t,T,x_{Ni}^{p,O,C}\right)} = k_1 \cdot \left(1 - \exp\left(-\left(k_0 \cdot \exp\left(-\frac{Q}{R \cdot T}\right) \cdot t\right)^n\right)\right) + k_3 \cdot \exp\left(-\left(k_2 \cdot \exp\left(-\frac{Q_a}{k \cdot T}\right) \cdot t\right)^m\right) + k_4, \quad (19)$$

where

$$k_1 = \frac{-k' \cdot \varepsilon^{t}_{ij}}{\Delta S}, \text{ in units of Kelvin (K)}, \quad (20)$$

and

$$k_3 = \frac{-\sigma_0^{RS} \cdot \varepsilon^{t}_{ij}}{\Delta S}, \text{ in units of K}, \quad (21)$$

and

$$k_4 = T_0 + a_1 + a_2 \cdot x_{Ni}^{p,O,C} + a_3 \cdot a_4{}^{x_{Ni}^{p,O,C}}, \quad (22)$$

and also has units of K.

Eq.19 gives the model that can be used to calculate the values of critical temperatures of NiTi alloy subjected to various ageing durations, temperatures and Ni concentration. As is mentioned, the value of k_0 and k_2 are fixed for samples obtained by different processing of NiTi alloy of the same composition. For both the start and finish temperatures of single-phase transformation process, i.e. A_s and A_f, R_s and R_f, M_s and M_f, the value of k_1 and k_3 can be assumed to be constant. In contrast, the value of k_4 varies due to the change in Gibbs free energy and parameters a_i as a function of temperature.

The model is verified by fitting it to six critical phase transformation temperatures data from DSC experiments. The R^2 value is used to find the best fit. Specific parameters for each critical temperature are shown in Table 1.

Table 1

Model parameters for each critical phase transformation temperature.

Model Parameters	A_s	A_f	R_s	R_f	M_s	M_f
k_0 (min^{-1})	3×10^7	3×10^7	3×10^7	3×10^7	3×10^7	3×10^7
k_1 (K)	25.4	25.4	18.9	18.9	52.2	52.2
k_2 (min^{-1})	2.5×10^5	2.5×10^5	2.5×10^5	2.5×10^5	2.5×10^5	2.5×10^5
k_3 (K)	22	22	13	13	0	0
k_4 (K)	0.2	17.0	8.2	3.4	-54.27	-81.15

For the critical temperatures given in Table 1, the experiment data and the theoretical curve from proposed model are illustrated in the same graph, as shown in Fig.8. Six graphs correspond to six critical phase transformation temperatures, respectively.

The proposed model describes well the evolution trends of the critical phase transformation temperatures, including the inversing trend of A_s, A_f, R_s and R_f within the first hour of ageing. Whether from the experiment data or from the model, the conclusion is drawn that these critical temperatures generally increase with the increasing ageing time, and finally converge to an upper limit. This “upper limit” prediction from the model coincides with the experimental results from other studies [9,10].

According to the thermodynamic and mathematical basis of the present model, the following conclusions can be drawn with respect to the model parameters:

(1) Whilst the number density of nucleation sites N_0 and the frequency factor A may change due to the variation in the composition of binary NiTi alloy, the geometrical

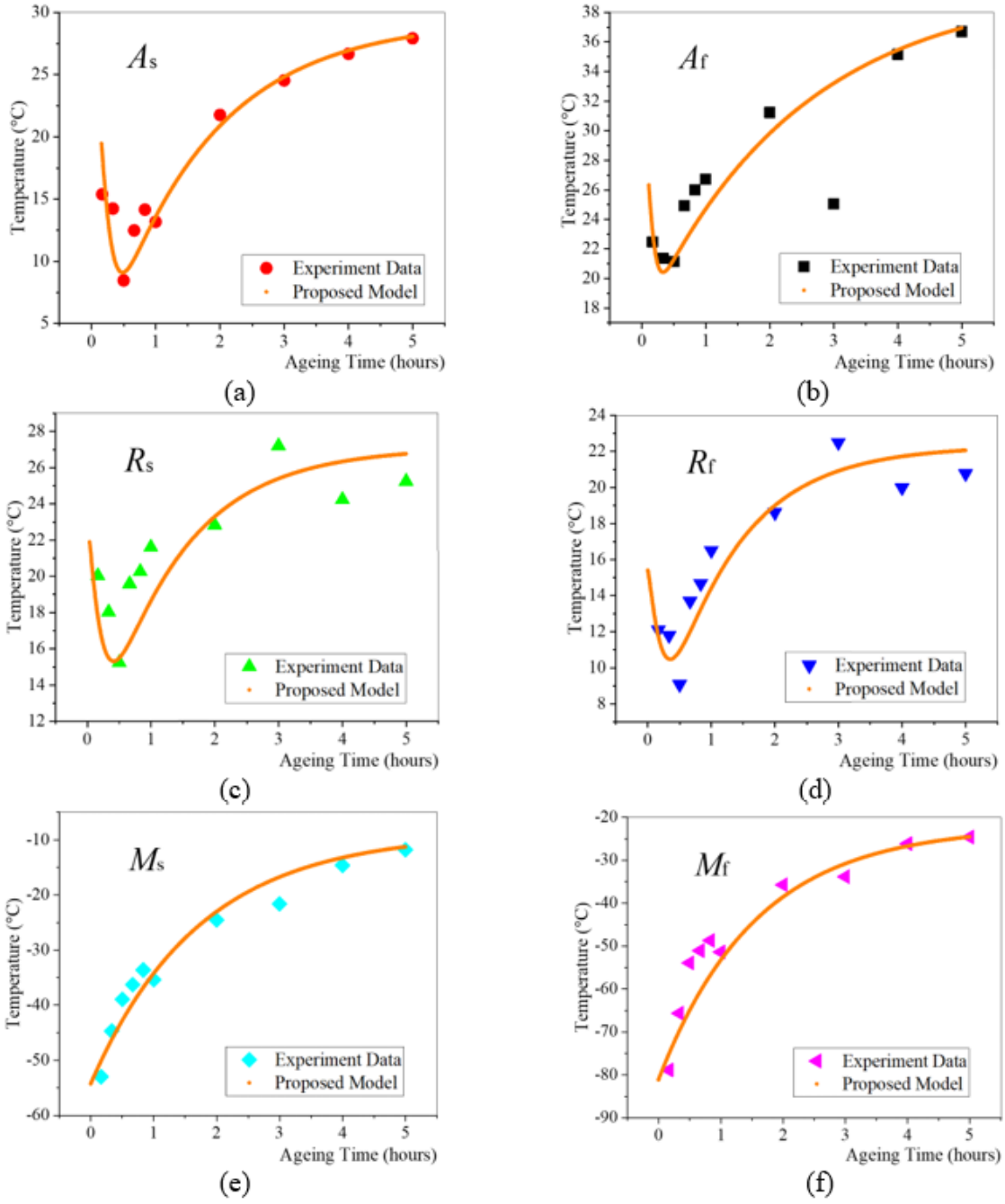


Figure.8 Comparison between experiment data and the proposed model, with abscissa being the ageing duration ranging from 0 to 5 hours, the ordinate is the critical temperatures, namely (a)A_s, (b)A_f, (c)R_s, (d)R_f, (e)M_s, (f)M_f, during thermally induced phase transformation process of binary NiTi alloy.

growth factor of precipitate g remains unchanged. For NiTi alloys with the same composition, N_0, A and g are fixed, therefore, Eq.6 shows that the value of k_0 is fixed.

From the mathematical perspective, Eq.7 shows that the larger the value of k_0, the steeper the curve, indicating the faster transformation rate and growth kinetics of Ni_4Ti_3 precipitates.

(2) For a particular phase transformation process, the entropy change ΔS, the elastic strain ε^t_{ij}, and the scale factor k' of volume ratio and internal stress field are fixed. For different phase transformation processes, the value of ΔS and ε^t_{ij} may change. Therefore, Eq.20 and Eq.21 show that the values of k_1 and k_3 are fixed for the start and finish temperatures of a given phase transformation process, but they change between different processes. From the mathematical perspective of Eq.19, the values of k_1 and k_3 determine the total variation of the critical temperatures due to ageing.

(3) The change in Gibbs free energy ΔG depends on temperature, though the values of chemical enthalpy and entropy remain the same for a particular phase transformation process. Therefore, the value of T_0 varies, resulting in different values of k_4 (see Eq.22) for different critical temperatures. From the mathematical perspective of Eq.19, the value of k_4 determines the starting point of critical temperature evolution.

The three conclusions above are verified by observing the fitted parameters in Table 1, and the good match obtained between the model predictions and experimental data in Fig.8.

The evolution progress of critical temperatures is defined in the following expression, derived from Eq.19:

$$P = \left(1 - \exp\left(-k_0 \cdot \exp\left(-\frac{Q}{R \cdot T}\right) \cdot t\right)\right) \times 100\%, \quad (23)$$

where P is the percentage of completion of evolution, and t is the ageing time in units of minutes.

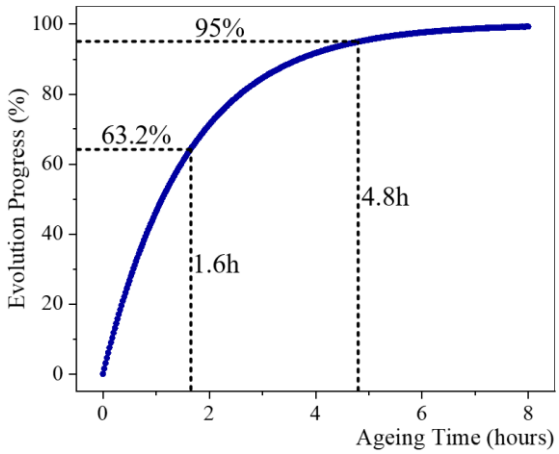


Figure.9 Percentage of completion of critical temperature evolution due to ageing treatment.

Substituting (k_0, Q, R, T) in Eq.23 with numerical values gives an exponential curve shown in Fig.9. The value of P indicates how much the critical temperatures have evolved towards the upper limit. The characteristic time t_c of temperature evolution is found as:

$$t_c = \left(k_0 \cdot \exp\left(-\frac{Q}{R \cdot T}\right)\right)^{-1} \approx 96 \text{ mins} \approx 1.6 \text{ hrs.} \quad (24)$$

Eq.23 gives the result that:

$$P = \left(1 - \exp(-1)\right) \times 100\% \approx 63.2\%, \quad (25)$$

i.e. the temperature evolution is about 2/3 completed at characteristic time t_c of ageing treatment for NiTi alloy.

Similarly, approximately 4.8 hours of ageing results in ~95% of completion of temperature evolution.

The characteristic time t_c may change due to different NiTi composition, since the value of k_0 is associated with intrinsic properties of materials.

Eq.23 describes the evolution progress of all critical temperatures of binary NiTi alloy, and for alloys with the same composition and fabrication method, the characteristic time is fixed for all critical temperatures due to the fixed value of k_0.

The applications of the proposed model are versatile and beneficial. In the first instance, based on DSC data of a NiTi alloy subjected to ageing treatment, the proposed model can fit and predict the maximum values of critical temperatures of the alloy. In the second instance, the manufacturers of NiTi shape memory alloy material and components, phase transformation temperature customization can be achieved. For example, NiTi stents for blood vessels need to display phase transformation response as precisely defined temperatures. The current model can be used to provide guidance to identify the most suitable ageing treatment schedule. It is worth noting that for as-received binary NiTi alloys, the present model may not be applicable, since thermally induced phase transformation does not appear to occur in NiTi alloys without ageing treatment.

3.4 Mechanically Induced Phase Transformation

The superelastic stress-strain curves are shown in Fig.10. The as-received sample hardly exhibits superelasticity. From the stress-strain curve it can be observed that the Young's modulus of as-received material is similar to the Young's modulus of austenite of aged samples, though it hardly transforms to martensite even at high stress level. Less stress hysteresis (at maximum around 100MPa) happens during loading / unloading process compared with those of other samples (over 300MPa), which means that small-scale phase transformation still exists in as-received sample during loading. In addition, as-received NiTi alloy has much higher ultimate tensile strength (up to 1200MPa) than aged ones, which corresponds with results from previous study [9].

For all these stress-strain curves, the presences of R-phase transformation are not readily observable. There are three possible situations. Firstly, the transformation from A to R may be merged with the transformation from R to M [46]. Secondly, strain measurement methods often overlook detecting the A to R transformation, as the

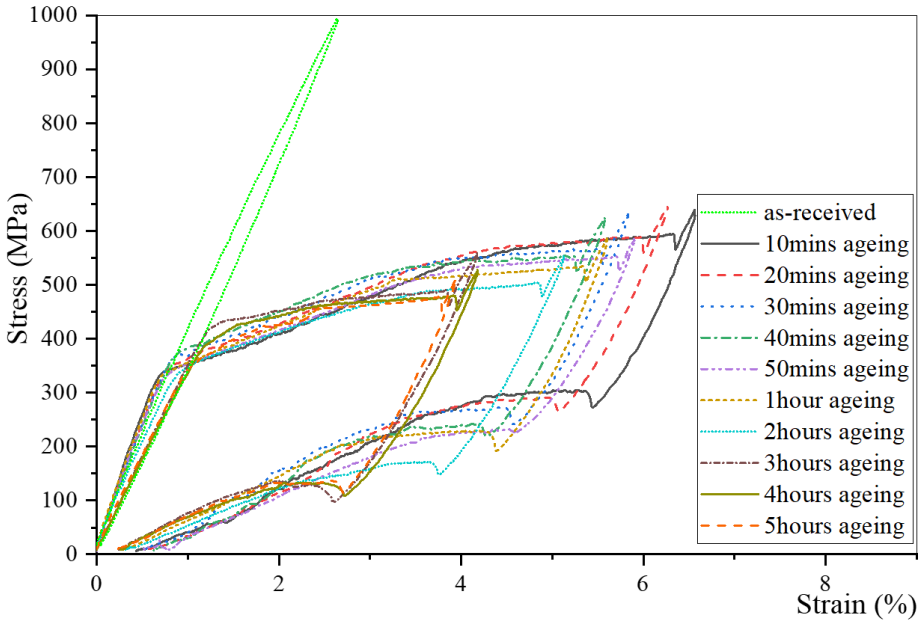


Figure.10 Isothermal complete superelastic stress-strain curves of samples at 323K.

associated transformation strains are much smaller than those of A to M [47]. Last but not least, even though DSC results show presence of R-phase, a direct A to M transformation may occur during superelasticity at temperature above A_f [46,48].

Ageing treatment exerts a huge influence on superelasticity of NiTi alloy even in a short duration. As can be observed from the curve of 10 minutes' ageing sample, NiTi alloy exhibits an immediate advancement in superelasticity after ageing treatment, that ductility increases and strength decreases. However, with the prolonging of ageing time, mechanical properties seem to continuously degrade. In the first instance, the completion strain for upper plateau of the sample with 10 minutes' ageing treatment was nearly 6.3%, then this value gradually decreases to about 3.5% for the sample with 5 hours' ageing treatment. In the second instance, upper plateau stress for the sample with 10 minutes' ageing was nearly 600MPa, while this value dropped to 450 MPa for the sample with 5 hours' ageing. This initial improvement and subsequent degradation of superelasticity of Nitinol caused by ageing treatment corresponds with previous studies [5,23].

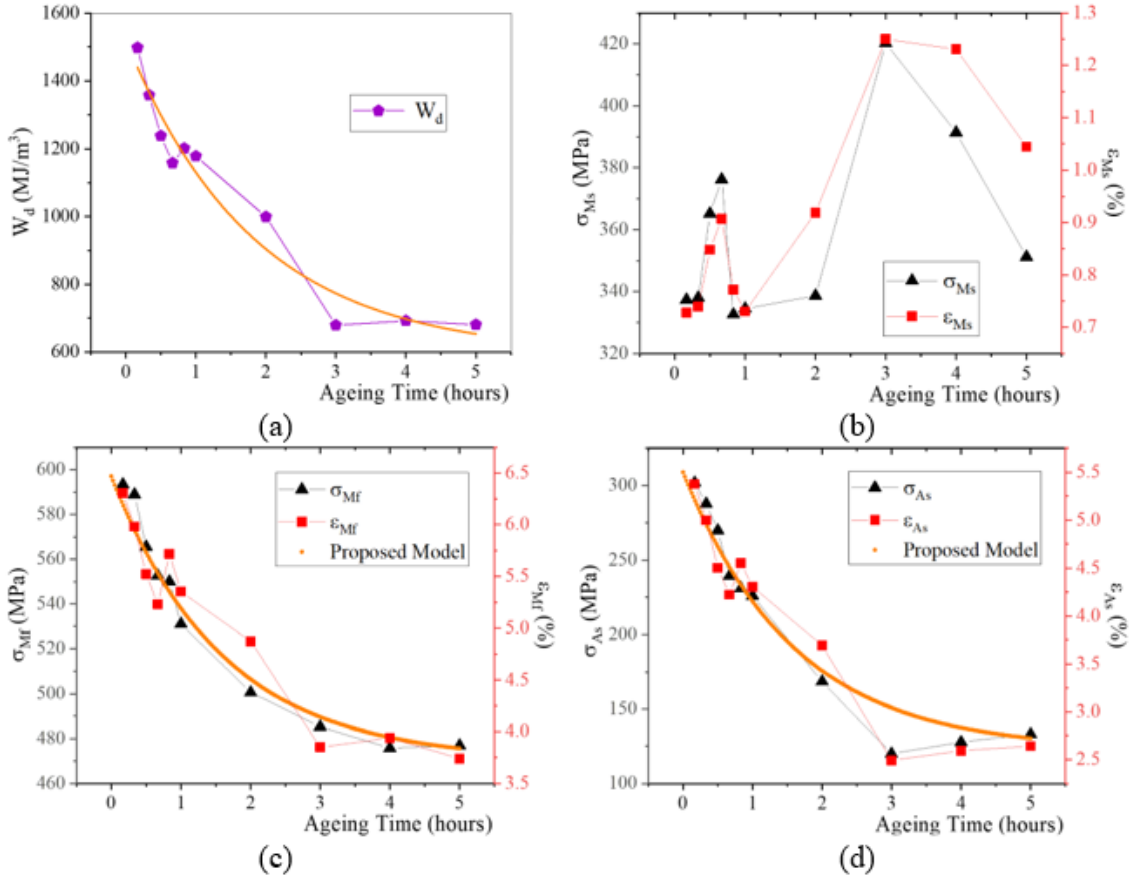


Figure.11 Evolution of Wd (a), σ_{Ms} and ε_{Ms} (b) with ageing time. Comparison between experiment data, namely σ_{Mf} and ε_{Mf} (c), σ_{As} and ε_{As} (d), with the proposed model.

As is quantified above, the volume fraction of Ni_4Ti_3 precipitate rises with ageing process. On one hand, previous researches have demonstrated that the improvement in superelastic performance after ageing treatment is mainly due to the change in internal stress state caused by Ni_4Ti_3 precipitate, to be more precise residual stress altered by Ni_4Ti_3 precipitate promotes phase transformation through altering internal free energy. On the other hand, the volume fraction of precipitate increase leads to the reduction in volume fraction of transformable part of the material, namely austenitic parent phase. Therefore, the NiTi alloy may exhibit lower critical stresses / strains after longer ageing time, which is the observation of this present experiment.

An interesting observation of present experiment result is the “trigger mechanism” before NiTi alloy turned from partially detwinned to fully detwinned, and vice versa. Stress-strain curves of aged samples exhibit two “sharp valley” regions. One appears after upper stress plateau during loading and the other appears before lower stress plateau during unloading. It is quite clear that the conversion between partially and fully detwinned martensite is not smooth-----there is a transition process between these two states and this process breaks the internal equilibrium of the material, which causes obvious fluctuation in stress level. The underlying reason for these dips may be the incomplete transformation of parent austenite phase at the end of stress plateau [26].

The effect of ageing treatment on dissipated energy density critical stresses / strains is outlined in Fig.11. In the first three hours’ heat treatment, samples exhibit rapid decrease in Wd, σ_{Mf}, ε_{Mf}, σ_{As}, ε_{As} and the continuous fluctuation of σ_{Ms} and ε_{Ms}.

Regarding Wd, the value exhibits an exponential decrease with ageing time, which is in agreement with previous studies [49]. This phenomenon can also be related to the precipitation. However, the value of Wd is relatively high compared with others (usually under 100 MJ/m^3) and this may attribute to the low temperature (just 20K above Af) during tension, that the phase transformation becomes less “active”.

Two peaks can be observed in the evolution of σ_{Ms} and ε_{Ms}, which is similar to the effect of ageing treatment on tensile strength of Aluminum alloys. Two microscopic processes take place simultaneously during ageing treatment of NiTi alloys. Firstly, the formation of precipitates induces local residual stress, which promotes the transformation from austenite to detwinned martensite at the beginning. With the prolonging ageing treatment, residual stress may be relaxed by atomic motion. This effect leads to the left small peak in Fig.11 (b). Secondly, defects/dislocations in austenite phase are pinned by the embedding of Ni_4Ti_3 precipitate. As the precipitate grows, its effect on preventing

dislocation motion is strengthened and then weakened due to the expanding size, which corresponds to the right peak. Therefore, competition between these two mechanisms leads to the undulation of σ_{Ms} and ε_{Ms}, which are sensitive to microstructure changes.

The sharp decline in σ_{Mf}, ε_{Mf}, σ_{As} and ε_{As} results from the increasing A_f due to precipitation. As A_f increases the stress required to drive full martensite transformation is reduced. It is noteworthy that the critical strains share the same trends as stresses, decreasing rapidly in the first three hours and reaching a platform stage. The evolution of (σ_{Mf}, ε_{Mf}, σ_{As}, ε_{As}) can be assumed to obey the same mathematical form with Rule of mixtures and is associated with the volume ratio of Ni_4Ti_3 precipitate. The expression can be written as:

$$(\sigma_{\mathrm{Mf}}, \varepsilon_{\mathrm{Mf}}, \sigma_{\mathrm{As}}, \varepsilon_{\mathrm{As}})_{\left(t,T,x_{\mathrm{Ni}}^{p,o,c}\right)} = f' \cdot a_1 + (1-f) \cdot a_2, \tag{26}$$

where f' is the volume fraction of parent austenite phase, which can be assumed to be 1. f is the volume ratio of precipitate, expression of which refers to Eq.(4). a_1 and a_2 are parameters that have the same units as the left side of the equation. The definition of characteristic time t_c is also applicable to describe the evolution of (σ_{Mf}, ε_{Mf}, σ_{As}, ε_{As}). The model is verified by fitting it to experimental data. The R^2 value is used to find the best fit. Specific parameters for each critical stresses / strains are shown in Table 2.

Table 2

Model parameters for each critical stresses / strains.

Model Parameters	σ_{Mf}	ε_{Mf}	σ_{As}	ε_{As}
k_0 (min^{-1})	3×10^7	3×10^7	3×10^7	3×10^7
a_1	470 (MPa)	3.75 (%)	122 (MPa)	2.79 (%)
a_2	127 (MPa)	2.65 (%)	187 (MPa)	2.71 (%)

According to the thermodynamic and mathematical basis of the present model, the following conclusions can be drawn with respect to the model parameters:

(1) k_0 is related to the intrinsic characteristics of the samples from the same batch of fabrication and holds a fixed value for different critical stresses / strains. This parameter is shared by both models. Detailed conclusion of this model parameter refers to section 3.3.

(2) a_1 and a_2 are universal parameters for specific properties of parent phase and precipitate, such as elastic modulus, mass density, ultimate tensile strength. In this case, a_1 and a_2 denote critical stresses / strains.

The conclusions above are verified by observing the fitted parameters in Table 2, and the good match obtained between the model predictions and experimental data in Fig.11.

4. Conclusion

The present work is consisted of three main sections, namely EBSD / BSE / EDS evaluation of grain growth and precipitate formation after ageing treatment, modelling and analysis of critical temperatures in thermally induced phase transformation as well as critical stresses / strains in mechanically induced phase transformation.

For various ageing durations at 773K, the dominant microstructural change in NiTi alloy is the formation and expansion of Ni_4Ti_3 precipitate, which in turn, results in the evolution of thermal and mechanical phase transformation behaviour.

Critical phase transformation temperatures show an overall exponential increases with increase of ageing time, while local inversion trend is also observed within the first hour. A model based on thermodynamics is proposed by combining JMA equation and Arrhenius equation to predict the values of critical temperatures as a function of ageing time. Fitting results show that the model well matches the evolution of critical phase

transformation temperatures and can be used as a reference to determine suitable ageing durations for NiTi shape memory alloys. Concept of characteristic time is also put forward, which is applicable to describe the evolution of all critical temperatures.

Ageing duration exerts a huge influence on dissipated energy density and critical stresses / strains. The stress and strain values (σ_{Mf}, ε_{Mf}, σ_{As}, ε_{As}) drop steeply before reaching a platform. A model that refers to Rule of Mixture is proposed to predict these values as a function of ageing time. Fitting results show excellent matches between the experiment and theory. The σ_{Ms} and ε_{Ms} values exhibit two peaks due to the competition between evolution of residual stress and strengthening effect of precipitates. Further study is required to provide more insight into modelling these behaviours.

References

[1] J.M. Jani, M. Leary, A. Subic, M.A. Gibson, A review of shape memory alloy research, applications and opportunities, Materials and Design 56 (2014) 1078-1113.

[2] P. Sittner, P. Sedlak, H. Seiner, P. Sedmak, et al., On the coupling between martensitic transformation and plasticity in NiTi: Experiments and continuum based modelling, Progress in Materials Science 98 (2018) 249-298.

[3] T. Daniels, Thermal Analysis, Halsted Press, London, 1973, pp.103.

[4] D.C. Lagoudas, Shape Memory Alloys Modeling and Engineering Applications, Springer Science+Business Media, LLC, New York, 2008, pp.71-95.

[5] X. Huang, Y. Liu, Effect of annealing on the transformation behavior and superelasticity of NiTi shape memory alloy, Scripta Materialia 45 (2001) 153-160.

[6] Y. Liu, The superelastic anisotropy in a NiTi shape memory alloy thin sheet, Acta Materialia 95 (2015) 411-427.

[7] J.P. Oliveira, R.M. Miranda, F.M. Braz Fernandes, Welding and Joining of NiTi Shape Memory Alloys: A Review, Progress in Materials Science 88 (2017) 412-466.

[8] M.J. Mahtabi, N. Shamsaei, A modified energy-based approach for fatigue life prediction of superelastic NiTi in presence of tensile mean strain and stress, International Journal of Mechanical Sciences 117 (2016) 321-333.

[9] M.J. Drexel, G.S. Selvaduray, A.R. Pelton, The effects of cold work and heat treatment on the properties of Nitinol wire, International Conference on Shape Memory and Superslastic Technologies (2006) 447-454.

[10] D. Xue, Y. Zhou, X. Ren, The effect of ageing on the B2-R transformation behaviors in Ti-51at%Ni alloy, Intermetallics 19 (2011) 1752-1758.

[11] X. Yan, J.V. Humbeeck, Effect of annealing on strain-temperature response under constant tensile stress in cold-worked NiTi thin wire, Smart Materials Research (2011) Article ID 160927.

[12] A. Ahadi, Q. Sun, Effect of grain size on the rate-dependent thermomechanical responses of nanostructured superelastic NiTi, Acta Materialia 76 (2014) 186-197.

[13] X. Wang, et al., Effect of grain size on aging microstructure as reflected in the transformation behavior of a low-temperature aged Ti-50.8 at.% Ni alloy, Scripta Materialia 69 (2013) 545-548.

[14] E. A. Prokofiev, et al., Suppression of Ni_4Ti_3 Precipitation by Grain Size Refinement in Ni-Rich NiTi Shape Memory Alloys, Advanced Engineering Materials 12 (2010) 747-753.

[15] A. Ahadi, Q. Sun, Stress-induced nanoscale phase transition in superelastic NiTi by in situ X-ray diffraction, Acta Materialia 90 (2015) 272-281.

[16] A.K. Srivastava, D. Schryvers, J.V. Humbeeck, Grain growth and precipitation in an annealed cold-rolled NiTi alloy, Intermetallics 12 (2007) 1538-1547

[17] K. Otsuka, X. Ren, Physical metallurgy of Ti-Ni-based shape memory alloys, Progress in Materials Science 50 (2005) 511-678.

[18] M. Carl, B. Zhang, M.L. Young, Texture and Strain Measurements from Bending of NiTi Shape Memory Alloy Wires, Shap. Mem. Superelasticity 2 (2016) 254-263.

[19] J.K. Allafi, A. Dlouhy, G. Eggeler, Ni4Ti3-precipitation during ageing of NiTi shape memory alloys and its influence on martensitic phase transformations, Acta Materialia 50 (2002) 4255-4274.

[20] O. Bojda, G. Eggeler, A. Dlouhy, Precipitation of Ni4Ti3-variants in a polycrystalline Ni-rich NiTi shape memory alloy, Scripta Materialia 53 (2005) 99-104.

[21] S. Jiang, Y. Zhang, L. Zhao, Y. Zheng, Influence of annealing on NiTi shape memory alloy subjected to severe plastic deformation, Intermetallics 32 (2013) 344-351.

[22] J.I. Kim, Y. Liu, S. Miyazaki, Ageing-induced two-stage R-phase transformation in Ti-50.9at.%Ni, Acta Materialia 52 (2004) 487-499.

[23] F. Jiang, Y. Liu, H. Yang, Effect of ageing treatment on the deformation behaviour of Ti-50.9at.%Ni, Acta Materialia 57 (2009) 4773-4781.

[24] W. Tirry, D. Schryvers, Linking a completely three-dimensional nanostrain to a structural transformation eigenstrain, Nature Materials 8 (2009) 752-757.

[25] W. Tirry, D. Schryvers, Quantitative determination of strain fields around Ni_4Ti_3 precipitates in NiTi, Acta Materialia 53 (2005) 1041-1049.

[26] G. Tan, Y. Liu, P. Sittner, Luders-like deformation associated with stress-induced martensitic transformation in NiTi, Scripta Materialia 50 (2004) 193-198.

[27] L. Neelakantan, A.W. Hassel, Rotating disc electrode study of the electropolishing mechanism of NiTi in methanolic sulfuric acid, Eletrochimica Acta 53 (2007) 915-919.

[28] M.E. Mitwally, M. Farag, Effect of cold work and annealing on the structure and characteristics of NiTi alloy, Materials Science and Engineering A 519 (2009) 155-166.

[29] M. Nishida, C.M. Wayman, T. Honma, Metal Trans 17A (1986) 1505.

[30] P.G. McCormick, Y. Liu, Thermodynamic analysis of the martensitic transformation in NiTi-II. Effect of transformation cycling, Acta metall. Mater. 42 (1994) 2407-2413.

[31] N. Zhou, C. Shen, M.F.-X. Wagner, G. Eggeler, M.J. Mills, Y. Wang, Effect of Ni4Ti3 precipitation on martensitic transformation in Ti-Ni, Acta Materialia 58 (2010) 6685-6694.

[32] L. Jordan, M. Chandrasekaran, M.M. Masse, G. Bouquet, Study of the phase transformation in Ni-Ti based shape memory alloys, Journal de Physique IV Colloque 05 (1995) C2-489-C2-494.

[33] J.K. Allafi, G. Eggeler, W.W. Schmahl, Quantitative phase analysis in microstructures which display multiple step martensitic transformations in Ni-rich NiTi shape memory alloys, Materials Science and Engineering A 438-440 (2006) 593-596.

[34] W.A. Johnson, R.F. Mehl, Reaction kinetics in processes of nucleation and growth, Tran. AIME 135 (1939) 416-458

[35] M. Avrami, Granulation, phase change and microstructure kinetics of phase change, III, J. Chem. Phys. 9 (2) (1941) 177-184.

[36] H. Li, K. Gai, L. He, C. Zhang, H. Cui, M. Li, Non-isothermal phase-transformation kinetics model for evaluating the austenization of 55CrMo steel based on Johnson-Mehl-Avrami equation, Materials and Design 92 (2016) 731-741.

[37] J. Bernardini, C. Lexcellent, L. Daroczi, D.L. Beke, Ni diffusion in near-equiatomic Ni-Ti and Ni-Ti(-Cu) alloys, Philosophical Magazine 83 (2003) 329-338.

[38] M. Kato, H-R. Pak, Thermodynamics of Stress-Induced First-Order Phase Transformations in Solids, Phys. Stat. Sol. (b) 123 (1984) 415-423.

[39] A. Planes, J. Ortin, Study of thermoelastic growth during martensitic transformations, Journal of Applied Physics 71 (1992) 950-957.

[40] L. Bataillard, J.E. Bidaux, R. Gotthard, Interaction between microstructure and multiple-step transformation in binary NiTi alloys using in-situ transmission electron microscopy observations, Philosophical Magazine A 78 (1998) 327-344.

[41] I. Nikitin, M. Besel, Residual stress relaxation of deep-rolled austenitic steel, Scripta Materialia 58 (2008) 239-242.

[42] O. Vohringer, Relaxation of residual stresses by annealing or mechanical treatment, International Guidebook on Residual Stresses, Pergamon Press (1987) 367-397.

[43] D.H. Ko, et al., Prediction and measurement of relieved residual stress by the cryogenic heat treatment for Al6061 alloy: mechanical properties and microstructure, Journal of Mechanical Science and Technology 27 (7) (2013) 1949-1955.

[44] J. Frenzel, E.P. George, A. Dlouhy, Ch. Somsen, M.F.-X. Wagner, G. Eggeler, Influence of Ni on martensitic phase transformations in NiTi shape memory alloys, Acta Materialia 58 (2010) 3444-3458.

[45] W. Tang, B. Sundman, R. Sandstorm, C. Qiu, New modelling of the B2 phase and its associated martensitic transformation in the Ti-Ni system, Acta Mater. 47 (1999) 3457-3468.

[46] P. Sittner, et al., In situ experimental evidence on R-phase related deformation processes in activated NiTi wires, Materials Science and Engineering A 438-440 (2006) 579-584.

[47] J. Olbricht, et al., Characteristics of the stress-induced formation of R-phase in ultrafine-grained NiTi shape memory wire, Journal of Alloys and Compounds 579 (2013) 249-252.

[48] K.L. Ng, Q.P. Sun, Stress-induced phase transformation and detwinning in NiTi polycrystalline shape memory alloy tubes, Mechanics of Materials 38 (2006) 41-56.

[49] X. Wang, et al., An experimental study of the superelastic behavior in NiTi shape memory alloys under biaxial proportional and non-proportional cyclic loadings, Mechanics of Materials 42 (2010) 365-373.

Chapter 4

Materials Characterization
Volume 186, April 2022, 111827

Ultra-fast quantification of polycrystalline texture via single shot synchrotron X-ray or neutron diffraction

Zifan Wang[1], Jingwei Chen[1], Oxana V. Magdysyuk[2], Fatih Uzun[1], Alexander M. Korsunsky[1,*]

[1]MBLEM, Department of Engineering Science, University of Oxford, Oxford OX1 3PJ

[2]Diamond Light Source, Harwell Campus, Oxfordshire, OX11 0DE, UK

Corresponding author: *

Abstract

Tracking texture evolution during *in situ* loading is critical to understand and simulating the dynamic behaviour of microstructure in polycrystalline materials, yet conventional texture quantification methods are sometimes restricted due to various factors, such as acquisition time, sample environment and complex setup. To address this, a novel approach to extract texture information from single shot Time-Of-Flight neutron diffraction pattern has been developed. Another texture refinement approach based on single shot synchrotron X-ray diffraction has also been demonstrated. The effectiveness of two methods are assessed on polycrystalline Nickel-based superalloys possessing different textures. Both two methods feature a significantly reduced acquisition time to ~10mins and 30 seconds respectively, as well as a simplified setup which allows adding

complex sample environments and the use of additional equipment. Comparison with the referential EBSD texture suggests that both approaches achieve a decent match in an approximate manner, though some detailed complex contour profiles in inverse pole figures may be missing. Besides that, a novel metric has been proposed to quantify the matching quality of pole figures. By employing the EPSC modelling approach, it shows that the texture deviation (error) induced by the refinement method exerts a subtle influence on macro- and mesoscale simulation results, implying the reliability and applicability of the approach on computational simulation.

1. Introduction and objectives

Preferred orientations, namely textures, extensively exist in polycrystalline metallic components as a consequence of their thermomechanical history [1,2,3]. Undoubtedly, the presence of texture exerts a huge influence on the thermomechanical and functional properties of alloys of all kinds [4], therefore it is considered as a crucial material input in dynamic modelling approaches, such as Finite Element model [28], Crystal Plasticity Finite Element model (CPFE) [5], Visco-Plastic Self-Consistent model (VPSC) [6], Elasto-Plastic Self-Consistent model (EPSC) [7], Elasto-Visco-Plastic Self-Consistent model (EVPSC) [23].

Acquiring texture in a bulk polycrystal is usually time-consuming and requires specific instrumental setup. Conventional methods mainly include large area EBSD, synchrotron X-ray/neutron diffraction or laboratory XRD diffractometer. Each of these methods has one or several drawbacks. Large area EBSD is time consuming. Prevailing EBSD systems can reach an acquisition speed of 10 frames per second (e.g. Oxford Instrument Nordlys 2013), therefore an EBSD map of adequate size for texture quantification (~10^5 frames) takes ~2.8 hours. In addition, EBSD technique needs strict

surface preparation, and the sample surface must be kept pristine throughout measurement, thus restricting the use of sample environment such as pressure, corrosion, vibration, etc. What is more, EBSD is not applicable to materials that contain large amount of amorphous phase or nano-size grains [8], instead only well-crystalized materials (e.g., after annealing treatment) can be used. Last but not least, EBSD is a surface probing technique, therefore for large/bulky samples, more than one map would be necessary to confirm the texture quantification result. Complete texture determination using synchrotron X-ray/neutron diffraction can be achieved either by applying sample rotation [9], or by enhancing the pole figure coverage area of the detector array, like HIPPO at LANSCE [10] and GEM at ISIS [11]. Sample rotation requires a range of at least 180°, within which no obstacles should be blocking the path of the X-ray/neutron beam. At facilities dedicated to texture refinement like HIPPO and GEM, detector array is arranged in such a way that covers the whole spherical space around the sample. Apparently, these two methods restrict the use of additional equipment, e.g. *in situ* loading machine, because any equipment that contacts or surrounds the sample is likely to block the diffracted beam from sample to the detector. The same principle applies to laboratory diffractometer (XRD). Therefore, in conventional SXRD/ND/XRD texture measurement setups, only initial and post-mortem texture quantification is readily feasible [10,11].

To resolve the dilemma described above, techniques have been developed to extract texture from single exposure synchrotron X-ray powder diffraction pattern [12,13,14,27,30,31]. In this setup, the relative position between the incident X-ray beam and the sample is fixed. The diffracted beam transmits through the sample thickness and finally reached an area detector at the back, as illustrated in Fig.1(b). Since the incident beam and the diffracted beam is small (~200μm cross-section lengths) and their travelling paths are fixed, this experimental setup gives plenty of space for additional equipment

such as *in situ* loading machine. Besides that, the 2D Debye-Scherrer ring diffraction pattern contains other valuable information such as microstrain, phase fraction, lattice strain and so on [4]. Most importantly, the acquisition for a single Debye-Scherrer ring diffraction pattern is vastly rapid owing to the high energy / flux of X-ray beam at Synchrotron facilities. For instance, the typical acquisition time for a 2mm thick Nickel-superalloy, which is considered as a high attenuation material, is merely 30 seconds at I12 JEEP beamline at DLS [12] or at ID15A beamline at ESRF [24]. The analysis routine for texture refinement based on a single Debye-Scherrer ring diffraction pattern has been partially integrated in analysis software such as MAUD [14] and GSAS-II [15].

Nevertheless, to the best of author's knowledge, the accuracy of texture being refined from such technique has rarely been verified through one of those conventional yet more reliable texture measurement methods, considering the fact that error occurs more or less due to the incomplete pole figure coverage of a single exposure synchrotron X-ray powder diffraction pattern [25]. Namely, there are potentially differences in Orientation Distribution Function (ODF) obtained by these texture refinement methods. Furthermore, though critical, the discrepancy in computational modelling results caused by such texture deviation (error) has never been examined. Besides that, this technique [12,13,14,15,16] is based on 2D synchrotron X-ray powder diffraction pattern, however, many neutron diffraction facilities for engineering strain measurement are only equipped with one detector, such as SALSA at ILL and POLDI at PSI, or two detectors, such as SMARTS at LANSCE and ENGIN-X at ISIS, capturing one or two 1D diffraction pattern(s) in a single acquisition period of ~10 minutes. An example of Time-Of-Flight neutron diffraction setup is shown in Fig.1(d). In these cases, the technique is no longer applicable.

Having identified the knowledge boundary and limitations of existing studies, the first objective of this work is to develop a novel technique that can extract texture information from a single shot Time-Of-Flight neutron diffraction (ND) pattern [29]. This novel texture refinement technique is applicable to any neutron diffraction facilities as mentioned above, viz SALSA, POLDI, SMARTS and ENGIN-X, and also other worldwide facilities that are not mentioned here. It enables texture quantification from a single shot diffraction pattern (single acquisition period), which takes around 10 minutes, without even the slightest alteration to the current diffraction setups at these facilities. This ensures the maximal flexibility of the use of any additional setups, such as sample environment equipment, loading rig, and so on. As the second objective, the texture analysis routine based on a single shot synchrotron X-ray diffraction pattern is demonstrated. This ultra-fast method allows texture quantification in ~30 seconds, depending on the X-ray energy and flux of the facility. Similarly, this method can be utilised at any beamlines with transmission diffraction capability, such as I12 at DLS, ID15A at ESRF, 1-ID at APS, and many more. Mostly importantly, the experimental setup is simple to operate, as has been discussed above and illustrated in Fig.1(b). Advancing from previous relevant studies, the third objective of this work involves the assessment of accuracy of the texture refined from the two methods. Large area EBSD is employed to quantify the texture as reference, and being compared with textures refined from both the single shot Time-Of-Flight neutron diffraction pattern and the single shot synchrotron X-ray diffraction pattern. Pole figure matching errors are quantified by introducing a novel metric E_p, and a more intuitive evaluation has been made based on the plot of complete Orientation Distribution Function (ODF). Finally, as the fourth objective, the effect of texture deviation (error) on computational modelling results is examined via the texture sensitive EPSC model.

The significance of this present work is the development and verification of two ultra-fast analysis routines for texture quantification based on simple experimental setups at synchrotron X-ray facilities and neutron facilities respectively. The application of these ultra-fast analysis routines allows *in situ* texture quantification under complex sample environment. In the present study, a newly invented polycrystalline Ni-based superalloy that has great potentiality in aerospace applications is chosen as the sample for demonstration, while the analysis routines are universally applicable to all polycrystalline materials.

2. Experimental methods and preliminary analysis

2.1 Material

The specimen material used in this study belongs to a family of recently invented polycrystalline high-temperature Ni-based superalloy [17], referred to as Alloy 11. Pancake forging was conducted by isothermally and isostatically pressing a cylindrical ingot. Extracted from different locations in the pancake forged bulk, the two miniature bar samples (nominal size of 30 × 2 × 1 mm^3) present contrasting textures. Two samples are named as Sample 1 and Sample 2 in the text below. Like other types of Ni-based superalloys, the major gamma (γ) phase of Alloy 11 has a face-centred cubic structure of H-M space group F m -3 m, of which the composition is provided in Table 1.

Table 1

Chemical composition of Alloy 11 (wt. %).

Ni	Co	Cr	Ta	W	Al	Ti	Mo	Nb	Fe	Mn	Si	Zr	C	Bo
bal	15.1	12.7	4.8	3.2	3.2	2.8	2.1	1.4	1	0.5	0.5	0.06	0.03	0.02

2.2 Single shot Synchrotron X-ray powder diffraction

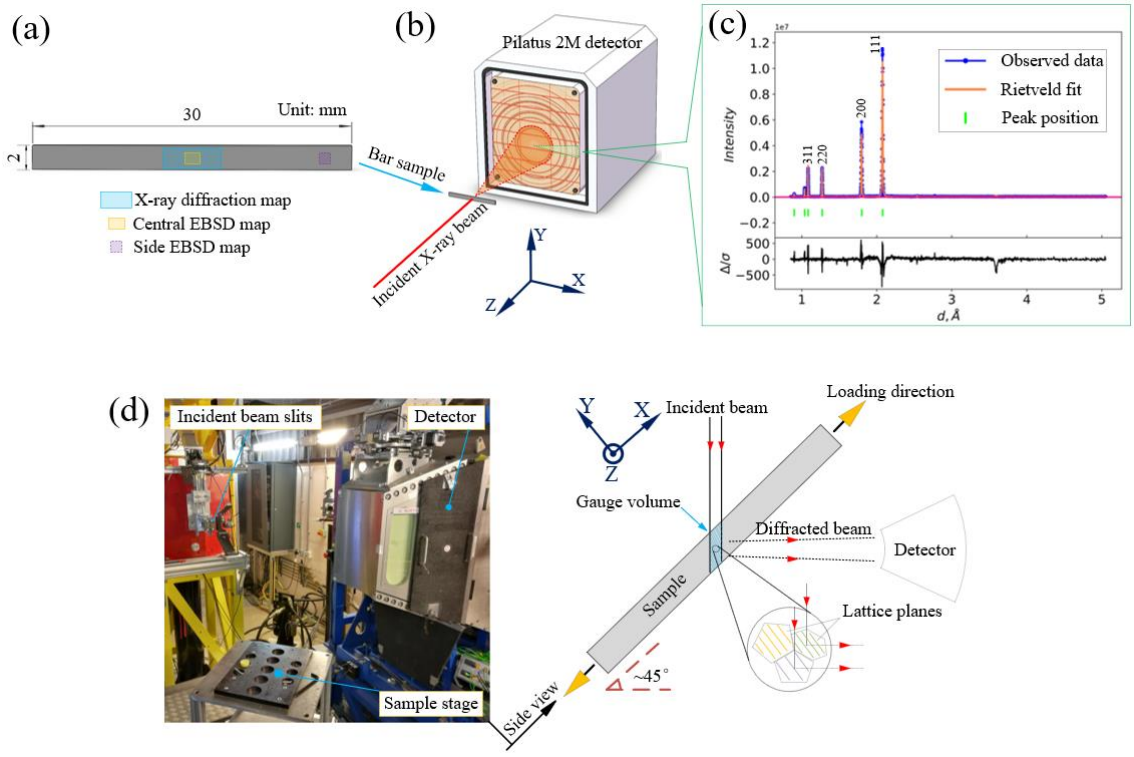


Figure 1. (a) Mapping scheme for X-ray diffraction and EBSD. (b) Overview of synchrotron X-ray diffraction setup at I12 DLS. (c) An example of integrated, indexed and refined diffraction pattern. (d) TOF neutron diffraction setup at ENGIN-X ISIS. Right hand side is a top view. The photo on the left hand side was captured from the side. Lab coordinate systems are given for both setups.

The single shot synchrotron X-ray diffraction measurements were carried out at I12 JEEP beamline at Diamond Light Source, UK. The bar sample(s) was mounted statically with its largest area surface perpendicular to the incident beam, as illustrated in Fig.1(b). Monochromatic beam energy was set to 93.7 keV with a spot size of 200μm×200μm. By moving along X and Y axis, large area diffraction mapping was conducted covering the central volume of the samples. Debye-Scherrer ring patterns were recorded by a large 2D area diffraction detector Pilatus 2M CdTe (1475×1679pixel, pixel size 172μm×172μm) sitting behind the sample. All 2D patterns from the mapping area were merged to a single pattern that represents the averaged texture of the whole area. Based on the setup

calibration from Data Analysis WorkbeNch (DAWN) platform, the Rietveld analysis was performed using GSAS II [15] and visualised by MTEX [18]. For peak indexation in Fig.1(c), the Crystallographic Information File of the major γ phase refers to database code ICSD-102819.

2.3 Single shot Time-Of-Flight neutron diffraction

The single shot Time-Of-Flight (TOF) neutron diffraction measurements were carried out at ENGIN-X hutch at ISIS, UK. As illustrated in Fig.1(d) right hand side, the bar sample was mounted horizontally at 45° relative to the incident beam. Polychromatic beam was delivered at a frequency of 50Hz with a spot size of 6mm×6mm. The beam is diffracted from lattice planes parallel to the YZ plane within the gauge volume. The 1D diffraction pattern is initially processed by the customised software OpenGenie, and imported into GSAS [15] to perform Rietveld Refinement.

2.4 EBSD characterization

To obtain the reference texture, electron backscatter diffraction (EBSD) observations were conducted in a Tescan LYRA3 system integrated with the superb SYMMETRY CMOS EBSD detector from Oxford Instruments. Samples were polished step by step till 0.25μm colloidal silica. Indexation of Kikuchi patterns was carried out under 20kV, 10mm working distance, and ~0.5 μm step size.

A rigorous strategy is followed to ensure the accuracy of reference texture. In the first instance, a large EBSD map (1.5mm×1mm) was acquired at the same central area as that of the X-ray diffraction mapping on each sample, as shown in Fig.1(a). In the second instance, another map (1mm×1mm) was acquired at the side region away from the central area. Then the pole figures that are constructed from the two maps are

compared to ensure that the texture is consistent across the sample. Finally, the textures from two maps are combined as the reference texture of that sample. The reference texture is referred to as EBSD texture in the text below. Pole figures of the two maps and their combination are shown in Fig.5&6.

3. Texture refinement techniques

3.1 Single shot Time-Of-Flight neutron diffraction

Neutrons and X-rays interact with matter differently in such a way that neutron interact directly with nucleus of atoms while X-rays interact with the electron cloud surrounding atoms. For powder diffraction of polycrystalline, the two techniques are similar, except the minor variance in diffraction intensity [19]. What is more, this difference can be compensated by detector calibration using reference crystals. Hence single shot Time-Of-Flight neutron diffraction pattern is substituted by a portion of synchrotron X-ray diffraction pattern, as shown in Fig.2(a).

3.1.1 Theoretical intensity and texture effect

Assuming a polycrystalline aggregate of any texture, and by taking into account the scattering geometry, crystallographic information, and detector calibration result, the theoretical diffraction profile can be estimated by a mathematical model [20]:

$$I_T = I_B + I_D = I_B + \sum_h S \cdot K \cdot F_h^2 \cdot P(\Delta T_h), \quad (1)$$

where I_T is theoretical intensity, I_B is background intensity. The last term I_D is diffraction intensity, which is a sum of contributions from each reflection h. Every contribution is multiplication of structure factor F_h^2, scale factor S, correction factor K, and peak profile function $P(\Delta T_h)$. The value of correction factor K is partially determined by another factor $A(h, y)$ that describes the variation of diffraction intensity due to texture effect:

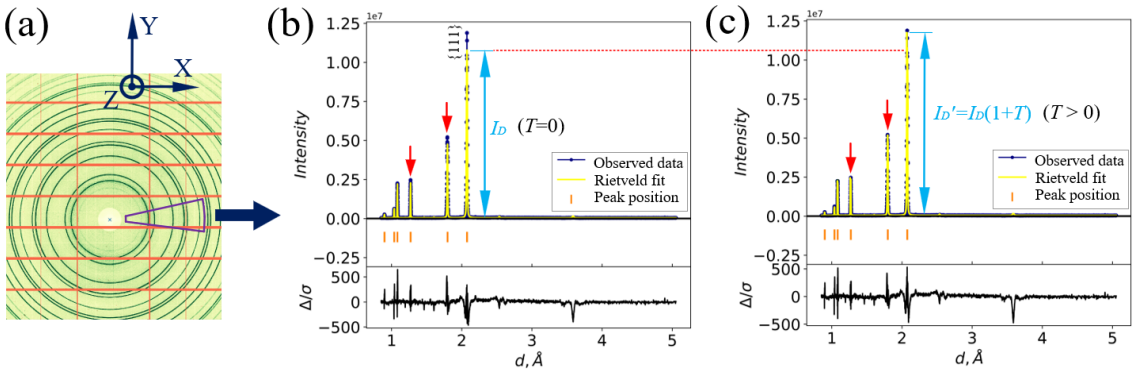


Figure 2. (a) Diffraction pattern from Sample 1 integrated around 15° azimuth in X direction. (b) Rietveld refinement without considering texture effect. (c) Correction of diffraction intensity via variation of grain population of all reflections in X direction.

$$A(\varphi,\beta,\psi,\gamma) = 1 + T, \tag{2}$$

where T is expressed by the generalized spherical-harmonics term:

$$T = \sum_{l=2}^{L} 4\pi/(2l+1) \sum_{m=-l}^{l} \sum_{n=-l}^{l} C_l^{mn} k_l^m(\varphi,\beta) k_l^n(\psi,\gamma), \tag{3}$$

where C_l^{mn} are harmonic coefficients, which can be determined by Rietveld refinement, and k_l^m and k_l^n depend on the crystal and sample symmetries respectively [21].

Apparently, in the case of an ideal polycrystalline material of random texture, $T = 0$. Take {111} reflection for instance as shown in Fig.2(b), I_D represents its intensity without the correction of texture effect. At this initial stage of refinement, there is a gap between observed data and Rietveld fit. Upon refining, the texture effect is corrected so that the intensity matches with observed data as shown in Fig.2(c). The intensity of {111} has been corrected from I_D to I_D'. Besides that, intensities of all other reflections in Fig.2(c), e.g. {200} and {220}, have also been corrected by taking into account the texture effect. These intensity corrections are recorded by the harmonics coefficients C_l^{mn} in Eq.(3), which contain quantitative orientation distribution of grain families of all reflections that are available in the diffraction pattern. Namely, the populations of grains that contributes to certain reflections are quantified. The proportion of the actual

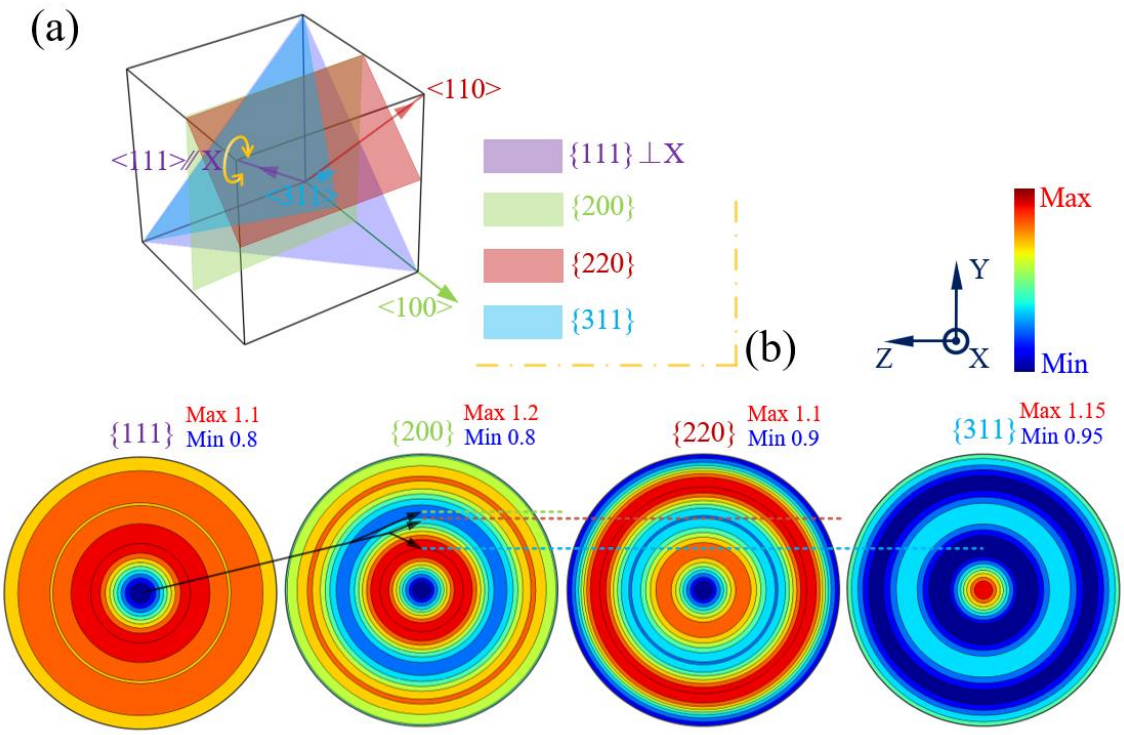


Figure 3. (a) Geometry of crystallographic reflections in FCC crystal, with {111} plane normal parallel to the X axis. (b) Constructed pole figures from single shot diffraction pattern of sample 2, in unit of MRD. Colour of dashed lines corresponds to the colour of {*hkl*} indices.

population to that of the ideal random texture state is termed Multiples of Random Distribution (MRD).

3.1.2 Justification of cylindrical symmetry

During the texture refinement using Eq.(3), the population of grains whose {*hkl*} reflection normal vectors are parallel to the diffraction scattering vector is quantified. However, the orientation information of how those grains rotating around that {*hkl*} reflection normal remains missing. Therefore, cylindrical symmetry must be chosen, assuming that those grains distribute homogeneously around that particular {*hkl*} normal vector.

Take the {111} reflection as an example, as depicted in Fig.3(a). Suppose that the population of grains whose {111} reflection normal vectors are parallel to the X direction is quantified via the theory introduced in Section 3.1.1. Since the quantity of <111> vector is known and the crystal structure is fixed, the quantity of <110>, <100>, <311> vectors in certain directions (pointed by the arrows in Fig.3(a))can be deduced, so as the corresponding lattice planes, namely {220}, {200}, {311}, etc. Nevertheless, as indicated by the circular yellow arrow, it cannot be determined how these crystals population distribute around the <111> direction, thus homogeneous distribution is presumed.

Based on the cylindrical symmetry and 8-order spherical harmonics, a series of inter-related pole figures can be constructed from the refined harmonics coefficients, as shown in Fig.3(b). The inter-relation can be explained in such a way that for each pole figure, only the intensity at the centre of the circle, i.e. projection of MRD parallel to the X direction, is directly refined from the texture correction of peak intensity from a diffraction pattern (Fig.2), whilst the intensity of the remaining area is deduced from central intensity of other pole figures. For instance, in Fig.3(b), the {111} pole figure centre has a low intensity of 0.8 MRD. According to the geometry of crystallographic reflection planes depicted in Fig.3(a), this causes the low intensity in {200}, {220}, {311} reflections in certain directions. As pointed out by the black arrows, this is reflected by the low intensity annular regions in the latter three pole figures {200}, {220} and {311}. The corresponding annular regions are marked by the dashed lines using the same colours as the colour of {*hkl*}, viz the top line indicates the diameter of the low intensity annular regions of {200} pole figure, the bottom line indicates the diameter of the low intensity annular regions of {311} pole figure. The diameters of these annular regions match well with relative geometry of *hkl* reflections in Fig.3(a). The blue colour of these marked

annular regions indicates their low MRD as a consequence of the low intensity at the centre of {111} pole figure.

3.1.3 ODF construction

The ODF can be reliably estimated from pole figures through a novel analysis routine introduced in [22]. Mathematically, the pole density function P with respect to the ODF can be expressed by a fundamental texture analysis equation [26]:

$$P(h,r) = \frac{1}{2}[\mathcal{R}f(h,r) + \mathcal{R}f(-h,r)], \quad (4)$$

where f is the ODF, $\mathcal{R}$ is the integral operator recognized as the geodesic Radon transform.

Based on Eq.4, the statistical model can be written as:

$$I_{ij} \simeq Pois\left[I_{ij}^{b} + [v_{true}]_i \mathcal{R}f_{true}(H_i, r_{ij})\right], \quad (5)$$

where I_{ij} is the statistical counts, I_{ij}^{b} is the background counts. $Pois$ means the parameterized Poisson process.

The ODF construction is equivalent to the classical parameter estimation. Given a random sample I_{ij}, i=1,…, N, j=1,…, N_i of counts, the modified least squares estimator can be written as:

$$f_{MLS} = \operatorname{argmin} \sum_{i=1}^{N} \sum_{j=1}^{N_i} \frac{|\alpha_i \mathcal{R}f(h_i,r_{ij}) - I_{ij}|^2}{I_{ij}}, \quad (6)$$

which includes a series of unknown normalization coefficients as variables. To numerically solve the minimization problem of Eq.6 requires discretization of ODF, which is approximated by Fourier expansion. The Fourier expansion can be identified as a composition of a spherical and an adjoint spherical Fourier transform. Finally, a modified steepest descent algorithm is applied to solve the minimization problem. The algorithm has been implemented in the texture analysis software MTEX. The pole figures

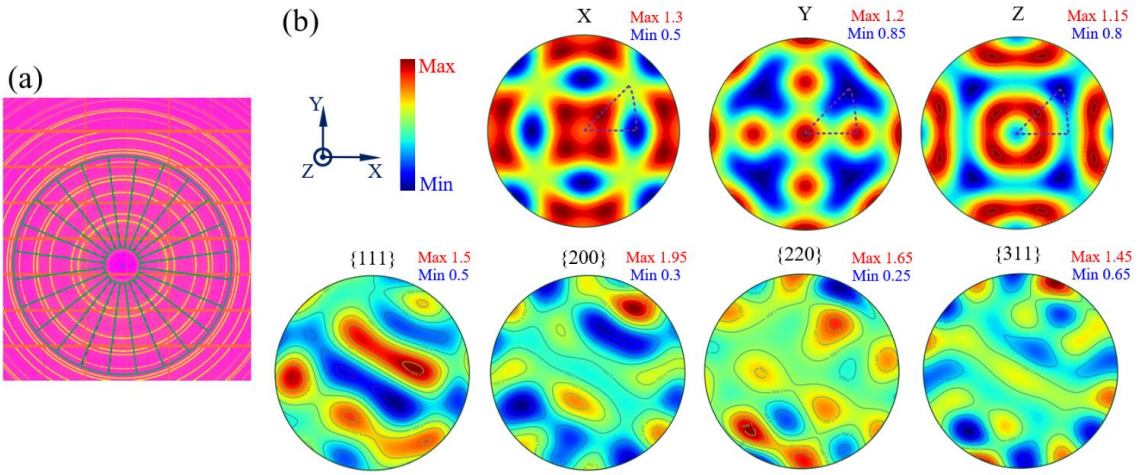


Figure 4. Texture refinement example of sample 1. (a) 24 segmentations of synchrotron X-ray 2D powder diffraction pattern. (b) Inverse pole figures and pole figures constructed from harmonics coefficients in GSAS II, in unit of MRD. Inverse pole figures are given in complete projection space, but the fundamental region for cubic structure is highlighted in dashed triangle.

constructed in Section 3.1.2 can be imported into the software, from which the ODF is estimated and inverse pole figures constructed.

3.2 Single shot synchrotron X-ray diffraction

For a single synchrotron X-ray powder diffraction pattern, the texture analysis routine has been elucidated in previous studies [15]. In the present work, 24 patterns are integrated around the diffraction rings with a step size of 15°, as illustrated in Fig.4(a). Pole figures and inverse pole figures are constructed based on the refined harmonics coefficients in GSAS II, as shown in Fig.4(b). No sample symmetry and 8-order spherical harmonics are assumed. The figures are then imported into the MTEX software for plotting and comparison in Section 4.2.

4. Results and discussion

4.1 EBSD maps and EBSD texture

The EBSD maps and texture information of Sample 1 and Sample 2 are shown in Fig.5 and Fig.6 respectively. Each map consists of a statistical counting of approximately half million grain orientations, from which pole figures are constructed. The four reflections of pole figures, namely {111}, {200}, {220} and {331} are selected according to the strongest diffraction peaks in Fig.1(c).

The grain orientation statistics of Sample 1 exhibits such distribution that does not belong to any commonly observed texture types. The highest / lowest intensity area dot around the whole hemisphere of the four pole figures. Nevertheless, the pole figures of central and side EBSD mapping area match well with each other in terms of maximum/minimum MRD value, contour profile and intensity distribution. This confirms the uniformness of texture across the length scale in Sample 1. Therefore, the EBSD texture, which represents the standard reference texture of the entire sample, can be established by synthesising texture from the two maps, as shown in Fig.5(c). Additionally, inverse pole figure in three principal directions (X, Y and Z) are given for comparison in Section 4.2.

Comparatively, the grain orientation statistics of Sample 2 demonstrate pretty much the same features as were observed in Sample 1, except the smaller grain size and less texture complexity. Fig.6(c) shows the EBSD texture of Sample 2.

The textures of Sample 1 and Sample 2 are relatively weak since the maximum MRD is less than 2, yet the preferred grain orientations are totally different. This makes them challenging practices as well as tenable verifications for the texture refinement techniques in this study.

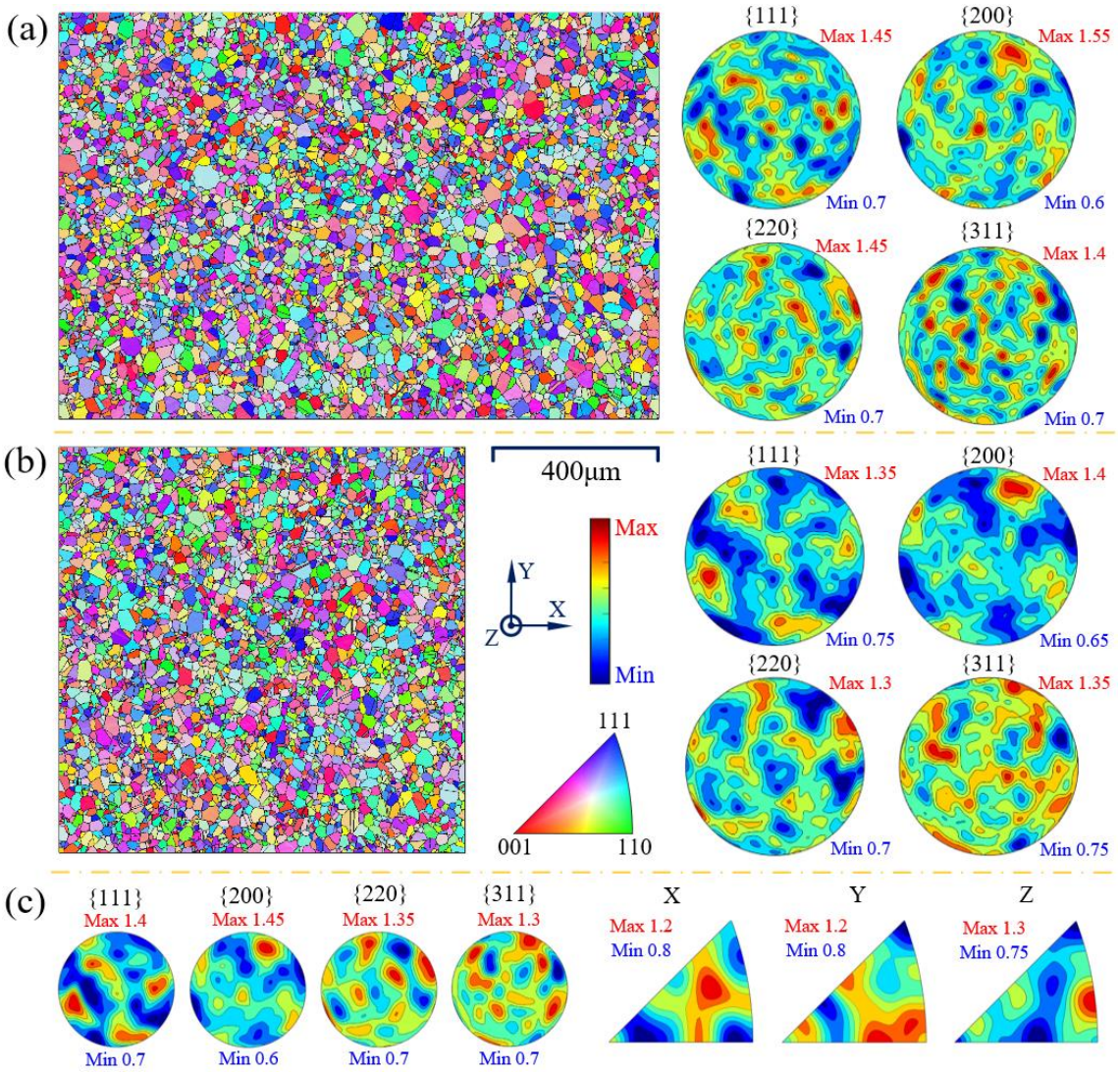


Figure 5. EBSD measurements of Sample 1. EBSD map scale bar, coordinate system for EBSD map and pole figures, colour key for Multiples of the Random Distribution (MRD), and colour key for EBSD maps in Z direction are presented together in the middle. (a) Central area map and pole figure texture statistics. (b) Side area map and pole figure texture statistics. (c) EBSD texture, a combination of texture statistics of both maps.

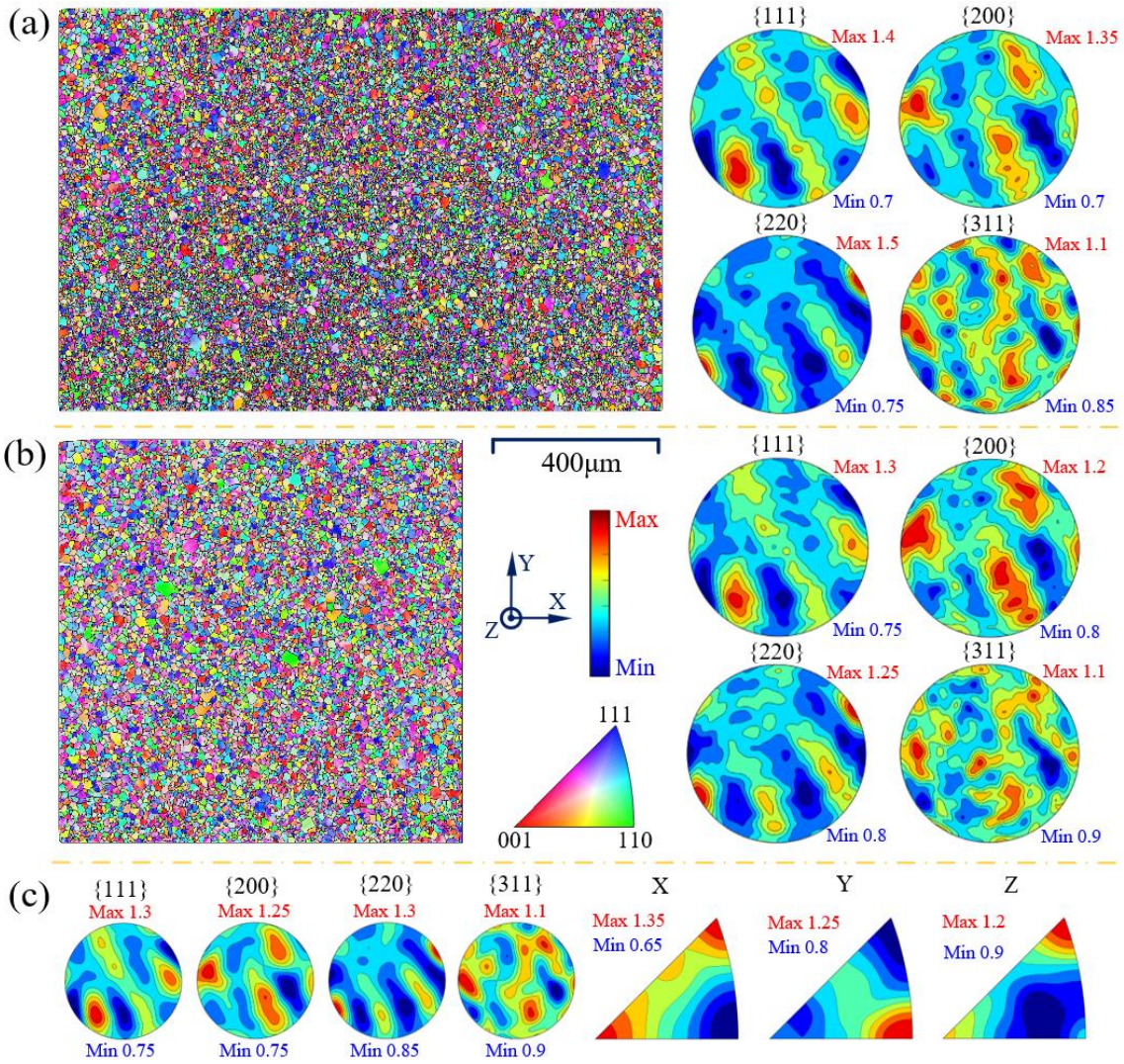


Figure 6. EBSD measurements of Sample 2. For detailed caption please refer to that of Fig.5.

4.2 Comparison of texture results

Based upon the texture refinement techniques being introduced in Section 3, texture information can be derived from diffraction patterns of both experimental setups, namely single shot Time-Of-Flight neutron diffraction and single shot synchrotron X-ray powder diffraction. For the purpose of accuracy assessment, results are plotted in contrast with the referential EBSD texture, as shown in Fig.7 and Fig.8 for Sample 1 and 2 respectively.

The texture results from single shot Time-Of-Flight neutron diffraction are shown in Fig.7(b) and Fig.8(b). As has been discussed in Section 3.1, a single diffraction pattern contains texture information of a specific direction, thus only inverse pole figure of that direction may be accurately constructed. Hence for each sample, two segmentations in the X and Y directions are made to produce two inverse pole figures. Compared with EBSD texture plots, single shot neutron diffraction well captures the overall texture in terms of intensity distribution and max/min intensity, for instance, <111>, <001> and <110> in both X and Y in Fig.7(b), similar in Fig.8(b). However, the detailed contours are blurred, such as Fig.7(b) Y direction, that the plot indicates the intense region in the middle of the triangular area, whilst the actual distribution consists of three peak regions (Fig.7(a) Y direction). The reason why the texture at <111>, <001> and <110> directions correspond well with the EBSD observation than other directions is obvious: their diffraction peaks are directly observable from the pattern (e.g. Fig.1(c)) whose intensities are corrected by texture effect.

The texture results from single shot synchrotron X-ray powder diffraction are shown in Fig.7(c) and Fig.8(c). Incomplete pole figures can be constructed from the input of 24 diffraction patterns around the azimuthal direction. Regarding Sample 1, pole figure contours exhibit decent matching between Fig.7(a) and Fig.7(c), particularly the most/least intense regions, though some deviations can be observed. The matching of pole figures in Sample 2 between Fig.8(a) and Fig.8(c) is better, especially the {111} and {220} plane groups. To quantify the matching quality, the difference pole figures are provided in Fig.7(d) and Fig.8(d), together with the novel metric E_p that evaluates the error between two pole figures. Metric E_p is defined as: $E_P = \frac{1}{n}\sum_1^n \frac{|M_i - N_i|}{M_i}$, where M_i is the MRD value at a point in the EBSD pole figure, N_i is that in the diffraction pole figure,

n is the number of discretised points in the pole figure domain. The calculated E_p values suggest that the errors are generally below 10% (10%=0.1), the average is around 5%. For a better visual evaluation, a quantitative comparison of complete ODF is made by plotting the ODF difference between EBSD reference and our refinement technique, as shown in Fig.7(e) and Fig.8(e). For FCC crystal structure, the standard Euler angle range is a 90°×90°×360° space, thus 9 sections are plotted at a step size of every 10°. It can be seen that the majority of ODF space shows a difference of 0-0.1 MRD for both Sample 1 and Sample 2. The accuracy of texture refinement of Sample 2 is slightly better because of less regions with peak values. Therefore, from both the parametric and visual evaluation, the result of our texture refinement technique exhibits decent agreement with EBSD.

It is note-worthy that the inverse pole figures of Sample 2 show excellent matching with EBSD in X and Y direction, whilst that of Sample 1 is more deviated but acceptable. Compared with inverse pole figures from neutron diffraction, those from synchrotron X-ray diffraction contain more details, though still not enough to capture the profile. Due to the combination of patterns from 24 azimuthal directions, single shot synchrotron X-ray powder diffraction provide texture information of satisfactory precision.

Nevertheless, it should be pointed out that the Z direction inverse pole figures from single shot synchrotron X-ray powder diffraction exhibit poor matching with EBSD result in both Sample 1 & 2. Reason is fairly straightforward, that the Z direction is parallel to the incident beam where lacks the diffraction information, leading to the faulty texture prediction.

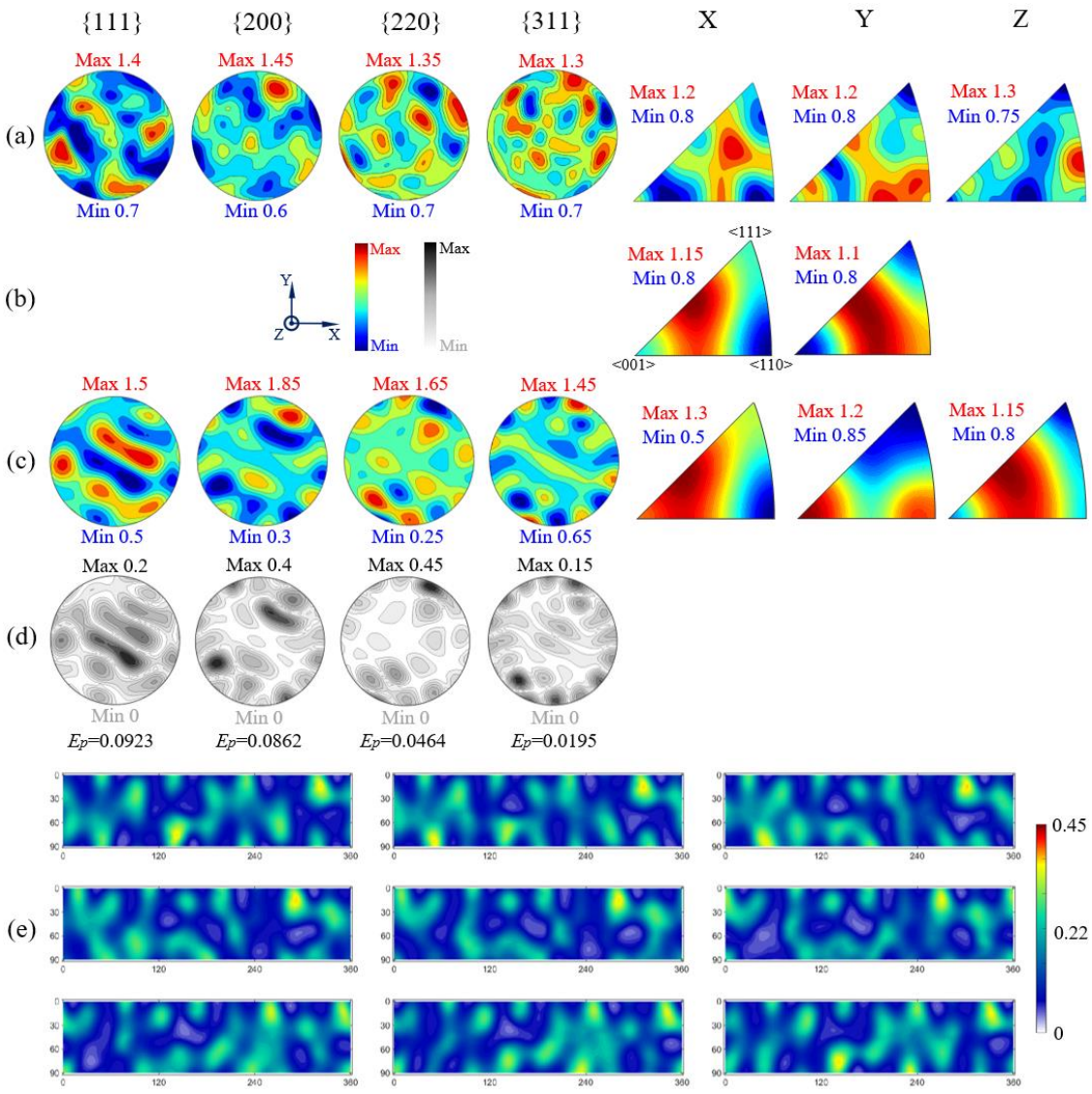


Figure 7. Comparison of texture results of Sample 1. Coordinate system and intensity colour key are near the picture centre, in units of MRD. Four *hkl* indices for pole figures and three directions for inverse pole figures are on the top line. (a) Referential EBSD texture. (b) Single shot Time-Of-Flight neutron diffraction pattern. (c) Single shot synchrotron X-ray powder diffraction. (d) Difference pole figures between EBSD and single shot synchrotron X-ray powder diffraction, with corresponding E_p values that indicate the matching quality. (e) Difference of complete ODF space between EBSD and single shot synchrotron X-ray powder diffraction, in unit of MRD. Top left is 0° section, and bottom left is 90° section.

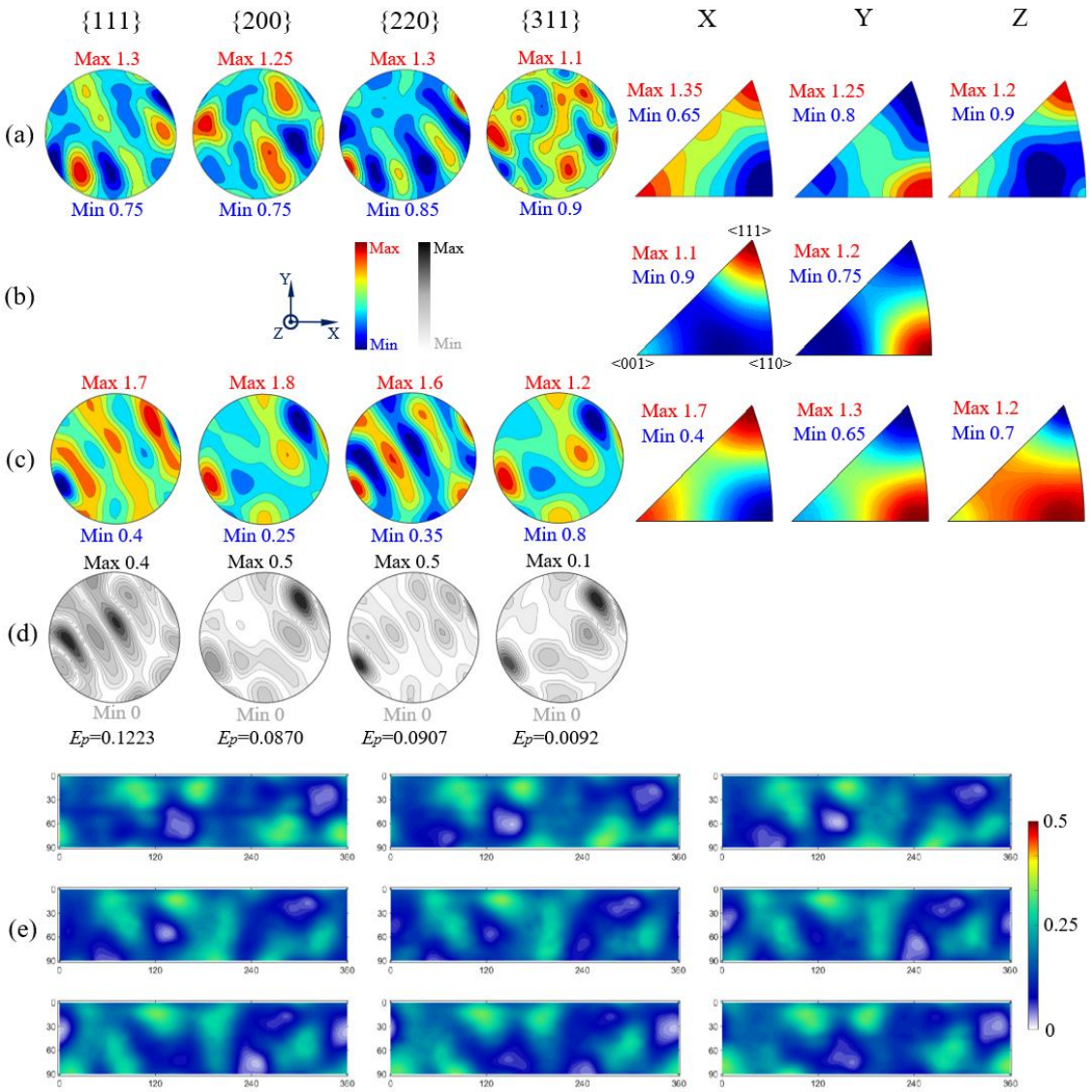


Figure 8. Comparison of texture results of Sample 2. For detailed caption please refer to that of Fig.7.

4.3 Effect of texture deviation on modelling approach

In Section 4.2, visual comparison has been made between the referential EBSD observation and diffraction results. For texture refinement techniques, deviations occur more or less, whose randomness is rather difficult to quantify. In practice, texture refined from diffraction patterns is used to predict material's thermomechanical properties, via either empirical or advanced modelling approaches. Therefore, what really concerns is the effect of such random deviations on modelling result, as is the topic of this section.

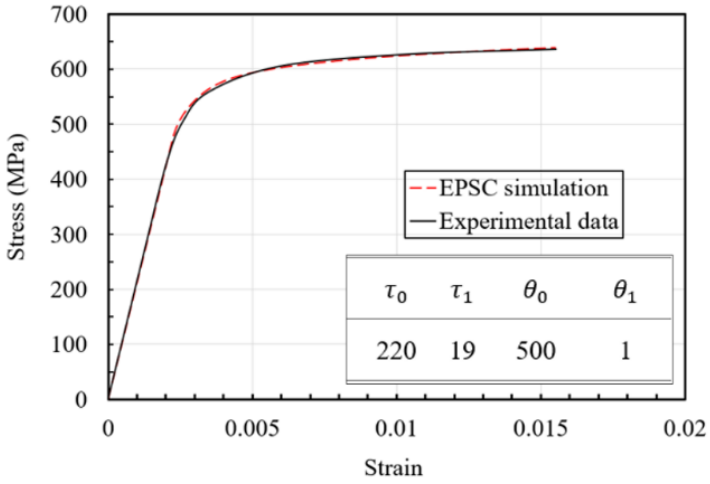


Figure 9. The EPSC model is calibrated with experimental data. Hardening parameters are tuned as shown in the table.

4.3.1 EPSC modelling approach

The Elasto-Plastic Self-Consistent (EPSC) modelling approach treats grains as ellipsoidal inclusion embedded in a homogeneous medium. Based on the Eshelby theory, the model implements Voce-type hardening law to describe the activation and hardening of slip system *s*:

$$\hat{\tau}^s = \tau_0^s + (\tau_1^s + \theta_1^s \Gamma)\left(1 - e^{-\left(\frac{\theta_0^s \Gamma}{\tau_1^s}\right)}\right), \tag{7}$$

where Γ is the accumulated shear in the grain, τ_0, τ_1, θ_0, θ_1 are hardening parameters. Detailed numerical implementation of the model refers to [7]. The tenability and universality of the EPSC model and its modified version has been validated by numerous studies in the past 30 years, including but not limited to [4,6,7,23]. In this study, the Version 4 is used, which was developed in recent years.

The model is calibrated through fitting macroscopic stress-strain behaviour with tensile loading experiment for a Ni-superalloy sample of random grain orientation distribution, as shown in Fig.9.

4.3.2 Effect of texture deviation on macroscale simulation results

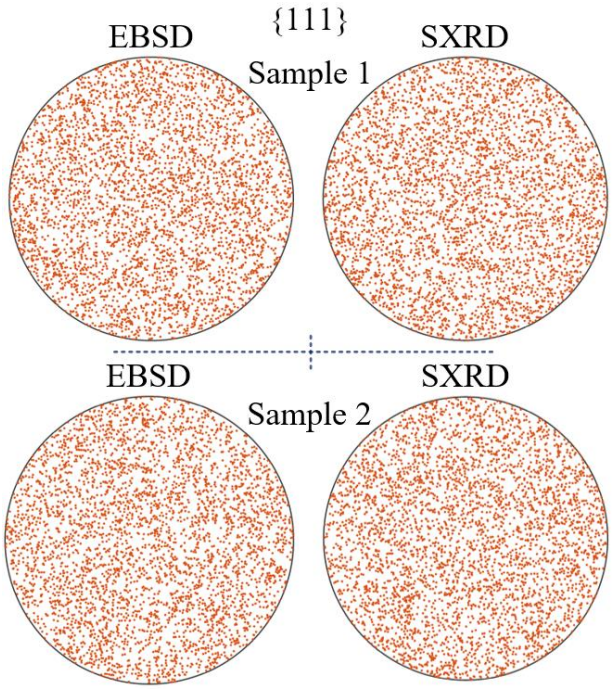


Figure 10. Orientation of 1000 grains among the 50000 grain aggregate, plotted in {111} pole figure.

The grain population file of the calibrated EPSC model is created by random sampling from the texture of EBSD and single shot synchrotron X-ray powder diffraction (below abbreviated as SXRD). 50000 orientations are randomly sampled from the constructed ODF using the discrete sample function integrated in MTEX. The orientation of 1000 grains among the 50000 aggregate is randomly picked and displayed in Fig.10 for both samples. Each spot in the pole figure represents one grain in the space, playing an individual role in the program. The grain ellipsoidal ratios for both samples are set to 1, viz equivalent to round shape. Texture evolution mode is enabled. Simulation was conducted in strain control mode, with a step size of 0.0001, altogether 200 steps from 0 till 0.02. Loading axis is set parallel to the X direction in Fig.1, and stress in Y and Z direction is set to 0. Strain in Y and Z and stress in X direction are outputs from the simulation.

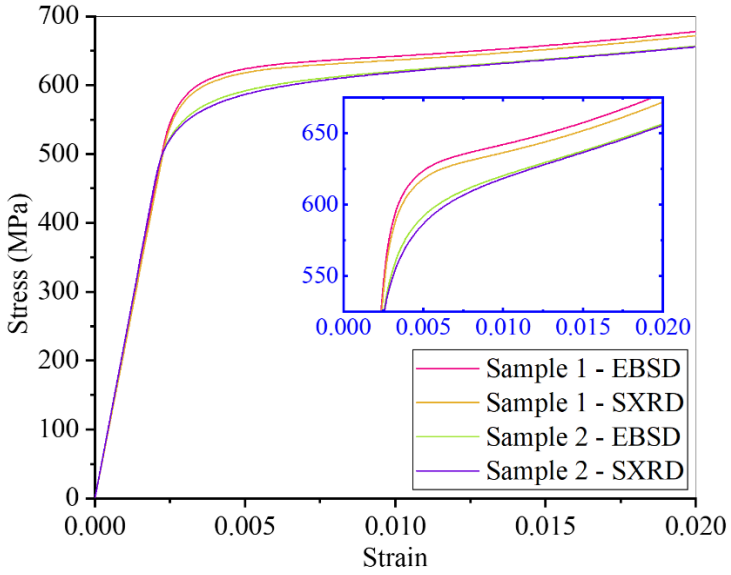


Figure 11. Macroscopic stress-strain loading simulation result from EPSC model. EBSD texture and single shot synchrotron X-ray powder diffraction (SXRD) texture files are used, presented by curves in different colours.

The macroscopic stress-strain loading simulation result is shown in Fig.11. The four curves show negligible difference in the elastic regime from 0 to 500 MPa. The yielding points are about the same level, whilst the texture exerts a huge influence on the hardening behaviour. Two curves of Sample 1 seem to exhibit a more gradual hardening than the Sample 2, clearly the four curves are separated into two distinct groups for different samples. The difference in stress-strain curve in the initial plastic regime between the two samples may be attributed to the enabled texture evolution mode in the simulation, while such discrepancy shows a tendency of convergence beyond the strain level of ~1.2%.

A zoom in view of plastic regime is displayed in the blue insert map. The two curves of EBSD texture and SXRD texture from Sample 1 fall more apart than Sample 2, agreeing well the fact that in the visual comparison of pole figures in Section 4.2, there shows a better match between EBSD texture and SXRD in Sample 2, which leads to a

nearly identical curve paths. What is more, the curves of Sample 1 remain steadily parallel with each other, not in a diverging manner.

Overall, it can be concluded that effect of texture deviation brought by the texture refinement technique is much less than that caused by the diversity of texture in different samples, even for weak textures, i.e. maxima less than 2 MRD.

4.3.2 Effect of texture deviation on mesoscale simulation results

Considering the fact that synchrotron X-ray powder diffraction provides mesoscale information of polycrystalline, which means the combination of grains that contribute to certain reflections as grain groups, within the gauge volume that is illuminated by X-ray beam, it is necessary to exam the mesoscale simulation results, as shown in Fig.12.

Comparing Fig.12(a)&(b), it is obvious that intrinsic texture in Sample 1&2 brings about different lattice strain evolution paths in both directions. In Axial Direction, the lattice strain paths of EBSD texture and SXRD texture show excellent match without visible diversity. By contrast, the paths split in the plastic regime in both samples in Radial Direction, for Sample 1, the divergence is larger, which explains the observation in its macroscopic curves. Despite that, the curves of the same grain group still follow the same tendency regardless of the extent. Additionally, the quantity of grains included in this simulation has been proved to be adequate to achieve a stable result, since a 20000 grain aggregate produces exactly the same stress-strain curve.

Overall, it can be concluded that the effect of texture deviation from texture refinement technique brings about subtle mismatch in the behaviour of grain groups in Radial Direction, whilst negligible in Axial Direction.

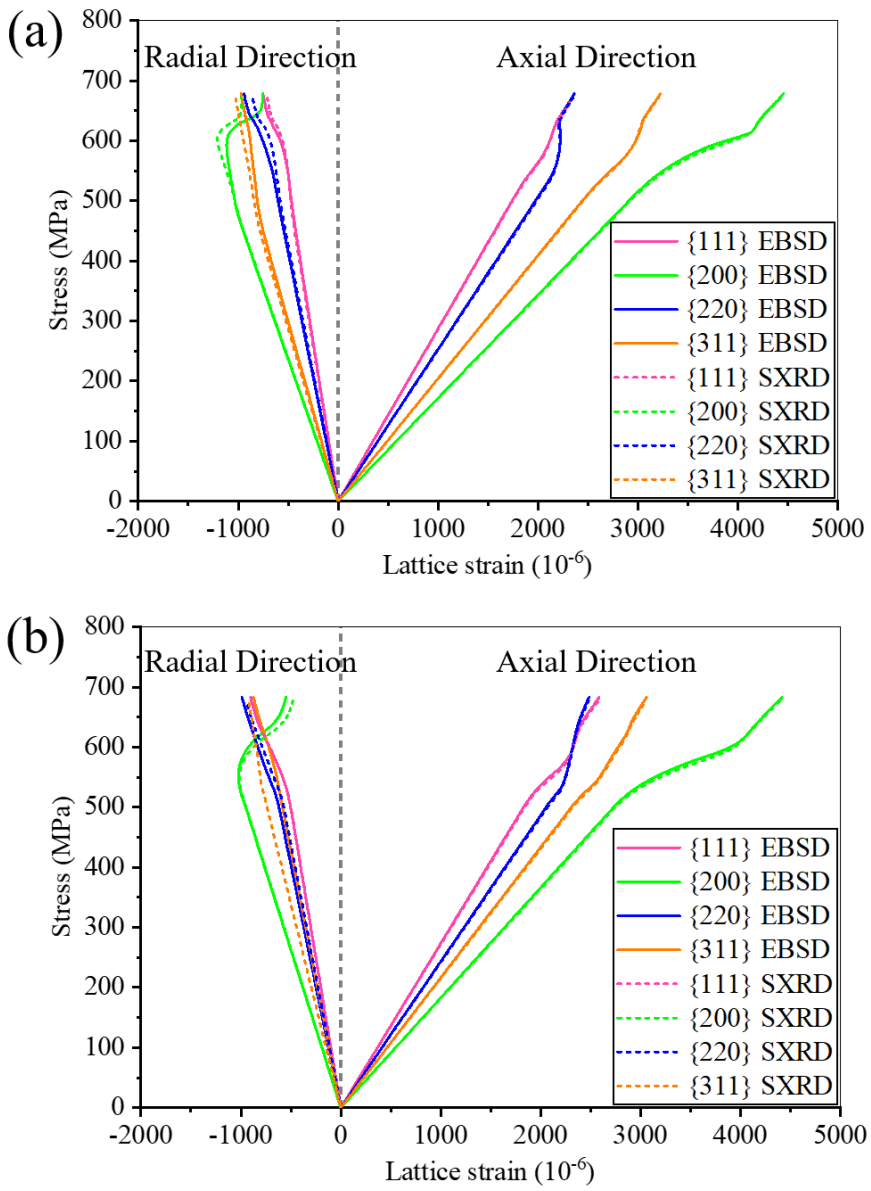


Figure 12. Lattice strain of {*hkl*} grain groups in loading direction (Axial Direction) and its vertical (Radial Direction). Results of EBSD texture are presented in solid lines whilst those of SXRD texture are in dashed lines (a) Sample 1. (b) Sample 2.

5. Summary and conclusions

In the present work, two ultra-fast texture refinement techniques have been developed and demonstrated. Firstly, a novel texture refinement method based on single shot Time-Of-Flight neutron diffraction (ND) pattern is elucidated. Secondly, texture refinement from single shot synchrotron X-ray diffraction (SXRD) pattern is conducted.

Both techniques are based on experimental setups that are simple to establish. Pole figures and inverse pole figures constructed from both texture refinement methods are assessed through comparison with the referential texture quantified by large-area EBSD. A novel metric E_p has been set up for a quantitative evaluation of the difference in pole figures. Visual assessment has also been made by plotting the ODF difference in full Euler space. Finally, the influence of texture deviation between SXRD and EBSD on macro- and mesoscale simulation results is examined by the EPSC modelling approach. Thus providing insight into the reliability of two texture refinement methods from a visual and computational point of view.

Conclusions are summarised as below:

Texture refined from single shot Time-Of-Flight neutron diffraction pattern is based on cylindrical symmetry assumption and is presented in the form of inverse pole figure, which contains texture information in the direction of diffraction scattering vector of that pattern. No sample symmetry assumption is needed for single shot synchrotron X-ray diffraction pattern, and the result can be presented in the form of pole figures in complete projection space.

Inverse pole figures obtained from single shot Time-Of-Flight neutron diffraction reflect orientation distribution in an approximate manner, whilst detailed contour profile may be missing.

Pole figures constructed from single shot synchrotron X-ray diffraction pattern show decent match with those from EBSD in terms of max/min intensity and intensity distribution, with errors generally below 10%. The ODF difference is around ~0.1MRD for majority of full Euler space. Meanwhile, the inverse pole figures display more details than those from neutron diffraction. Inverse pole figures in Z direction are less accurate due to the lack of diffraction information.

On macroscale simulation result, the effect of texture deviation brought by the texture refinement technique is much less than that caused by the diversity of texture in different samples. On mesoscale, the texture deviation brings about no influence on the behaviour of grain groups in loading direction, whilst vertically, the lattice strain evolution paths show divergence in plastic regime but general tendencies remain consistent between EBSD and SXRD texture.

Acknowledgements

We are very grateful to Dr. Carlos N. Tomé from Los Alamos National Laboratory for authorising the access to EPSC simulation code (Version 4). AMK and ZW wish to acknowledge the support from EPSRC IAA Doctoral Impact Scheme grant. ZW is grateful for the support from Mr. Weizhong Wang and Mrs. Yong Qian. The authors would like to thank Diamond Light Source for allocation of beamtime MG25467 at I12 JEEP beamline.

Data Availability

The raw/processed data required to reproduce these findings cannot be shared at this time as the data also forms part of an ongoing study.

References

[1] Z. Wang, J. Chen, C. Besnard, A.M. Korsunsky, Microstructure evolution in a severely cold-worked NiTi wire during ageing treatment: An in situ neutron diffraction study, Materials Letters 281 (2020) 128676. https://doi.org/10.1016/j.matlet.2020.128676.

[2] U.F. Kocks, C.N. Tome, H.-R.Wenk, Texture and Anisotropy, Cambridge University Press 1998, United Kingdom.

[3] Z. Wang, A.M. Korsunsky, Effect of Temperature on Shape Memory Materials, Reference Module in Materials Science and Materials Engineering, Elsevier Inc. https://doi.org/10.1016/B978-0-12-803581-8.11793-X.

[4] Z. Wang, J. Chen, C. Besnard, L. Kuncicka, R. Kocich, A.M. Korsunsky, In-situ neutron diffraction investigation of texture-dependent Shape Memory Effect in a near equiatomic NiTi alloy, Acta Materialia 202 (2021) 135-148. https://doi.org/10.1016/j.actamat.2020.10.049.

[5] J. Chen, Z. Wang, A.M. Korsunsky, Multiscale stress and strain statistics in the deformation of polycrystalline alloys, International Journal of Plasticity (2022).

[6] M. Knezevic, L. Capolungo, C.N. Tome, R.A. Lebensohn, D.J. Alexander, B. Mihaila, R.J. McCabe, Anisotropic stress-strain response and microstructure evolution of textured α-uranium, Acta Materialia 60 (2012) 702-715. https://doi.org/10.1016/j.actamat.2011.10.041.

[7] B. Clausen, C.N. Tome, D.W. Brown, S.R. Agnew, Reorientation and stress relaxation due to twinning: Modeling and experimental characterization for Mg, Acta Materialia 56 (2008) 2456-2468. https://doi.org/10.1016/j.actamat.2008.01.057.

[8] Z. Wang, J. Everaerts, E. Salvati, A.M. Korsunsky, Evolution of thermal and mechanical properties of Nitinol wire as a function of ageing treatment conditions, Journal of Alloys and Compounds 819 (2020) 153024. https://doi.org/10.1016/j.jallcom.2019.153024.

[9] E. Jimenez-Melero, N.H. van Dijk, L. Zhao, J. Sietsma, J.P. Wright, S. van der Zwaag, In situ synchrotron study on the interplay between martensite formation texture evolution and load partitioning in low-alloyed TRIP steels, Mater. Sci. Eng. A 528 (2011) 6407-6416. https://doi.org/10.1016/j.msea.2011.04.087.

[10] A. Pesach, E. Tiferet, S.C. Vogel, M. Chonin, A. Diskin, L. Zilberman, O. Rivin, O. Yeheskel, E.N. Caspi, Texture analysis of additively manufactured Ti-6Al-4V using neutron diffraction, Additive Manufacturing 23 (2018) 394-401. https://doi.org/10.1016/j.addma.2018.08.010.

[11] S. Kabra, S. Danion, W. Kockelmann, S.Y. Zhang, An neutron diffraction study of texture evolution under deformation in a hot rolled TWIP steel, Materials Today: Proceedings 2S (2015) S261-S266. https://doi.org/10.1016/j.matpr.2015.05.036.

[12] M.Y. Xie, N. Baimpas, C. Reinhard, A.M. Korsunsky, Texture analysis in cubic phase polycrystals by single exposure synchrotron X-ray diffraction, Journal of Applied Physics 114 (2013) 163502. https://doi.org/10.1063/1.4825120.

[13] L. Lutterotti, M. Voltolini, H.-R. Wenk, K. Bandyopadhyay, T. Vanorio, Texture analysis of a turbostratically disordered Ca-montmorillonite, American Mineralogist 95 (2010) 98-103. https://doi.org/10.2138/am.2010.3238.

[14] L. Lutterotti, R. Vasin, H.-R. Wenk, Rietveld texture analysis from synchrotron diffraction images. I. Calibration and basic analysis, Powder Diffraction 29 (2014) 76-84. https://doi.org/10.1017/S0885715613001346.

[15] B.H. Toby, R.B. Von Dreele, GSAS-II: the genesis of a modern open-source all purpose crystallography software package, Journal of Applied Crystallography 46 (2013) 544-549. https://doi.org/10.1107/S0021889813003531.

[16] L. Lutterotti, M. Bortolotti, G. Ischia, I. Lonardelli, H.-R. Wenk, Rietveld texture analysis from diffraction images, Z. Kristallogr. Suppl. 26 (2007) 125-130.

[17] C. Papadaki, W. Li, A.M. Korsunsky, On the Dependence of γ' Precipitate Size in a Nickel-Based Superalloy on the cooling Rate from Super-Solvus Temperature Heat Treatment, Materials 11 (2018) 11 1528. https://doi.org/10.3390/ma11091528.

[18] F. Bachmann, R. Hielscher, H. Schaeben, Texture analysis with MTEX-Free and open source software toolbox, Solid State Phenom. 160 (2010) 63-68. https://doi.org/10.4028/www.scientific.net/SSP.160.63.

[19] P. Staron, A. Schreyer, H. Clemens, S. Mayer, Neutrons and Synchrotron Radiation in Engineering Materials Science, Wiley-VCH (2017) 73-123.

[20] R.B. Von Dreele, Quantitative texture analysis by Rietveld refinement, Journal of Applied Crystallography, 30 (1997) 517-525. https://doi.org/10.1107/S0021889897005918.

[21] H.J. Bunge, Texture analysis in Materials Science: Mathematical Methods, London: Butterworth-Heinemann (1982) 49-57.

[22] R. Hielscher, H. Schaeben, A novel pole figure inversion method: specification of the MTEX algorithm, Journal of Applied Crystallography 41 (2008) 1024-1037. https://doi.org/10.1107/S0021889808030112.

[23] H. Wang, B. Clausen, C.N. Tome, P.D. Wu, Studying the effect of stress relaxation and creep on lattice strain evolution of stainless steel under tension, Acta Materialia 61 (2013) 1179-1188. https://doi.org/10.1016/j.actamat.2012.10.027.

[24] F. Hofmann, B. Abbey, L. Connor, N. Baimpas, X. Song, S. Keegan, A.M. Korsunsky, Imaging of grain-level orientation and strain in thicker metallic polycrystals by high energy transmission micro-beam Laue (HETL) diffraction techniques, International Journal of Materials Research 103 (2012) 192-199. https://doi.org/10.3139/146.110660.

[25] S. Takajo, S.C. Vogel, Determination of pole figure coverage for texture measurements with neutron time-of-flight diffractometers, Journal of Applied Crystallography 51 (2018) 895-900. https://doi.org/10.1107/S1600576718007732.

[26] H.J. Bunge, Texture Analysis in Materials Science, Mathematical Methods. London: Butterworths (1982).

[27] L.R. Brandt, J.J. Marie, T. Moxham, D.P. Forstermann, E. Salvati, C. Besnard, C. Papadaki, Z. Wang, P.G. Bruce, A.M. Korsunsky, Synchrotron X-ray quantitative evaluation of transient deformation and damage phenomena in a single nickel-rich cathode particle, Energy Environmental Science 13 (2020) 3556-3566. https://doi.org/10.1039/D0EE02290J.

[28] J. Chen, E. Salvati, F. Uzun, C. Papadaki, Z. Wang, J. Everaerts, A.M. Korsunsky, An experimental and numerical analysis of residual stresses in a TIG weldment of a single crystal nickel-base superalloy, Journal of Manufacturing Processes 53 (2020) 190-200. https://doi.org/10.1016/j.jmapro.2020.02.007.

[29] F. Uzun, C. Papadaki, Z. Wang, A.M. Korsunsky, Neutron strain scanning for experimental validation of the artificial intelligence based eigenstrain contour method, Mechanics of Materials 143 (2020) 103316. https://doi.org/10.1016/j.mechmat.2020.103316.

[30] F. Uzun, A.I. Salimon, E.S. Statnik, C. Besnard, J. Chen, T. Moxham, E. Salvati, Z. Wang, A.M. Korsunsky, Polar transformation of 2D X-ray diffraction patterns and the experimental validation fo the hDIC technique, Measurement 151 (2020) 107193. https://doi.org/10.1016/j.measurement.2019.107193.

[31] E.S. Statnik, A.I. Salimon, C. Besnard, J. Chen, Z. Wang, T. Moxham, I.P. Dolbnya, A.M. Korsunsky, Ovine Bone Morphology and Deformation Analysis Using Synchrotron X-ray Imaging and Scattering, Quantum Beam Science 4(3) (2020) 29. https://doi.org/10.3390/qubs4030029.

Chapter 5

Materials Letters
Volume 281, 15 December 2020, 128676



Microstructure evolution in a severely cold-worked NiTi wire during ageing treatment: An *in situ* Neutron Diffraction study

Zifan Wang, Jingwei Chen, Cyril Besnard, Alexander M. Korsunsky*

MBLEM, Department of Engineering Science, University of Oxford, Oxford OX1 3PJ, U.K.

*Corresponding author. E-mail address: alexander.korsunsky@eng.ox.ac.uk

Abstract

Cold-worked NiTi wire was subjected to ageing treatment, during which *in situ* neutron diffraction technique was employed to investigate the microstructure evolution in terms of crystallinity, precipitation, texture, grain size and microstrain. It was found that both heating and rapid cooling brings about significant change in microstructure, whilst precipitation process is dominant at high temperature. Besides, the approaches to extracting microstructural information, including texture, grain size and microstrain, from individual neutron diffraction pattern are proposed and verified.

Keywords:

NiTi shape memory alloys, *In situ* neutron diffraction, Heat treatment, Microstructure

1. Introduction

Among the category of shape memory alloys, near-equiatomic NiTi always remains the first choice in engineering application due to its excellent thermomechanical performance [1]. Our recent study demonstrated that ageing treatment exerts huge impact on the microstructure, thereby leading to the variation of functional properties [2]. Nevertheless, the details of microstructural evolution are not well understood, since up-to-date studies only focused on the heating process of heat treatment while cooling is neglected [3,4].

In situ neutron diffraction technique provides highly reliable statistical data from enormous gauge volume instead of local regions, thus enabling probing the microstructure at its most representative form. In the present study, probably the first attempt so far, we completely tracked the microstructure before, during and after ageing treatment, thus giving insight into the optimization of ageing treatment conditions.

2. Experimental and analytical methods

A commercially available cold drawn binary NiTi wire (Goodfellow, Ni55/Ti45 wt%) of 0.8mm diameter was used. The as-received wire was segmented and mounted on the radiant air furnace at ENGIN-X beamline, ISIS RAL, UK. Illustrated in Fig. 1, the wire was horizontally arranged in such a way that the cylindrical axis was 45° relative to the incident beam. Two detector banks were opposed in a line perpendicular to the beam direction [5]. This setup enables probing the microstructure of grains whose *hkl* lattice planes are either parallel (Bank 2) or perpendicular (Bank 1) to the wire axial direction. Note that the word "(*hkl*) variant" has been adopted in the present study, and many others, to represent the grain family that contributes to a single *hkl* peak in the diffraction spectra.

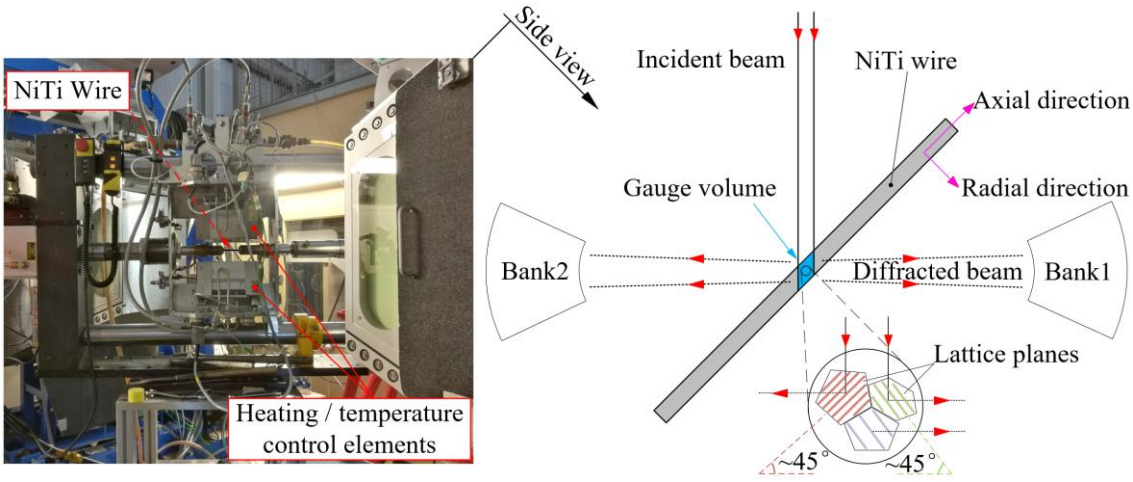


Fig. 1. Side view photo (left) and top view sketch (right) of setup.

The ageing treatment scheme is described in Fig. 2(a). The temperature quickly elevated and stabilized at 500 °C. One sample was water quenched after ~1 hour and the other after ~5 hours. The time and temperature at which the diffraction spectra were collected were identified by numbers in yellow-coloured marks.

Data were analysed using Rietveld refinement technique implemented in the GSAS [6]. Raw pole figures were constructed from the refined spherical harmonics, after which the orientation distribution functions (ODFs) were reconstructed using MTEX code [7]. Hence the plotted inverse pole figures present texture information in the axial and radial direction of the wire. Pseudo-voigt function was utilized in the single peak fitting, extracting full width half maximum (FWHM) from individual peak profile.

3. Results and discussion

3.1 Recrystallization and precipitation

Cold drawing introduces a large amount of amorphous phase with embedded nano-crystalline regions in the NiTi alloy [3]. The phenomenon is reflected in Fig. 2(b1), as both spectra show profile containing much noise caused by diffuse scattering

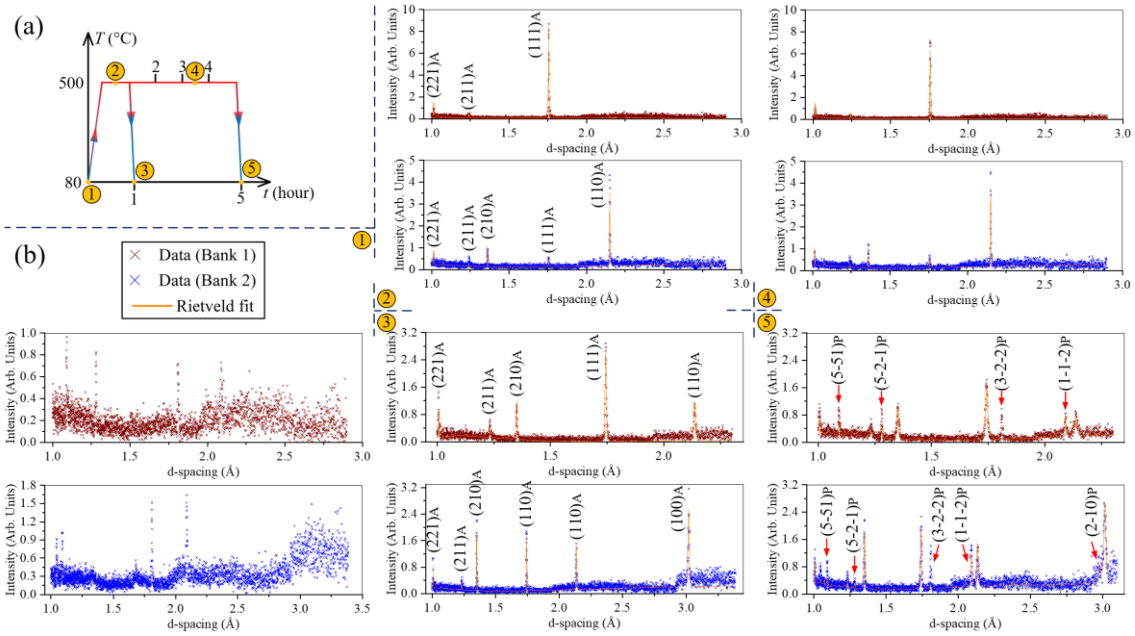


Fig. 2. Ageing treatment scheme (a) and sets of diffraction spectra of corresponding data acquisition points(b). Peaks of *hkl* variants are indexed for both parent austenite phase ("A") and Ni_4Ti_3 precipitate ("P").

corresponding to the amorphous phase. Only a few low-intensity peaks can be observed, implying a low degree of crystallinity. Moreover, the peaks are shifted far away from standard d-spacing positions due to the distortion of crystal structure, making it impossible to analyse via Rietveld method.

Upon heating up to 500 °C, the emergence of diffraction peaks reveals the recrystallization of amorphous phase. The peak of (111) variant is particularly intense in the wire axial direction (bank 1) whilst it is the (110) variant in the radial direction, which suggests strong texture at high temperature. There is no significant change in the microstructure during ageing treatment, judging from the comparison between Fig. 2(b2) and (b4).

After water quenching, the rising intensities of other peaks infers a more homogenous distribution of crystallite orientation, i.e. the comparison between Fig. 2(b2)

and (b3). In addition to the parent phase, diffraction peaks from Ni_4Ti_3 precipitate can be observed after 5 hours' ageing treatment and water quenching, shown in Fig. 2(b5).

3.2 Texture variation

Texture information extracted from the spectra in Fig. 2(b2-b5) is shown as inverse pole figures in Fig. 3. Units of m.r.d. is adopted, e.g. 1 m.r.d. represents random distribution and 3 m.r.d. means the quantity of a *hkl* variant is 3 times that of its randomly distributed state.

During the ageing treatment, the cold drawn NiTi wire exhibited strong fibre texture near <111> in axial direction, which is commonly reported in other studies, e.g. [8]. This agrees well with the intense (111) peak in Fig. 2(b2). In radial direction, orientation of crystallite was distributed along the direction path from <112> to <101>, as indicated by the purple dash line. This implies that the crystallites were oriented in such a way homogenously rotating around the <111> axial texture. There is no significant variation in texture during the 5-hour period at high temperature (Fig. 3(2 and 4)).

Nevertheless, water quenching brings about huge changes in texture (Fig. 3(3 and 5)). The original texture orientation, namely <111> in axial direction and <101> in radial direction, was broadened, forming a new emphasis within the <111> ~ <101> domain. Similarly, there is no significant variation in texture after water quenching as the ageing time increases.

Moreover, the texture of Ni_4Ti_3 precipitate is refined, shown in the 120° circular arc area according to the hexagonal symmetry of the rhombohedral structure of Ni_4Ti_3 precipitate. There is a high concentration of <0001> in axial direction, around which crystallite rotates homogenously so that there is an intense edge in the plot of radial

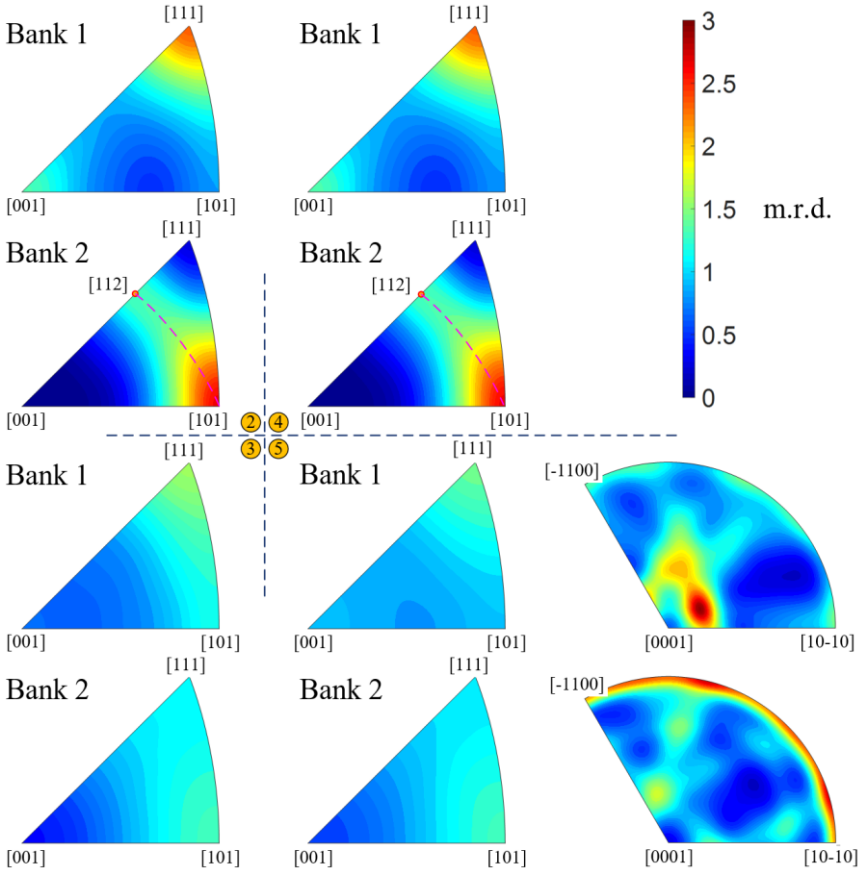


Fig. 3. Texture evolution of NiTi wire in axial (bank 1) and radial direction (bank 2). The scale of plots is normalized, ranging from 0 to 3 m.r.d.

direction. It can be inferred that the orientation relationship between the parent phase and precipitate is $(0001)_P \| (111)_A$, consistent with [9].

3.3 Microstrain and grain size

To evaluate the change in microstrain, the full width at half maximum (FWHM) can be deconvoluted into multiple contributions from instrumental broadening (Δd_{ins}), grain size (Δd_{size}) and microstrain (Δd_{ε}) [10]. By considering the strain expression as $\varepsilon = \Delta d/d$ that directly reveals the non-uniform lattice deformation from $d+\delta d$ to $d-\delta d$ for a specific *hkl* variant, we obtain:

$$FWHM^2 = \Delta d^2 = \Delta d_{ins}^2 + \Delta d_{size}^2 + \Delta d_{\varepsilon}^2 = \Delta d_{ins}^2 + \Delta d_{size}^2 + \varepsilon^2 d^2, \quad (1)$$

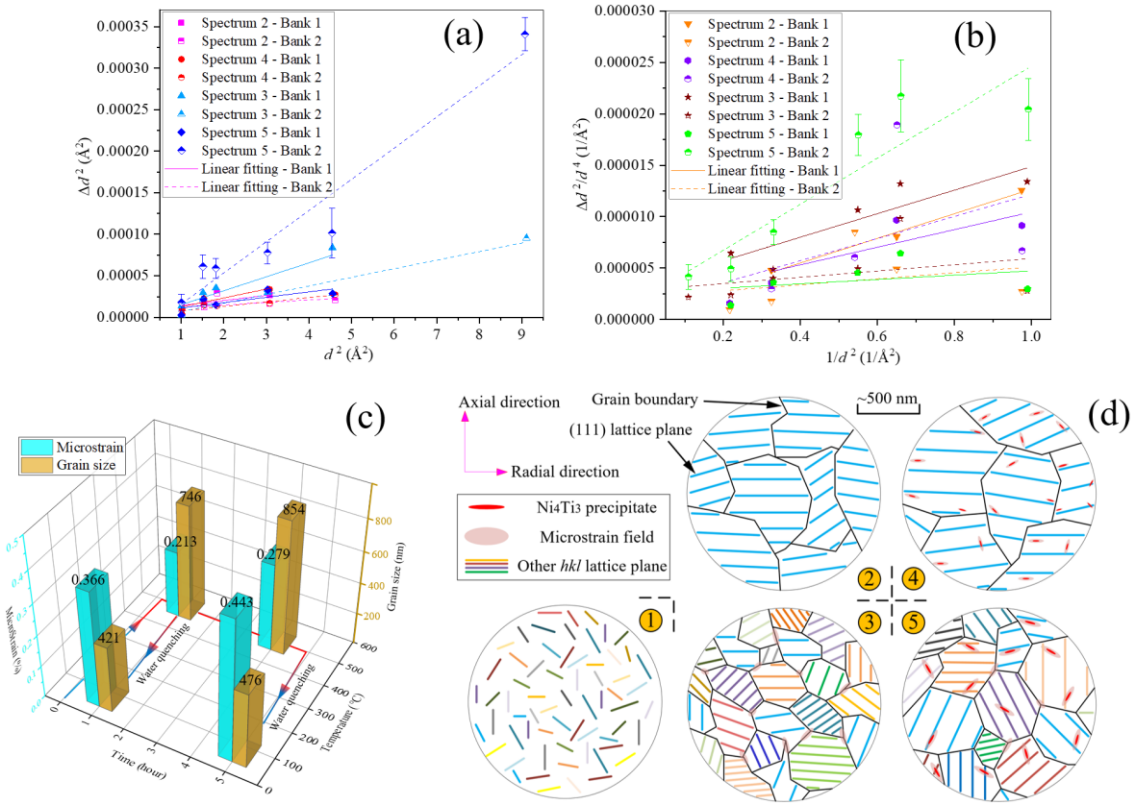


Fig. 4. Evaluation of microstrain (a) and grain size (b), results summarized in (c). Schematic illustration of microstructure evolution (d).

where d is the d-spacing of peak centre of a hkl variant. Eq. (1) is a typical $y=a+bx$ equation from which slope (ε^2) the value of microstrain can be determined by plotting Δd^2 versus d^2, as shown in Fig. 4(a).

To evaluate the grain size, a modified Williamson-Hall approach can be used [11], written as:

$$\frac{\Delta d^2}{d^4} = \left(\frac{C}{D}\right)^2 + \frac{A}{d^2}, \qquad (2)$$

where A is a constant depending on the physical properties of lattice defects that dominate the microstrain, C is the Scherrer constant which is calibrated by our EBSD study [2] and taken as 0.75, and D is the average grain (crystallite) size in unit of nm. Similarly, the ordinate intercept of a linear fitting of Eq. (2) provides the value of $(0.75/D)^2$, from which the grain size D can be calculated, as shown in Fig. 4(b).

Calculated values of microstrain and grain size are averaged between bank 1 & 2, as summarized in Fig. 4(c). The increase of grain size during ageing treatment at 500 °C is negligible, whilst the microstrain increment is attributed to the strain field arising with the nucleation and growth of precipitate [9]. The significant elevation of microstrain after water quenching results from the fragmentation of the large grains that causes intergranular constraint among smaller grains.

4. Conclusions

The volume averaged microstructure evolution of NiTi during the entire ageing treatment process was investigated. Conclusions are sketched in Fig. 4(d) and outlined as below:

(1) The initial microstructure of as-drawn wire contains a large amount of amorphous phase. Recrystallization takes place upon heating, leading to the strong <111> texture in axial direction.

(2) Precipitation is the dominant microstructural change during ageing treatment, while the change in texture and grain size is negligible.

(3) Water quenching results in the fragmentation of large grains, hence the increase of microstrain and variation of texture.

Acknowledgements

We gratefully acknowledge the STFC for access to neutron beamtime RB1920246 at the ISIS Pulsed Neutron and Muon Source.

References

[1] Z. Wang, A.M. Korsunsky, Effect of Temperature on Shape Memory Materials, in: Reference Module in Materials Science and Materials Engineering, Elsevier Inc., 2020.

[2] Z. Wang, J. Everaerts, E. Salvati, A.M. Korsusnky, Evolution of thermal and mechanical properties of Nitinol wire as a function of ageing treatment conditions, J. Alloys Compd. 819 (2020) 153024.

[3] C. Yu, B. Aoun, L. Cui, Y. Liu, H. Yang, X. Jiang, S. Cai, D. Jiang, Z. Liu, D.E. Brown, Y. Ren, Synchrotron high energy X-ray diffraction study of microstructure evolution of severely cold drawn NiTi wire during annealing, Acta Mater. 115 (2016) 35-44.

[4] M. Carl, J. Smith, R.W. Wheeler, Y. Ren, B.V. Doren, M.L. Young, High-energy synchrotron radiation X-ray diffraction measurements during in situ aging of a NiTi-15 at. % Hf high temperature shape memory alloy, Materialia 5 (2019) 100220.

[5] J.R. Santisteban, M.R. Daymond, J.A. James, L. Edwards, ENGIN-X: a third-generation neutron strain scanner, J. Appl. Cryst. 39 (2006) 812-825.

[6] A.C. Larson, R.B. Von Dreele, General structure analysis system, Los Alamos National Laboratory Report LAUR (1994) 86-748.

[7] F. Bachmann, R. Hielscher, H. Schaeben, Texture analysis with MTEX-Free and open source software toolbox, Solid State Phenom. 160 (2010) 63-68.

[8] K. Gall, J. Tyber, V. Brice, C.P. Frick, H.J. Maier, N. Morgan, Tensile deformation of NiTi wires, Mater. Res. Part A 75 (2005) 810-823.

[9] N. Zhou, C. Shen, M.F.-X. Wagner, G. Eggeler, M.J. Mills, Y. Wang, Effect of Ni_4Ti_3 precipitation on martensitic transformation in Ti-Ni, Acta Materialia 58 (2010) 6685-6694.

[10] Y. Zhao, J. Zhang, Microstrain and grain-size analysis from diffraction peak width and graphical derivation of high-pressure thermomechanics, J. Appl. Crystallogr. 41 (2008) 1095-1108.

[11] W. Woo, T. Ungar, Z. Feng, E. Kenik, B. Clausen, X-ray and neutron diffraction measurements of dislocation density and subgrain size in a friction-stir-welded aluminum alloy, Metall. Mater. Trans. A 41A (2010) 1210-1216.

Chapter 6

Acta Materialia
Volume 202, 1 January 2021, Pages 135-148



In situ neutron diffraction investigation of texture-dependent Shape Memory Effect in a near equiatomic NiTi alloy

Zifan Wang[a], Jingwei Chen[a], Cyril Besnard[a], Lenka Kuncicka[b], Radim Kocich[b], Alexander M. Korsunsky[a,*]

[a] *MBLEM, Department of Engineering Science, University of Oxford, Oxford OX1 3PJ, U.K.*

[b] *Faculty of Materials Science and Technology, VŠB-Technical University of Ostrava, Ostrava 8, Czech Republic*

*Corresponding author. E-mail address: alexander.korsunsky@eng.ox.ac.uk

Abstract

To explore the possibility of customising the functional behaviour of NiTi shape memory alloy via controlling texture, binary $Ni_{55}Ti_{45}$ (wt.%) alloys were manufactured in *as cast* and *hot swaged* conditions, presenting contrasting initial texture and macroscopic performance. *In situ* time-of-flight neutron diffraction technique was employed to study the texture effect on the microstructural evolution during Shape Memory Effect (SME), and a range of properties were evaluated. It was found that (i) hot swaging process leads to change in grain morphology and increase in microstrain; (ii) thermal expansion coefficients of martensite and austenite variants were weakly affected

by the texture and phase transformation constraint; (iii) significant texture effect on the elastic properties at both macro- and micro-scale was quantified by Elasto-Plastic Self-Consistent (EPSC) modelling approach, while the anisotropic elastic moduli lie within the range for single crystal state and twinned structure; (iv) texture evolution during SME is weakly related to the initial microstructure; (v) grains reoriented so that the <010> axis became aligned parallel to the loading direction, and retained this orientation upon unloading, revealing the underlying correlation between texture evolution and detwinning. Based on the experimental results, a multi-variant model was proposed to quantify the lattice strain evolution during SME. Validity of the conceptually simple and parametrically parsimonious model was confirmed by validation against experimental data.

Keywords:

Bespoke NiTi Shape Memory Alloys, Texture, Shape memory effect, EPSC, *In situ* neutron diffraction

1.Introduction and objectives

Probably the most important category of shape memory materials that exhibit useful functional behaviour under specific stimuli, Shape Memory Alloys (SMAs) have been widely utilized in applications of medical actuators, aerospace, micromechanical systems, and the elastocaloric cooling devices that recently come into fashion [1]. Among the three extensively developed and used alloy systems, namely NiTi-based, Cu-based and Fe-based, the binary NiTi always remain the first choice in engineering applications due to its excellent thermomechanical performance and biocompatibility.

Two widely utilised functional types of behaviour of NiTi are Superelasticity (SE) and Shape Memory Effect (SME). The latter lies in the focus of interest for the present study. To induce SME, deformation begins at a critical temperature below M_f. When stress is applied, the martensite (M) phase deforms pseudo-plastically through self-accommodated twinning to detwinning process, showing pronounced macroscopic strain up to ~8%. After stress is withdrawn, detwinned martensite retains its shape until being heated above critical temperature A_s, at which the reverse phase transformation to austenite (A) initiates. The full strain recovery is reached above A_f temperature.

Over the years, numerous investigations attempted to identify and clarify the underlying crystallographic mechanisms that affect SME in NiTi alloys. The contribution of elastic strain was studied for different forms of NiTi, including single crystal and twinned structure, through ultrasonic measurements [2], first-principles calculations [3], and other computational modelling approaches [4,5]. The investigation of pseudo-plastic strain, namely the stress-induced detwinning, elucidated the mechanism from various aspects of energetics [6,7], microstructural characterisation [8,9,10,11], thermodynamics [12,13] and texture evolution [4,14].

These studies lay a solid foundation to the understanding of mechanisms of SME. However, recent research demonstrated that the actual SME performance of NiTi alloy is greatly influenced by thermomechanical processing methods that produce NiTi products of different shapes, dimensions and microstructure in terms of phase composition [12], internal strain field [15], crystallite morphology [16] and texture [17,18].

The aforementioned studies and others not reported here appear to have failed to address systematically the texture effect on SME from the microscopic point of view. The subject was somewhat superficially investigated in a limited number of studies, most of

which were based on *ex situ* rather than *in situ* analyses, so that the details of the microstructural evolution during SME remain to be explored.

In situ time-of-flight (TOF) neutron diffraction (ND) may be the most advantageous technique in probing the mesoscale volume-averaged deformation response of microstructure, since neutron beams penetrate several millimetres deep into the material, thus providing highly reliable statistical data from bulk polycrystalline samples [11,14,19]. Most importantly, the technique allows the extraction of refined crystallographic information from diffraction spectra, including reflection-dependent lattice *d*-spacings, grain orientation, and phase volume fraction evolution that is essential to evaluate the morphological and mechanical texture effect on the microstructural evolution during SME [20,21]. Furthermore, accurate quantification of macroscopic deformation response of NiTi alloy requires attendant and supportive models that consider various properties such as microstrain, orientation- and phase-dependent thermal expansion coefficients, elastic moduli, texture, and so on. However, the experimental data related to these factors is scarce.

Having identified the significance of this topic and the boundary of existing knowledge, the objective of this work is to study the texture-dependent SME in NiTi alloy using *in situ* TOF neutron diffraction analysis. NiTi samples of contrasting initial texture were manufactured via two conditions, namely as cast (AC) and hot swaging (HS). Experimental efforts were aimed at evaluating grain morphology, microstrain, thermal expansion coefficients, lattice strain evolution, elastic properties, and texture evolution. Based on the experimental observations, the texture effect on lattice strain evolution was quantified via EPSC and a novel multi-variant model. Being the likely first attempt of this kind so far, the potential outcome of the present study aims to give guidance in

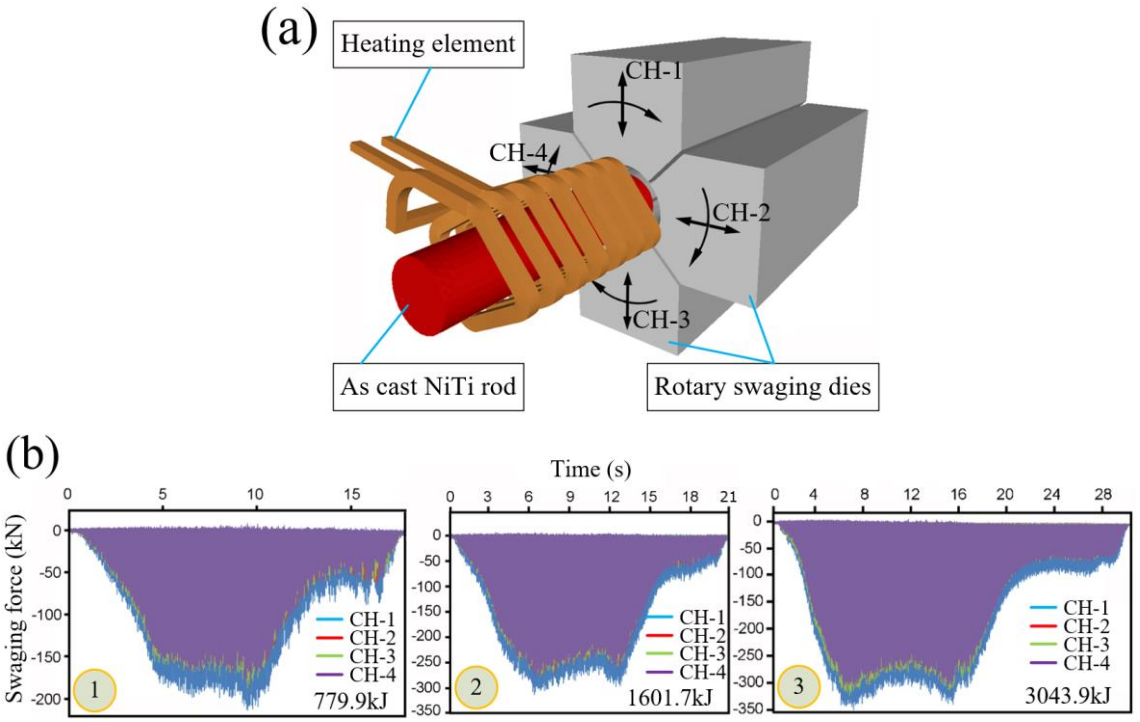


Fig. 1. Three-step hot rotary swaging using four pressing dies (a). The corresponding deformation work of each step was recorded in unit of kJ (b).

customising the functional behaviour in NiTi alloy by means of controlling different textures.

Note that in this study, the term "variant" is equivalent to *hkl* grain groups or *hkl* reflections, which correspond to the diffraction peaks in the ND spectrum [4,11,15,16,19].

2.Experimental and analytical procedures

2.1 Material processing methodology

For raw material, nickel cubes of 4N purity and commercially pure (>99.3%) Grade 2 titanium were used. A polycrystalline $Ni_{55}Ti_{45}$ wt.% ϕ 20mm rod was cast into an iso-statically pressed graphite crucible via vacuum induction melting (VIM) at 150 Mbar under Argon atmosphere of 6N purity.

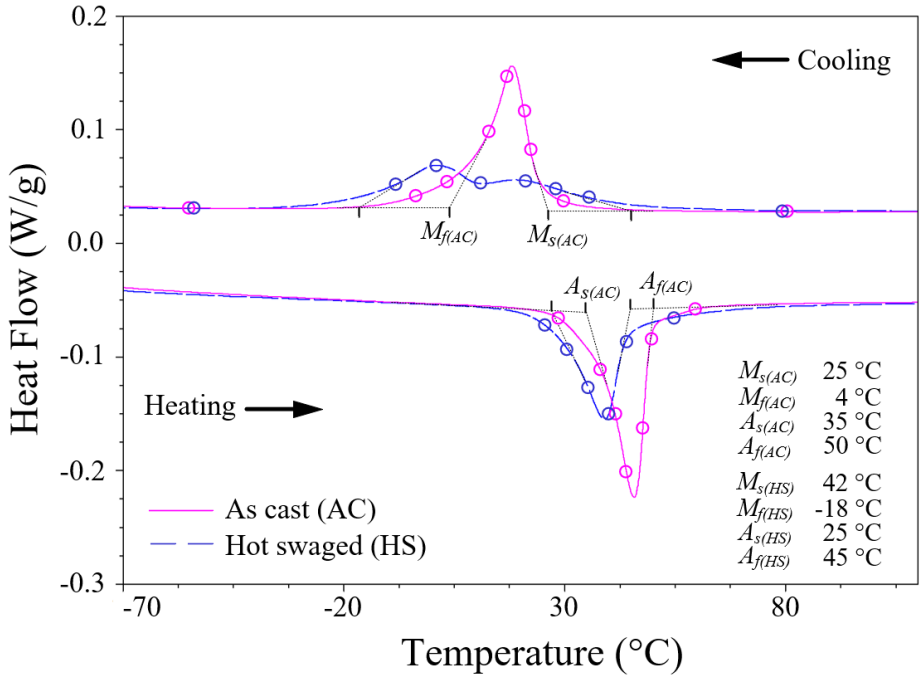


Fig. 2. The measured values of critical phase transformation temperatures, definitions refer to the introduction [12]. Circles denote the temperatures at which stress-free ND measurements were performed.

The as cast rod was split into two pieces, one of which was subjected to hot rotary swaging at 950°C (see Ref. [22,23] for details on manufacturing). Rotary swaging is a versatile industrially applicable technology that reduces diameter of the processed axisymmetric workpiece by incrementally imposing intensive shear strain via a set of four rotating dies, as shown in Fig. 1. The three swaging passes were performed and monitored by the KOMAFU S600 system developed by us [24,25]. With the diameter reduced to ϕ12mm, the as cast (AC) and hot swaged (HS) rods present contrasting texture (Fig. 12 & 13).

2.2 DSC analysis

To determine the deformation and recovery temperature of SME, stress-free transformation temperatures were measured by a TA DSC Q2000 differential scanning

calorimetry (DSC) instrument in the wide temperature range between -90°C and 200°C to cover the complete transformation process. During the test, the samples were first cooled down to -90°C and stabilized for 2 min, then cycled two loops to ensure consistent experimental result. The ramp rates for heating / cooling were both 5°C/min. Result is shown in Fig. 2.

2.3 EBSD Characterization

To assess the change in grain morphology after thermomechanical processing, electron backscatter diffraction (EBSD) observations were carried out in a Tescan LYRA3 system integrated with a SYMMETRY EBSD detector from Oxford Instruments. Samples were polished down to a final step of 0.25μm colloidal silica and heated to induce the cubic austenite phase. Kikuchi pattern indexing was performed at an accelerating voltage of 20kV, a working distance of 9mm, a step size of 0.12μm, and an acquisition speed of 7Hz.

2.4 Neutron diffraction experiments

In situ time-of-flight (TOF) neutron diffraction experiments were conducted using the pulsed spallation source at ISIS, Rutherford Appleton Laboratory managed by Science & Technology Facilities Council (STFC) in the UK. ENGIN-X beamline is a 50m flight path instrument equipped with a 50kN hydraulic loading rig custom-built by Instron. The cryobox, capable of cooling and heating in a range of -200 to 100°C, was attached to the rig. During operation, the box chamber was pumped vacuum ($<10^{-4}$ Pa) to ensure homogenous temperature distribution on the specimen. An extensometer was clamped in the middle for macroscopic strain measurement.

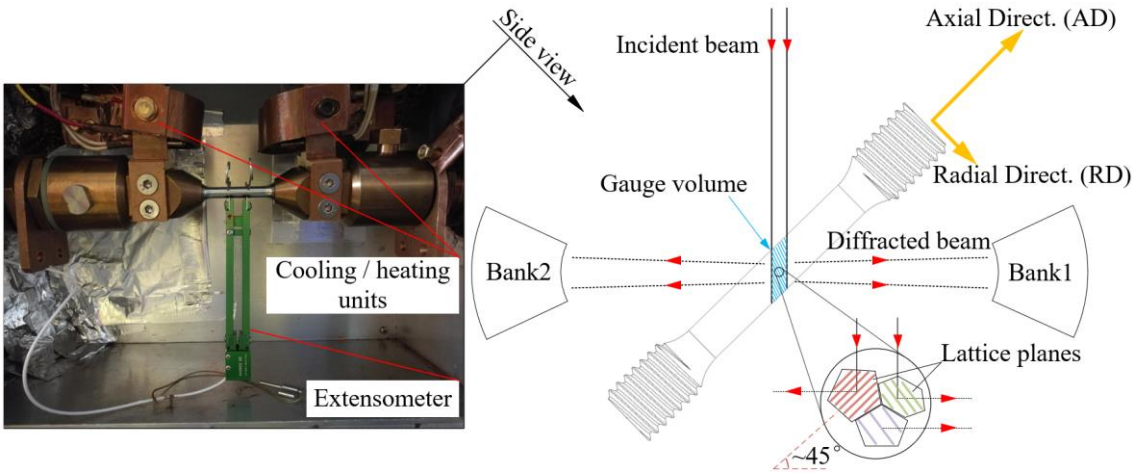


Fig. 3. Side view photograph (left). The sketch of setup from top view (right). Note that specimen coordinate is defined by the orthogonal AD and RD axes.

The loading frame was horizontally arranged in such a way that the loading direction is 45° relative to the incident beam, with two opposing ∓90°detector banks whose span angular ranges ∓7° in both horizontal and vertical directions. The beam spot size defined by radial collimators was 4×4mm throughout the experiment. Setup illustration is shown in Fig. 3. Additional details in [26,27].

Prior to the ND experiment, the rods were machined into cylindrical dog-bone specimens with a gauge diameter of 6mm. The scheme of stress-free thermal cyclic test is shown in Fig. 2. To ensure virgin state, a new sample of each type was used for SME. Samples were maintained at -35°C during the uniaxial tensile loading / unloading with a strain rate of $1\times10^{-4}s^{-1}$. Upon unloading to zero stress, the sample was gradually heated to 85°C to induce shape recovery. At each measurement point, the sample was held at a constant strain for ~43 minutes to collect spectra of adequate statistical quality. The scheme of ND during the SME process is shown in Fig. 4.

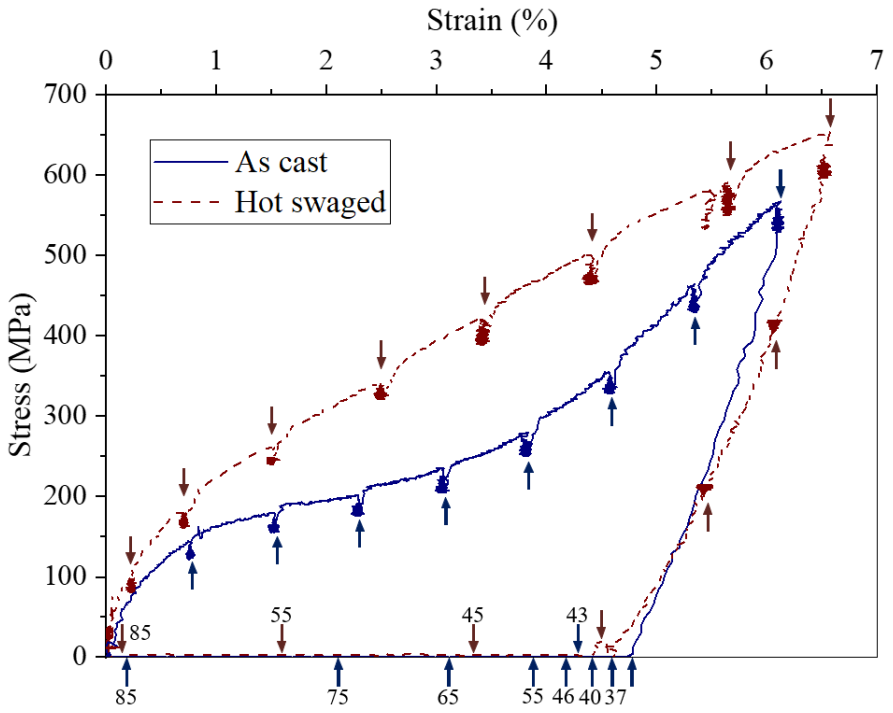


Fig. 4. Macroscopic SME response of both samples. Arrows denote the strain levels at which the samples were held for ND data acquisition. Digits in small font indicate corresponding temperatures during strain recovery upon heating, otherwise at -35°C. Stress relaxations of approximately 10MPa are considered negligible.

2.5 Neutron diffraction spectra analysis

In the first instance, data were analysed using Rietveld refinement technique [28] implemented in the General Structures and Analysis System (GSAS) code [29]. Based on a least-squares scheme that minimizes the differences between the theoretical and experimental spectra, the method allows the refinement of phase fractions, lattice parameters, lattice strains, texture, etc., that are averaged in the gauge volume. As a metric of goodness of fit, the typical χ^2 value in this study is ~0.9, which is considered decent. The initial crystal structure for calculation of theoretical spectrum is referred to [30]. As shown in Fig. 14, one of the two conventions describing NiTi monoclinic structure is adopted in the analysis of spectra data, such that c-axis as the diad axis and γ as the non-

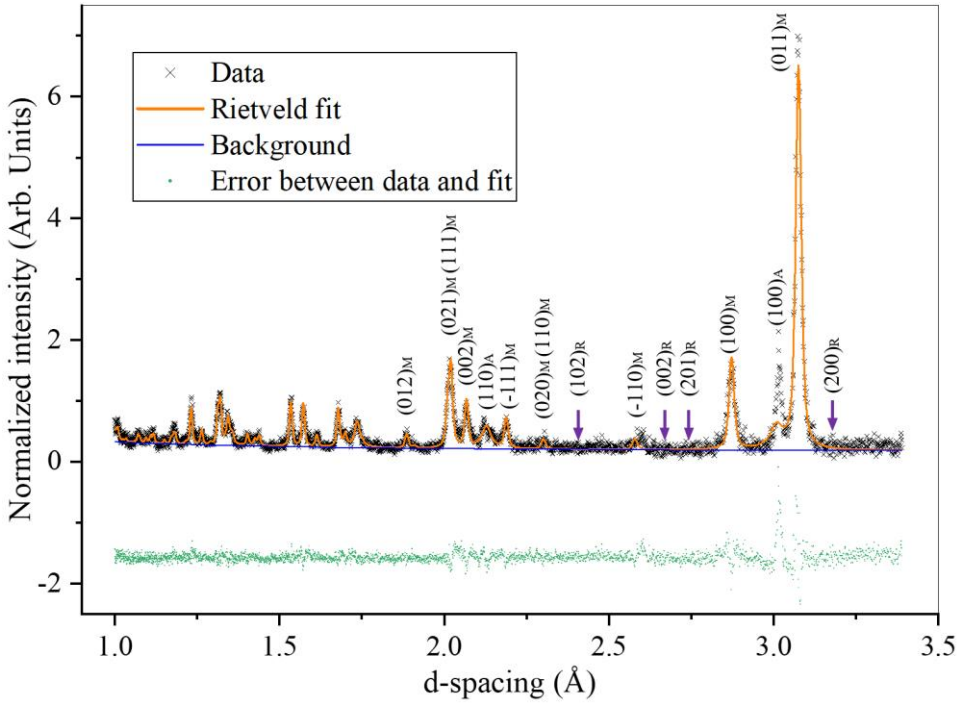


Fig. 5. Refined and indexed spectrum at 10°C during thermally induced phase transformation from austenite (A) to martensite (M) of hot swaged NiTi (AD). Peak positions for low index *hkl* variants are marked for A, M and R-phase.

orthogonal angle, consistent with [4,30,31]. An example of refined spectrum is shown in Fig. 5.

In the second instance, Pseudo-Voigt single peak fitting method imbedded in ENGIN-X analysis routine [32] was used to compute lattice strains of individual *hkl* variants parallel to the axial loading direction (AD) and radial direction (RD), as illustrated in Fig. 3.

Furthermore, the texture evolution was captured using analysis procedures outlined in [33]. Raw pole figures were constructed from the refined 6th order spherical harmonics in GSAS, assuming cylindrical symmetry of texture produced by the symmetric rotary swaging process. The orientation distribution functions (ODFs) were then reconstructed using MTEX software [34]. Hence the plotted inverse pole figures (IPFs) enable tracking

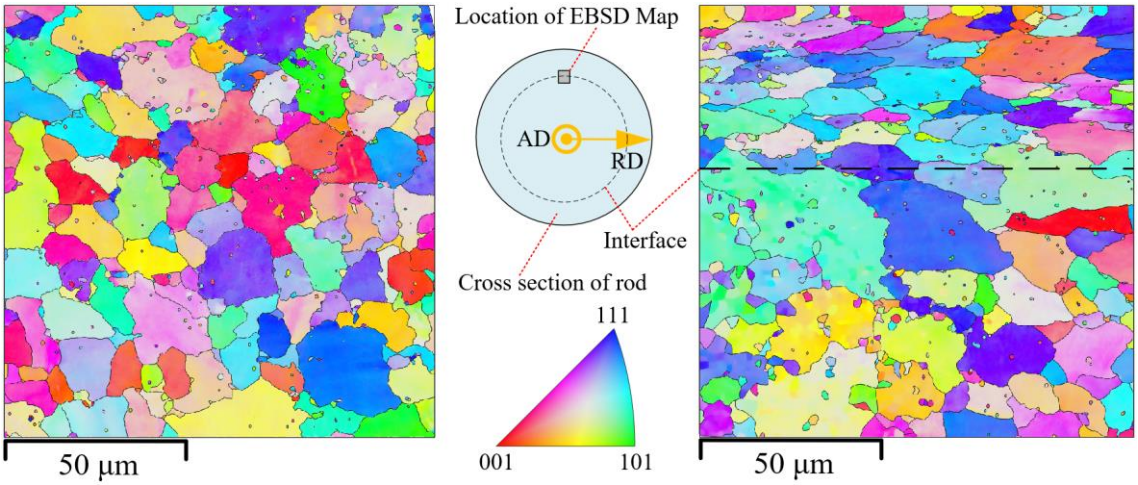


Fig. 6. Colour-coded inverse pole figure maps on cross-section of as cast (left) and hot swaged (right) NiTi rods. The triangular colour key indicates grain orientations parallel to the axial direction (AD). Location of the two EBSD maps was carefully selected so as to exhibit the interface that reveals the grain morphology heterogeneity in the HS rod.

the texture in the axial (AD) and radial (RD) direction of the cylindrical gauge volume [4].

3.Experimental results and discussion

3.1 Microstructural evolution

3.1.1 Grain morphology

EBSD analysis is shown in Fig. 6. The compressive and shearing force of hot swaging induces the heterogeneity in grain morphology in such a way that grains at the outer radius of cross section were heavily deformed with their dimension along RD reduced, while the grain at the inner region retain the equi-axed shape analogous to the as cast rod. From a macroscopic point of view, the ovality of grain shape increases after hot swaging, which coincides well with observation from the EPSC modelling approach in section 3.3.3.

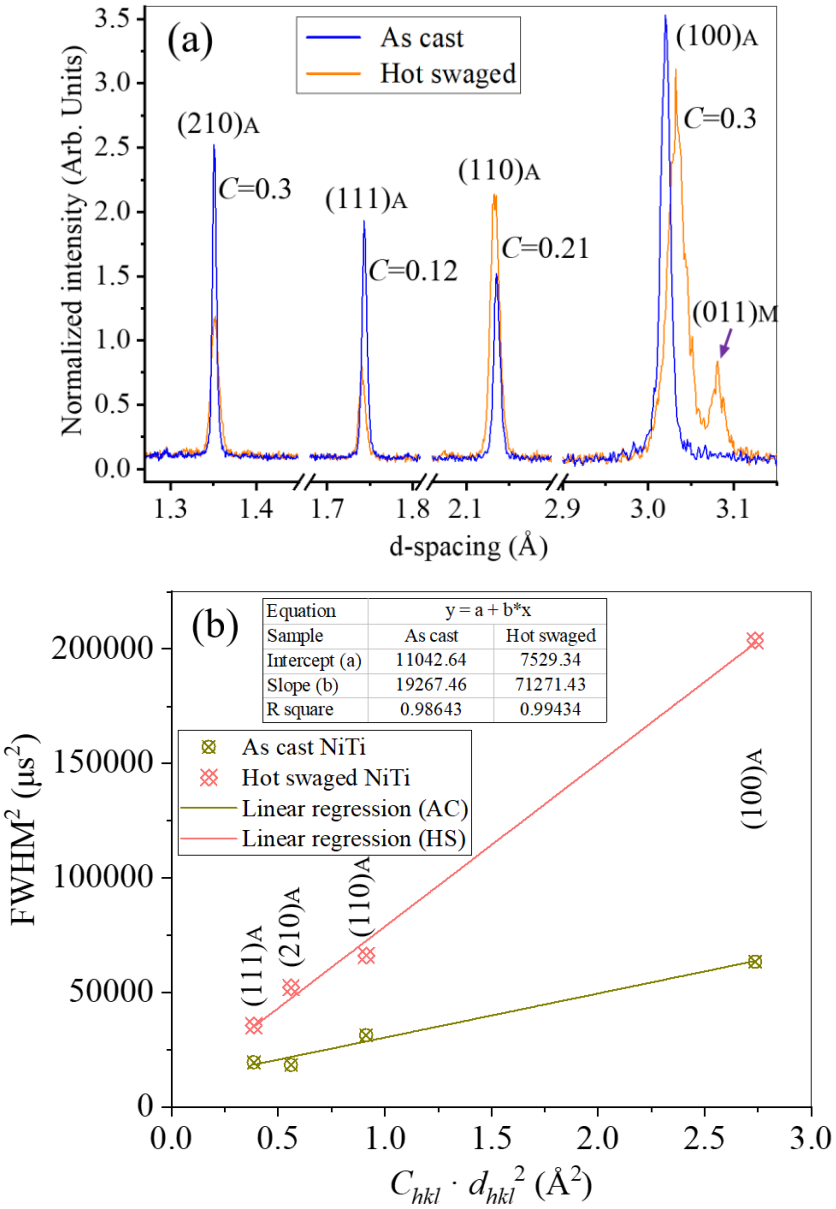


Fig. 7. (a) The comparison of peak profile of cubic austenite phase at 80°C. (b) A modified W-H plot, the slope of the linear fittings contain information of the microstrain in AC and HS NiTi. The uncertainties of $FWHM^2$ are comparable to the size of plotted symbols.

3.1.2 Microstrain

The peak profile of austenite phase of AC and HS NiTi are shown in Fig. 7a.

To evaluate the change in microstrain caused by hot swaging, the full width at half maximum (FWHM) of the observed diffraction peaks can be deconvoluted into multiple

contributions from instrument response (Δd_{ins}), grain size (Δd_{size}) and microstrain (Δd_{ε}) through Fourier transformation [35]. Consider the strain expression as $\varepsilon=\Delta d_{\varepsilon}/d_{hkl}$, which directly reveals the non-uniform lattice deformation from $d_{hkl}+\delta d$ to $d_{hkl}-\delta d$ for a specific *hkl* variant. Note that the microstrain induced by lattice defects is assumed to be homogeneously distributed among variants. The effect of elastic anisotropy in B2 cubic austenite phase in NiTi alloy can be eliminated via introducing the contrast factors *C* [36], so that we obtain:

$$FWHM^2 = \Delta d_{ins}^2 + \Delta d_{size}^2 + \Delta d_{\varepsilon}^2 = \Delta d_{ins}^2 + \Delta d_{size}^2 + \varepsilon^2 d_{hkl}^2 C, \quad (1)$$

where d_{hkl} is the d-spacing of an *hkl* plane (peak profile centre). The calculated *C* values for each *hkl* are marked in Fig. 7a, details refer to [36]. Eq. (1) is a typical $y=a+bx$ equation, *a* being the intercept and *b* the slope. This modified Williamson-Hall approach provides information on the microstrain (ε^2) from the slope of the plot, as shown in Fig. 7b. The fitting parameters are listed in the inset. It can be qualitatively concluded that the hot swaging process brings about a significant increase in non-uniform lattice deformation (microstrain), which is mostly associated with lattice defects.

3.2 Thermal expansion of martensite & austenite

To study the texture effect on thermal expansion, the hydraulic loading rig was set to stress control at 0 MPa during thermal cycling, therefore the samples can move freely in the loading direction, allowing the measurement of both macroscopic and microscopic phase transformation strain. The extensometer data shows that the variation of macroscopic shape-change strain is less than 0.1% after formation of nascent phase during cooling / heating. This suggests the accommodative nature of the twinned M phase, wherein the elastic, thermal and allotropic mismatch is minimised [37].

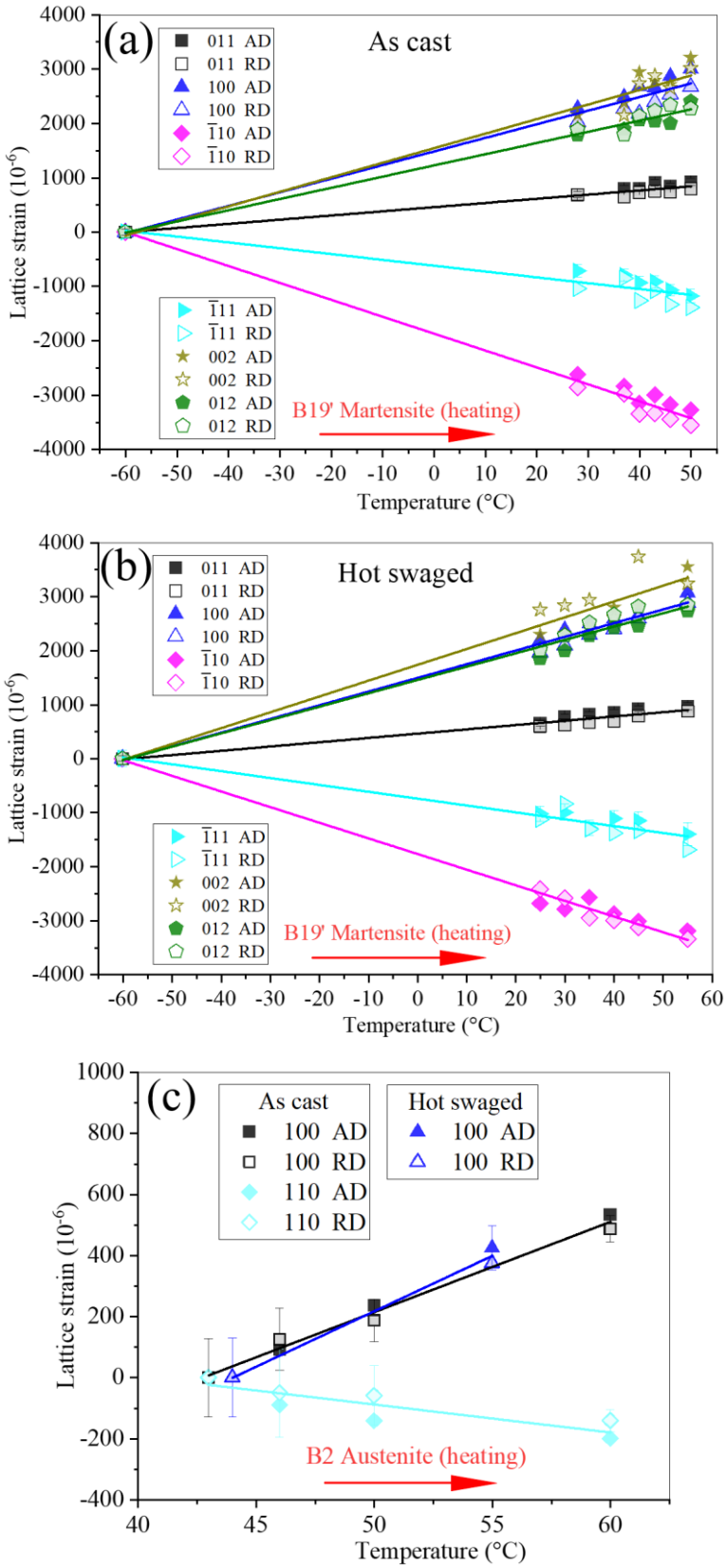


Fig. 8. Lattice strain as a function of temperature upon heating. As cast (a) and hot swaged (b) NiTi martensite phase. NiTi austenite phase (c). Linear regression is

performed for each variant. Uncertainties are displayed either as error bars or comparable to the size of plotted symbols.

Mesoscopic thermal expansion of variants can be obtained from lattice strains, which are quantified via the shifts in positions of individual *hkl* reflections:

$$\varepsilon_{hkl} = \frac{d^{hkl} - d_0^{hkl}}{d_0^{hkl}}, \quad (2)$$

where d_0^{hkl} and d^{hkl} denote the *d*-spacing of specific *hkl* at initial state and after thermomechanical deformation, respectively. Using Eq. (2), the lattice strains of M and A are determined, as plotted in Fig. 8. The relative rather than absolute strains are considered in the analyses.

It is noteworthy that the thermal expansion in both M and A phases retain a good linearity throughout the heating process, including the phase transformation process (10-60°C, according to DSC). Whilst the variation in coefficient of thermal expansion in *hkl* variants is attributed to anisotropy arising from crystal symmetry, the linearity suggests the accommodative nature of M phase and its capability to selectively transform to A, thereby minimising the intergranular stress between M and A grains.

The coefficient of thermal expansion of *hkl* variants can be obtained from linear fit in Fig. 8, and listed in Table 1. It is also worth mentioning that unlike the significant effect of texture on elastic properties which is discussed in the next section, the coefficients of thermal expansion are relatively independent of texture, since their values are similar between AC, HS and hot-drawn [37] NiTi. Components of thermal expansion tensor can be further determined using the values in Table 1, details refer to [37].

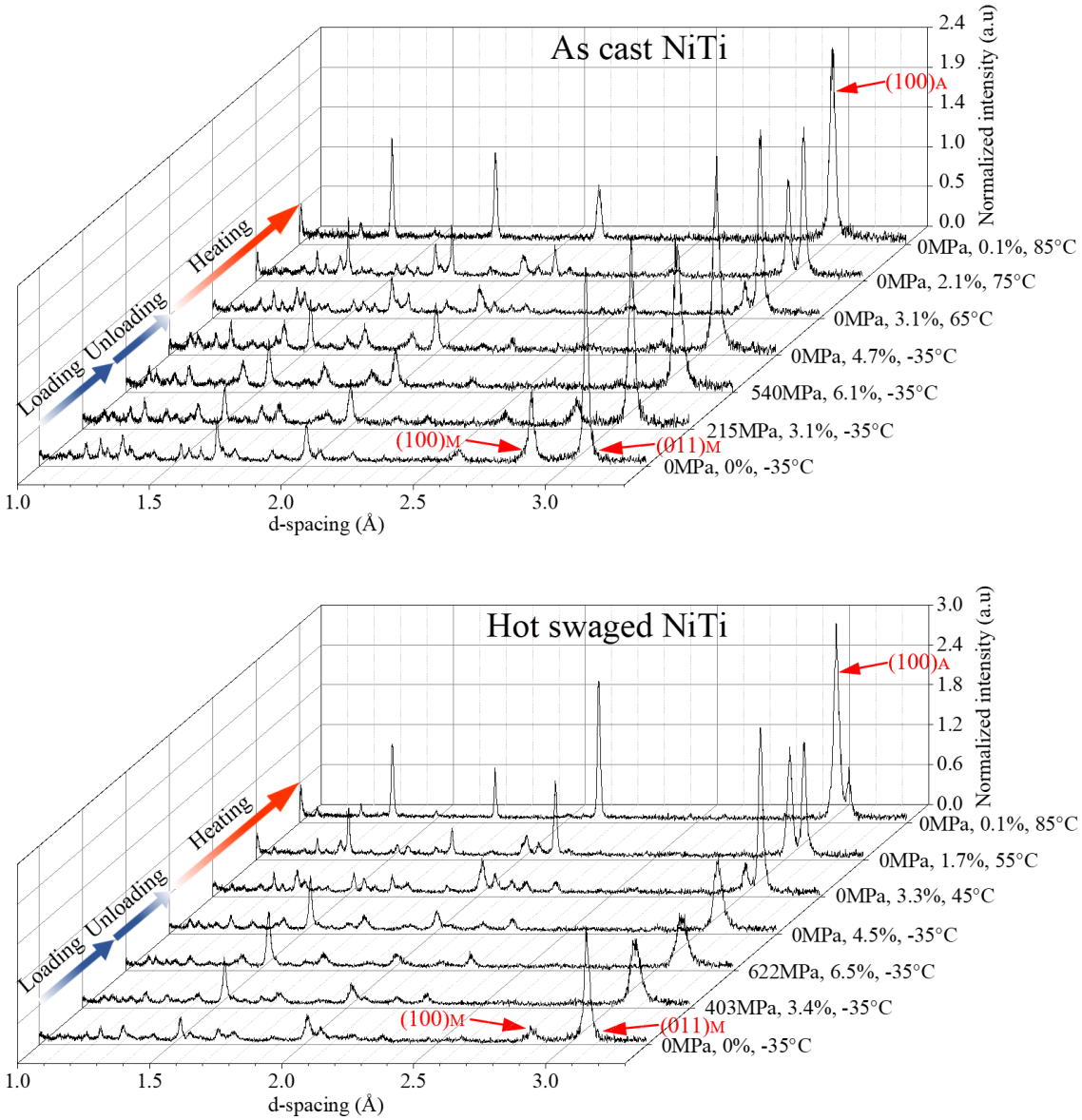


Fig. 9. The overview of spectra of AC and HS NiTi during SME, corresponding stress, strain and temperature of each spectrum are recorded on the right. Detailed peak index refers to Fig. 5 and Fig. 7a.

The measured thermal expansion coefficients of variants are used to compensate thermal expansion effect in the calculation of lattice strain during shape recovery in section 3.4.

Table 1

Coefficient of thermal expansion of NiTi martensite and austenite variants.

Unit:10^{-6}/°C	011_M	100_M	-110_M	-111_M	002_M	012_M	100_A	110_A
As cast	7.7	25.1	-30.2	-10.7	26.8	20.6	29.6	-9.2
Hot swaged	7.9	25.3	-29.0	-12.7	29.3	23.7	32.3	

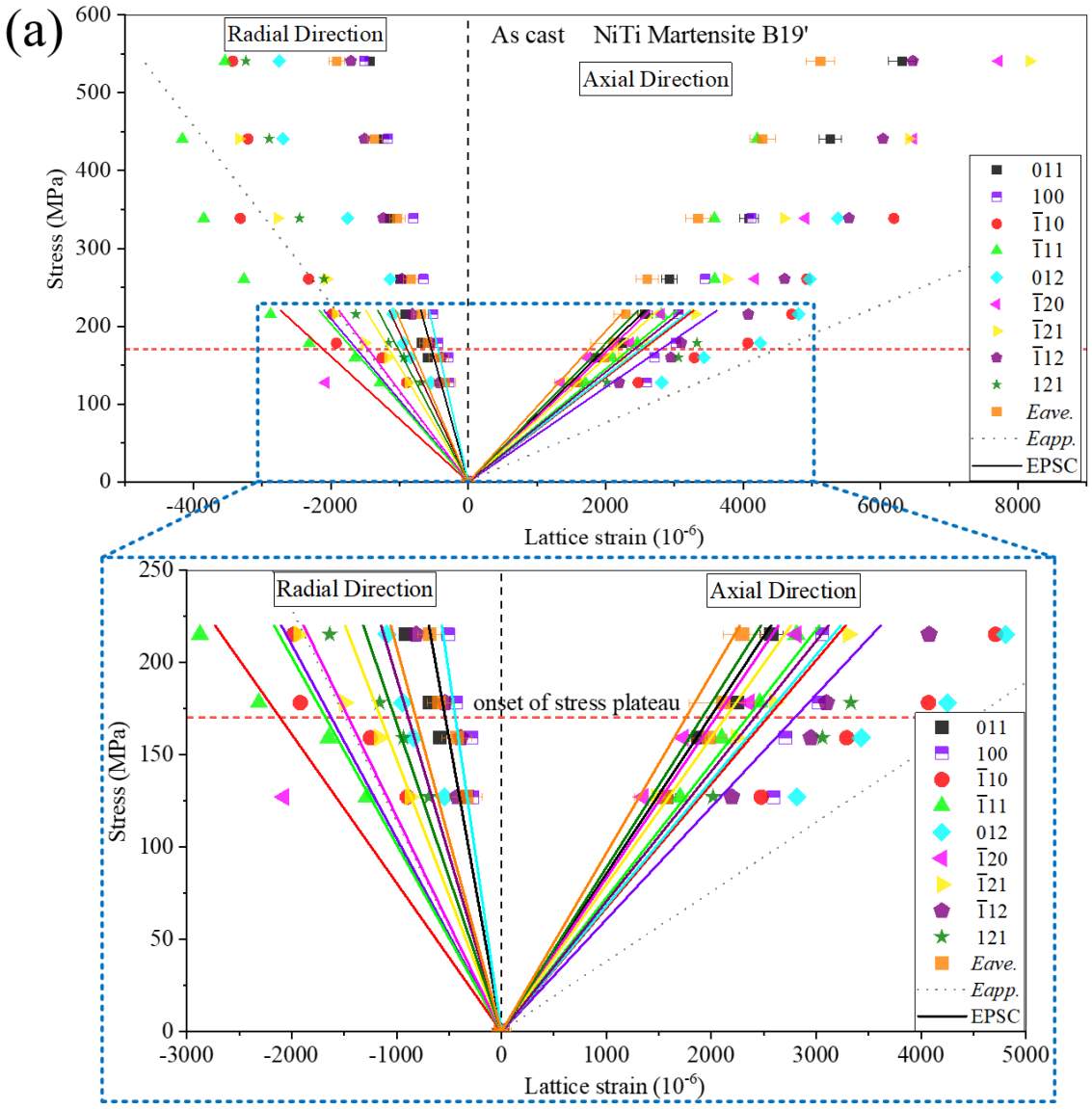
3.3 *In situ* neutron diffraction of SME

The overview of SME ND spectra is shown in Fig. 9, the evolution of which exhibits the difference in microstructural behaviour between AC and HS NiTi. Detailed analyses are in the sections below.

3.3.1 Lattice strain evolution

The shifts in positions of individual peaks can be converted into lattice strains of *hkl* variants using Eq. (2), the evolution of which is shown in Fig. 10. The lattice strain shown here are from variants whose *hkl* plane normal are parallel to the AD and RD (Fig. 3). It should be noted that these variants are freely distributed around the normal of scattering *hkl* planes since this does not interfere with the Bragg's condition. This means that the strains perceived from individual peaks are peculiar average from a subset of all grains in the gauge volume.

During the SME tensile loading, the integrated intensity of some reflections gradually decrease to zero, for example, (100), (-110) and (121) in AD of both samples. Since the integrated intensity of an individual peak is proportional to the number of grains involved in the diffraction, the disappearance of the peak is caused by the rotation of these grains and hence the interference of Bragg condition. This phenomenon can also be


(a)
Radial Direction
As cast NiTi Martensite B19'
Axial Direction
Stress (MPa)
Lattice strain (10^{-6})
011
100
$\bar{1}10$
$\bar{1}11$
012
$\bar{1}20$
$\bar{1}21$
$\bar{1}12$
121
Eave.
Eapp.
EPSC
onset of stress plateau

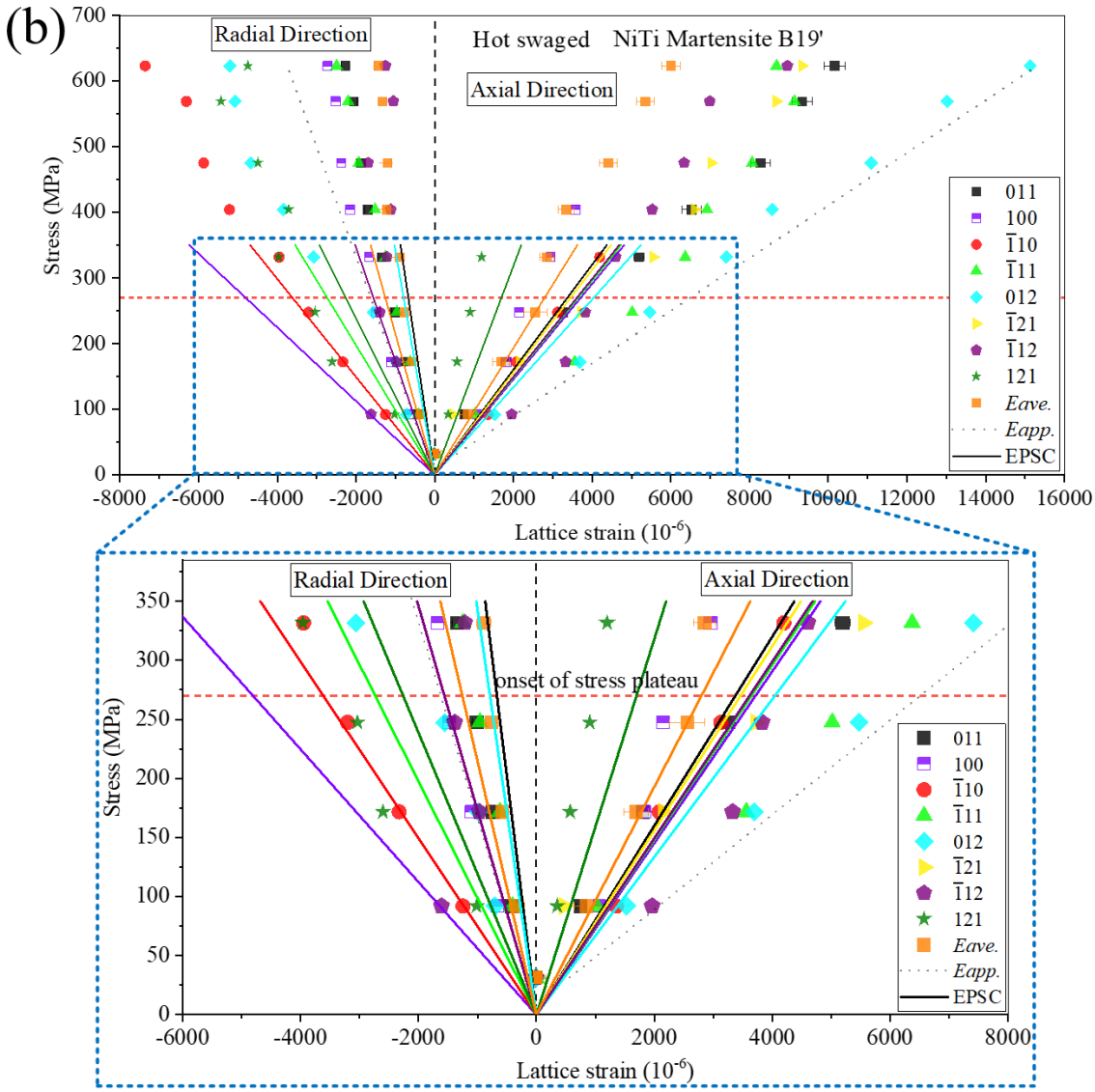


Fig. 10. The lattice strain evolution of AC (a) and HS (b) martensitic NiTi during loading. Typical uncertainties are displayed for (011), those of other variants are of similar magnitude. EPSC simulation of elastic response of each variant is drawn in solid lines using the same colour.

intuitively viewed from the peak profiles in Fig. 9. The general observation here is that the grain reorientation tend to favour those variants with either relatively low or high stiffness compared with the average level, for instance, AC (-110) and (012) in AD, (110), AC (020) and (-120) in RD, HS (121) and (002) in AD, thus interacting with the matrix and rotating.

3.3.2 Elastic properties

Apparent elastic moduli ($E_{app.}$) were determined from the gradient of initial slopes of the tensile stress-strain curves. Rietveld refinement method can be used to evaluate a volume averaged elastic modulus ($E_{ave.}$) in polycrystalline materials [4]. The elastic strain associated with a lattice plane, ε_{hkl}, can be described incorporating isotropic and anisotropic contributions with two fitting parameters, α and β:

$$\varepsilon_{hkl} = \varepsilon_{isotropic} - \varepsilon_{anisotropic} = \frac{\alpha}{C} - \frac{\beta \cdot \cos\phi}{C}, \quad (3)$$

where C is a diffractometer constant. α fits peaks in spectrum by varying the lattice parameters (a, b and c) such that $\Delta a/a = \Delta b/b = \Delta c/c$, thus capturing the isotropic strain. β accounts for the anisotropy component. For a given *hkl*, ϕ is the angle between the plane normal and [100] for martensitic NiTi. Following the refinement using Eq. (3), $E_{ave.}$ can be obtained by setting β to zero.

Theoretical elastic moduli of variants can be calculated for two extreme states of the martensite phase, namely the single crystal and twinned structure. Single crystal without internal twinning is known to possess the highest stiffness while the presence of twinned structure would significantly reduce the value [5]. Therefore, the twinned structure may represent the martensite at its lowest stiffness. For martensite NiTi, the elastic modulus E_{hkl} in the direction perpendicular to a *hkl* plane can be calculated using equation [38]:

Table 2

Values of E_{hkl}, E_{app} and $E_{ave.}$ from both experiment and EPSC, together with Hill-average elastic moduli from DFT simulation are listed. Poisson ratios (v) are calculated by dividing E_{hkl} in RD into that in AD. Expt. stands for experiment.

hkl	As cast NiTi				Hot swaged NiTi				Hot drawn NiTi [4]	Single crystal	Twinned structure
	E_{hkl}		v		E_{hkl}		v		E_{hkl}	E_{hkl}	E_{hkl}
	Expt.	EPSC	Expt.	EPSC	Expt.	EPSC	Expt.	EPSC			
011	85.4	85.6	0.31	0.21	63.7	80	0.23	0.08	117.1	183.9	60.5
100	69.2	64.4	0.18	1.2	100.5	72.7	0.59	1.34	132.2	152.6	26
-110	52.5	69.2	0.39	0.85	78.9	74.4	0.87	0.9	78.2	169	23.4
-111	92.2	74.2	0.95	0.89	58.2	74.7	0.23	0.76	104.7	76.2	11.2
012	52.3	72.6	0.27	0.08	41.3	67.1	0.36	0.07	145.4	159.7	40.3
-120	68.8	80.2	0.78	0.69					101.4	150.8	35.4
-121	69	78.7	0.44	0.47	67.5	78.1			93.3	98	21.1
-112	72.9	73.5	0.23	0.4	74.8	76.6	0.27	0.41	165.1	79.4	20.2
121	62.8	88.2	0.41	0.34	366	105.4	3.45	1.41	104.6	120.1	31.7

$E_{app.}$	37.8				55				50		
$E_{ave.}$	99.7	96.84	0.31	0.44	107.4	98.6	0.32	0.51	134		
E_{DFT}										180($v =$ 0.31)[29]	71($v = 0.35$) [5]

$$E_{hkl} = (l_1^4 S_{11} + 2l_1^2 l_2^2 S_{12} + 2l_1^2 l_3^2 S_{13} + 2l_1^3 l_3 S_{15} + l_2^4 S_{22} + 2l_2^2 l_3^2 S_{23} + 2l_1 l_2^2 l_3 S_{25} + l_3^4 S_{33} + 2l_1 l_3^3 S_{35} + l_2^2 l_3^2 S_{44} + 2l_1 l_2^2 l_3 S_{46} + l_1^2 l_3^2 S_{55} + l_1^2 l_2^2 S_{66})^{-1}, \quad (4)$$

where S_{ij} are the 13 independent compliance constants obtained through DFT simulation, given in [5] for both single crystal and twinned structure.

Determined by least square linear fit of data points, values of $E_{app.}$, $E_{ave.}$, E_{hkl} are listed in Table 2. The experimental results from a hot drawn NiTi rod are also included for comparison.

$E_{ave.}$ of HS NiTi is higher than that of AC NiTi, while the hot drawn (HD) NiTi is the highest. These experimental results of $E_{ave.}$ agree well with DFT simulation, all within the range of 71-180 GPa. This indicates that the AC NiTi contains the original amount of twinned structures while those in HS and HD samples were detwinned due to the compressive forming process. The averaged Poisson ratios from experiment and DFT are similar (~0.31-0.35) regardless of the microstructure.

The values of E_{app} (37.77-55 GPa) are consistent with those reported in previous studies (40-70 GPa) and has been mistakenly considered to be the actual martensite modulus of NiTi in many literatures. The fact is that the real elastic modulus $E_{ave.}$ is more than two times the value of $E_{app.}$. This confusing dilemma of elastic modulus implies that

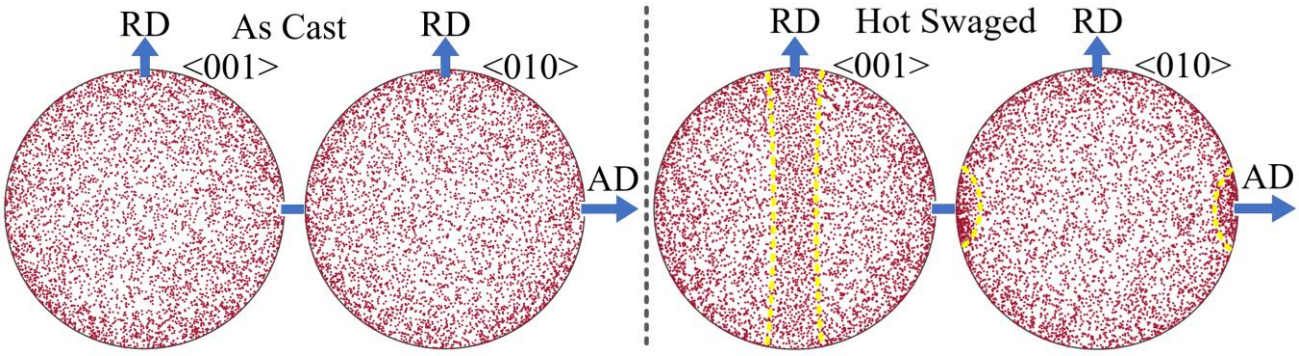


Fig. 11. Orientation of 6000 grains among 12000 that used in EPSC simulation. Yellow dashed line highlights the enhanced fibre texture in grain population file.

considerable amount of martensite twins are inelastically detwinned before the onset of stress-plateau [39,40].

The experimental results of E_{hkl} lie within the range of single crystal and twinned structure. However, few exceptions exist such as the E_{-111} of AC NiTi and E_{121} of HS NiTi, which suggests that the intergranular constraint arising in polycrystalline materials exerts non-negligible influence on the anisotropic elasticity. The abnormal value of Poisson ratio (>0.5) is another evidence of the effect. Therefore, EPSC simulation that takes into account the influence of microstructure, was carried out to quantify the elastic response of variant.

3.3.3 EPSC quantification of elastic properties

The Elasto-Plastic Self-Consistent (EPSC) approach was employed to simulate the effect of texture and grain morphology on anisotropic elastic response of variants. Based on Eshelby theory, the model treats each variant as an ellipsoidal inclusion embedded in a homogeneous medium. Numerical implementation is described in [41].

Grain population files (Fig. 11) were generated consistent with the texture observed from ND. The simulation parameters, namely ellipsoid ratios and elastic constants were tuned to fit the experimental result of AC NiTi. Then the grain population file was

substituted by that of HS NiTi to verify the texture effect. Parameters are listed in Table 3.

Table 3

EPSC simulation parameters.

	Ellipsoid Ratios			C_{11}	C_{12}	C_{13}	C_{14}	C_{22}	C_{23}	C_{25}	C_{32}	C_{35}	C_{44}	C_{46}	C_{55}	C_{66}
	x	y	z													
AC	0.4	1.2	2	35	102	120	1	135	120	27	80	7	67	5	13	52
HS	0.4	1.2	20													

Most variants exhibit crooked stress-strain response above the onset of stress plateau, as indicated by dashed line in Fig. 10. This non-linear behaviour in the stress-strain curve is mainly attributed to plastic deformation of variants from twinned to detwinned structure [4], hence simulation results is plotted in the elastic regime. Numerical comparison between experiment and EPSC result refers to Table 2.

This EPSC simulation demonstrates the texture-dependent elastic properties of variants. Furthermore, the effect of grain morphology was confirmed by the ellipsoid ratios in Table 3, in that the higher ovality of HS NiTi agrees well with the EBSD observation in Fig. 6.

3.3.4 Texture evolution

Fig. 12&13 are IPFs of AC and HS NiTi, respectively. The first IPF is plotted in full spherical space to illustrate the symmetry arising from the monoclinic crystal structure, indicating that only half circle is necessary to present a full map of texture. For the sake

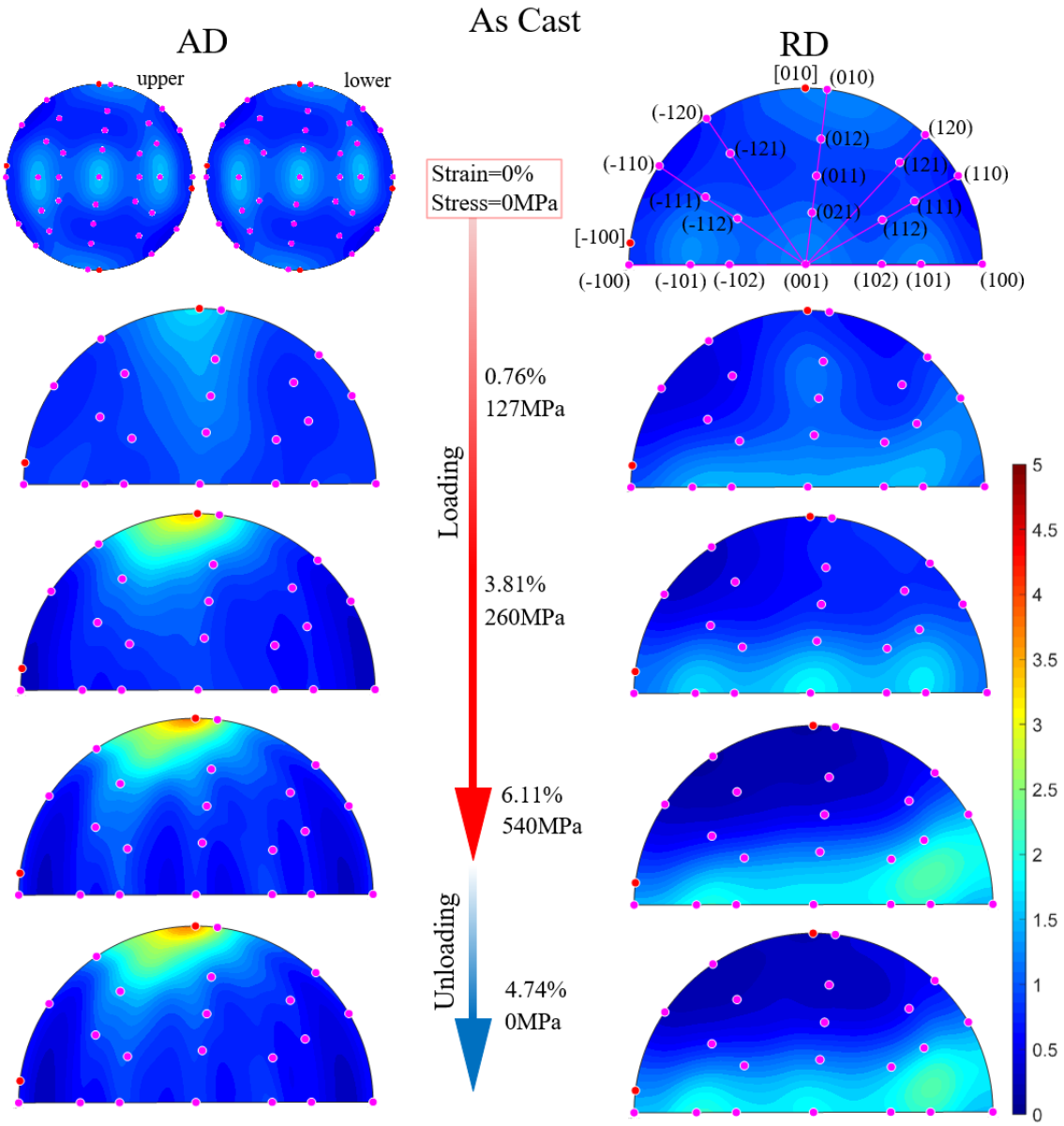


Fig. 12. Inverse pole figures (IPFs) of AC NiTi. The corresponding stress and strain levels are indicated in the middle. The *hkl* variant of low index are marked with pink dots. Four directions, namely <100> and <010> are drawn in red dots for reference.

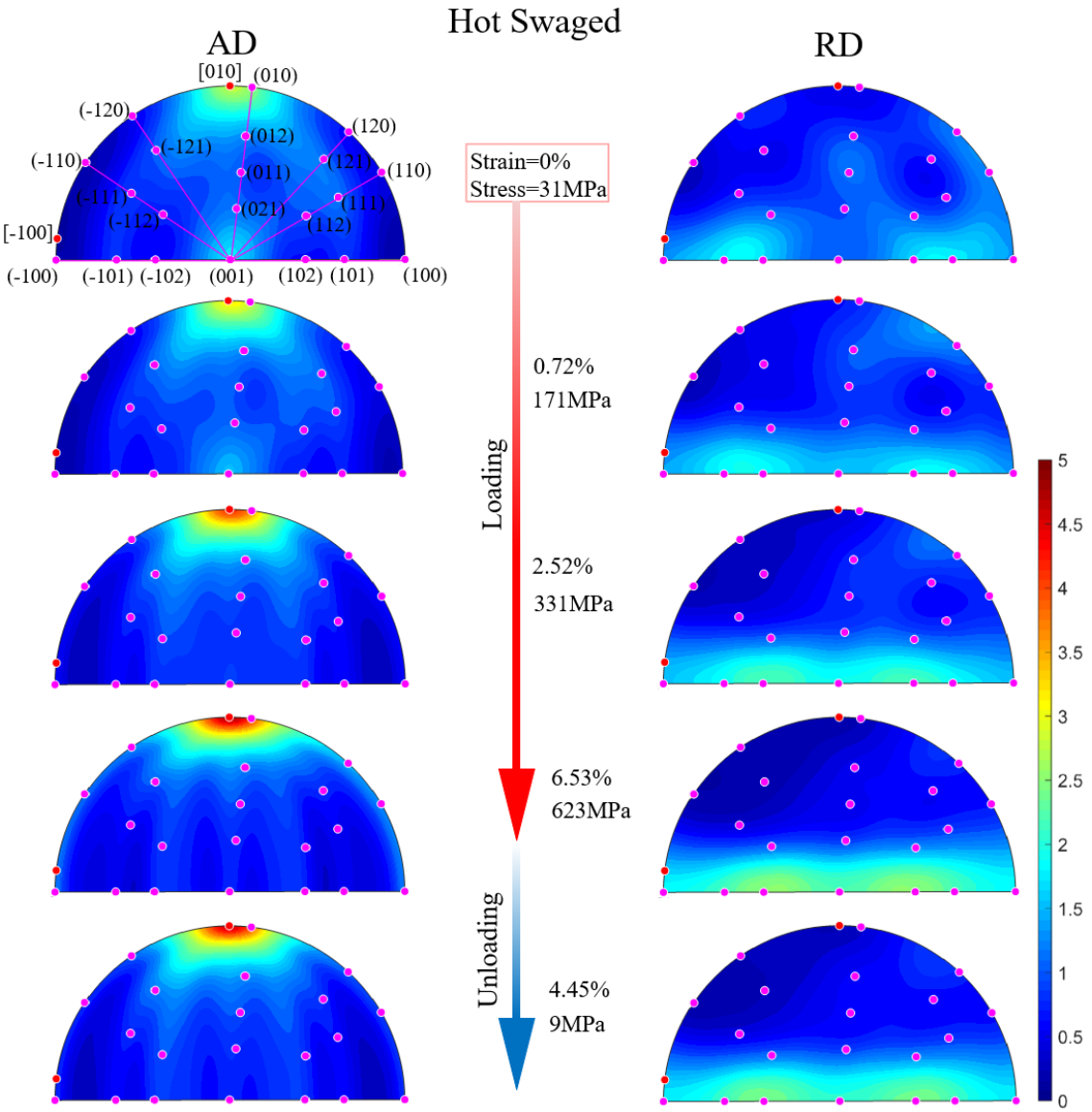


Fig. 13. IPFs of HS NiTi.

of clarity in comparison of textures in different directions and samples, all figures adopt the equal range of scale bar from 0-5, in units of m.r.d. (multiples of random distribution).

The initial texture of AC NiTi is weak, consistent with the low value of texture index of 1.32 (AD) and 1.13 (RD) obtained by Rietveld method. At virgin state, the texture distributions in two directions are similar that the density of (-101), (101), (001) and (010) are slightly higher. In comparison, HS NiTi exhibits distinct initial texture that the density of (010) in AD and (-101,101) in RD are around 2.8 m.r.d and 1.9 m.r.d., respectively.

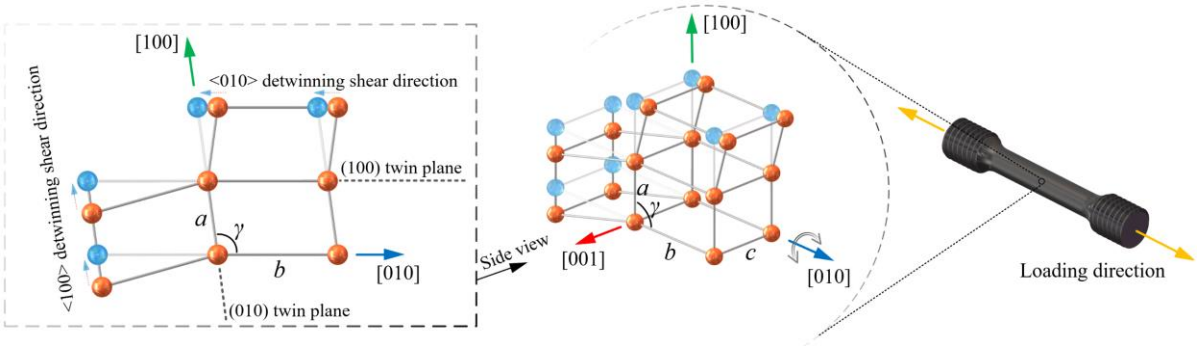


Fig. 14. Schematic illustration of detwinning of the (010) & (100) compound twin structures of martensite B19' NiTi. The texture information from IPFs indicate that grains reorient with the [010] direction parallel to the loading direction and distribute homogeneously around the [010] pole, thus accommodating the detwinning shear strain along the loading direction.

With the gradual increase of applied stress, the majority of variants in AC NiTi are rearranged in such a way that the [010] direction (i.e. b-axis) being parallel to the axial loading direction and (-101), (001) and (101) being perpendicular. However, the texture rearrangement of both banks tends to saturate at the stress level of 260MPa and above, corresponding to the end of stress-plateau in the macroscopic curve. The maximum density near [010] direction in AD merely increases from 3.7 to 3.9 m.r.d. upon the stress increment from 260 to 540 MPa. This means that major part of texture evolution takes place within the region of stress plateau. It may be inferred from the phenomenon that the texture evolution is closely correlated to detwinning process, since the grains reorient in such a way to accommodate the detwinning strain of (010) compound twins and (100) compound twins in the loading direction, as illustrated in Fig. 14. This inference and the observation of macroscopic SME curves suggests that the prevalent detwinning modes are related to both the <011> Type II twin and (010) & (100) compound twin [42], and the rearrangement of compound twins and others (e.g. <2-10> twin) after the plateau may

be trivial in contribution to deformation [43]. Upon unloading from maximal stress to zero, the evolved texture does not show an obvious evidence of recovery, implying that the grain reorientation is inelastic.

The texture evolution of HS NiTi is very similar to that of AC NiTi, except that the density reaches ~4.9 m.r.d. at maximal stress. Nevertheless, the higher density is attributed to the advantage of initial texture in HS sample rather than better adaptability of grains, since the variation in [010] density in AC NiTi (~2.9 m.r.d.) is higher than HS NiTi (~2.1 m.r.d.). Surprisingly, the texture evolution of AC and HS samples are not only similar but also has a good agreement with those reported in other studies [4,44] using NiTi samples of different composition and processing methods. Hence it may be qualitatively assumed that the texture evolution in NiTi during SME is largely independent of initial microstructure. Besides, it should be noted that texture evolution takes place in AC and HS sample at low stress (~100 MPa), consistent with TEM studies [39,43] that the pseudo-plastic deformation starts in the "elastic regime" of deformation, which strongly supports the discussion in section 3.3.1 and 3.3.2.

3.4 Quantification of lattice strain evolution

The lattice strain evolution in NiTi can be captured by a "bi-crystal model", the concept of which was proposed in [16]. As illustrated in Fig. 15(a), the model is based on the assumption of anisotropic hybrid deformation in variants whose elongation are equally constrained by the boundary along the loading axis. Suppose two variants A and B having the same length (Step 1). Although both variants are martensite phase, they exhibit different modes of elastic and plastic deformation due to the anisotropy when external stress is applied (Step 2). In this case, the deformation of variant A may contain more inelastic component (i.e. pseudo-plastic detwinning and plastic slip) than B.

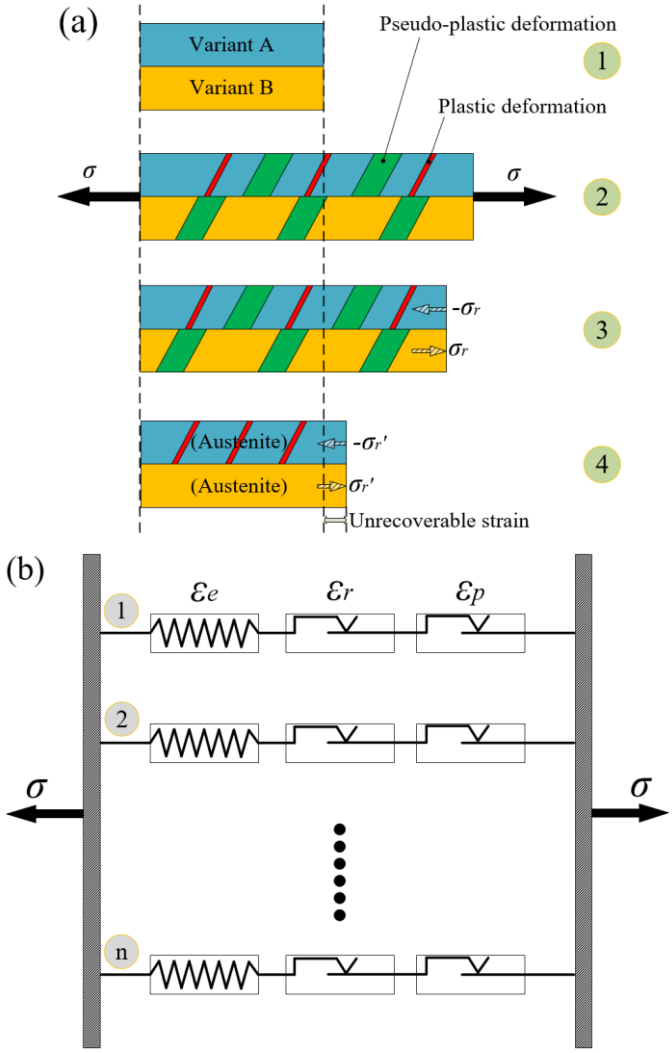


Fig. 15. The conceptual sketch of four deformation steps during SME of the bi-crystal model (a). Its generalized version proposed in this study (b).

Therefore, after unloading the difference in inelastic deformation results in the residual lattice strain distribution in the two grains (compression in A and tension in B), and hence the residual stress (σ_r) (Step 3). Upon heating, the detwinned martensite transforms to austenite such that the pseudo-plastic deformation (green colour) is recovered, causing the redistribution of lattice strain and residual stress (σ_r') due to the change of inelastic deformation in A and B (Step 4).

The bi-crystal model can be further generalized to an assemblage of *N* elasto-plastic *hkl* variants connected in parallel, as shown in Fig. 13(b). The deformation of each variant

is comprised of three strain modes, namely lattice strain (i.e. elastic strain) (ε_e), plastic strain (ε_p) and pseudo-plastic strain (i.e. recoverable strain) (ε_r). Assuming that the total strain (ε_t) of variants are equally constrained by the boundary on both sides, in that $\varepsilon_t = \varepsilon_e + \varepsilon_p + \varepsilon_r$. ε_t is the only independent variable, while ε_e is the dependent variable that this model aims to quantify.

The elastic strain of a variant can be given as: $\varepsilon_e = \sigma / E_{hkl}$, where σ and E_{hkl} are the applied stress and elastic property of the variant in loading direction, respectively. The value of σ corresponds to a given ε_t from the macroscopic stress-strain curve (Fig. 4), whilst the value of E_{hkl} is known from the texture-dependent EPSC results in section 3.3.2. Detwinning and phase transformation strain are considered to be the underlying mechanisms of shape recovery [45], whilst the latter can be neglected in this case because the phase transformation strain from twinned martensite to austenite is typically less than ~0.1%, which has been confirmed by stress-free thermal cycling in section 3.2. Therefore, the pseudo-plastic strain ε_r is equivalent to the martensite detwinning strain that can be further split into two components:

$$\varepsilon_r = \varepsilon_{Type\ II} + \varepsilon_{Compound}, \quad (5)$$

where $\varepsilon_{Type\ II}$ denotes the detwinning strain of <011> Type II twins and $\varepsilon_{Compound}$ is that of compound twins. Given that the twining shear strain for (010) & (100) twin systems are equivalent [43], only the (010) compound twin is considered in the model. Details of these dominant twinning modes have been elucidated in [39,42,43,45,46].

In the process of detwinning, one variant of the CVP (Correspondence Variant Pair, denoting a martensite plate contains two twin-related martensite single-crystal variants) grows in the expense of the other, finally resulting in a single crystal of martensite. $\varepsilon_{Type\ II}$ can be calculated by:

$$\varepsilon_{Type\ II} = \sum_{n=1}^{24} \xi^n (\lambda^n - \lambda_0^n) R \mathbf{P}_{dt}^n R^T, \quad (6)$$

where λ^n is volume fraction of one variant (that of the other is $1-\lambda^n$) after detwinning. λ_0^n is the initial value [47]. Hence the term $\lambda^n - \lambda_0^n$ denotes the amount of transition between the two variants. ξ^n is the volume fraction of nth CVP in the matrix. R^T is the transpose of *R*, the strain transformation tensor that transforms the detwinning strain tensor $\mathbf{P}_{dt}^n$ from the original coordinate system to the direction of *hkl* normal:

$$R = \begin{bmatrix} \cos\alpha\cos\beta & \cos\alpha\sin\beta & \sin\alpha \\ -\sin\alpha\cos\beta & -\sin\alpha\sin\beta & \cos\alpha \\ \sin\beta & -\cos\beta & 0 \end{bmatrix}, \quad (7)$$

where $\alpha = \tan^{-1}(h/k)$, $\beta = \tan^{-1}\left((1.01l + 0.12h)/\sqrt{h^2+k^2}\right)$. $\mathbf{P}_{dt}^n$ can be obtained from:

$$\mathbf{P}_{dt}^n = \frac{1}{2}(\boldsymbol{a}^n \otimes \boldsymbol{w}^n + \boldsymbol{w}^n \otimes \boldsymbol{a}^n), \quad (8)$$

where $\boldsymbol{w}^n$ is the unit normal vector of shear plane, $\boldsymbol{a}^n$ is the vector of shear direction. λ^n, λ_0^n, $\boldsymbol{a}^n$, $\boldsymbol{w}^n$ of 24 CVPs in NiTi alloy are listed in Table 4.

Table 4

g=0.5846, *h*=0.8133, *k*=0.2804, *o*=0, *p*=0.271, *q*=0.729, *r*=1. [48]

n	$\boldsymbol{w_1^n}$	$\boldsymbol{w_2^n}$	$\boldsymbol{w_3^n}$	$\boldsymbol{a_1^n}$	$\boldsymbol{a_2^n}$	$\boldsymbol{a_3^n}$	$\boldsymbol{\lambda_0^n}$	$\boldsymbol{\lambda^n}$
1	*-g*	*o*	*h*	*o*	*k*	*o*	*p*	*r*
2	*o*	*-g*	*-h*	*k*	*o*	*o*	*p*	*r*
3	*-g*	*o*	*-h*	*o*	*k*	*o*	*p*	*r*
4	*o*	*-g*	*h*	*k*	*o*	*o*	*p*	*r*
5	*-g*	*o*	*-h*	*o*	*k*	*o*	*q*	*r*
6	*o*	*-g*	*h*	*k*	*o*	*o*	*q*	*r*
7	*-g*	*o*	*h*	*o*	*k*	*o*	*q*	*r*
8	*o*	*-g*	*-h*	*k*	*o*	*o*	*q*	*r*

9	-*h*	-*g*	*o*	*o*	*o*	*k*	*p*	*r*
10	-*h*	*g*	*o*	*o*	*o*	*k*	*q*	*r*
11	-*h*	*o*	-*g*	*o*	*k*	*o*	*p*	*r*
12	-*h*	*o*	*g*	*o*	*k*	*o*	*q*	*r*
13	*h*	*g*	*o*	*o*	*o*	*k*	*p*	*r*
14	-*h*	-*g*	*o*	*o*	*o*	*k*	*q*	*r*
15	-*h*	*o*	*g*	*o*	*k*	*o*	*p*	*r*
16	-*h*	*o*	-*g*	*o*	*k*	*o*	*q*	*r*
17	*g*	-*h*	*o*	*o*	*o*	*k*	*q*	*r*
18	-*g*	-*h*	*o*	*o*	*o*	*k*	*p*	*r*
19	*o*	-*h*	-*g*	*k*	*o*	*o*	*p*	*r*
20	*o*	-*h*	*g*	*k*	*o*	*o*	*q*	*r*
21	-*g*	-*h*	*o*	*o*	*o*	*k*	*q*	*r*
22	*g*	-*h*	*o*	*o*	*o*	*k*	*p*	*r*
23	*o*	-*h*	*g*	*k*	*o*	*o*	*p*	*r*
24	*o*	-*h*	-*g*	*k*	*o*	*o*	*q*	*r*

The detwinning strain tensor of (010) compound twin $\varepsilon_{Compound}$ can be determined by [45]:

$$\varepsilon_{Compound} = \xi\lambda R\frac{1}{2}s(\boldsymbol{m}\otimes\boldsymbol{n}+\boldsymbol{n}\otimes\boldsymbol{m})R^{T}, \quad (9)$$

where $\boldsymbol{m}$ and $\boldsymbol{n}$ are unit normal vector of habit plane and unit vector of twinning direction respectively. s is the shear magnitude and ξ is the volume fraction of the compound twin in the matrix. λ is the amount of transition by detwinning [47]. Details are listed in Table 5 [46].

Table 5

$\boldsymbol{m_1}$	$\boldsymbol{m_2}$	$\boldsymbol{m_3}$	$\boldsymbol{n_1}$	$\boldsymbol{n_2}$	$\boldsymbol{n_3}$	$\boldsymbol{s}$	$\boldsymbol{\lambda}$
0	0	1	1	0	0	0.238	0.5

Assuming the volume fraction of two detwinning modes satisfies the normalized condition: $\xi + \sum_{n=1}^{24} \xi^n = 1$, and $\xi^i = \xi^j \ (i, j = 1,\ 2,\ 3, \dots, 24)$ [48]. The value of ξ and ξ^n can be calibrated by fitting the average detwinning strains of the two modes, i.e. 6.79% for <011> Type II and 2.98% for (001) compound [47], to the macroscopic recoverable strain of the two samples. The calibrated values are listed in Table 6. Thereby the pseudo-plastic strain ε_r can be obtained by combining Eq. 5, 6 and 9:

$$\varepsilon_r = \sum_{n=1}^{24} \xi^n \, (\lambda^n - \lambda_0^n) R \mathbf{P}_{dt}^n R^T + \xi \lambda R \frac{1}{2} s (\boldsymbol{m} \otimes \boldsymbol{n} + \boldsymbol{n} \otimes \boldsymbol{m}) R^T. \quad (10)$$

The plastic strain is permanent whose value can only increase. At maximum ε_t, the values of ε_r and ε_e are known, hence the plastic strain of each variant: $\varepsilon_p = \varepsilon_t - \varepsilon_r - \varepsilon_e$.

Upon unloading, the lattice strain changes freely in such a way to accommodate the difference between total strain and other strain components: $\varepsilon_e = \varepsilon_t - \varepsilon_r - \varepsilon_p$.

During shape recovery, the instant pseudo-plastic strain ($\varepsilon_r{}'$) of each variant gradually recovers, whose value is related to the macroscopic recovered strain:

$$\varepsilon_r{}' = \varepsilon_r \cdot (\tfrac{\varepsilon - \Delta\varepsilon}{\varepsilon}) = \varepsilon_r \cdot (\tfrac{\varepsilon - \varepsilon_m + \varepsilon_t}{\varepsilon}), \quad (11)$$

where ε_r is the pseudo-plastic strain before shape recovery obtained from Eq. 10. ε is the macroscopic recoverable strain obtained from the macroscopic stress-strain curve (Fig. 4). $\Delta\varepsilon$ is the change in macroscopic strain during shape recovery. ε_m is the macroscopic strain before shape recovery. Similarly, the lattice strain can be obtained from: $\varepsilon_e = \varepsilon_t - \varepsilon_r' - \varepsilon_p$. Arising from grain boundaries and textures, the intergranular constraint is found to retard the shape recovery in polycrystalline NiTi [49]. Hence the

gradient of lattice strain evolution is multiplied by *k*, representing the average intergranular constraint from the matrix:

$$\frac{d\varepsilon_e'}{d\varepsilon_t} = k\frac{\partial\varepsilon_e}{\partial\varepsilon_t}, \quad (12)$$

where ε_e' is the lattice strain predicted by the model. The calibrated parameters are listed in Table 6.

Table 6

Sample Condition	ξ	ξ^n	ε_m	ε	k
AC	0.35	0.027	6.11	5.46	0.03
HS	0.26	0.031	6.53	5.81	0.04

The calibrated value of ξ and ξ^n indicates that the amount of compound twin in AC NiTi is higher than that in HS NiTi, which well agrees the observation in section 3.3.4 that more grains in AC NiTi are reoriented with [010] parallel to the AD so as to accommodate the detwinning strain. Texture effect is considered in the model via the anisotropic elastic property of variant (E_{hkl}), which is quantified by EPSC in section 3.3.3. The lower value of *k* in AC NiTi implies that random texture induces stronger intergranular constraint, consistent with observations from [49].

The comparison between experiment and proposed model are shown in Fig. 16. The loading process described by the model well fits the data since the elastic properties of variants are given in section 3.3.2. The novelty of the proposed model comes to the quantification of lattice strain evolution during the unloading and shape recovery. Upon

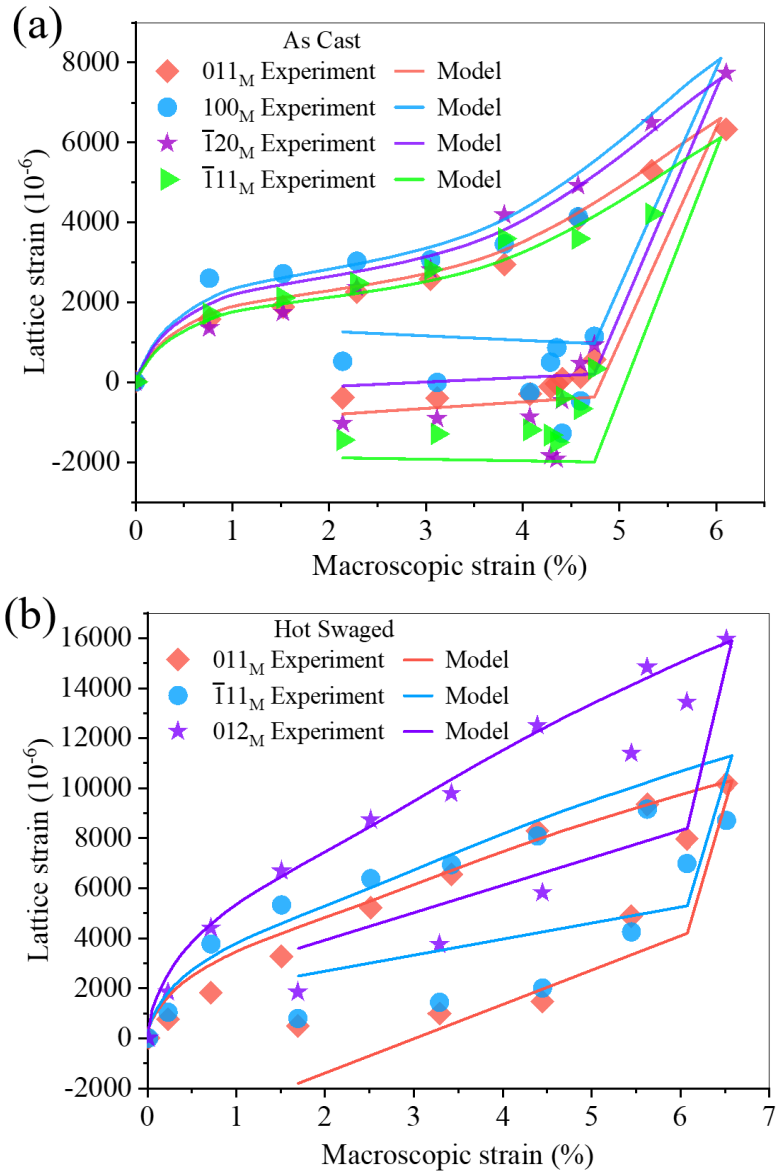


Fig. 16. Lattice strain evolution: comparison between experiment and proposed model. Uncertainties are comparable or smaller than the size of plotted symbols.

unloading, lattice strain depends on the plastic and pseudo-plastic strain calculated at maximum stress level. During shape recovery, the instant pseudo-plastic strain of variant is estimated, thereby the lattice strain being calculated. It can be seen that lattice strain evolution of variant is linear, either positive or negative. The positive ones, for instance the (100) variant of AC NiTi, indicate that the strain recovery of that variant is larger than the average matrix, so that the difference in strain between the variant and matrix has to

be compensated by the increasing of elastic lattice strain. And vice versa. Although concise as it is, the model effectively captures the overall trend of the texture-dependent lattice strain evolution in different variants, particularly the unloading and shape recovery process.

4. Summary and conclusions

This work has provided insight into the effect of texture introduced by different processing methods on the SME behaviour of variants as they exist in bulk polycrystalline NiTi alloys. Attentions were drawn to various properties of NiTi alloy, namely, grain morphology, microstrain, thermal expansion coefficient, lattice strain evolution, elastic properties and texture evolution. Based upon the experimental results, a multi-variant model that quantifies the lattice strain evolution during SME was constructed, shedding light on the degradation of functional behaviour from a mesoscopic point of view.

Conclusions are summarised as below:

Hot swaging process brings about reduction in grain dimension along RD, increase in microstrain, and formation of <010> fibre texture along AD.

The linearity of lattice strain evolution during stress-free thermal cycling suggests the accommodative nature of M phase to minimise the intergranular stress between M and A grains. The thermal expansion of M and A variants are demonstrated to be weakly affected by the texture.

The elastic response of variants show large extent of anisotropy. Elastic properties of both variants and macroscopic averaged value of AC, HS, HD samples lie within the range for single crystal state (the highest stiffness) and twinned structure (the lowest stiffness). Attributed to the texture effect, the same *hkl* variant in AC, HS and HD NiTi

exhibits distinct elastic modulus. Texture and grain morphology effect on elastic properties are quantified by EPSC approach.

Major part of texture evolution during SME takes place within the region of stress-plateau. The rearranged texture retained upon unloading. Although AC, HS and HD NiTi presents different microstructure initially, the way of texture rearrangement are similar such that the [010] direction is reoriented parallel to the loading axis, thus accommodating the detwinning strain of (001) & (100) compound twins.

Being the likely first attempt so far, the proposed multi-variant model well captures the overall trend of the anisotropic lattice strain evolution during SME. The proportion of three strain modes of a variant largely depends on the orientation and texture. Random texture is found to induce more intergranular constraint during shape recovery.

Apart from the new findings, conclusions in the present work well match those from literature.

Data availability

The processed data used to support the conclusions of this study are included within the article. The raw data will be made available upon request.

Acknowledgements

AMK wishes to acknowledge the support of EPSRC through grants EP/S005072/1 and EP/P005381/1. Dr. Lenka Kuncicka and Prof. Radim Kocich acknowledge the financial support of the 19-15479S Project of the Grant Agency of the Czech Republic. We gratefully acknowledge the Science and Technology Facilities Council (STFC) for access to neutron beamtime RB1920246 at the ISIS Pulsed Neutron and Muon Source.

References

[1] Z. Wang, A.M. Korsunsky, Effect of Temperature on Shape Memory Materials, in: Reference Module in Materials Science and Materials Engineering, Elsevier Inc., 2020. https://doi.org/10.1016/B978-0-12-803581-8.11793-X.

[2] T.M. Brill, S. Mittelbach, W. Assmus, M.Mullner, B. Luthi, Elastic properties of NiTi, J. Condens. Matter Phys. 4 (1991) 9621-9627. https://doi.org/10.1088/0953-8984/3/48/004.

[3] M.F.-X. Wagner, W. Windl, Lattice stability, elastic constants and macroscopic moduli of NiTi martensites from first principles, Acta Mater. 56 (2008) 6232-6245. https://doi.org/10.1016/j.actamat.2008.08.043.

[4] S. Qiu, B. Clausen, S.A. Padula II, R.D. Noebe, R. Vaidyanathan, On elastic moduli and elastic anisotropy in polycrystalline martensitic NiTi, Acta Mater. 59 (2011) 5055-5066. https://doi.org/10.1016/j.actamat.2011.04.018.

[5] J. Wang, H. Sehitoglu, Martensite modulus dilemma in monoclinic NiTi-theory and experiments, Int. J. Plast. 61 (2014) 17-31. https://doi.org/10.1016/j.ijplas.2014.05.005.

[6] T. Ezaz, H. Sehitoglu, H.J. Maier, Energetics of twinning in martensitic NiTi, Acta Mater. 59 (2011) 5893-5904. https://doi.org/10.1016/j.actamat.2011.05.063.

[7] T. Ezaz, H. Sehitoglu, Type II detwinning in NiTi, Appl. Phys. Lett. 98 (2011) 141906. https://doi.org/10.1063/1.3574775.

[8] S.C. Mao, J.F. Luo, Z. Zhang, M.H. Wu, Y. Liu, X.D. Han, EBSD studies of the stress-induced B2-B19' martensitic transformation in NiTi tubes under uniaxial tension and compression, Acta Mater. 58 (2010) 3357-3366. https://doi.org/10.1016/j.actamat.2010.02.009.

[9] Y. Liu, Z. Xie, J.Van Humbeeck, L. Delaey, Effect of texture orientation on the martensite deformation of NiTi shape memory alloy sheet, Acta Mater. 47 (1999) 645-660. https://doi.org/10.1016/S1359-6454(98)00376-0.

[10] Y. Liu, Z. Xie, J.Van Humbeeck, L. Delaey, Some results on the detwinning process in NiTi shape memory alloys, Scr. Mater. 41 (1999) 1273-1281. https://doi.org/10.1016/S1359-6462(99)00299-7.

[11] O. Benafan, R.D. Noebe, S.A. Padula II, D.W. Brown, S. Vogel, R. Vaidyanathan, Thermomechanical cycling of a NiTi shape memory alloy-macroscopic response and microstructural evolution, Int. J. Plast. 56 (2014) 99-118. https://doi.org/10.1016/j.ijplas.2014.01.006.

[12] Z. Wang, J. Everaerts, E. Salvati, A.M. Korsusnky, Evolution of thermal and mechanical properties of Nitinol wire as a function of ageing treatment conditions, J. Alloys Compd. 819 (2020) 153024. https://doi.org/10.1016/j.jallcom.2019.153024.

[13] Z. Zheng, C. Hu, L. Cai, X. Chen, F. Jing, First-principles determination of the structure, elastic constant, phase diagram and thermodynamics of NiTi alloy, Physica B 405 (2010) 3665-3672. https://doi.org/10.1016/j.physb.2010.05.062.

[14] B. Ye, B.S. Majumadar, I. Dutta, Texture development and strain hysteresis in a NiTi shape-memory alloy during thermal cycling under load, Acta Mater. 57 (2009) 2403-2417. https://doi.org/10.1016/j.actamat.2009.01.032.

[15] C. Yu, B. Aoun, L. Cui, Y. Liu, H. Yang, X. Jiang, S. Cai, D. Jiang, Z. Liu, D.E. Brown, Y. Ren, Synchrotron high energy X-ray diffraction study of microstructure evolution of severely cold drawn NiTi wire during annealing, Acta Mater. 115 (2016) 35-44. https://doi.org/10.1016/j.actamat.2016.05.039.

[16] P. Sedmak, P. Sittner, J. Pilch, C. Curfs, Instability of cyclic superelastic deformation of NiTi investigated by synchrotron X-ray diffraction, Acta Mater. 94 (2015) 257-270. https://doi.org/10.1016/j.actamat.2015.04.039.

[17] R. Kocich, L. Szurman, M. Kursa, The methods of preparation of Ti-Ni-X alloys and their forming, Shape Memory Alloys-Processing, Characterization and Applications, Croatia: InTech, pp.27-52. http://dx.doi.org/10.5772/50067.

[18] G. Laplanche, T. Birk, S. Schneider, J. Frenzel, G. Eggler, Effect of temperature and texture on the reorientation of martensite variants in NiTi shape memory alloys, Acta Mater. 127 (2017) 143-152. https://doi.org/10.1016/j.actamat.2017.01.023.

[19] O. Benafan, R.D. Noebe, S.A. Padual II, A. Garg, B. Clausen, S. Vogel, Temperature dependent deformation of the B2 austenite phase of a NiTi shape memory alloy, Int. J. Plast. 51 (2013) 103-121. https://doi.org/10.1016/j.ijplas.2013.06.003.

[20] E.S. Statnik, A.I. Salimon, C. Besnard, J. Chen, Z. Wang, T. Moxham, I.P. Dolbnya, A.M. Korsunsky, Ovine Bone Morphology and Deformation Analysis Using Synchrotron X-ray Imaging and Scattering, Quantum Beam Sci. 4 (2020) 29. https://doi.org/10.3390/qubs4030029.

[21] F. Uzun, A.I. Salimon, E.S. Statnik, C. Besnard, J. Chen, T. Moxham, Z. Wang, A.M. Korsunsky, Polar transformation of 2D X-ray diffraction patterns and the experimental validation of the hDIC technique, Measurement 151 (2020) 107193. https://doi.org/10.1016/j.measurement.2019.107193.

[22] L. Kuncicka, R. Kocich, Deformation behaviour of Cu-Al clad composites produced by rotary swaging, IOP Conf. Ser. Mater. Sci. Eng. 369 (2018) 012029. https://doi.org/10.1088/1757-899X/369/1/012029.

[23] R. Kocich, M. Kursa, I. Szurman, A. Dlouhy, The influence of imposed strain on the development of microstructure and transformation characteristics of Ni-Ti shape memory alloys, J. Alloys Compd. 509 (2011) 2716-2722. https://doi.org/10.1016/j.jallcom.2010.12.003.

[24] R. Kocich, L. Kuncicka, P. Kral, P. Strunz, Characterization of innovative rotary swaged Cu-Al clad composite wire conductors, Mater. Des. 160 (2018) 828–835. https://doi.org/10.1016/j.matdes.2018.10.027.

[25] R. Kocich, L. Kuncicka, D. Dohnalik, A. Machackova, M. Sofer, Cold rotary swaging of a tungsten heavy alloy: Numerical and experimental investigations, Int. J. Refract. Met. Hard Mater. 61 (2016) 264–272. https://doi.org/10.1016/j.ijrmhm.2016.10.005.

[26] J.R. Santisteban, M.R. Daymond, J.A. James, L. Edwards, ENGIN-X: a third-generation neutron strain scanner, J. Appl. Cryst. 39 (2006) 812-825. https://doi.org/10.1107/S0021889806042245.

[27] F. Uzun, C. Papadaki, Z. Wang, A.M. Korsunsky, Neutron strain scanning for experimental validation of the artificial intelligence based eigenstrain contour method, Mech. Mater. 143 (2020) 103316. https://doi.org/10.1016/j.mechmat.2020.103316.

[28] H.M. Rietveld, A profile refinement method for nuclear and magnetic structures, J. Appl. Cryst. 2 (1969) 65-71. https://doi.org/10.1107/S0021889869006558.

[29] A.C. Larson, R.B. Von Dreele, General structure analysis system, Los Alamos National Laboratory Report LAUR (1994) 86-748. https://personal.ems.psu.edu/~ryba/coursework/Advanced%20Powder%20Diffraction/GSASManual.pdf.

[30] H. Sitepu, Texture and structural refinement using neutron diffraction data from molybdite (MoO3) and calcite (CaCO3) powders and a Ni-rich Ni50.7Ti49.3 alloy, Powder Diffr. 24 (2009) 315-326. https://doi.org/10.1154/1.3257906.

[31] N. Hatcher, O.Y. Kontsevoi, A.J. Freeman, Role of elastic and shear stabilities in the martensitic transformation path of NiTi, Phys. Rev. B 80 (2009) 144203. https://doi.org/10.1103/PhysRevB.80.144203.

[32] E. Oliver, J. Santisteban, J. James, M. Daymond, J. Dann, ENGIN-X user manual, isis.stfc.ac.uk (2004). https://www.isis.stfc.ac.uk/Pages/engin-x-manual6870.pdf.

[33] Z. Wang, J. Chen, C. Besnard, A.M. Korsunsky, Microstructure evolution in a severely cold-worked NiTi wire during ageing treatment: An in situ neutron diffraction study, Mater. Lett. 281 (2020) 128676. https://doi.org/10.1016/j.matlet.2020.128676.

[34] F. Bachmann, R. Hielscher, H. Schaeben, Texture analysis with MTEX-Free and open source software toolbox, Solid State Phenom. 160 (2010) 63-68. https://doi.org/10.4028/www.scientific.net/SSP.160.63.

[35] Y. Zhao, J. Zhang, Microstrain and grain-size analysis from diffraction peak width and graphical derivation of high-pressure thermomechanics, J. Appl. Cryst. 41 (2008) 1095-1108. http://dx.doi.org/10.1107/S0021889808031762.

[36] T. Ungar, I. Dragomir, A. Revesz, A. Borbely, The contrast factors of dislocations in cubic crystals: the dislocation model of strain anisotropy in practice, J. Appl. Cryst. 32 (1999) 992-1002. https://doi.org/10.1107/S0021889899009334.

[37] S. Qiu, V.B. Krishnan, S.A. Padula, R.D. Noebe, D.W. Brown, B. Clausen, R. Vaidyanathan, Measurement of the lattice plane strain and phase fraction evolution during heating and cooling in shape memory NiTi, Appl. Phys. Lett. 95 (2009) 141906. https://doi.org/10.1063/1.3245308.

[38] J.F. Nye, Physical properties of crystals, Oxford: Clarendon Press (1985).

[39] Y. Liu, Z. Xie, J.Van Humbeeck, L. Delaey, Some results on the detwinning process in NiTi shape memory alloys, Scr. Mater. 41 (1999) 1273-1281. https://doi.org/10.1016/S1359-6462(99)00299-7.

[40] S. Rajagopalan, A.L. Little, M.A.M. Bourke, R. Vaidyanathan, Elastic modulus of shape-memory NiTi from in situ neutron diffraction during macroscopic loading, instrumented indentation, and extensometry, Appl. Phys. Lett. 86 (2005) 081901. https://doi.org/10.1063/1.1863437.

[41] B. Clausen, C.N. Tome, D.W. Brown, S.R. Agnew, Reorientation and stress relaxation due to twinning: Modeling and experimental characterization for Mg, Acta Mater. 56 (2008) 2456-2468.

[42] P. Chowdhury, H. Sehitoglu, Deformation physics of shape memory alloys – Fundamentals at atomistic frontier, Prog. Mater. Sci. 88 (2017) 49-88. https://doi.org/10.1016/j.pmatsci.2017.03.003.

[43] Y. Liu, Z. Xie, Detwinning in shape memory alloy, in: P.L. Reece, Progress in Smart Materials and Structures 3, Nova Science Publishers Inc., 2007, pp. 29-65.

[44] S. Cai, J.E. Schaffer, Y. Ren, C. Yu, Texture evolution during nitinol martensite detwinning and phase transformation, Appl. Phys. Lett. 103 (2013) 241909. https://doi.org/10.1063/1.4846495.

[45] K. Gall, H. Sehitoglu, Y.I. Chumlyakov, I.V. Kireeva, Tension-compression asymmetry of the stress-strain response in aged single crystal and polycrystalline NiTi, Acta Mater. 47 (1999) 1203-1217. https://doi.org/10.1016/S1359-6454(98)00432-7.

[46] O. Matsumoto, S. Miyazaki, K. Otsuka, H. Tamura, Crystallography of martensitic transformation in Ti-Ni single crystals, Acta Metall. 35 (1987) 2137-2144. https://doi.org/10.1016/0001-6160(87)90042-3.

[47] Q.S. Zheng, Y. Liu, Prediction of the detwinning anisotropy in textured NiTi shape memory alloy, Philos. Mag A 82 (2002) 665-683. https://doi.org/10.1080/01418610208243195.

[48] C. Yu, G. Kang, Q. Kan, Crystal plasticity based constitutive model of NiTi shape memory alloy considering different mechanisms of inelastic deformation, Int. J. Plast. 54 (2014) 132-162. https://doi.org/10.1016/j.ijplas.2013.08.012.

[49] K. Gall, T.J. Lim, D.L. McDowell, H. Sehitoglu, Y.I. Chumlyakov, The role of intergranular constraint on the stress-induced martensitic transformation in textured polycrystalline NiTi, Int. J. Plast. 16 (2000) 1189-1214. https://doi.org/10.1016/S0749-6419(00)00007-3.

Chapter 7

ACS APPLIED MATERIALS & INTERFACES

www.acsami.org Research Article

Grain Structure Engineering of NiTi Shape Memory Alloys by Intensive Plastic Deformation

Zifan Wang[a,*], Jingwei Chen[a], Radim Kocich[b], Samuel Tardif[c,d], Igor P. Dolbnya[e], Lenka Kunčická[b], Jean-Sébastien Micha[c,d], Konstantinos Liogas[a], Oxana V. Magdysyuk[e], Ivo Szurman[f], Alexander M. Korsunsky[a,*]

[a] *MBLEM, Department of Engineering Science, University of Oxford, Oxford OX1 3PJ, U.K.*

[b] *Faculty of Mechanical Engineering, Brno University of Technology, Technická 2896/2, Brno 61669, Czech Republic*

[c] *Université Grenoble Alpes, CEA-Grenoble/IRIG, 38043 Grenoble Cedex 9, France*

[d] *CRG-IF BM32 Beamline, European Synchrotron Radiation Facility, 38043 Grenoble Cedex 9, France*

[e] *Diamond Light Source, Harwell Campus, Oxfordshire, OX11 0DE, U.K.*

[f] *Faculty of Materials Science and Technology, VŠB-Technical University of Ostrava, Ostrava 8, Czech Republic*

*Corresponding author.

Abstract

To explore an effective route of customising the Superelasticity (SE) of NiTi Shape Memory Alloys via modifying the grain structure, binary $Ni_{55}Ti_{45}$ (wt.%) alloys were fabricated in As Cast, Hot Swaged and Hot Rolled conditions, presenting contrasting

grain sizes and grain boundary types. *In situ* synchrotron X-ray Laue micro-diffraction and *in situ* synchrotron X-ray powder diffraction techniques have been employed to unravel the underlying grain structure mechanisms that causes the diversity of SE performance among the three materials. Evolution of lattice rotation, strain field and phase transformation has been revealed at micro- and mesoscale, and the effect of grain structure on SE performance has been quantified. It was found that (i) The Ni_4Ti_3 and $NiTi_2$ precipitate is similar among the three materials in terms of morphology, size, and orientation distribution; (ii) phase transformation happens preferentially near High Angle Grain Boundaries (HAGBs), yet randomly in Low Angle Grain Boundaries (LAGBs) structure; (iii) the smaller the grain size, the higher the phase transformation nucleation kinetics, and the lower the propagation kinetics; (iv) stress concentration happens near HAGBs while no obvious stress concentration can be observed in LAGB grain structure during loading; (v) the statistical strain distribution of the three materials becomes asymmetric during loading; (vi) three grain lattice rotation modes are identified and termed for the first time, namely multi-extension rotation, rigid rotation and non-dispersive rotation; (vii) texture evolution of B2 austenite and B19' martensite is not strongly dependent on the grain structure.

Keywords:

Bespoke NiTi Shape Memory Alloys, Grain structure, Multiscale, Lattice rotation, Phase transformation, Laue micro-diffraction, Powder diffraction

1. Introduction and objectives

Shape Memory Alloys (SMAs) is probably the most important category of Shape Memory Materials. In recent years, the utilisation of SMAs has been extended to cutting-

edge engineering applications, including but not limited to, medical devices, actuators, micromechanical systems, deployable structures, and elastocaloric devices [1]. Among the three prevalent SMA systems, viz NiTi-based, Cu-based, and Fe-based, the binary NiTi alloy is always preferred in engineering applications because of its excellent functional performance and bio-compatibility [2].

Two extensively utilised functional behaviour of NiTi alloy are Shape Memory Effect (SME) and Superelasticity (SE). SME is commonly used in actuators and deployable structures, while SE has more application fields, the most popular ones being medical stents and elastocaloric cooling systems. The latter falls within the focus of the present study. To induce SE, the material operation temperature should be kept above the critical temperature at which the major phase is austenite. When stress is applied, cubic austenite transforms to monoclinic martensite in an non-diffusive way, thus pseudo-plastically accommodating the deformation. After stress is withdrawn, reverse phase transformation occurs so that the component recovers to its original shape.

A critical challenge about NiTi alloy that is awaiting to be resolved is to find a reliable method to customise its SE performance for different application scenarios. For instance, the phase transformation stress needs to be as low as possible in elastocaloric cooling device, and to be at a moderate level in medical stents. When used in orthodontics, a gradually increased phase transformation stress during deformation is required so that the component acts like a spring, while in medical stent, a stress plateau would be favoured to apply constant pressure to the vascular wall. In reality, numerous studies have found that this stress-induced phase transformation process can be affected by many crystallographic factors: grain size [3], texture [1,4], composition ratio [5], dislocation density [1,6], tertiary element [7], and precipitation [8]. Furthermore, thermomechanical

processing history can also be influential, namely fabrication methods [7,9] and heat treatment [8,10].

The aforementioned studies and others not reported here seem to fail to explore the effect of grain structure and the possibility of customising the SE through via grain structure engineering. Besides that, most studies were based on *ex situ* rather than *in situ* experiment, so that the underlying mechanisms of how these factors influence SE performance were somewhat superficially investigated. Grain structure describes the overall properties of grains: grain boundary type, morphology and size. Grain boundary type can be classified into two categories, viz high angle grain boundary (HAGB) and low angle grain boundary (LAGB).

In situ synchrotron X-ray Laue micro-diffraction (μLaue) may be the most advantageous technique in probing the microscale evolution of microstructure at the scale of a few thousand microns with a typical resolution of one micron. White X-ray beam is focused to a size of less than one micron, illuminating a volume depth of approximately ten microns in individual crystallite, thus the diffraction pattern contains valuable crystallographic information, namely crystal orientation, micro defects and local elastic strain. Due to the simplicity of the setup, a great flexibility can be offered to the use of sample environment equipment, such as heating stage and loading rig. It has to be pointed out that, though μLaue has always been compared with HR-EBSD which can provide similar crystallographic information, the former is undoubtedly superior [11]: the elastic strain resolution of μLaue is 10^{-5} while that of HR-EBSD is 10^{-4}, the orientation resolution of μLaue is <0.01 degree while that of HR-EBSD is ~0.01 degree, the sample environment of μLaue can be of any type while HR-EBSD must be in the vacuum, most importantly, the penetration depth of μLaue is tens of microns while that of HR-EBSD is

merely a few nanometres, therefore μLaue provides much more representative information of the probed bulky crystal.

In situ synchrotron X-ray powder diffraction (HE-XRD) has been universally acknowledged to be one of the most advanced techniques in probing the evolution of mesoscale microstructure. The diffraction pattern contains crystallographic information including texture, phase volume fraction, elastic strain, micro defects and lattice d-spacing. The superiority of this technique has been elucidated in numerous studies, details refer to [12].

Having identified the significance of customising SE performance in NiTi SMA and the boundary of existing studies, the objective of this work is to bespoke SE in NiTi SMA via grain structure engineering, namely the modification of grain boundary type and grain size. NiTi samples of different grain sizes were fabricated via two processing routes: As Cast (AC) and Hot Swaging (HS). The grain boundary type of these two samples is dominated by HAGB. The other NiTi sample was manufactured by Hot Rolling (HR), of which the majority of grain boundaries are LAGBs, and very few HAGBs can be observed. These three NiTi SMAs exhibit diverse SE performance, during which *in situ* synchrotron X-ray Laue micro-diffraction and *in situ* synchrotron X-ray powder diffraction techniques were employed to unravel the underlying grain structure mechanisms. Multiscale lattice rotation, strain field, and phase transformation behaviour of different grain structures were quantified, and the effect of grain structure on SE performance has been evaluated. Other supplementary probing and simulation techniques were also employed to support the findings, including DSC, FIB-SEM, TEM, EBSD and CPFE.

The significance of present study being probably the first ever theoretical and practical guidance that opens up new possibilities to customise the Superelasticity of NiTi

Shape Memory Alloys by means of grain structure engineering, thereby vastly broadening the application scenarios in deployable structures which require precise control of reaction force of the Superelasticity.

2. Experimental and analytical details

2.1 Material processing methodology

Nickel cubes of 99.99% purity and Grade 2 titanium of >99.3% purity were used as raw material. A polycrystalline $Ni_{55}Ti_{45}$ wt.% ingot was cast in an iso-statically pressed graphite crucible via vacuum induction melting (VIM) under 99.9999% purity Argon protection at 150 Mbar.

The as cast ingot was split into three pieces. The first one remained as cast (AC) state. The second piece was subjected to hot rotary swaging (HS) at 950°C using the self-developed KOMAFU S600 system [13,14], details on this manufacturing technique refer to [1,15,16]. The last piece was subjected to hot rolling (HR) at 950°C, details refer to [2,9]. Manufacturing details for grain structure engineering are elucidated in Appendix A.

All three pieces were cut into flat dog-bone shaped samples using electrical discharge machining (EDM), and heat treated at 900°C for 4 hours in a vacuum furnace to minimize the amount of lattice defects and to produce well-crystallized microstructure. Immediately after heat treatment, all samples were water-quenched to room temperature. Two samples from each sample states, namely AC, HS and HR, were used in two different *in situ* experiments. Since the two samples were originally one piece and separated by EDM, they are considered as possessing identical material properties.

2.2 Differential Scanning Calorimetry analysis

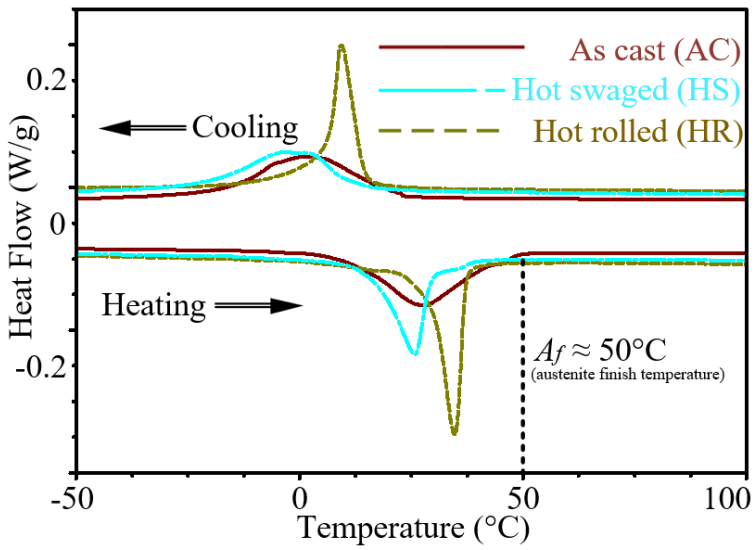


Figure 1. DSC measurement of critical temperatures for thermally induced phase transformation in AC, HS and HR NiTi.

To ensure the samples containing maximal fraction of B2 austenite phase prior to superelastic deformation, austenite finish temperatures of the three sample states were measured by a TA DSC Q2000 instrument. The measurements were performed between -90°C to 200°C with ramp rate of ±5°C/min. Results are shown in Fig.1. All materials possess the austenite finish temperature (A_f) at approx. 50°C, above which the materials contain the maximal fraction of B2 austenite phase. Detailed explanations of A_f as well as other critical phase transformation temperatures of NiTi alloys refer to [8]. Judging from that, for all the three NiTi materials, the *in situ* superelastic loading experiments were conducted at 50°C.

2.3 Microscopy characterization

To investigate the microstructural effect of material processing method and to identify suitable mapping area for *in situ* Laue micro-diffraction, electron backscatter diffraction (EBSD) observations were conducted in a Tescan LYRA3 FIB/SEM system

integrated with SYMMETRY EBSD detector from Oxford Instruments. Samples were finely polished by gradually decreasing the size of diamond particle suspension from 9µm to 0.25µm colloidal silica. Kikuchi pattern indexing was carried out at an accelerating voltage of 20kV, a working distance of 9mm, a step size of 0.5µm, and an acquisition speed of 5Hz.

Transmission electron microscopy (TEM) lamellae of thickness ~120nm were prepared by a refined lift-out technique [17] in the above mentioned LYRA3 system. Observations were carried out at ePSIC at Diamond Light Source, using a JEOL ARM200CF system at 200kV. Composition ratios of precipitates and matrix were quantified by TEM-EDX technique by focusing at precipitation region and matrix region in the elemental map.

2.4 *In situ* synchrotron X-ray Laue micro-diffraction (µLaue)

In situ µLaue experiments were performed at two synchrotron facilities. At CRG-IF BM32 beamline at ESRF [18], a polychromatic X-ray beam with an energy range of 5-25keV was focused by a set of Kirkpatrick-Baez (KB) mirrors to a typical size <0.8µm. At B16 test beamline at DLS [19], the white beam with an energy range of 8-30keV was collimated to a size of ~5-10µm, using a nearly identical experimental setup as illustrated in Fig.2(a).

The flat dog-bone shaped samples were clamped on a 5kN DEBEN tensile rig integrated with a heating stage to maintain the sample temperature at 50°C. An extensometer was also attached to the sample. The rig was mounted in such a way that the sample surface was 45° relative to the incident focused beam. The centre position of the 2D X-ray large-area CCD detector (ImageStar 9000, Photonic Science Ltd.) was aligned at a 2θ position of ~90°, and the distance between detector and sample was

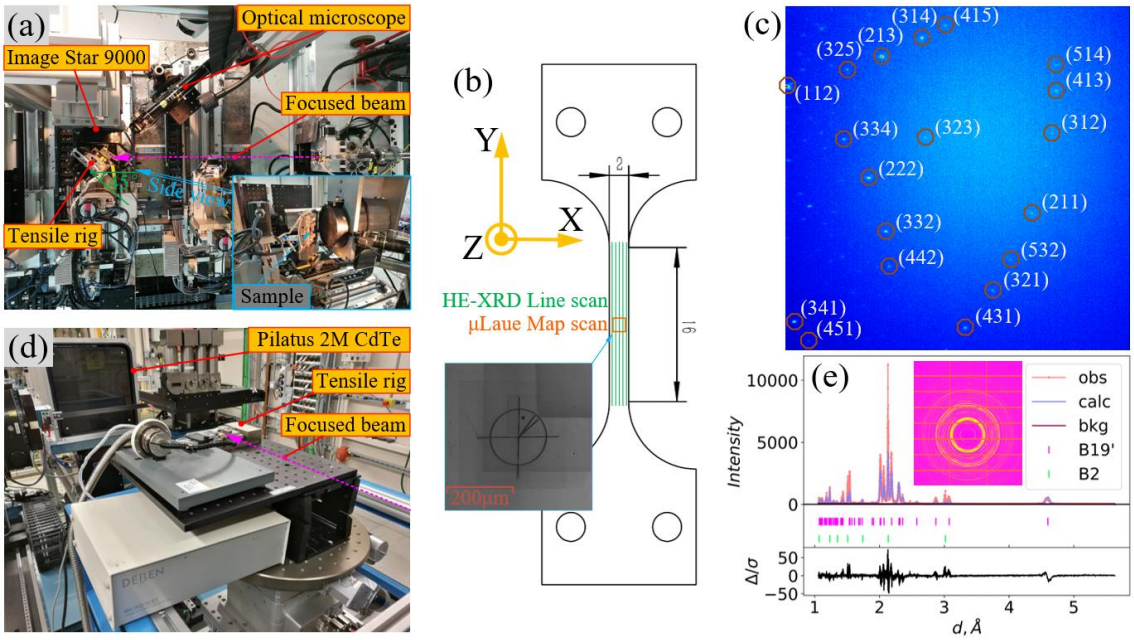


Figure 2. (a) Experimental setup for *in situ* synchrotron X-ray Laue micro-diffraction (μLaue). (b) Sample geometry (Unit: mm). Laue micro-diffraction map scan is indicated by a FIB marker at the corner, overlapping with EBSD map. HE-XRD line scan covers the whole gauge length of the sample. (c) A typical indexed Laue micro-diffraction pattern for NiTi B2 austenite phase. (d) Experimental setup for *in situ* synchrotron high energy X-ray powder diffraction (HE-XRD). (e) An example of integrated HE-XRD pattern, both B2 austenite and B19' martensite have been identified and refined via Rietveld method.

bringing as close as 60mm to capture maximal number of Laue diffraction spots. The optical microscope was fixed, whose sight coincided with the incident beam. A single crystal Germanium of orientation 111 was used for precise detector geometry calibration.

Prior to the experiments, designated surface region was selected from corresponding EBSD maps and marked with a "cross-circle" sign at the square region corner as shown in Fig.2(b). The sign was readily observable under the optical microscope, therefore being

used as a reference to assure the same *in situ* μLaue map scan area during incremental tensile loading levels.

Since the beam size is significantly smaller than the grain size observed from EBSD, only one grain was illuminated in vast majority of the scanning points. A representative μLaue diffraction pattern for body-centred cubic NiTi B2 austenite phase is shown in Fig.2(c), indexed using LaueTools software [20]. Upon further refinement of the indexed diffraction spots, all 6 components of deviatoric elastic strain tensor and 3 Euler angles of crystallographic orientation can be determined with superior accuracy [18]. As an initial input to LaueTools, the lattice parameters for cubic B2 phase of undeformed virgin state were determined by Rietveld refinement of Time-Of-Flight neutron diffraction spectrum in our previous work [1,21]. Visualization of μLaue maps was achieved by MTEX package [22].

2.5 *In situ* synchrotron high energy X-ray powder diffraction (HE-XRD)

In situ HE-XRD measurements were carried out at I12 JEEP beamline at DLS [12,21]. The same tensile rig was used, which has been described in section 2.4. The setup is illustrated in Fig.2(d). Monochromatic beam energy was set to 85 keV with a spot size of 200μm×200μm. At each loading step of tensile deformation, large area scan was conducted covering the central volume of the samples, shown in Fig.2(b), 5 line scans contain 72 scanning points each. Debye-Scherrer patterns were recorded by a large 2D area diffraction detector Pilatus 2M CdTe (1475×1679pixel, pixel size 172μm×172μm). Based on the setup calibration from Data Analysis WorkbeNch (DAWN) platform, the Rietveld analysis was performed using GSAS II [23]. An example of diffraction pattern and its refinement is shown in Fig.2(e), showing the decent identification of both B19'

martensite and B2 austenite phases of NiTi shape memory alloy. The texture of both phases was precisely quantified by the analysis routine in [21].

3. Results and discussion

3.1 Precipitation

During heat treatment, remarkable precipitation activities take place in as cast (AC), hot rotary swaged (HS) and hot rolled (HR) NiTi materials. It can be observed from FIB-SEM imaging that precipitation is very similar among the three materials in terms of type, size and orientation, as shown in Fig.3(a)(b)(c) for AC, HS and HR respectively. From TEM-EDX analysis of Ni-Ti composition ratio in Fig.3(d)(e) for AC and HS NiTi respectively, it can be confirmed that lenticular shape structures are Ni_4Ti_3 precipitates, whilst the round shape ones are $NiTi_2$ precipitates randomly embedded in the matrix and in the Ni_4Ti_3. Fig.3(f) and Fig.3(g) demonstrate the X-ray intensity distribution in TEM-EDX elemental mapping of Ni and Ti respectively. Due to the stress-free heat treatment condition, three orientations of Ni_4Ti_3 are homogeneously distributed, whose length ranges from 2 to 10μm and aspect ratio around 10:1, which agrees well with previous studies [8]. From the observations, it can be concluded and assumed that precipitation is similar among the three NiTi materials in terms of precipitate type, fraction, shape, size, and spatial distribution. Therefore it is not considered as a factor that causes the difference in superelastic tensile loading behaviour.

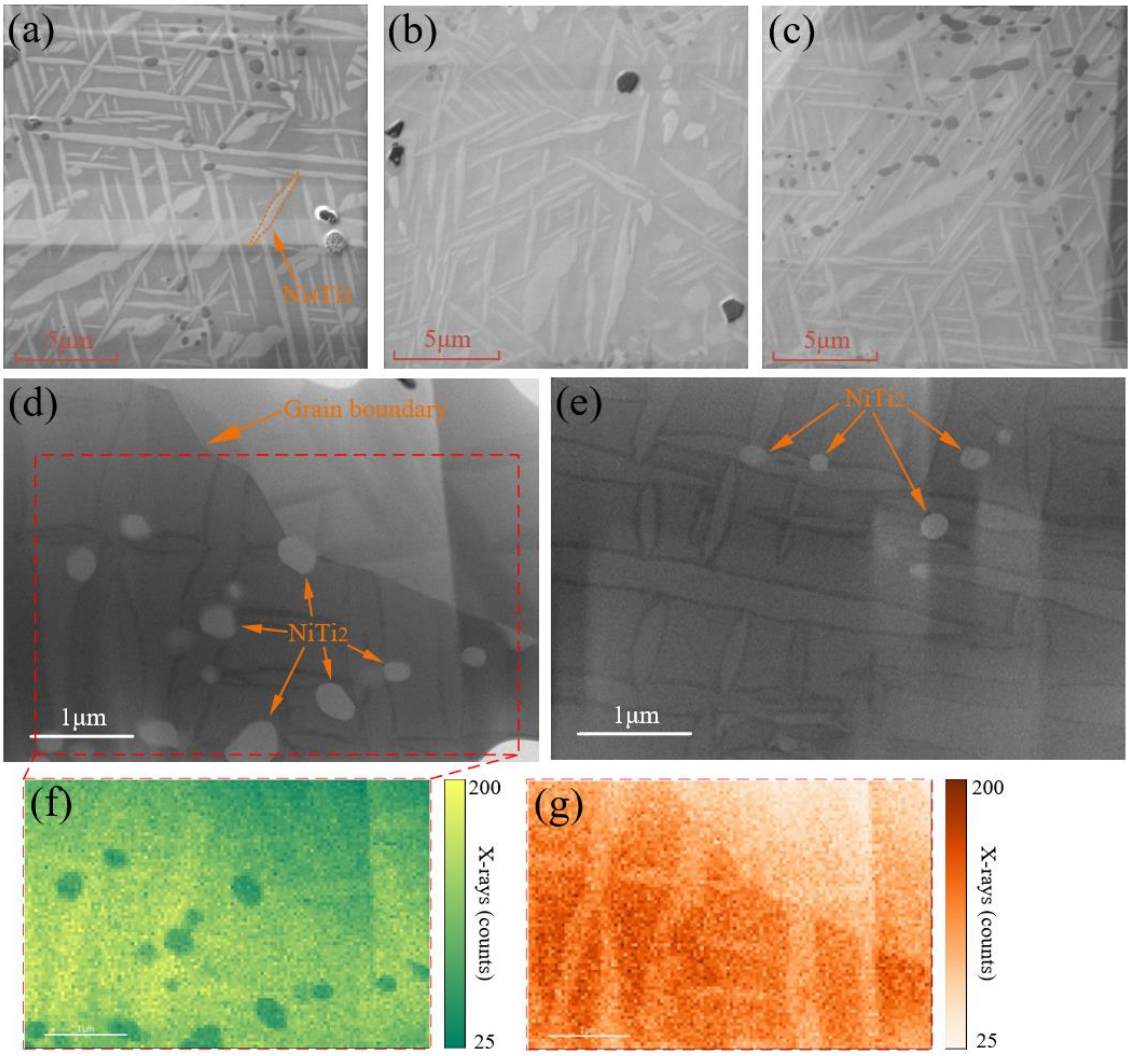


Figure 3. FIB-SEM imaging of precipitation in (a) AC, (b) HS, (c) HR NiTi. TEM imaging of precipitation in (d) AC and (e) HS NiTi, <100> lattice direction is perpendicular to the surface. TEM-EDX elemental mapping of Ni (f) and Ti (g) in the dash line area in (d). Signal intensity of Ni Ka at 7.48 keV and Ti Ka at 4.51 keV are shown here. Precipitation types are identified and tagged.

3.2 Superelastic stress-strain response

The superelastic tensile loading behaviour of the three materials are shown in Fig.4. Strain level is defined by $\Delta L/L$, ΔL refers to extension measured by the extensometer,

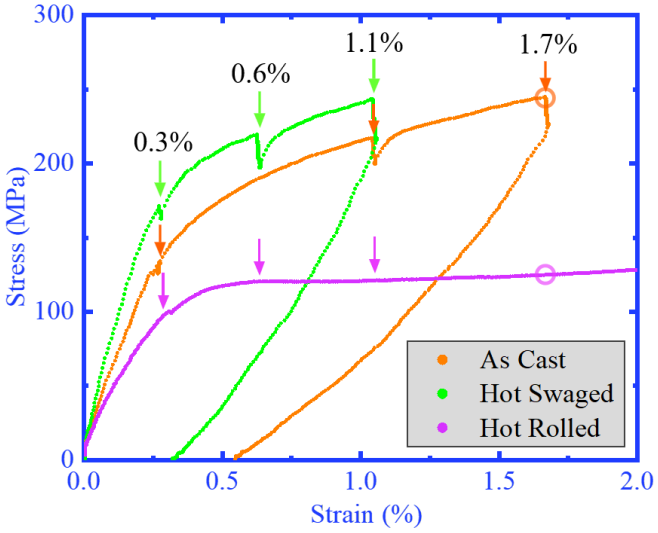


Figure 4. Superelastic stress-strain response during tensile loading. The strain levels at which *in situ* µLaue scan was conducted were denoted by arrows, and position of the *in situ* HE-XRD scans are denoted by hollow circles. The AC and HS curves were recorded during *in situ* µLaue experiment so that there is an obvious stress-relaxation at each scanning point, whilst the HR curve was recorded during *in situ* HE-XRD experiment without any visible stress drops thanks to the short acquisition time.

and L is the original length of the sample. Although the strain level at which major phase transformation activity was triggered was almost the same value at around 0.3~0.4% for all three materials, the stress level is a huge difference: HS NiTi has the largest phase transformation stress of nearly 200 MPa, followed by AC NiTi at ~150MPa, and HR NiTi is merely ~110MPa. It is worth mentioning that cold-drawn NiTi wires with nano-crystallites possess a phase transformation stress level as high as 350MPa [8]. In addition, AC and HS NiTi exhibit incremental stress level during superelasticity, while the HR NiTi shows a flat stress plateau. The cause of such diverse superelasticity is mainly due to the phase transformation kinetics, which is further discussed in Section 3.4.

3.3 Grain structure: EBSD – µLaue comparison

The EBSD maps of AC, HS and HR NiTi are of the same size of exact 1000µm length square, as displayed in the upper row of Fig.5(a)(b)(c), whilst the µLaue maps are displayed in the lower row. Inverse pole figures (IPF) of three sample coordinate directions X, Y and Z, as defined in Fig.2(b), are arrayed from left to right.

Due to the visibility of FIB marker in both SEM and optical microscope, EBSD and Laue map are conducted at precisely the same area, one of which overlaps the another, depending on the grain size observed from EBSD map.

Both AC and HS NiTi have clearly identified grain structures: each grain is separated from its neighbours by high-angle grain boundaries (HAGB). Despite the inhomogeneous distribution of grain size in both materials, the average grain size of AC NiTi is quantified as ~400µm, while that of HS NiTi is much smaller at ~220µm. The comparison of IPF maps between EBSD and µLaue indicates excellent orientation matches in all three directions, implying the correctness of the indexation of µLaue diffraction patterns, though disagreement may be observed at regions where small grains crowded together. These disagreements are mainly attributed to the difference of several orders of magnitude in penetration depth between EBSD and µLaue: EBSD map is generated within a small interaction volume at the sample surface with a typical depth of 10-50nm [24], by contrast, the energy of synchrotron X-ray beam for µLaue allows a probing depth of 15-20µm under the surface, very likely to illuminate another grain under the surface other than the one shown in the EBSD map.

HR NiTi material possesses a smoothly-changing grain structure with few HAGB. Instead, low-angle grain boundary (LAGB) is more prevailing, which has been outlined by the thin black lines in EBSD map. These thin lines rarely form a close loop. To some degree, the grain structure of HR NiTi can be regarded as a colossal grain, within which

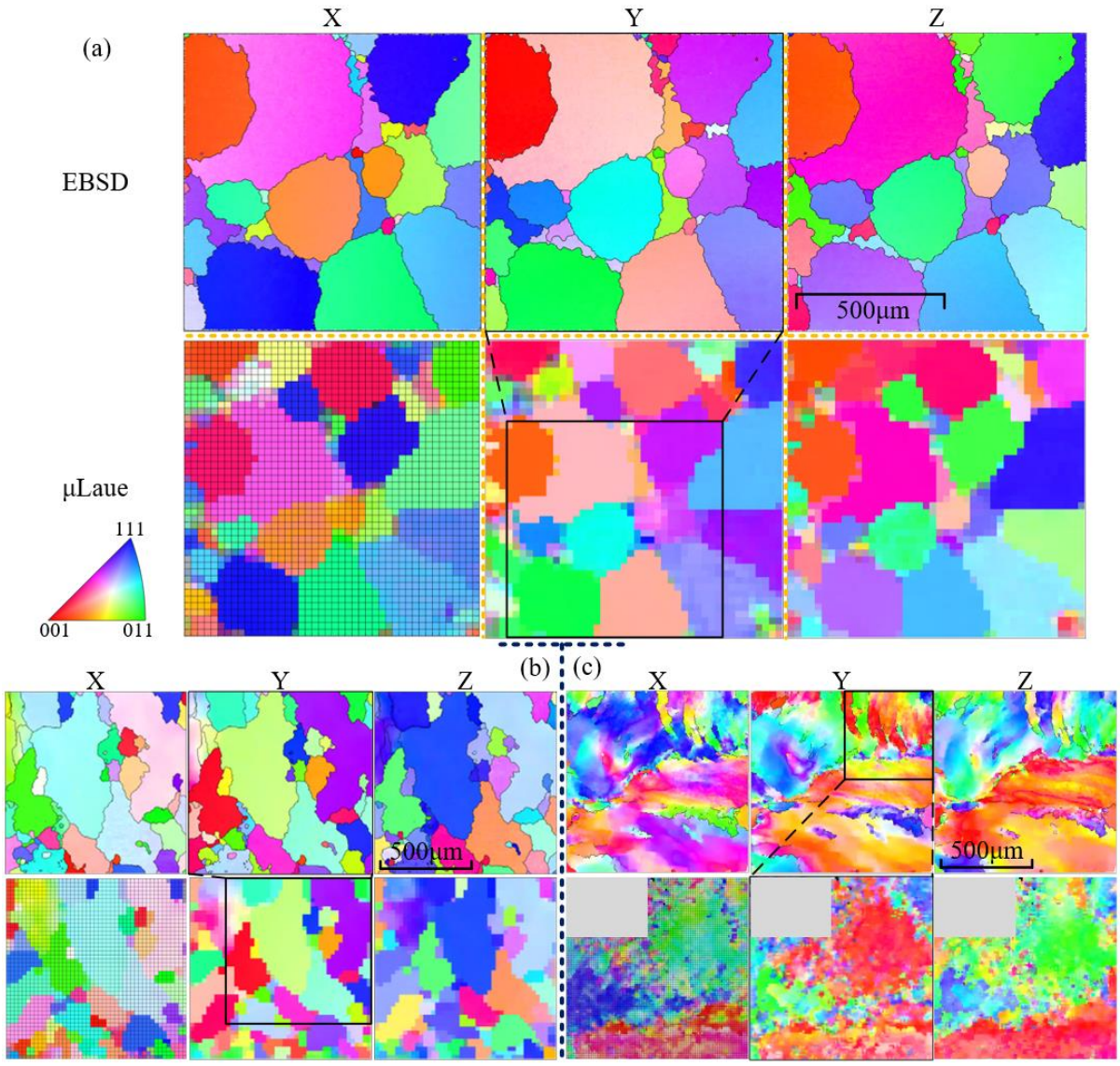


Figure 5. EBSD - µLaue lattice orientation map comparison of (a) AC, (b) HS and (c) HR NiTi. The grid in X-direction µLaue map indicates the positions of scanning points (pixel sizes): 44×44, 45×45, 101×101 for AC, HS and HR respectively. Each grid is a scanning point. The step sizes are: 30µm, 30µm and 5µm for AC, HS and HR respectively. The black box in the Y-direction µLaue map indicates the region of EBSD map in (a) and (b), vice versa in (c) as µLaue map is smaller due to the complexity in grain structure. The grey area in (c) is an non-indexed area due to unknown detector error during experiment.

sub-grain regions possessing different orientations are separated by LAGB. Because of this peculiarity of grain structure and the difference in probing depth, the μLaue map mismatches EBSD map in fine details, however, the orientations (colour) obtained from the two techniques show a close match from a general point of view.

3.4 Charting phase transformation morphology

The evolution of μLaue lattice orientation maps of AC, HS, HR NiTi during superelastic loading is shown in Fig.6, the strain levels at which the maps were acquired are indicated by arrows in Fig.4.

Before tensile loading, μLaue map of all three samples has nearly 100% indexation rate for B2 austenite phase. With the increment of strain levels, the indexation rate drops, leaving some blank area in the map, which is concluded to be closely linked to the formation of large amount of stress-induced martensite phase [25]. However, due to the intrinsic feature of μLaue technique that the diffraction pattern has to be originated from a single crystal illuminated by X-ray, having more than one crystal structure causes misinterpretation in the indexation process. Considering the fact that multiple martensitic variants [26] could emerge during stress-induced phase transformation, and their relatively small volume (i.e. needle-like structure [27]) compared to the size of X-ray beam, these areas are left blank to avoid being indexed improperly.

During elastic loading from 0%-0.3% strain, a slight elongation of grain morphology along loading direction can be perceived on some colossal grains from AC NiTi (grain No.3&No.5), though not obvious on HS NiTi with smaller grain size. It can be easily observed from strain level 0.3% to 1.1%, that during superelastic loading, phase transformation happens preferentially at high angle grain boundaries (HAGB) in AC and HS NiTi, while for HR NiTi which features low angle grain boundaries (LAGB), phase

transformation happens randomly in certain regions but overall heterogenous. This phenomenon is attributed to the concentration of elastic strain near HAGB, as will be discussed later in Section 3.5. At 1.1% strain level, large fraction of all the three materials transforms to martensite. For AC and HS NiTi, phase transformation nucleates at HAGB and propagates to other area, and this nucleation-propagation process continuously happens throughout the deformation. For HR NiTi, the triggering of nucleation is slow, as at 0.3% strain, the indexation rate is still 100%. However, its propagation is much quicker, that a much larger proportion transforms to martensite at 1.1% strain. In all three materials, some grains/regions seem to be more rigid than others as they retain an untransformed state at high strain level, e.g. grain No.1-No.4 in AC NiTi.

The local colour within individual grains keep changing subtly throughout the loading process, indicating local lattice rotation, particularly on AC and HS NiTi, that local colour variations becomes significant at higher strain level in grains which originally have relatively homogenous colour distribution. This phenomenon can be clearly observed from grains No.1-No.6 in AC & HS NiTi. For instance, the No.3 grain in AC NiTi shows a homogeneous orange colour at 0% strain, upon loading small colour variation becomes obvious among grids, at 1.7% strain, the grid colour ranges from dark orange to light orange. While for HR NiTi, local lattice rotation happens in a more complete manner, viz. local colour gradually becomes consistent with its neighbouring regions, as demonstrated in the five regions marked by dashed squares. A quantitative analysis of individual grain lattice rotation is given in Section 3.6.

The fraction of martensite phase can be estimated from the ratio of non-indexed area to the whole area at each strain level, as shown in Fig.7(a). Since the martensite fraction obtained from μLaue map can be overestimated because of the residual austenite [28], a complementary measurement is conducted via HE-XRD to estimate the error range. The

nucleation and propagation kinetics of martensitic phase transformation can be quantified by a modified Johnson-Mehl-Avrami-Zifan equation proposed in [8]:

$$f = F \cdot \left(1 - e^{-k_0 \cdot e^{k_1 \cdot \varepsilon}}\right), \quad (1)$$

where F is the saturated maximal fraction of martensite, k_0 and k_1 are parameters representing nucleation and propagation kinetics. The least-square fitted values are listed in Table 1, and plotted in Fig.7(b) as a function of the reciprocal of average grain size. It is of great importance to note that the smaller the grain size, the higher the nucleation kinetics, the lower the propagation kinetics. Nucleation kinetics determines the rate of nucleation of phase transformation in an aggregate of grains, whilst propagation kinetics determines the rate of propagation of phase transformation in an individual grain. This insight well explains why excellent superelastic performance is always achieved in nano-crystalline NiTi materials. Namely, these materials have higher nucleation rate of new phase so as to accommodate the incremental strain level homogeneously throughout the whole piece (an aggregate of grains), rather than trying to propagate the new phase inside individual grains so that phase transformation takes place in a more inhomogeneous way. Because if phase transformation happens heterogeneously in the macroscale, those large austenite regions that are not transformed are more likely to be plasticly deformed. This conclusion is supported by the residual plastic strain of AC and HS NiTi after superelastic loading as shown in Fig.4: AC NiTi exhibits a residual strain of ~0.55% whilst that of HS NiTi is ~0.3%, which indicates that plastic deformation plays a bigger role in material with larger grain size.

On the other hand, higher propagation kinetics allows the material to accommodate the incremental strain level by pseudo-plastic phase transformation rather than by elastic

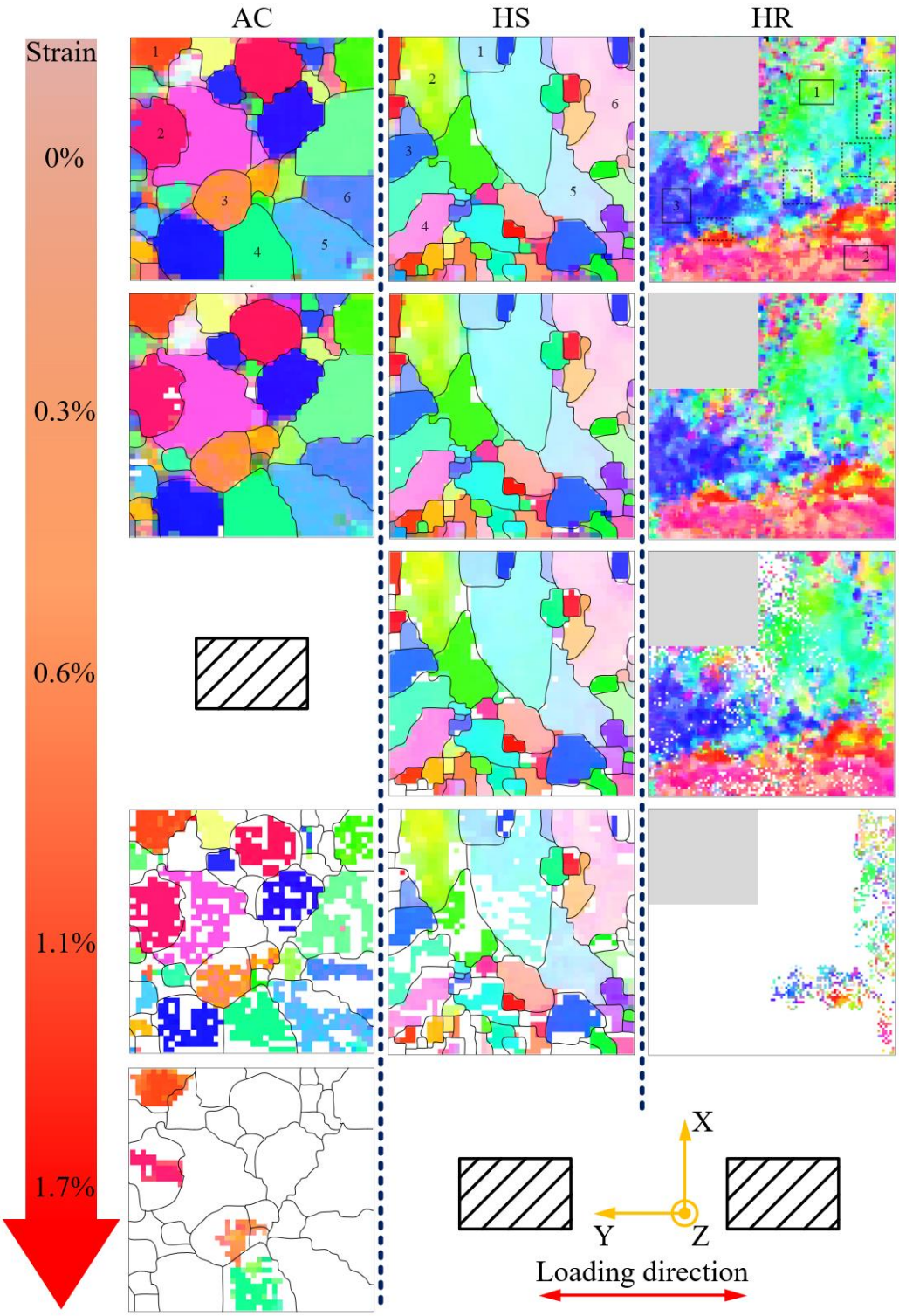


Figure 6. Evolution of μLaue orientation maps of AC, HS, HR NiTi from virgin state till 1.7% strain. Three maps are not available, one at 0.6% and two at 1.7% strain. Sample coordinate is displayed at the bottom: loading direction is parallel to Y axis. For demonstration of lattice rotation, 6 grains are numbered for AC & HS NiTi, and 8 regions are marked by dashed/solid squares for HR NiTi at 0% strain.

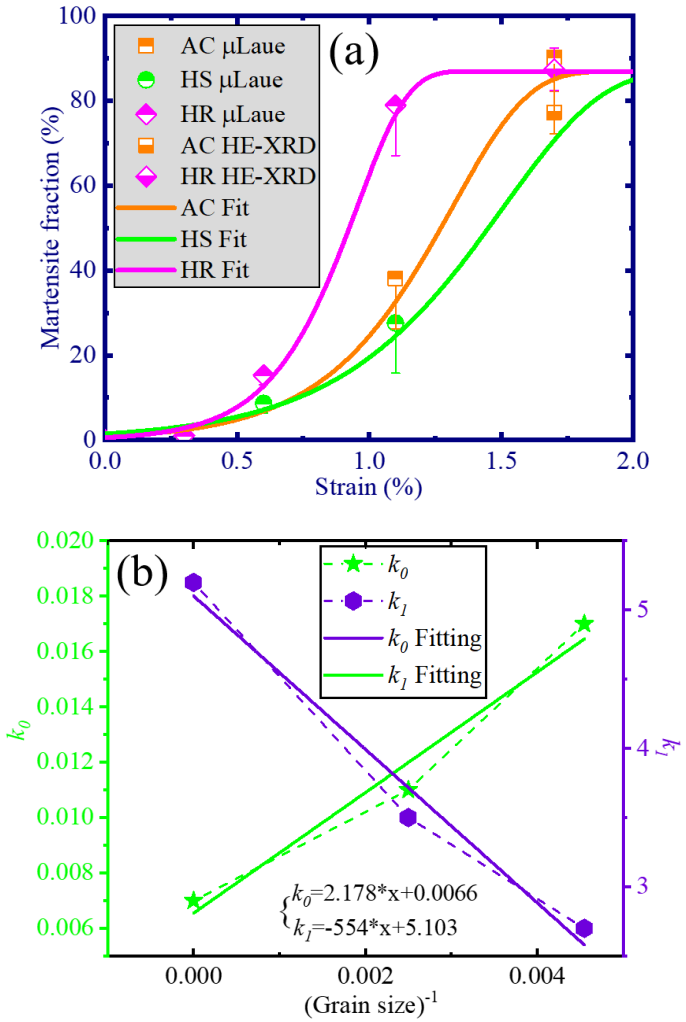


Figure 7. (a) Evolution of martensite fraction during loading. Error bar for μLaue is estimated by comparison to the phase fraction quantified by Rietveld method from *in situ* HE-XRD experiment. (b) Nucleation and propagation kinetics as a function of average grain size reciprocal.

Table 1. Fitted parameters k_0 and k_1: nucleation and propagation kinetics.

	Mean grain Size (μm)	k_0	k_1
HR NiTi	∞	0.007	5.2
AC NiTi	400	0.011	3.5
HS NiTi	220	0.017	2.7

deformation, thus resulting in a lower stress level. This matches well with the results in Fig.4, where HR NiTi exhibits the gentlest increase in stress level.

3.5 Spatial & statistical distribution of elastic strain

The elastic deviatoric strain can be precisely quantified from μLaue diffraction patterns [11]. Each pattern gives all 6 components of the diagonal strain tensor at that scanning point. Therefore, the strain map can be established for every of the 6 strain component, as shown in Fig.8 & Fig.9 & Fig.10 for AC, HS and HR NiTi respectively. Note that the loading direction is parallel to the direction of ε_{yy}. It should also pointed out that elastic strain is equivalent to stress, so the two concepts are considered the same in the text below.

In the case of AC NiTi, the material exhibit small residual stress at initial state, though some stress concentration can be seen particularly at HAGB. The majority of strain values lie within the range $\pm 0.05\%$. However, some variations can be observed from shear strain components ε_{xz} and ε_{yz}, whose direction is perpendicular to the surface. Upon loading to 0.3% strain, which is at the end of the elastic region in the macroscopic stress-strain curve, the overall colour of ε_{yy} map changes to yellow (~0.25% elastic strain), indicating tensile force in Y direction, and those of ε_{xx} and ε_{zz} map changes to light blue (<0.1% strain), indicating compression. Stress concentration intensifies in all the 6 strain maps. Interestingly, most concentrations still happen near HAGB, which explains the phenomenon in Fig.6 that phase transformation preferentially nucleates at HAGB. Namely, phase transformation is more easily triggered at high stress regions near HAGB. At macroscopic strain level of 1.1%, local strain variation significantly broadens, particularly the shear strains, which show a range of nearly $\pm 2.5\%$. However, the exact strain value may be unreliable at this state due to the

heavy distortion of reflections in the μLaue diffraction pattern, which leads to error in refinement. Another interesting phenomenon that is worth mentioning is the difference in stiffness among grains during the loading process. For instance the ε_{yy} map, in grain No.2, No.3 and No.4 (Fig.6), they exhibit deeper yellow colour (especially grain No.2) than other grains at 0.3% and 1.1% strain. This means these grains are stiffer and undertake higher stress. They are also the three among the only four grains that survive at 1.7% strain. On the contrary, grain No.5 exhibit a lighter yellow colour at 1.1% strain, representing lower stiffness.

In the case of HS NiTi, the general observations agree well with those from AC NiTi, that the stress concentration occurs mostly at HAGB, and stress concentration intensifies throughout the loading process. Nevertheless, via comparison between AC and HS NiTi, some extra findings can be observed. Firstly, at the virgin state, HS NiTi shows more residual stress than AC NiTi, which is attributed to metal forming process, though careful heat treatment has been conducted. Secondly, at 0.3% strain, HS NiTi exhibits denser stress concentration due to the higher amount of HAGBs in HS NiTi than that of AC NiTi. This explains the higher phase transformation nucleation kinetics in material with denser HAGB in section 3.4.

HAGB between two neighbour grains indicates a large misorientation of crystallographic direction, usually greater than ~15 degrees. Because of this incoherency in lattice structure, vast majority of stress concentration occurs at HAGB both at initial state and during superelastic loading.

The HR NiTi material shows a completely different spatial distribution of strain. At initial state, the residual strain is exceptionally low, ranging from $\pm 0.025\%$ for the majority of the ε_{yy} map. Because the grain structure is dominated by LAGB, there is no obvious stress concentration upon loading to 0.3% strain and further to 0.6% strain. For

ε_{yy}, some individual points show significantly higher stress than others, but they are not clustered together as those in AC and HS NiTi, so strain distribution seems to be rather homogeneous over the entire map. This phenomenon explains the higher phase transformation propagation kinetics in a LAGB-dominated NiTi.

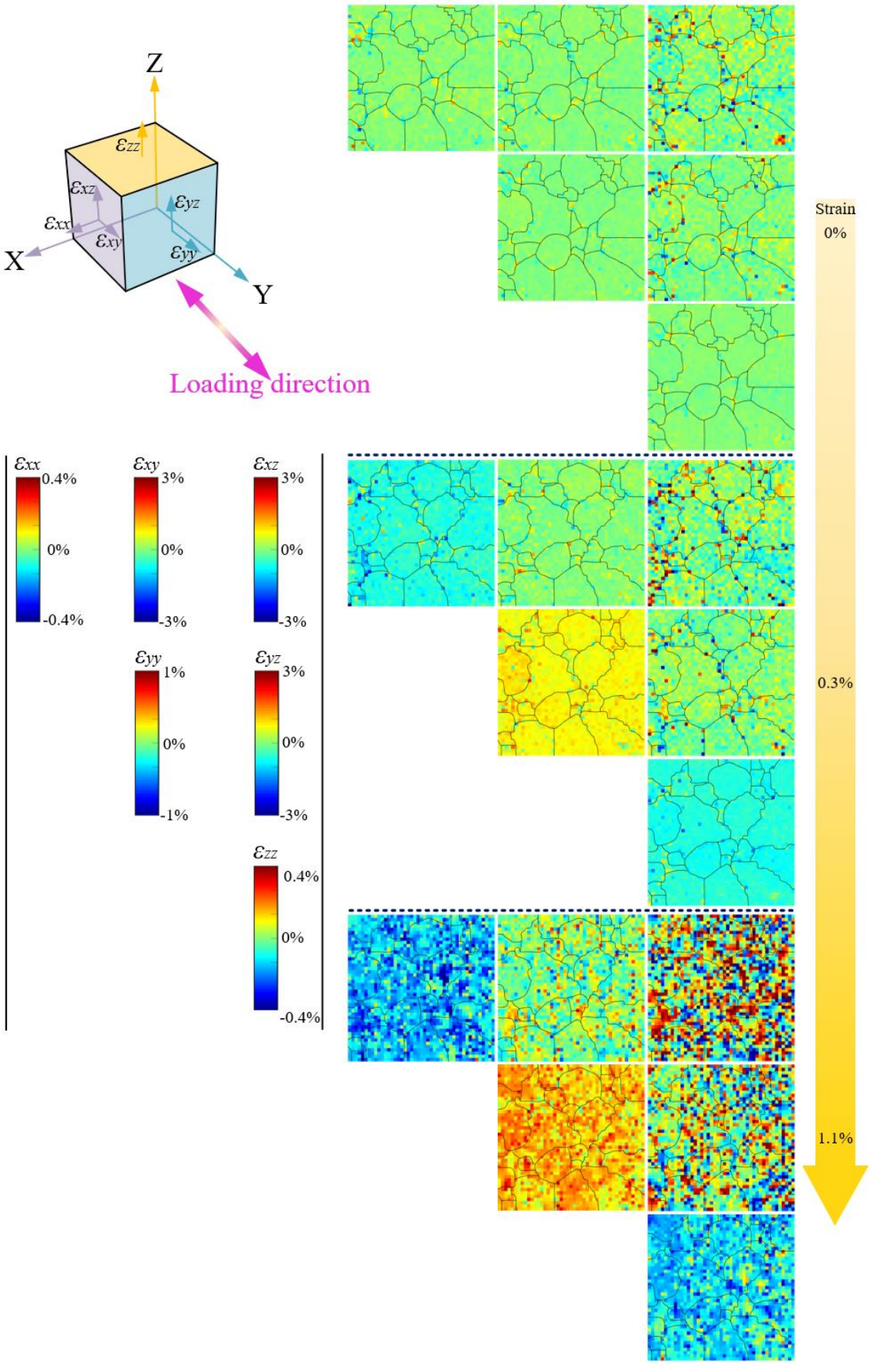


Figure 8. The evolution of elastic deviatoric strain map of AC NiTi during superelastic

tensile loading. The maps were measured at 0%, 0.3% and 1.1% strain. The scale bars of components of the diagonal strain tensor are displayed on the left hand side, with the component name sitting on top of the bar. The definition of each strain components is drawn on the top left infinitesimal cube, representing the local material volume illuminated by micro X-ray beam. The grain boundaries are derived from μLaue lattice orientation maps in Fig.6. The coordinate system corresponds to the one in Fig.6. The loading direction is parallel to Y axis. For a few scanning points where data is missing, the values are filled by linear interpolation.

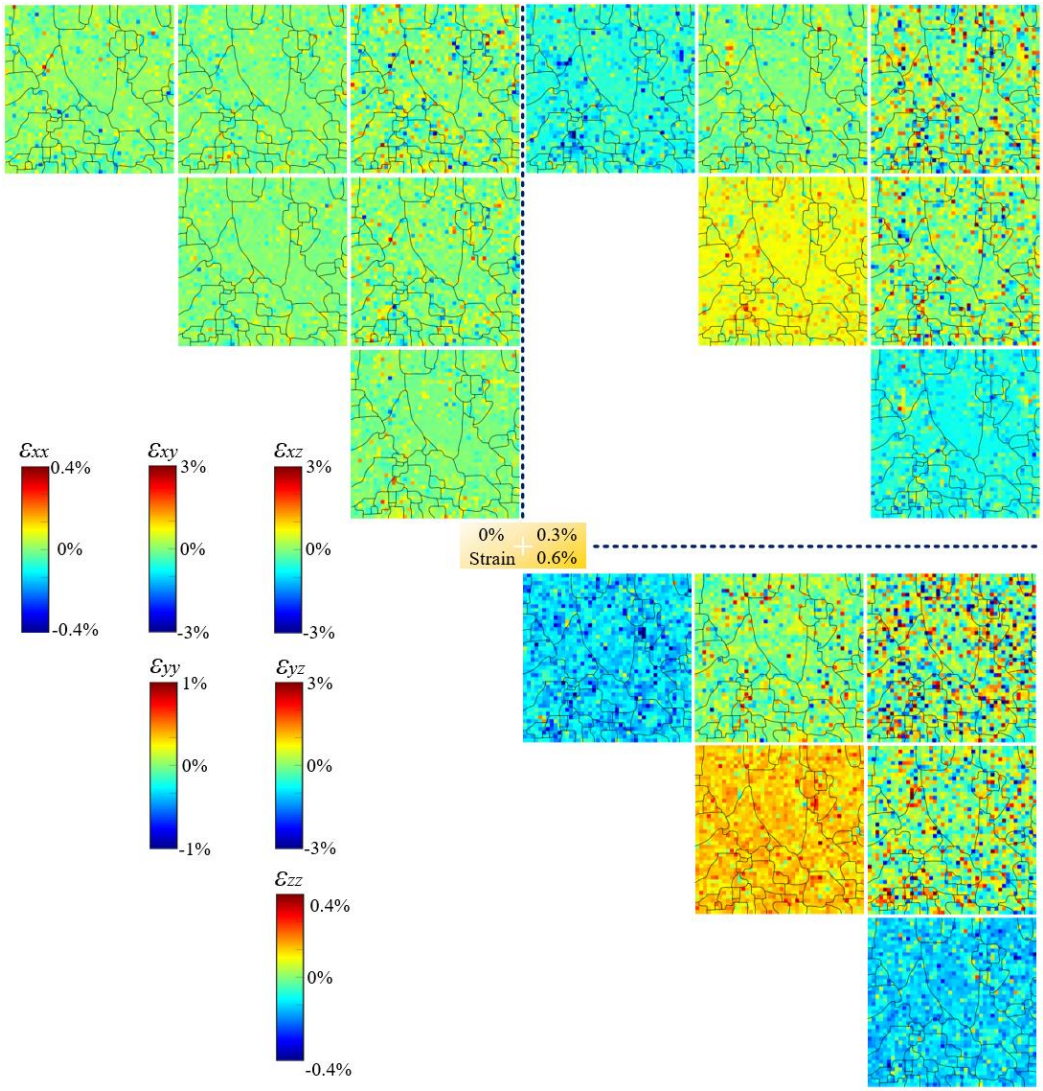


Figure 9. The evolution of elastic deviatoric strain map of HS NiTi during superelastic tensile loading. The maps were measured at 0%, 0.3% and 0.6% strain. Detailed caption refers to that of Fig.8.

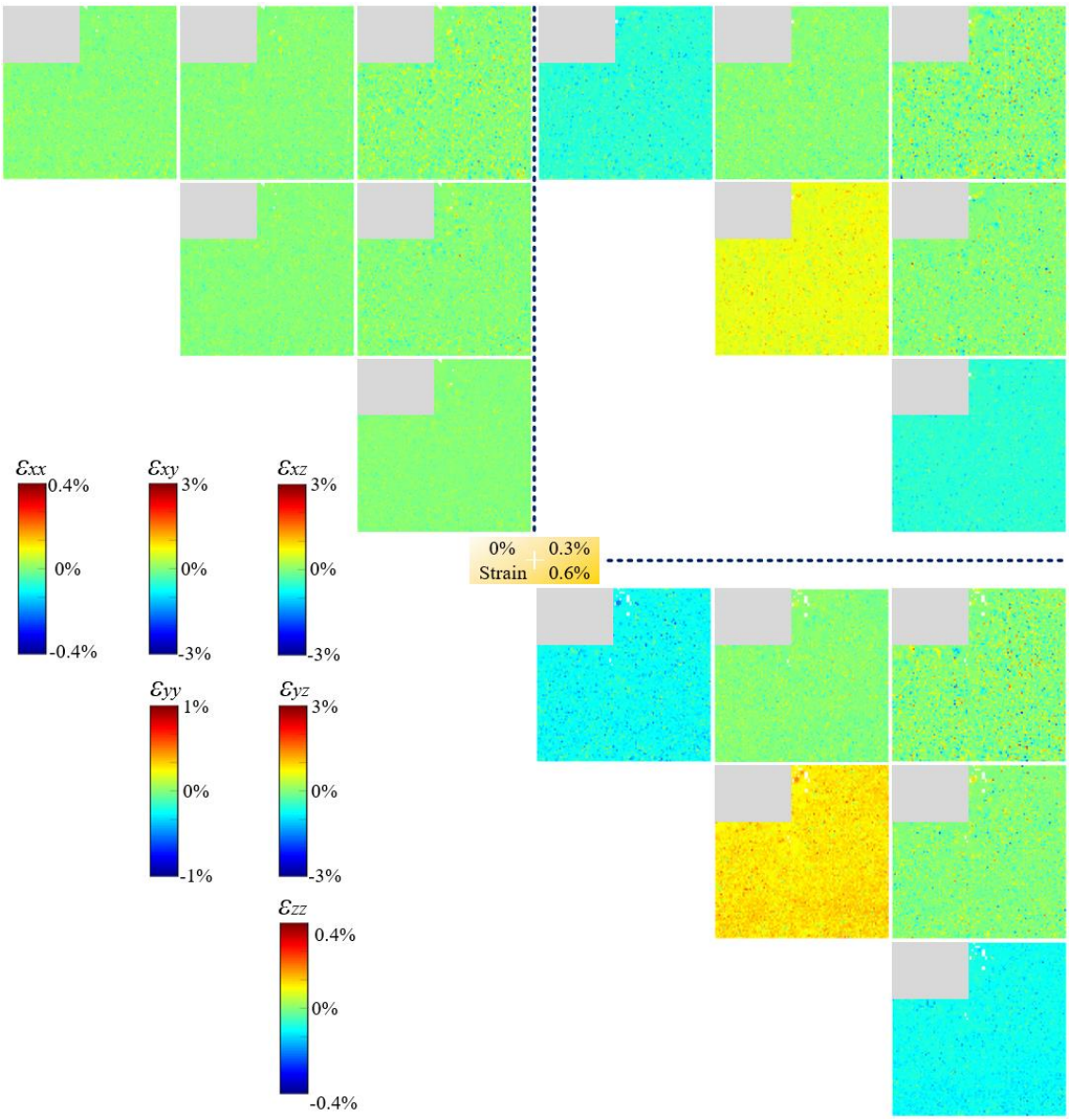


Figure 10. The evolution of elastic deviatoric strain map of HR NiTi during superelastic tensile loading. The maps were measured at 0%, 0.3% and 0.6% strain. The grey region is an non-indexed area due to unknown detector error during experiment. Detailed caption refers to that of Fig.8.

The statistical distribution of elastic strain ε_{yy} has been extracted from the maps in the previous figures and plotted in Fig.11(a-i) for all three materials.

At virgin state, HS NiTi possesses the highest residual strain as seen from the wide peak range, followed by AC NiTi, while the strain of HR NiTi mostly concentrates within

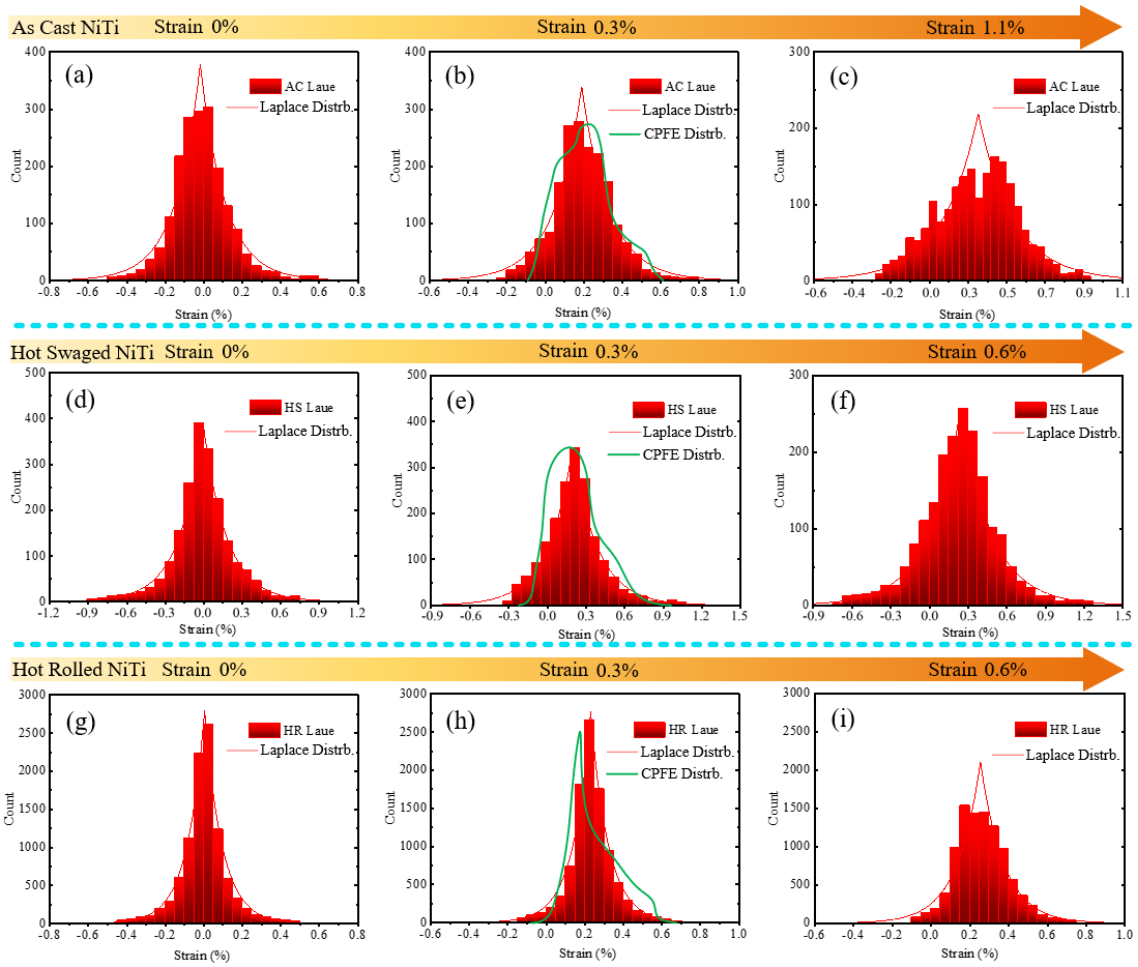


Figure 11. The evolution of statistical distribution of elastic strain ε_{yy} for AC (a,b,c), HS (d,e,f), and HR (g,h,i) NiTi during superelastic tensile loading. Red curve is the fitted Laplace distribution. Green curve is profile shape obtained from CPFE simulation in Appendix B.

$\pm$0.025%. Despite that, it is found that the statistical strain distribution of all three materials matches well with Laplace distribution, as outlined by the red line. Upon loading to 0.3% strain, the distribution profile becomes asymmetric for AC and HS NiTi, that the left side of the peak becomes steeper, and the right side extends to a much higher strain level than the average. However, the profile of HR NiTi still remains in Laplace distribution, and there is no significant broadening of peak width, except that the peak

centre shifted to ~0.24% strain. A CPFE simulation has been conducted to verify the distribution profile shape at this strain state. Detailed simulation settings refer to Appendix B. It can be seen that asymmetry feature of the strain distribution is well capture by the model, in which the distribution profile of HS NiTi exhibits a more gradual slope extending to higher strain level. At 0.6% strain, the strain distribution of HR NiTi changes to an asymmetric profile. At 1.1% strain, AC NiTi exhibits a bimodal distribution.

When the three materials are loaded to the same strain level, HS NiTi always shows the highest maximal elastic strain. For example at 0.3% strain, HS NiTi shows the maximal elastic strain of ~1%. Similar observations can be made at 0.6% strain between HS and HR NiTi. The strain distribution of HR NiTi is always the narrowest of all. This diversity in strain distribution is closely linked with grain structure, that HAGB contributes to the broadening of the distribution range and the increase in maximal strain value, whilst LAGB has less such effect. Subsequently, such difference in strain distribution causes the different phase transformation behaviour among the three materials, as discussed in Section 3.4, that a higher maximal strain and wider strain distribution range results in the higher nucleation kinetics and lower propagation kinetics, and the contrary is also true.

It should be noted that the mean elastic strain is not necessarily equal to the total strain due to phase transformation happening at the early stage of superelastic loading. At total strain of 0.3%, HR NiTi has the largest proportion new phase, hence the lowest value of mean elastic strain (~0.22%) because the rest of the total strain is accommodated by pseudo-plastic phase transformation process. Similarly, HS NiTi exhibits the highest value of elastic strain (~0.25%).

3.6 Lattice rotation of individual grains

Certain grains/regions are selected from the three materials and plotted in Fig.12(a-h). These grains and regions are labelled in Fig.6. Each coloured sphere represent a μLaue scanning point.

For AC NiTi, three of the four stiffest grains are chosen, namely grain No.1, No.3 and No.4. Interestingly, though these three grains survived at high strain level of 1.7%, they exhibit diverse rotation mode: grain No.1 starts with a cluster of orientations in the middle, upon deformation, the lattice splits into two parts, rotating to two different directions, as can be seen from the evolution from red points to green points and finally to blue points. On the contrary, grain No.4 rotates to three different directions and Grain No.3 rotates to one direction. Despite the various number of rotation directions, one thing is common, that some parts of the grain remains in their original orientation. Therefore, this rotation mode can be categorised as multi-extension rotation.

For HS NiTi, the two selected grains behave differently. No obvious rotation direction can be observed in Grain No.5, since lattice orientations seem to be constrained within a certain volume upon deformation, though slight rotations may happen locally. In comparison, grain No.6 shows a complete rotation that the entire cluster of orientations shift to another region, as can be seen in Fig.12(e). Since the whole grain is rotated in a homogeneous manner, this rotation mode can be categorised as rigid rotation.

For HR NiTi, the three regions show similar rotation behaviour as Fig.12(d). Upon deformation, the orientations changes slightly from place to place but always confined within the same limitation. Since all three regions exhibit similar behaviour, it can be assumed that this rotation mode is dominant in LAGB structure in NiTi alloy, which can be termed as non-dispersive rotation.

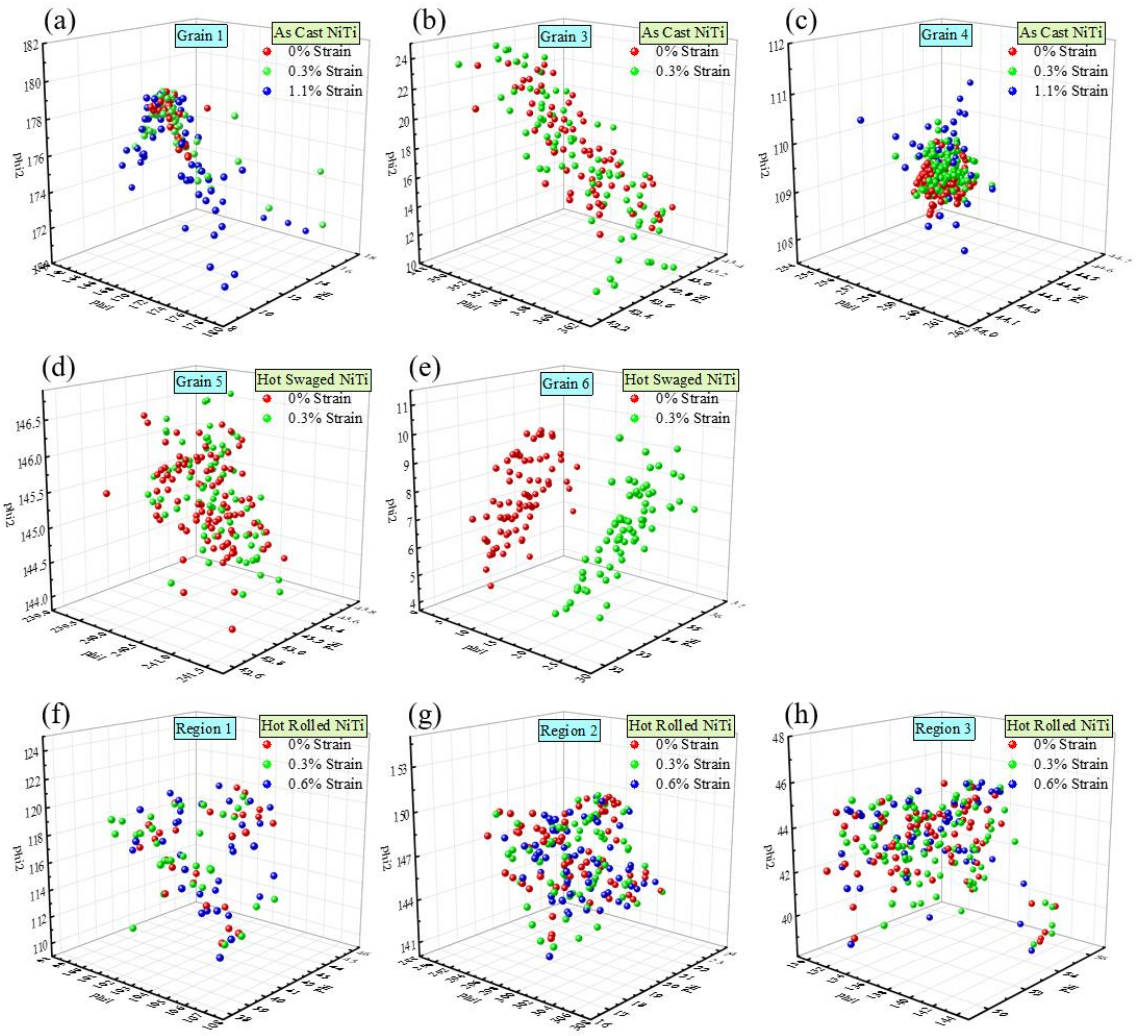


Figure 12. Lattice rotation of selected grains from the three materials: AC (a,b,c), HS (d, e), and HR (f,g,h) NiTi. Each sphere represents one scanning point. Different colours represent different loading steps. Three axes represent three Euler angles in Bunge notation (ϕ_1, Φ, ϕ_2).

3.7 Texture evolution and phase transformation preference

The mesoscale texture information is obtained from *in situ* HE-XRD experiment for all three materials. Data was recorded at virgin state and 1.7% strain. The refined texture is shown in Fig.13. Inverse pole figure is plotted in Y direction in the coordinate system defined in Fig.2. Y direction is parallel to the loading direction. Although the tensile

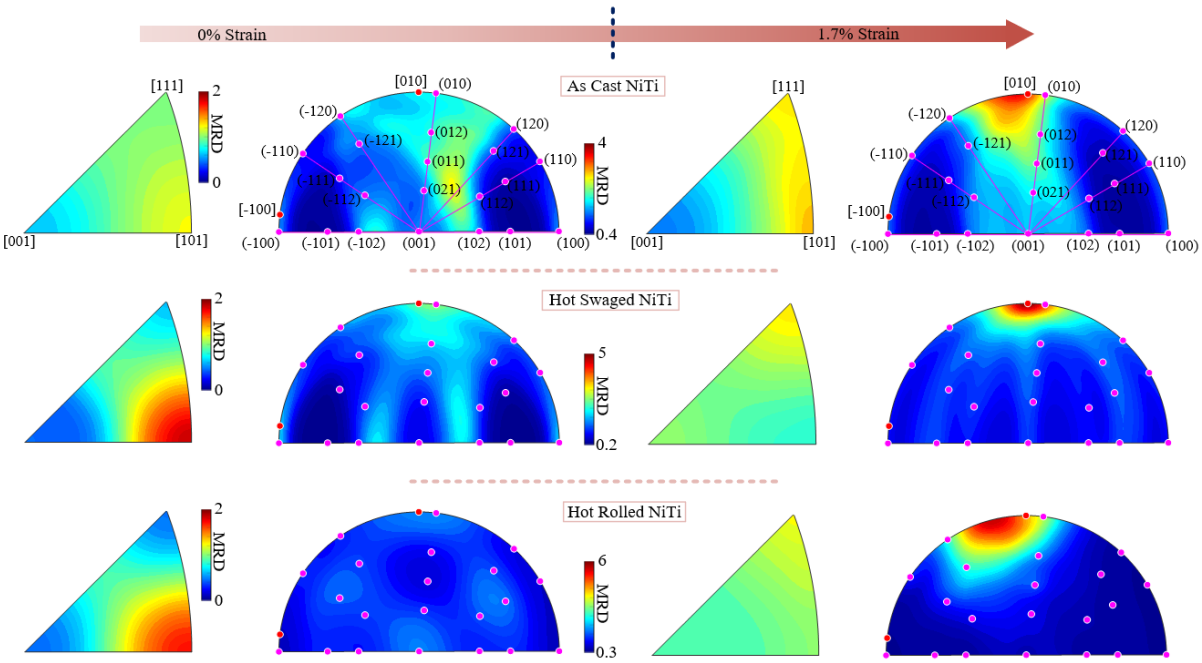


Figure 13. Texture evolution of AC, HS and HR NiTi during deformation. Inverse pole figure is plotted in loading direction (Y axis in Fig.2). The same scale bar is used for one phase, but varies in different materials.

loading was conducted above A_f temperature, some residual martensite presents in the material, thus texture of both phases can be refined at 0% strain.

At initial state, AC NiTi possesses a weak B2 phase texture of ~1.2 MRD, whilst HS NiTi and HR NiTi show stronger [101] texture. After loading to 1.7% strain, the strong texture disappears in all the three materials, and the texture reorientates to [111], but not as strong as the original state. Generally for all three materials, the texture of B2 austenite in loading direction is weakened upon loading, exhibiting a more homogenous distribution.

Regarding martensite, initial texture of the three materials were different. However, the texture evolution shows similar tendency upon deformation, that texture concentrates in [010] direction at high strain. This phenomenon agrees well with recent studies on a

nanocrystalline NiTi wire [1,4]. This behaviour of martensite phase may be related to the naturally preferred detwinning mode to accommodate the applied strain.

Overall, combined with the observations on local lattice rotation in Section 3.6, it can be concluded that the texture evolution of B2 austenite phase is not strongly dependent on lattice rotation mode and grain structure. Besides that, the texture evolution of B19' martensite is also not strongly dependent on the grain structure. All three NiTi materials show similar texture evolution mode in both phases.

4. Summary and conclusions

In the present study, NiTi Shape Memory Alloys of different grain structures have been produced using novel forming techniques. The grain structure in As Cast (AC) NiTi and Hot Swaged (HS) NiTi is composed of high angle grain boundaries (HAGBs) of different grain size: ~400μm for AC NiTi and ~220μm for HS NiTi. Meanwhile, the grain structure in Hot Rolled (HR) NiTi is dominated by low angle grain boundaries (LAGBs), very few HAGBs can be observed. These three materials exhibit diverse superelastic behaviour, and the insights into such discrepancy is given via conducting *in situ* synchrotron X-ray μLaue diffraction and powder diffraction experiment. This study serves as a guidance and opens up possibilities to customise the Superelasticity of NiTi Shape Memory Alloy by means of grain structure engineering.

Conclusions are summarised as below:

The precipitation is similar among the three materials in terms of precipitate type, size, and orientation distribution. The majority is the Ni_4Ti_3 precipitates, and the $NiTi_2$ precipitates randomly embedded in the matrix and in the Ni_4Ti_3.

Upon deformation, slight elongation of grain morphology can be observed in HAGB NiTi. Also phase transformation happens preferentially near HAGBs, while for LAGB structure, phase transformation happens randomly but overall heterogenous.

The stress-induced phase transformation kinetics is quantified by a proposed equation consisting of two kinetics parameters. It is found that the smaller the grain size, the higher the nucleation kinetics, and the lower the propagation kinetics.

Upon loading, most stress concentration happens near HAGBs for all the 6 components of the elastic deviatoric strain tensor. In HAGB structure, stress state varies among different grains. Nevertheless, no obvious stress concentration can be observed in LAGB structure during loading. The stress concentration phenomenon well explains the physical significance of the two kinetics parameters.

At virgin state, the statistical strain distribution of all three materials matches well with Laplace distribution, while it may become asymmetric during loading. Upon deformation, HAGB contributes to the broadening of the distribution range and the increase in maximal strain value, whilst LAGB has less such effect.

Three grain lattice rotation modes are identified and termed, namely multi-extension rotation, rigid rotation and non-dispersive rotation. The rotation mode in HAGB structure is a mixture of the three, whilst in LAGB, the dominant mode is non-dispersive rotation.

The texture evolution of both B2 austenite and B19’ martensite is not strongly dependent on the grain structure.

Declaration of Competing Interest

The authors declare that they have no competing interests in finance and personal relationships, which are related to the present work.

Acknowledgements

AMK and ZW wish to acknowledge the support from EPSRC IAA Doctoral Impact Scheme grant. ZW is grateful for the all-round support from Mr. Weizhong Wang and Mrs. Yong Qian. The authors would like to thank Diamond Light Source for allocation of beamtime MG25467 at I12 JEEP beamline, beamtime MM28397 at B16 beamline, and beamtime MG28418 at ePSIC E01 beamline. Meanwhile, the authors would like to thank European Synchrotron Radiation Facility for allocation of beamtime MA4478 at BM32 beamline. This research is supported by the 19-15479S project of the Czech Science Foundation. The authors are grateful for the assistance from Dr. Christopher Allen for the TEM experiment.

Data Availability

The raw/processed data required to reproduce these findings cannot be shared at this time as the data also forms part of an ongoing study.

Appendix A: Grain structure engineering methods

The manufacturing routes for grain structure engineering is depicted in Fig.S1.

Hot rotary swaging (HS) is a near-net plastic deformation method used to process solid and hollow workpieces of variable cross-sections using high-speed action of a set of dies. As a relatively rapid and low-cost industrially applied continuous manufacturing process, HS features advantageous stress-strain conditions that enable to impose very high shear strain into the processed material. HS can favourably be used to manufacture metals with Ultra-Fine-Grain structures. It can be applied to manufacture challenging materials, such as metals with low plasticity (e.g., W, Mg), powder-based pseudomaterials, and composites. Since the process imparts gradient stress/strain

distribution across cross-sections of processed workpieces, it also provides a solution for preparation of gradient microstructures [1] and residual stress distribution [29,30,31,32,33]. The NiTi workpiece was gradually swaged down from the initial diameter of 20 mm to the final diameter of 12.5 mm. Induction heating system was applied during swaging. Corresponding diagrams of deformation forces detected during the individual swaging passes are shown in Fig.S2. It is evident that the slopes of increase in the swaging force before and after the swaging time of ~2 seconds were steep for all the three passes. The total reduction ratio upon HS was 0.94.

Hot rolling was executed using a two-high rolling mill stand with the diameter of rolls of 180 mm. In order to reduce thermal loses during rolling, a higher rotational speed of the rolls was used (40 RPM). Rolling was performed in a total of eight passes with identical rolling reductions in each pass. The deformation force during the individual passes gradually increased due to the incremental imposed strain, as can be seen from the Fig.S3. The rolling force developments during the individual passes exhibited non-uniform behaviour. The maximal measured deformation force for the first pass was 43 kN, while for the second pass the value increased up to 50 kN. Similar increasing trend was monitored for the third pass. Nevertheless, after this pass, the increasing trend changed. The fourth rolling pass featured the absolute maximal force of ~72 kN and subsequent passes exhibited an opposite trend, i.e. the next three passes featured gradual decreases in the maximum achieved rolling force. The decreasing trend in the maximal force values was caused by the development of dynamic restoration processes, which plays an important role during these rolling passes. For the last pass, an increase in the rolling force was observed, which can be attributed to work hardening dominating over structure softening. The total logarithmic strain of the workpiece was 0.625.

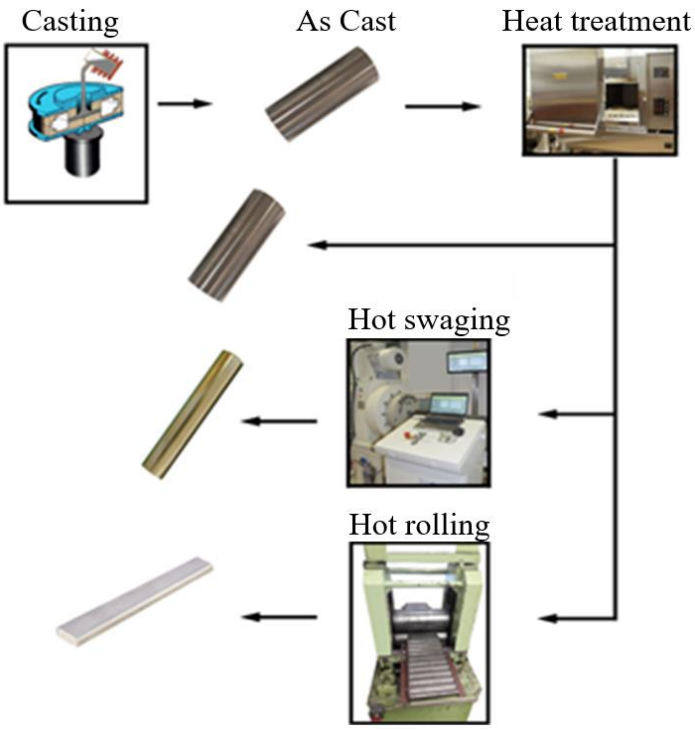


Figure S1. Grain structure engineering routes and equipment.

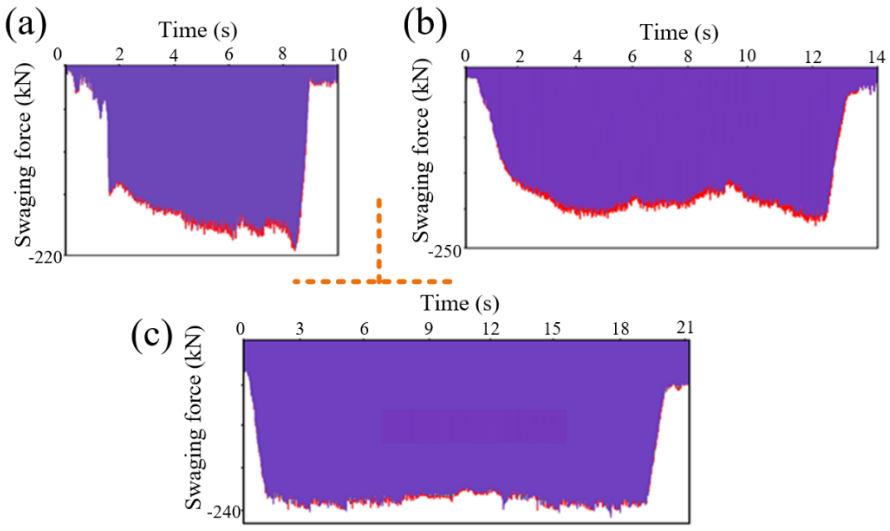


Figure S2. Swaging forces measured during NiTi HS. (a) First pass. (b) Second pass. (c) Third pass.

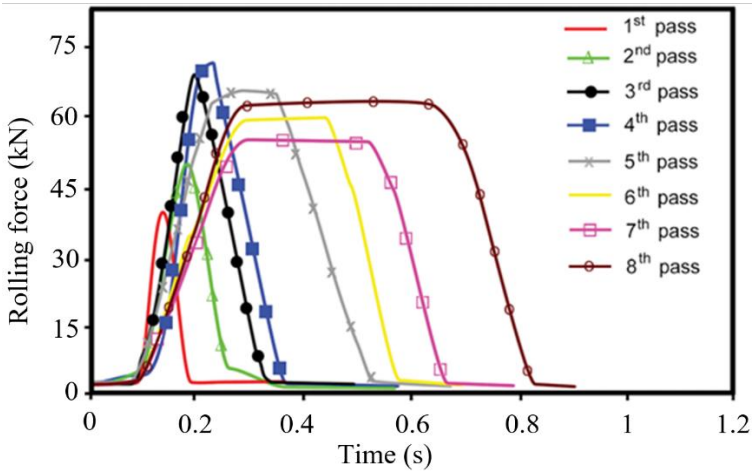


Figure S3. Rolling force development during hot rolling

Appendix B: CPFE modelling

Crystal Plasticity Finite Element (CPFE) simulation was conducted by using a strain-controlled model in our recent study [34]. The home-made Fortran code was imported in Abaqus 2021 via UMAT portal.

To prepare the crystal model properties, EBSD maps of the three materials were imported into DREAM.3D software [35]. Those EBSD maps display the grain structure at the surface layer, while that underneath is unknown. Because the thickness of the flat dog-bone sample is 1mm, which is exactly the same dimension as the width and height of the EBSD maps, columnar grain structure is assumed, and the crystal model is a 1mm×1mm×1mm cube, as illustrated in the upper row in Fig.S4. The crystal models are coloured in IPF Y direction, identical to the EBSD maps in Fig.5.

The uniaxial tensile loading is applied in X direction from 0% strain to 0.3% strain. The loading process was set to completely falls within elastic region without any plastic activity. This is confirmed by checking the model output that the plastic strain at all integration points is equal to zero. C3D8 element configuration was used, and the meshing strategy is shown in the lower row in Fig.S4. Periodic boundary condition was set using

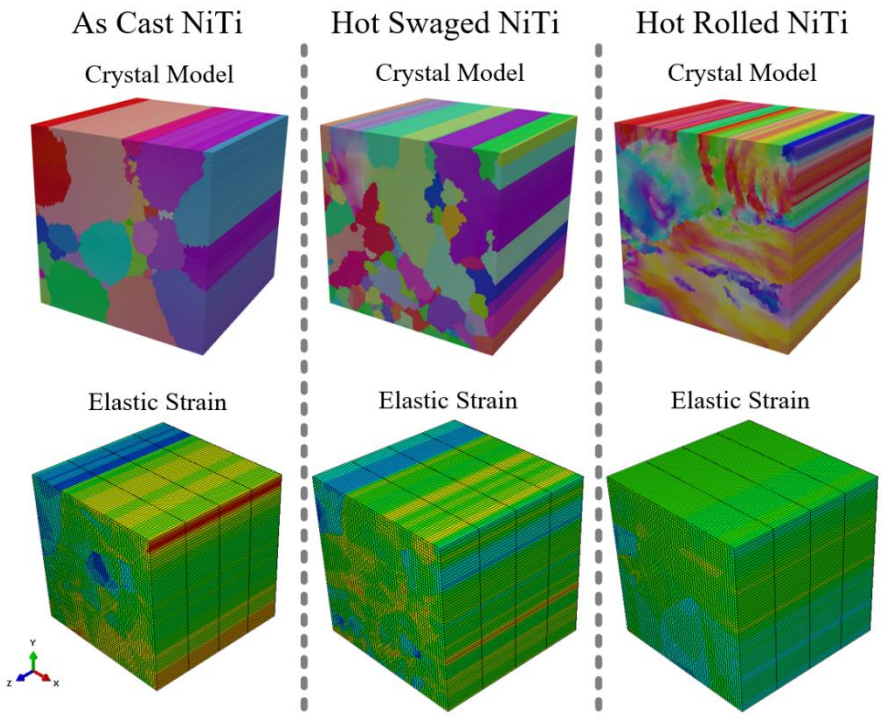


Figure S4. Crystal models (upper row) and simulation results (lower row) of the three materials. Coordinate system is given at the bottom left corner.

an Abaqus plugin tool EasyPBC. The elastic constants for B2 austenite phase were determined from literature [36], viz C_{11}=169, C_{12}=138, C_{44}=40.

The simulation result is displayed in Fig.S4. The statistical distribution of the ε_{xx} was exported from all integration points, and plotted in histogram. The profile of the histogram was fitted by a kernel smooth function, which is also known as kernel density estimation (KDE), to capture the precise shape profile. The shape profile is corrected by the function: $\varepsilon' = A \cdot (\varepsilon - \varepsilon_{mean})$, where ε_{mean} is the mean value of the entire strain distribution, the fitting parameter A is determined to be 3.5, 4.4 and 4.1 for AC, HS and HR NiTi.

References

[1] Wang, Z.; Chen, J.; Besnard, C.; Kuncicka, L.; Kocich, R.; Korsunsky, A.M. In-situ neutron diffraction investigation of texture-dependent Shape Memory Effect in a near equiatomic NiTi alloy, Acta Materialia 202 (2021) 135-148. https://doi.org/10.1016/j.actamat.2020.10.049.

[2] Wang, Z.; Korsunsky, A.M. Effect of Temperature on Shape Memory Materials, Encyclopedia of Smart Materials 4 (2022) 239-253. https://doi.org/10.1016/B978-0-12-803581-8.11793-X.

[3] Ahadi, A.; Sun, Q. Effects of grain size on the rate-dependent thermomechanical response of nanostructured superelastic NiTi, Acta Materialia 76 (2014) 186-197. https://doi.org/10.1016/j.actamat.2014.05.007.

[4] Bian, X.; Heller, L.; Kaderavek, L.; Sittner, P. In-situ synchrotron X-ray diffraction texture analysis of tensile deformation of nanocrystalline NiTi wire in martensite state, Applied Materials Today 26 (2022) 101378. https://doi.org/10.1016/j.apmt.2022.101378.

[5] Frenzel, J.; George, E.P.; Dlouhy, A.; Somsen, C.; Wagner, M.F.-X.; Eggeler, G. Influence of Ni on martensitic phase transformations in NiTi shape memory alloys, Acta Materialia 58 (2010) 3444-3458. https://doi.org/10.1016/j.actamat.2010.02.019.

[6] Benafan, O.; Noebe, R.D.; Padula II, S.A.; Garg, A.; Clausen, B.; Vogel, S.; Vaidyanathan, R. Temperature dependent deformation of the B2 austenite phase of a NiTi shape memory alloy, International Journal of Plasticity 51 (2013) 103-121.

[7] Taylor, S.L.; Ibeh, A.J.; Jakus, A.E.; Shah, R.N.; Dunand, D.C. NiTi-Nb micro-trusses fabricated via extrusion-based 3D-printing of powders and transient-liquid-phase sintering, Acta Biomaterialia 76 (2018) 359-370. https://doi.org/10.1016/j.actbio.2018.06.015.

[8] Wang, Z.; Everaerts, J.; Salvati, E.; Korsunsky, A.M. Evolution of thermal and mechanical properties of Nitinol wire as a function of ageing treatment conditions, Journal of Alloys and Compounds 819 (2020) 153024. https://doi.org/10.1016/j.jallcom.2019.153024.

[9] Kocich, R.; Szurman, I.; Kursa, M. The methods of preparation of Ti-Ni-X alloys and their forming, Shape Memory Alloys-Processing, Characterization and Applications, Croatia: InTech, pp.27-52. http://dx.doi.org/10.5772/50067.

[10] Wang, Z.; Chen, J.; Besnard, C.; Korsunsky, A.M. Microstructure evolution in a severely cold-worked NiTi wire during ageing treatment: An in situ neutron diffraction study, Materials Letters 281 (2020) 128676. https://doi.org/10.1016/j.matlet.2020.128676.

[11] Plancher, E.; Petit, J.; Maurice, C.; Favier, V.; Saintoyant, L.; Loisnard, D.; Rupin, N.; Marijon, J.B.; Ulrich, O.; Bornert, M.; Micha, J.S.; Robach, O.; Castelnau, O. On the Accuracy of Elastic Strain Field Measurements by Laue Microdiffraction and High-Resolution EBSD: a Cross-Validation Experiment, Experimental Mechanics 56 (2016) 483-492. https://doi.org/ 10.1007/s11340-015-0114-1.

[12] Korsunsky, A.M.; Song, X.; Hofmann, F.; Abbey, B.; Xie, M.; Connolley, T.; Reinhard, C.; Atwood, R.C.; Connor, L.; Drakopoulos, M. Polycrystal deformation analysis by high energy synchrotron X-ray diffraction on the I12 JEEP beamline at Diamond Light Source, Mater. Lett. 64 (2010) 1724-1727. https://doi.org/10.1016/j.matlet.2010.04.023.

[13] Kuncicka, L.; Kocich, R. Deformation behaviour of Cu-Al clad composites produced by rotary swaging, IOP Conf. Ser. Mater. Sci. Eng. 369 (2018) 012029. https://doi.org/10.1088/1757-899X/369/1/012029.

[14] Kocich, R.; Kursa, M.; Szurman, I.; A. Dlouhy, The influence of imposed strain on the development of microstructure and transformation characteristics of Ni-Ti shape memory alloys, J. Alloys Compd. 509 (2011) 2716-2722. https://doi.org/10.1016/j.jallcom.2010.12.003

[15] Kocich, R.; Kuncicka, L.; Kral, P.; Strunz, P. Characterization of innovative rotary swaged Cu-Al clad composite wire conductors, Mater. Des. 160 (2018) 828–835. https://doi.org/10.1016/j.matdes.2018.10.027.

[16] Kocich, R.; Kuncicka, L.; Dohnalik, D.; Machackova, A.; Sofer, M. Cold rotary swaging of a tungsten heavy alloy: Numerical and experimental investigations, Int. J. Refract. Met. Hard Mater. 61 (2016) 264–272. https://doi.org/10.1016/j.ijrmhm.2016.10.005.

[17] Schaffer, M.; Schaffer, B.; Ramasse, Q. Sample preparation for atomic-resolution STEM at low voltages by FIB, Ultramicroscopy 114 (2012) 62-71. https://doi.org/10.1016/j.ultramic.2012.01.005.

[18] Ulrich, O.; Biquard, X.; Bleuet, P. A new white beam X-ray microdiffraction setup on the BM32 beamline at the European Synchrotron Radiation Facility, Rev. Sci. Instrum. 82 (2011) 033908. https://doi.org/10.1063/1.3555068.

[19] Statnik, E.S.; Salimon, A.I.; Besnard, C.; Chen, J.; Wang, Z.; Moxham, T.; Dolbnya, I.P.; Korsunsky, A.M. Ovine Bone Morphology and Deformation Analysis Using Synchrotron X-ray Imaging and Scattering, Quantum Beam Science 4(3) (2020) 29. https://doi.org/10.3390/qubs4030029.

[20] Micha, J.S. lauetools: A Software Package for Laue Microdiffraction Data Analysis, (unpublished).

[21] Wang, Z.; Chen, J.; Magdysyuk, O.V.; Uzun, F.; Korsunsky, A.M. Ultra-fast quantification of polycrystalline texture via single shot synchrotron X-ray or neutron diffraction, Materials Characterization 186 (2022) 111827. https://doi.org/10.1016/j.matchar.2022.111827.

[22] Bachmann, F.; Hielscher, R.; Schaeben, H. Texture analysis with MTEX-Free and open source software toolbox, Solid State Phenom. 160 (2010) 63-68. https://doi.org/10.4028/www.scientific.net/SSP.160.63.

[23] Toby, B.H.; Von Dreele, R.B. GSAS-II: the genesis of a modern open-source all purpose crystallography software package, Journal of Applied Crystallography 46 (2013) 544-549. https://doi.org/10.1107/S0021889813003531.

[24] Bordin, S.F.; Limandri, S.; Ranalli, J.M.; Castellano, G. EBSD spatial resolution for detecting sigma phase in steels, Ultramicroscopy 171 (2016) 177-185. https://doi.org/10.1016/j.ultramic.2016.09.010.

[25] Berveiller, S.; Malard, B.; Wright, J.; Patoor, E.; Geandier, G. In situ synchrotron analysis of lattice rotations in individual grains during stress-induced martensitic transformations in a polycrystalline CuAlBe shape memory alloy, Acta Materialia 59 (2011) 3636-3645. https://doi.org/10.1016/j.actamat.2011.02.037.

[26] Polatidis, E.; Smid, M.; Kubena, I.; Hsu, W.N.; Laplanche, G.; Van Swygenhoven, H. Deformation mechanisms in a superelastic NiTi alloy: An in-situ high resolution digital image correlation study, Materials&Design 191 (2020) 108622. https://doi.org/10.1016/j.matdes.2020.108622.

[27] Molnarova, O.; Tyc, O.; Heller, L.; Seiner, H.; Sittner, P. Evolution of martensitic microstructures in nanocrystalline NiTi wires deformed in tension, Acta Materialia 218 (2021) 117166. https://doi.org/10.1016/j.actamat.2021.117166.

[28] Sedmak, P.; Sittner, P.; Pilch, J.; Curfs, C. Instability of cyclic superelastic deformation of NiTi investigated by synchrotron X-ray diffraction, Acta Materialia 94 (2015) 257-270. https://doi.org/10.1016/j.actamat.2015.04.039.

[29] Canelo-Yubero, D.; Kocich, R.; Hervoches, C.; Strunz, P.; Kuncicka, L.; Kratka, L. Neutron Diffraction Study of Residual Stresses in a W-Ni-Co Heavy Alloy Processed by Rotary Swaging at Room and High Temperatures, Metals and Materials International (2021) https://doi.org/10.1007/s12540-020-00963-8.

[30] Uzun, F.; Papadaki, C.; Wang, Z.; Korsunsky, A.M. Neutron strain scanning for experimental validation of the artificial intelligence based eigenstrain contour method, Mechanics of Materials 143 (2020) 103316. https://doi.org/10.1016/j.mechmat.2020.103316.

[31] Uzun, F.; Salimon, A.I.; Statnik, E.S.; Besnard, C.; Chen, J.; Moxham, T.; Salvati, E.; Wang, Z.; Korsunsky, A.M. Polar transformation of 2D X-ray diffraction patterns and the experimental validation of the hDIC technique, Measurement 151 (2020) 107193. https://doi.org/10.1016/j.measurement.2019.107193.

[32] Brandt, L.R.; Marie, J.; Moxham, T.; Forstermann, D.P.; Salvati, E.; Besnard, C.; Papadaki, C.; Wang, Z.; Bruce, P.G.; Korsunsky, A.M. Synchrotron X-ray quantitative evaluation of transient deformation and damage phenomena in a single nickel-rich cathode particle, Energy & Environmental Science 13 (2020) 3556-3566. https://doi.org/10.1039/D0EE02290J.

[33] Chen, J.; Salvati, E.; Uzun, F.; Papadaki, C.; Wang, Z.; Everaerts, J.; Korsunsky, A.M. An experimental and numerical analysis of residual stresses in a TIG weldment of

a single crystal nickel-base superalloy, Journal of Manufacturing Processes 53 (2020) 190-200. https://doi.org/10.1016/j.jmapro.2020.02.007.

[34] Chen, J.; Wang, Z.; Korsunsky, A.M. Multiscale stress and strain statistics in the deformation of polycrystalline alloys, International Journal of Plasticity 152 (2022) 103260. https://doi.org/10.1016/j.ijplas.2022.103260.

[35] Groeber, M.A.; Jackson, M.A. DREAM.3D: A Digital Representation Environment for the Analysis of Microstructure in 3D, Integrating Materials and Manufacturing Innovation 3 (2014) 56-72. https://doi.org/10.1186/2193-9772-3-5.

[36] Sittner, P.; Heller, L.; Pilch, J.; Curfs, C.; Alonso, T.; Favier, D. Young's Modulus of Austenite and Martensite Phases in Superelastic NiTi Wires, Journal of Materials Engineering and Performance 23 (2014) 2303-2314. https://doi.org/10.1007/s11665-014-0976-x.

Chapter 8 - Conclusions and outlook

Nitinol, the archetypal "mechanically functional" material exhibiting shape memory, actuation and superelastic deformation, is capable of undergoing internal phase transformation that is highly sensitive to its processing history and determines its performance. This important linkage was thoroughly researched in this project. Specifically, four metal forming procedures were taken into consideration in this thesis, viz. casting, hot rotary swaging, hot rolling, and cold drawing. Together with heat treatment, there were five processing methods investigated. The two most important aspects of functional properties were covered, namely, the shape memory effect, and superelasticity. Observations were made right across the range of scales, namely, macroscale, mesoscale, microscale, and nanoscale. Thus, the work reported has fully engaged with and addressed the topic defined in the Thesis title: "Influence of Processing Methods on Microstructure and Multiscale Functional Properties of Nitinol".

It was found that the metal forming method exerts an overwhelming influence on the functional properties of Nitinol. The origin of this phenomenon lies to the fact that materials produced by different methods possess diverse microstructures. The microstructures discussed in this thesis were considered and classified in terms of the following aspects: grain morphology, grain size, grain boundary type, crystallinity, preferred grain orientation, precipitation, lattice defects, phase composition. The different mechanisms and extent of influence of these factors on the functional properties were identified and pinpointed. For instance, the grain boundary type mainly controls the phase transformation kinetics, whilst the phase composition is the main parameter that controls

the recoverable strain, and the preferred grain orientation (texture) has a dominant effect on the elastic response during functional behaviour.

On the other hand, the heat treatment effect was found to be readily understood and predicted. The microstructural modification due to heat treatment is limited in its complexity. For instance, the grain size can be increased by the annealing treatment, lattice defect density can also be reduced by annealing, and further ageing treatment brings about the formation of various types of precipitate. These changes in the microstructure, in turn, affect the functional properties. However, the evidence collected shows that these effects quickly reach a saturation level, for example, the critical phase transformation stresses show a major decrease of ~100MPa after 3 hours of heat treatment. Similarly, the critical phase transformation temperature shows a major increase of merely 10°C after 3 hours of heat treatment. One of the key conclusions that was drawn is that only carefully selected and controlled heat treatment conditions can improve the material functional properties. In fact, in most cases heat treatment leads to the degradation of the alloy's thermomechanical performance.

This thesis presents detailed insights into the processing-structure-property relationships for Nitinol material. The knowledge assembled provides the theoretical guidance for the customization of the functional properties of Nitinol. The process of collecting and distilling knowledge proceeds from left-to-right, from specific aspects to overall picture, from detail to broad brush. Whilst this cognitive process is a widely recognised and familiar paradise for mankind understanding Nature, the knowledge thus extracted and enriched to the form of science should also support the right-to-left movement, in that it should serve real life needs. In the engineering application scenarios, problem needs to be solved in a reverse way, namely, for a given property determined by specific application, it is necessary to find out the corresponding microstructure that

delivers this certain property, and furthermore, the proper processing method to obtain this certain microstructure. This is a much harder challenge, and notable success in pursuing this paradigm form the underpinning pillars of materials industry.

The same paradigm applies to Nitinol material and its study, including in the present project. Considering that this material already enjoys extensive applications in everyday life, it is of great commercial value to find a property-structure-processing route for specific customised needs. To help tackle this challenge, the author has recently been granted an EPSRC IAA project entitled “Customising/ Enhancing the thermomechanical performance of Shape Memory Alloy for deployable structures”. As a follow-up of this thesis, the potential outcome of this project will be the establishment of a customization route that can be used to produce the material of desired properties, say, within a certain range of technical specifications.

Another future objective is the development of a two-way Shape Memory Effect. In this thesis, only the one-way Shape Memory Effect has been studied. In applications, the two-way Shape Memory Effect may prove to be much more useful. The two-way Shape Memory Effect refers to the functional property of the alloy that enables it to “remember” two different configurations (shapes), one at low temperature, and the other at high temperature. For instance, in a deployable structure such as a vascular stent, the current approach is to wrap the stent in a “scabbard”. Upon delivering it to the right position in the body, the scabbard is removed by sliding along the stent base, so that the stent is fully exposed to the blood stream and expands by the one-way Shape Memory Effect. However, to extract the stent, the scabbard has to be reinserted in a difficult and dangerous procedure. In comparison, if the two-way Shape Memory Effect could be utilised, the structure could be expanded by the application of local heating. Upon the removal of local

heating the structure would be cooled by the blood stream, to ease the process of its extraction. This topic will be explored in the upcoming EPSRC IAA project.

The last aspect of outlook and recommendation concerns the introduction of the third alloying element in Nitinol, changing the material to NiTi-based Shape Memory Alloy. This is a challenging topic, as the discovery of the third element to enable new effects often depends on fortune. Until now, there has not been extensive relevant studies, nor systematic reviews. From the author's perspective, the best way forward would be to seek to develop a theory prior to undertake experiments to avoid overusing the trial-and-error approach. It is clear, however, that even a small-scale discovery in this topic could bring huge impact to the industry.

To conclude, it is apparent that to a degree, this thesis is probably not the end but rather the start of a journey.